**FACULTÉ DES ÉTUDES SUPÉRIEURES ET POSTOCTORALES**

uOttawa
L'Université canadienne
Canada's university

**FACULTY OF GRADUATE AND POSDOCTORAL STUDIES**

Timothy C. Gorjanc
AUTEUR DE LA THÈSE / AUTHOR OF THESIS

Ph.D. (Physics)
GRADE / DEGREE

Department of Physics
FACULTÉ, ÉCOLE, DÉPARTEMENT / FACULTY, SCHOOL, DEPARTMENT

Organic Electronic and Photonic Devices Based on Pentacene and Modified Oligo-p-phenylenevinylenes
TITRE DE LA THÈSE / TITLE OF THESIS

Marie D'Iorio
DIRECTEUR (DIRECTRICE) DE LA THÈSE / THESIS SUPERVISOR

CO-DIRECTEUR (CO-DIRECTRICE) DE LA THÈSE / THESIS CO-SUPERVISOR

EXAMINATEURS (EXAMINATRICES) DE LA THÈSE / THESIS EXAMINERS

Serge Desgreniers
Frank Hegmann
Rejean Munger
Gerlad Oakham

Gary W. Slater
LE DOYEN DE LA FACULTÉ DES ÉTUDES SUPÉRIEURES ET POSTDOCTORALES / DEAN OF THE FACULTY OF GRADUATE AND POSTDOCORAL STUDIES

# Organic Electronic and Photonic Devices Based on Pentacene and Modified Oligo-p-phenylenevinylenes

Timothy C. Gorjanc

Thesis submitted to the
Faculty of Graduate and Postdoctoral Studies
in partial fulfillment of the requirements for the degree of

Doctor of Philosophy
in
Physics

Department of Physics
Faculty of Science
University of Ottawa

May 2005

Library and
Archives Canada

Published Heritage
Branch

395 Wellington Street
Ottawa ON K1A 0N4
Canada

Bibliothèque et
Archives Canada

Direction du
Patrimoine de l'édition

395, rue Wellington
Ottawa ON K1A 0N4
Canada

*Your file Votre référence*
*ISBN: 0-494-10968-8*
*Our file Notre référence*
*ISBN: 0-494-10968-8*

NOTICE:
The author has granted a non-exclusive license allowing Library and Archives Canada to reproduce, publish, archive, preserve, conserve, communicate to the public by telecommunication or on the Internet, loan, distribute and sell theses worldwide, for commercial or non-commercial purposes, in microform, paper, electronic and/or any other formats.

The author retains copyright ownership and moral rights in this thesis. Neither the thesis nor substantial extracts from it may be printed or otherwise reproduced without the author's permission.

AVIS:
L'auteur a accordé une licence non exclusive permettant à la Bibliothèque et Archives Canada de reproduire, publier, archiver, sauvegarder, conserver, transmettre au public par télécommunication ou par l'Internet, prêter, distribuer et vendre des thèses partout dans le monde, à des fins commerciales ou autres, sur support microforme, papier, électronique et/ou autres formats.

L'auteur conserve la propriété du droit d'auteur et des droits moraux qui protège cette thèse. Ni la thèse ni des extraits substantiels de celle-ci ne doivent être imprimés ou autrement reproduits sans son autorisation.

---

In compliance with the Canadian Privacy Act some supporting forms may have been removed from this thesis.

While these forms may be included in the document page count, their removal does not represent any loss of content from the thesis.

Conformément à la loi canadienne sur la protection de la vie privée, quelques formulaires secondaires ont été enlevés de cette thèse.

Bien que ces formulaires aient inclus dans la pagination, il n'y aura aucun contenu manquant.

Canada

# Abstract

This thesis is an account of the fabrication of organic field effect transistors using pentacene and two novel oligomers; bis-(4,4'-(biphenyl)ethenyl)phenyl and bis-(4,4'-(octylbiphenyl)ethenyl)phenyl. Organic light emitting diodes were also fabricated using bis-(4,4'-(biphenyl)ethenyl)phenyl and bis-(4,4'-(octylbiphenyl)ethenyl)phenyl in various configurations.

A hole field effect mobility of 2.4 cm$^2$/Vs was observed in pentacene transistor. To our knowledge, this is one of the highest field effect mobilities obtained from a polycrystalline pentacene thin film. bis-(4,4'-(biphenyl)ethenyl)phenyl displayed extremely poor film forming qualities and did not exhibit any significant field effect. A hole field effect mobility of 0.31 cm$^2$/Vs was achieved using bis-(4,4'-(octylbiphenyl)ethenyl)phenyl.

In order to fabricate high quality organic field effect transistors, a self assembled monolayer is usually applied to the gate dielectric prior to the deposition of the organic semiconductor. Three monolayers have been studied: hexamethyldisilazane,*n*-octyltrichlorosilane, and *n*-octadecyltrichlorosilane. Through a systematic process, monolayer deposition recipes were developed which resulted in the formation of ultra-smooth surfaces with contact angles of 75-80° for hexamethyldisilazane and 105-110° for the two trichlorosilane derivatives. The formation of ultra-smooth monolayers is critical to fabricating an organic transistor with superior operating characteristics.

The oligomers were characterized using cyclic voltammetry to determine the energy levels and differential scanning calorimetry to study their thermal behaviour. Optical absorption and fluorescence spectroscopy was performed to determine the onset of absorption and the main emission wavelengths. The electronic spectra of the oligomers were modeled using semi-empirical quantum mechanical calculations (PM3 and Zindo).

Polycrystalline thin films were grown in high vacuum using a Knudsen cell. The substrate temperature was held between room temperature and 225°C. The resulting films were characterized by powder x-ray diffraction and atomic for microscopy. Both of these techniques indicated that the thin films formed a lamellar structure parallel to the substrate surface with the lamella thickness corresponding to the length of the molecule, between 42 and 44 Å. The different monolayers did not seem to effect the thickness of the lamella but did increase the size of the grains.

Both oligomers were used in single and multi-layer organic light emitting diodes. The single layer organic light emitting diodes displayed faint electroluminescence while the multi-layer devices displayed more intense electroluminescence. The electroluminescence and fluorescence spectra are identical, indicating that recombination occurs solely within the oligomer layer. In the multi-layer organic light emitting diodes, different hole transporting materials such as were used in conjunction with the oligomers, which were employed as the emitter. The devices that generated the most intense electroluminescence were the N,N'-diphenyl-N,N'-bis(3-methylphenyl benzadine)/bis-(4,4'-(octylbiphenyl)ethenyl)phenyl device had a luminance of 174 cd/m$^2$ and the N,N'-diphenyl-N,N'-bis(3-methylphenyl benzadine)/bis-(4,4'-(biphenyl)ethenyl)phenyl device was brighter with a luminance of 580 cd/m$^2$.

# Statement of Originality

The results presented in this thesis were obtained by the author during the duration of his Ph.D. research project under the supervision of Dr. Marie D'Iorio at the Institute for Microstructural Sciences (IMS), National Research Council Canada. Extensive searches of the literature have not revealed any previous publications regarding the synthesis of BBEP or 8H-BBEP or of their use in any form of organic light emitting diodes (OLEDs) and organic field effect transistors (OFETs). To the best of the author's knowledge, these results are unique and original.

Prior to January 1999, there was no research effort at IMS on OFETs. The results which are presented in this thesis are the product of my initiation of this project within the Organic Materials and Devices Group (OMDG). The two novel materials which are the main focus of this work were first synthesized by Dr. Isabelle Lévesque. In addition to the synthesis, Dr. Lévesque performed cyclic voltammetry measurements on both materials and fabricated the OLEDs with TPD. The data resulting from measurements made by Dr. Lévesque are identified as unpublished data or personal communication.

Jeff Fraser and Michel Beaulieu aided in the acquisition of the SEM images Michel Beaulieu and Simona Moisa aided in the acquisition of the AFM images. The XRD of powder samples were performed at the Steacie Institute for Molecular Sciences (SIMS) by Dr. Gary Enright. The differential scanning calorimetry measurements were performed by Dr. Jianping Lu of the OMDG.

Over the course of my Ph.D. project, I have performed the following tasks:

1. The design and fabrication of photolithography masks.

2. The development of a process to fabricate top-contact OFETs.
3. The optimization of a purification system for organic materials.
4. The development of processes to grow high quality self assembled monolayers.
5. The growth of OFET and OLED structures.
6. The microfabrication of OFET and OLED structures.
7. The electrical measurements of pentacene, BBEP, and 8H-BBEP OFETs.
8. The electrical and optical measurements of BBEP and 8H-BBEP OLEDs.
9. The powder XRD on thin film samples of BBEP and 8H-BBEP.
10. The quantum chemical calculations on BBEP and 8H-BBEP structures.

I have also fabricated Canada's first flexible OLED. This was displayed by former NRC President Dr. Arthur Carty in Time Magazine (Time Canada; 03/12/2001, 157, 10, p.54). I also participated in the commissioning of an RF magnetron sputtering system for sputtering indium tin oxide (ITO) at room temperatures. This system used on a regular basis and a paper on the characteristics of room-temperature RF magnetron sputtered ITO was published. Concurrently, I created several computer controlled data acquisition programs which are regularly used by group members to characterize OLEDs. I have also assisted in the commissioning of laboratory equipment, high vacuum deposition systems, characterization systems, and participated in the daily operations of the clean room and characterization labs belonging to the Organic Materials and Devices group.

The following papers have been published during the tenure of my Ph.D.:

1. C. Py, T.C. Gorjanc, T. Hadizad, J. Zhang, Z.-Y. Wang, *Dithiophene-Substituted Indenofluorene as a potential laser material: charge transport and emitting properties*, Applied Physics Letters, submitted (2005).

2. T. Hadizad, J. Zhang, Z.-Y. Wang, C. Py, and T.C. Gorjanc, *A new general route to indenofluorene derivatives as potential new organic semiconductors*, Organic

Letters, 7, 795-797 (2005).

3. T. C. Gorjanc, I. Lévesque, C. Py, and M. D'Iorio, *Oligo-p-phenylenevinylene organic thin film transistors with chemically modified dielectric surfaces*, Journal of Vacuum Science and Technology A, 22, 760-763 (2004).

4. T. C. Gorjanc, I. Lévesque, and M. D'Iorio, *Organic FETs based on modified oligo-p-phenylenevinylenes*, Applied Physics Letters, 84, 930 (2004).

5. T.C. Gorjanc, D. Leong, C. Py, and D. Roth, *Room temperature deposition of ITO using r.f. magnetron sputtering*, Thin Solid Films, 413, 181-185 (2002).

6. J. Lam, Y. Tao, M. D'Iorio, and T.C. Gorjanc, *Selective doping of multilayer organic light emitting devices*, Journal of Vacuum Science and Technology A, 18, 593-596 (2000).

7. S. Gauvin, F. Santerre, J.P. Dodelet, Y. Ding, A.R. Hlil, A.S. Hay, J. Anderson, N.R. Armstrong, T.C. Gorjanc, and M. D'Iorio, *Organic light emitting devices containing a highly substituted isoindole or polyisoindole*, Thin Solid Films, 353, 218-222, (2000).

8. Y. Tao, A. Donat-Bouillud, M. D'Iorio, J. Lam, T.C. Gorjanc, C. Py, M.S. Wong, and Z.H. Li, *Organic light emitting diodes based on end-substituted oligo(phenylenevinylene)s*, Thin Solid Films, 363, 298-301 (2000).

9. Y. Tao, A. Donat-Bouillud, M. D'Iorio, J. Lam, T.C. Gorjanc, C. Py, and M.S. Wong, *Luminance properties of end-substituted oligo(phenylenevinylene)s*, Synthetic Metals 111-112, 417-420 (2000).

And to the following presentations and posters:

10. T.C. Gorjanc, *Organic Light Emitting and Electronic Devices*, Department of Chemistry, University of British Columbia, Vancouver, British Columbia, Canada, March 2004 (invited).

11. T.C. Gorjanc, I. Lévesque, and M. D'Iorio, *Organic Field Effect Transistors Based On A Novel p-type oligo-p-phenylevinylene oligomer,* 11th Canadian Semiconductor Technology Conference, Ottawa, Ontario, Canada, August 2003.

12. T.C. Gorjanc and C. Py, *A Flexible Organic LED Display on a Polyester Substrate*, Canada-France Conference on Molecular Photonics and Electronics, Montebello, Quebec, Canada, October 15-17 2001.

13. T.C. Gorjanc and C. Py, *A Flexible Organic LED Display on a Polyester*

*Substrate*, 10th Canadian Semiconductor Technology Conference, Ottawa, Ontario, Canada, August 2001.

14. D. Leong, C. Py, D. Roth, and T.C. Gorjanc, *Room Temperature RF Magnetron Sputtered ITO for Reversed OLEDs*, Workshop on Organics for Photonics and Electronics, Ottawa, Ontario, Canada, August 12, 2001.

15. D. Leong, C. Py, D. Roth, and T.C. Gorjanc, *Room Temperature RF Magnetron Sputtered ITO for Reversed OLEDs*, 10th Canadian Semiconductor Technology Conference, Ottawa, Ontario, Canada, August 2001.

# Acknowledgments

I would like to extend my deepest gratitude to my supervisor, Dr. Marie D'Iorio, and the Institute for Microstructural Sciences for providing me the opportunity to carry out research in one of the world's premier research institutions. I also gratefully acknowledge the support and guidance that I have received from Drs. Ye Tao and Christophe Py during my tenure within the Organic Materials and Devices group. This thesis would not have been possible without the outstanding technical support from Eric Estwick and Hiroshi Fukutani, to whom I am forever indebted and to Dr. Isabelle Lévesque, who performed the synthesis of BBEP and 8H-BBEP. I also appreciate the interesting discussions, suggestions, coffee, and friendship from the other members of the Organic Materials and Decvices Group.

I am grateful for the work performed by Jeff Fraser, Michel Beaulieu, Simona Moisa, and Irwin Sproule for the SEM, AFM, XPS, and AES characterization of my samples and not complaining (too much!) when I gave them a few dozen samples on a Friday afternoon. This work would not have been possible without your help.

Thanks to Dr. Margaret Buchanan, Paul Marshall, Dan Roth and Mark Malloy and the rest of the Nanofabrication group for their help and support. I am also grateful to Craig Storey for his help and suggestions regarding the electrical measurements of OFETs and to Dr. Chandre Dharma-wardana for our discussions involving the modeling of organic molecules and interpreting the results.

To Jennifer, Bruno, and Nicolas, with whom I have shared an office with at one point or another over the years: you are the reason why it was so fun. Thanks for all of the good times and memories.

I would like to thank Ed Hiscoe and the people whom I befriended at his Dojo for the blood, sweat, and tears: Dan, Lyle, Norm, Ron, and Tom.

Last, but definitely not least, I would like to thank Renée P. Harling for her moral support and help in preparing this manuscript and to my parents, Maria and Marjan. Words cannot convey the thanks you deserve.

# Contents

**Chapter**

Appendix

# Figures

# Tables

# Abbreviations

| | |
|---|---|
| 8H-BBEP | bis-(4,4'-(octylbiphenyl)ethenyl)phenyl |
| AFM | Atomic Force Microscopy |
| Alq | tris (8-hydroxy quinolate)-aluminum |
| BBEP | bis-(4,4'-(biphenyl)ethenyl) phenyl |
| Bu-PBD | 2-(4-biphenyl)5-(4-tert-butylphenyl)1,3,4-oxidiazole |
| DSC | Differential Scanning Calorimetry |
| EA | Electroabsorption Spectroscopy |
| EL | Electroluminescence |
| HMDS | Hexamethyldisilazane |
| HOMO | Highest Occupied Molecular Orbital |
| IPS | Internal Photoelectron Spectroscopy |
| ITO | Indium Tin Oxide |
| LUMO | Lowest Unoccupied Molecular Orbital |
| NPB | 4,4-bis(1-naphthyl phenylamino)biphenyl |
| OFET | Organic Field Effect Transistor |
| OLED | Organic Light Emitting Diode |
| OTS-18 | *n*-octadecyltrichlorosilane |
| OTS-8 | *n*-octyltrichlorosilane |
| PL | Photoluminescence |
| PPV | Poly-p-phenylenevinylene |
| PVT | Physical Vapour Transport |
| S | Subthreshold Slope |
| SAM | Self Assembled Monolayer |
| SEM | Scanning Electron Microscopy |
| $\Delta T/T$ | Differential Transmittance |

| | |
|---|---|
| T | Temperature |
| TPD | N,N'-diphenyl-N,N'-bis(3-methylphenyl benzadine) |
| UPS | Ultraviolet Photoelectron Spectroscopy |
| VRH | Variable Range Hopping |
| $V_t$ | Threshold Voltage |
| XPS | X-Ray Photoelectron Spectroscopy |
| XRD | X-Ray Diffraction |

# Chapter 1
# Introduction and Motivation

## 1.1 Organic Electronics Prior to 1987

The field of organic electronics and photonics is very young compared to inorganic electronics such as silicon, germanium, gallium arsenide, indium phosphide and other compound semiconductors. In the early part of the 20th century, there was considerable effort put forth in studying the physics of inorganic semiconductors. Spurred on by the advent of quantum mechanics, many researchers tried to explain elementary device behavior such as rectification. It was not until 1938 when Schottky[1] and Mott,[2] and later in 1939 by Davydov,[3]independently explained the observed rectification behavior by using quantum mechanical techniques. After the Second World War, there was intense activity in the field of semiconductor physics which, in 1947, eventually lead to the development of the bipolar transistor by Bardeen, Brattain, and Shockley while working at Bell Laboratories. Since this invention, an entire global economy has formed based on the silicon transistor.

By contrast, organic transistors and light emitting diodes are still in their infancy stage, but have also followed a different route in their development. While chemists have been synthesizing materials for many decades, it was only in the early 1960s when Pope *et al* [4] and Schneider *et al* [5,6] at the National Research Council Canada in Ottawa observed electroluminescence (EL) from a thin film of single crystal anthracene. Later, Dresner considered the use of anthracene single crystals in practical devices.[7] This work was later abandoned due to technological reasons: the devices required high voltages to achieve EL and growing large, high quality single crystals of anthracene was difficult.

In 1977, Heeger, MacDiarmid, and Shirakawa discovered that when polyacetylene, a black, powdery insulator, was exposed to chlorine, bromine, or iodine vapours, the conductivity increased more than nine orders of magnitude to $10^5$ $Sm^{-1}$.[8] As a comparison, Teflon has a conductivity of $10^{-16}$ $Sm^{-1}$ while silver and copper have conductivities of $10^8$ $Sm^{-1}$. In 2000, they were awarded the Nobel Prize in Chemistry for the discovery and development of electrically conductive polymers.

## 1.2 Organic Electronics After 1987

In 1987 Tang and Van Slyke reported on the development of an organic light emitting diode (OLED) which displayed efficient EL at low voltages (below 10 V).[9] Using a double layers of amorphous molecular organic materials, they achieved luminance values in excess of 1000 cd/m$^2$ in constant direct current mode. Later, Tang *et al* reported that OLEDs fabricated with doped organic thin films, dramatically increased the luminance and also changing the emission colour.[10] In 1990, Burroughes and co-workers reported on the fabrication of polymer organic light emission diodes (PLEDs) based on poly(*p*-phenylene vinylene).[11] Since these papers, there has been an unprecedented effort by industry to capitalize on the advantages that both molecular and polymeric OLEDs can offer: low cost materials, low processing cost, ease of processing and fabrication, light weight, flexibility, high viewing angle, and low power consumption compared to other display technologies. To date, there are several companies that offer organic electroluminescent (OEL) displays in their products ranging from car stereos to cellular phones to personal shavers spanning all visible colours.

The first report of an organic field effect transistors (OFETs) was in 1986 by Tsumura.[12] Devices fabricated with polythiophene showed hole mobility of about $10^{-5}$ cm$^2$/Vs. In the almost two decades following this discovery, field effect mobilities have been reported on molecular and polymeric materials, and amorphous, polycrystalline thin films, and single crystals with mobilities ranging from $10^{-3}$ cm$^2$/Vs to 15 cm$^2$/Vs.[13-22]

As high as these mobilities are for organic semiconductors, they still cannot compete with silicon of germanium which typically have hole mobilities orders of magnitude higher. Consequently, it is envisioned that OFETs are positioned to emerge in niche markets such as disposable or flexible electronics where high speed devices are not needed. The processing characteristics of OFETs are similar to those of OLEDs: large area processing, structural flexibility, low temperature processing, and low cost are making OFETs an attractive alternative to hydrogenated amorphous silicon (a-Si:H) technology. Applications such as disposable smart cards and electronic identification tags,[14] electronic paper displays,[23] driving circuitry for active matrix displays based on LCDs (AMLCDs) or OLED displays (AMOLEDDs) are a logical progression given the material characteristics and cost of fabrication compared to a-Si:H circuitry.[14]

An important distinction must be made between the evolution of inorganic electronics and photonics to that of their organic counterparts. In the case of inorganic technology, there was a substantial amount of theoretical and experimental knowledge present before practical devices were developed. In this case, researchers and engineers were able to explain device behavior using existing tools, such as band theory and tunneling, to explain the observations in real devices. In fact, there were several decades of academic research on silicon to aid in the design of practical devices and it was not until the 1980s when two dimensional electron gases were developed and substantially increased the performance of devices.

Organic electronics and photonics, in contrast, were developed in the reverse process; the application was found before substantial "academic" knowledge of the fundamental material and device processes were understood. However, the last decade has seen more and more researchers becoming involved in studying the basic physical processes involved in organic electronic and photonic devices. Most of the present theory of device operation comes from the adaptation of theories for inorganic single crystal devices and applying correction factors where needed.

## 1.3 Context of This Thesis

This thesis focuses on the use of two novel semiconducting oligomers, bis-(4,4'-(biphenyl)ethenyl) phenyl, also called BBEP, and bis-(4,4'-(octylbiphenyl)ethenyl)phenyl, also called 8H-BBEP, in OLEDs and OFETs. In Chapter 2 the basic physics of organic semiconducting materials will be introduced. Concepts and theories of charge transport and optical processes will be discussed. Analogies between organic semiconductors and their inorganic counterparts will be made to aid in the understanding of certain concepts. Chapter 3 will review the optical properties of organic materials. The device physics behind the operation of OFETs and OLEDs will be discussed in Chapter 4. Theories of charge transport in OLEDs and OFETs, metal-semiconductor contacts and carrier injection, and the process behind photon generation and emission in OLEDs will be discussed. Chapter 5 will introduce the concept of self assembled monolayers (SAMs) and their formation. Film formation parameters will be discussed as well as contact angle data. The experimental details are outlined in Chapter 6 with summaries of the purification system, fabrication process, and measurement techniques. Chapter 7 details the theoretical modeling performed with the *Hyperchem* software package. Semiempirical calculations using the Zindo algorithms were performed to determine energetically favorable geometric molecular structures, binding energies, UV-visible spectra, molecular orbitals and HOMO-LUMO energy levels. The experimental results are given in Chapter 8. Chemical characterization performed by DSC and cyclic voltammetry are presented. The UV-vis absorption and PL spectra are given and compared to the calculated absorption spectra. Data on the thin film morphology gathered from XRD, AFM and SEM are given for different substrate temperatures and surface SAMs. The electrical results from the OFETs are presented and the dependence of the field effect mobility on the substrate temperature during deposition is shown. The I-V and L-V curves along with the EL spectra for OLEDs fabricated are presented. Chapter 9 summarizes the results presented in this work and discusses the implications of these results on the field of organic electronics and photonics.

## 1.4 References

1 W. Schottky, Z. Phys. **113,** 367 (1939).

2 N. F. Mott, proc. Cambr. Phil. Soc. **34,** 568 (1938).

3 B. Davydov, J. Phys. USSR **4,** 335 (1939).

4 M. Pope, H. Kallmann, and P. Magnante, J. Chem. Phys. **38,** 2540 (1963).

5 W. Helfrich and W. G. Schneider, J. Chem. Phys. **44,** 2902 (1966).

6 W. Helfrich and W. G. Schneider, Phys. Rev. Lett. **14,** 229 (1965).

7 J. Dresber, RCA Rev. **30,** 322 (1969).

8 H. Shirakawa, E. J. Louis, A. G. MacDiarmid, C. K. Chiang, and A. J. Heeger, J. Chem. Soc. Chem. Comm., 579 (1977).

9 C. W. Tang and S. A. Van Slyke, Appl. Phys. Lett. **51,** 913 (1987).

10 C. W. Tang, S. A. Van Slyke, and C. H. Chen, J. Appl. Phys. **65,** 3610 (1989).

11 J. H. Burroughes, D. D. C. Bradley, A. R. Brown, R. N. Marks, K. Mackay, R. H. Friend, P. L. Burns, and A. B. Holmes, Nature **347,** 539 (1990).

12 A. Tsumura, H. Koezuka, and T. Ando, Appl. Phys. Lett. **49,** 1210 (1986).

13 R. W. I. de Boer, M. E. Gershenson, A. F. Morpurgo, and V. Podzorov, Phys. Stat. Sol. A. **201,** 1302 (2004).

14 C. D. Dimitrakopolous and D. J. Mascaro, IBM J. Res. & Dev. **45,** 11 (2001).

15 N. C. Greenham and R. H. Friend, in *Solid State Physics: Advances in Research and Applications*; *Vol. 49*, edited by H. Ehrenreich and F. Spaepen (Academic Press, Toronto, 1995).

16 A. J. Lovinger and L. J. Rothberg, J. Mater. Res. **11,** 1581 (1996).

17 H. E. Katz, J. Mater. Chem. **7,** 369 (1997).

18 A. R. Brown, C. P. Jarrett, D. M. de Leeuw, and M. Matters, Synth. Met. **88,** 37 (1997).

19 G. Horowitz, Adv. Mater. **10,** 365 (1998).

20 F. Garnier, Chem. Phys. **227,** 253 (1998).

21 H. E. Katz and Z. Bao, J. Phys. Chem. B **104,** 671 (2000).

22 D. J. Gundlach, Y. Y. Lin, T. N. Jackson, S. F. Nelson, and D. G. Schlom, IEEE Electron Device Lett. **18,** 87 (1997).

23 F. Eder, H. Klauk, M. Halik, U. Zschieschang, G. Schmid, and C. Dehm, Appl. Phys. Lett. **84,** 2673 (2004).

# Chapter 2

# Physics of Organic Semiconductors

## 2.1 Introduction

The molecular and polymeric materials used in OLEDs and OFETs belong to a larger class of materials called π-conjugated materials. They are semi-insulating at room temperature and have π-π* energy gaps between 1.5 eV and 3.5 eV.[1,2] Three of the organic semiconductors that were originally used in OLEDs and OFETs are shown in Figure 2.1: (a) tris-(8-hydroxy quinolate)-aluminum, commonly known as Alq, (b) poly(p-phenylene vinylene), or PPV, and (c) pentacene. Alq and PPV were the materials that were used in the first OLED and polymer LED, respectively.[3-5] PPV is unique in that it is an exception to the usual rule that polymers are solution processable. In fact, PPV is insoluble and is prepared by thermal conversion of a precursor polymer.[5] Soluble derivatives of PPV are available and are more widely used.[1,2] Pentacene is one of the most commonly used materials in OFETs.[6,7]

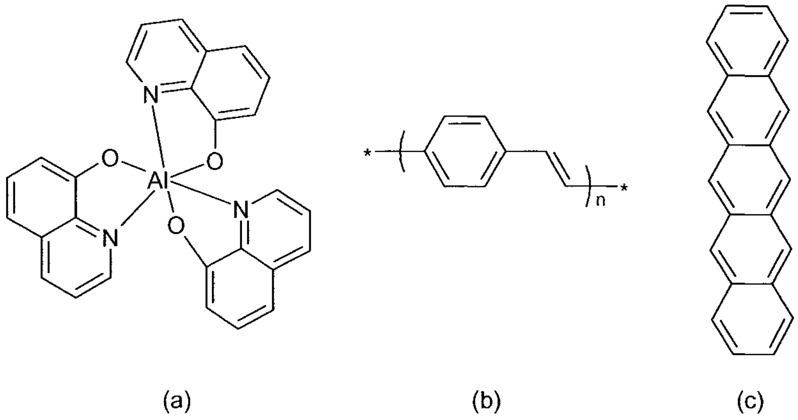

(a) (b) (c)

**Figure 2.1:** Chemical structures for three of the "original" organic semiconducting materials: (a) Alq, (b) PPV, and (c) pentacene.

The principal differences between small molecules (such as Alq and pentacene) and polymers (such as PPV) are in their processing methods and mechanical properties. Thin films of small molecules are usually prepared by sublimation in high vacuum whereas polymer films are usually formed by spin casting from solution. In either case, the resulting films are amorphous or polycrystalline with small grains and can be highly disordered.[2,3,8] Organic films typically have densities of about 1 g/cm$^3$, thermal conductivity of about 10$^{-3}$ W/cmK and specific heat around 1 J/g K.[9,10] The mechanical properties of polymer films are more robust than films of small molecules.

In Section 2.2 an overview of molecular organic single crystals and thin films and their growth mechanisms is presented followed in Section 2.3 by a discussion of the electronic properties of organic materials. The concept of the configuration coordinate diagram is introduced followed by a discussion of molecular energy levels and electronic structure. The concept of molecular orbitals, and some of the important theories describing the electronic properties of organic molecules are discussed. The concepts of polarons and bipolarons are introduced and their transport properties are summarized.

## 2.2 Physical Properties of Organic Molecules and Thin Films

### 2.2.1 Organic Thin Films and Single Crystals

There are two main growth techniques used for depositing organic films: thermal vapour deposition performed in a vacuum[11-13] and spin casting from solution.[14-20] There are other less common techniques which are also used such as physical vapour deposition[21] and laser-assisted deposition.[22-26]

Spin casting an organic film from solution is a common low-cost technique which is used to deposit organic thin films, especially in the fabrication of OLEDs. It provides a relatively smooth amorphous film which is ideal for OLED applications. However, when used in OFETs, spin casted devices typically display lower mobilities when compared to thermally evaporated devices using the same materials.[27,28] An obvious requirement for spin casting devices is that the organic material must be soluble in a given solvent and not undergo any irreversible chemical reaction during the entire process. Spin casting is usually performed in an a glove box which has been purged for several hours with an inert gas such as nitrogen or argon to eliminate water vapour and oxygen from the atmosphere to prevent oxidation and/or degradation of the material. Some materials, notably pentacene and Alq, are not soluble and must be deposited by evaporation techniques. Another issue which must be considered when fabricating organic heterostructure devices using spin casting techniques is mutual solvation. When an organic film is spin cast on top of a previously deposited film, both solvents and materials should be selected such that the material in the first layer is not soluble in the solvent used in the second layer. Moreover, the solvent used in the second layer must not adversely effect the previously deposited film by reacting with it chemically or physically. These requirements impose large constraints on which materials can be used in organic heterostructure devices. An alternative method is to use a material which can be converted by a thermal or radiative process into a stable form, for example, exposing the first spin cast film to ultraviolet radiation to cross-link the polymer chains to give a robust, chemically inert film.

Physical vapour transport (PVT) is a technique that is used to grow high quality organic films or single crystals for use in OLEDs or OFETs.[29,30] In PVT, the source material is placed in the hottest region of the reactor and the crystal growth occurs within a narrow temperature range near the cold end. Although a PVT apparatus is similar to that used to purify organic materials the primary differences between them are the rate of sublimation of the source material and the flow rate of the carrier gas being used, which are carefully controlled in a PVT system.

Some examples of PVT-grown organic single crystals are tetracene grown in an argon carrier gas[31] and rubrene grown in a pure $H_2$ atmosphere.[32,33] Figure 2.2 shows single crystals of rubrene, tetracene, and anthracene grown by PVT.[21] In the case of rubrene, many different carrier gases were tried such as Ar, $N_2$ and $H_2$, but the hydrogen atmosphere yielded the best

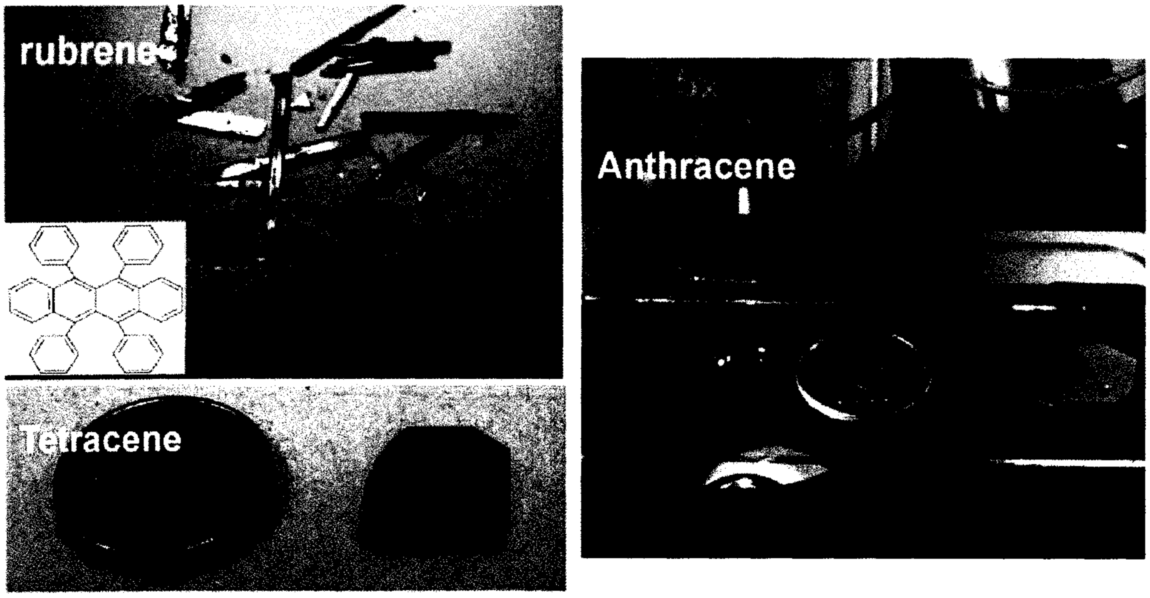

**Figure 2.2:** Single crystals of rubrene, tetracene, and anthracene grown by PVT. The anthracene crystal is intrinsically transparent and is shown luminescing in the blue by illuminating with UV light. From de Boer *et al.* (reference 29).

mobility results in rubrene OFETs. It is still not understood how variations in carrier gas can affects crystal quality. One possibility may be the presence of residual water vapour or oxygen in the reactors or even in the gas itself. Photo-induced reactions with $O_2$ are well known for most organic molecules and the result of these reactions can act as traps for charge carriers.[34] PVT reactors are pumped down to a low vacuum and are shielded from light to help prevent photo-oxidation.[21,34]

The amount of impurities present in the starting material is critical to the number of re-growth cycles the organic material must undergo before high quality single crystals are produced. The ultimate purification technique which can be used on organic materials is zone refining in which the impurity concentration is decreased to the parts per billion level.[35-38]

The equipment which is used for organic vapour deposition is essentially the same as that used to deposit inorganic materials. Knudsen cells, shown in Figure 2.3, or refractory metal boats contain the source material which are heated using resistive heating under high vacuum (less than $10^{-6}$ torr). The process of evaporating (liquid to vapour) or subliming (solid to vapour) organic molecules generates a flux of molecules which is directed towards the substrate. The substrate holder can be connected to a temperature controller and heater. Usually the deposition rates vary from 1 Å/min to several Å/sec depending on the material and the desired film characteristics. An organic material can be evaporated if it is vacuum compatible, does not decompose when heated or undergo any irreversible chemical changes, and its molecular weight is low enough for evaporation to occur. Polymers do not meet these required criterion for thermal evaporation to be sustained. All of the organic semiconductors used in this work were deposited using thermal deposition in high vacuum and, in the case of BBEP and 8H-BBEP, were marginally soluble in some solvents.

### 2.2.2 Thin Films Formed by Vacuum Deposition

There are several types of interfaces which exist in OLEDs and OFETs: organic on organic, organic on metals, metal on organic, and organic on dielectrics or transparent conducting oxides. The deposition of organic materials onto metals is significant in some types of OLEDs (for example, an ultra-thin semitransparent gold anode and inverted OLEDs) and OFETs (a bottom contact device with gold source and drain electrodes) and has been studied extensively using ultraviolet photoelectron spectroscopy, x-ray photoelectron spectroscopy, Kelvin probe, and other analytical surface and interface techniques.[39-52] In these devices the deposition of the organic material onto the metal is a low energy process and occurs at relatively low temperature. In contrast, depositing metal onto soft organic materials can be detrimental if an energetic deposition process is used such as electron beam (e-beam) evaporation or sputtering where the metal atoms

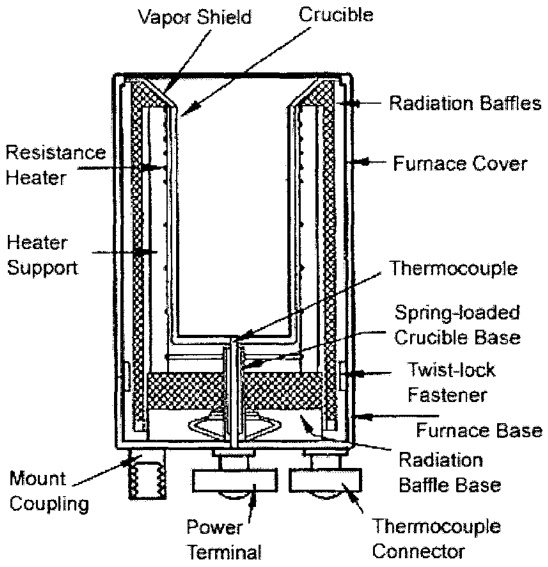

**Figure 2.3:** Schematic drawing of the inside of a Knudsen cell. The source material is placed inside the crucible and the flux is emitted through an opening at the top of the crucible. Figure from http://www.lesker.com.

impinging on the organic surface possess high energies, soft x-ray radiation (approximately 10 keV in the case of e-beam evaporation), or energetically intense plasma (as in magnetron sputtering). The presence of an organic-metal interface with minimal contact resistance and optimum energy level matching is critical to efficient device operation, and will be discussed in greater detail in Chapter 4.

For OFET applications, it is useful to know the crystal structure likely to result from the material's growth. Materials can have several different polymorphs and multiple phases in a given film. For example, it has been shown by several groups that pentacene possesses two distinct phases, referred to as the "thin film" and "single crystal" phases in the literature.[53-55] When a thin film is grown in which both phases are present the hole mobility is very low, which is thought to be directly related to the high defect concentration at the grain boundaries. Figure 2.4 illustrates the effect of the different phases on the crystallinity and the hole mobility in a pentacene film. When the film is grown at a substrate temperature of -196 °C, the pentacene molecules "freeze" in position as soon as they contact the substrate, producing an amorphous film which is essentially insulating. The $\pi$ orbital overlap between nearest neighbour molecules is minimal due to the disorder in the film. When the substrate temperature is kept at around room temperature, a highly ordered film is formed showing a hole mobility of 0.6 $cm^2/Vs$. The pentacene is in the "thin film" phase and possesses strong peaks in the XRD spectrum. When the film is comprised of a mixture of "thin film" and "single crystal" phase pentacene, there are numerous defects due to the boundaries between the phases. These films possess low hole mobility and the XRD spectrum shows a splitting of the (001) and (002) peaks.[54-56]

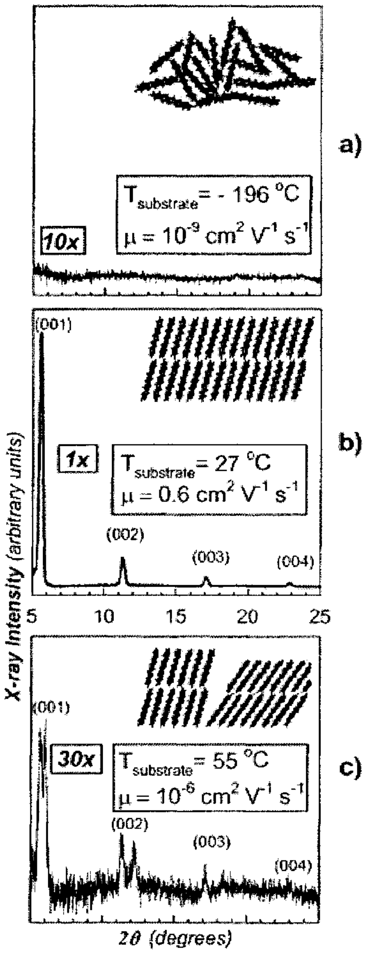

**Figure 2.4:** XRD spectra and schematic representations of structural order and field effect mobilities corresponding to three different thin films of pentacene. (a) an amorphous phased deposited at a substrate temperature $T_{sub}$ = -196 °C. (b) A single phase deposited at $T_{sub}$ = 27 °C. This phase is referred to as a "thin film" phase in the literature. (c) Illustrates two co-existing phases: the "thin film" and the "single crystal" phase deposted at $T_{sub}$ = 55 °C. The difference between the two phases is related to the packing and orientation of the molecules. The deposition rates were 0.5 Å/sec, 1 Å/sec, and 0.25 Å/sec, respectively. Figure from Dimitrakopolous and Mascaro (reference 61).

As demonstrated by the results in Figure 2.4, knowledge of the degree of order of the crystalline or polycrystalline film and any defects which may be present is essential in preparing a high quality transistor. Minimizing the number of grain boundaries will decrease the number of carrier trap sites, carrier scattering, and increase the mobility as well as forming a densely packed homogeneous film which possesses π orbital overlap.

The film formation process can be described using the concept of surface and interface energies, $\gamma$, similar to the description of a wetting phenomena. The surface energies are related to three different growth modes: islands starting at the first monolayer (Vollmer-Webber), layers plus islands after a certain critical thickness (Stranksi-Krastanov), and layer-by-layer (Frank-van der Merve).[57,58] These growth modes are illustrated in Figure 2.5. An example of a Vollmer-Webber growth is provided Figure 2.6 in an AFM image of a pentacene film grown at 60 °C on a $SiO_2$ surface treated with hexamethyldisilazane (HMDS) at about 0.2 Å/sec. A sectional analysis of this film is shown in Figure 2.7. In this film, the islands are pyramid-like with terraces corresponding to 1 monolayer of pentacene oriented perpendicular to the surface.

The initial growth of pentacene on $SiO_2$ has been studied by Ruiz *et al.*[59] Their analysis of sub-monolayer island distributions revealed that the smallest stable island size consisted of four pentacene molecules. In contrast, Meyer zu Heringdord and co-workers have reported growth of single crystal grains in pentacene approaching 0.1 mm.[60] An effective approach to increase the size of pentacene grains is the use of a self assembled monolayer on the $SiO_2$ surface (see, for example, reference 66 and references therein). Meyer zu Heringdord soaked a Si (001) surface in cyclohexane prior to pentacene growth to modify the growth dynamics.[60]

Jackson *et al* first demonstrated the effectiveness of a silane-based SAM to increase the mobility in pentacene OFETs.[8,61,62] Voigt and co-workers have studied a non-conventional

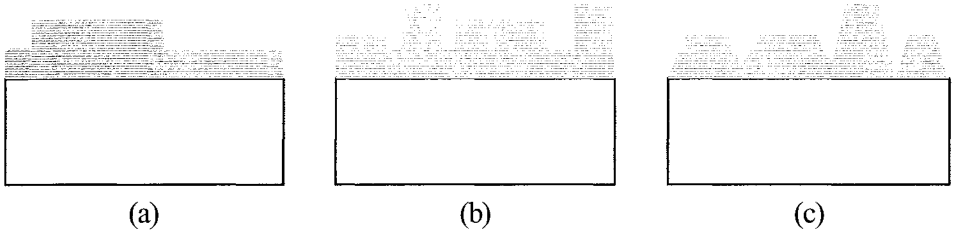
(a) (b) (c)

**Figure 2.5:** Three modes of epitaxial growth: (a) layer-by-layer (Frank-van der Merwe, (b) layer and island (Stranski-Krastonov), and (c) island (Volmer-Weber).

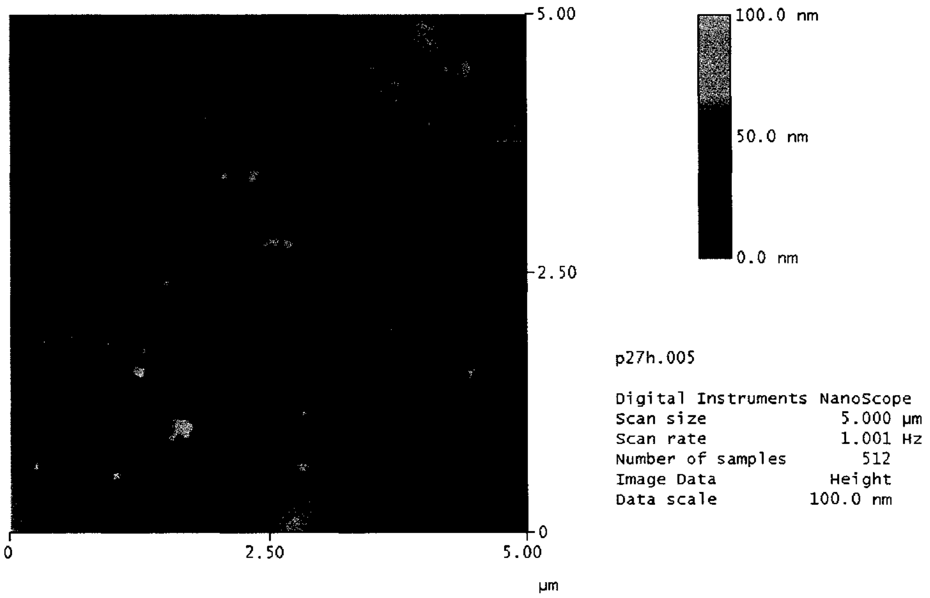

```
p27h.005

Digital Instruments NanoScope
Scan size              5.000 µm
Scan rate              1.001 Hz
Number of samples        512
Image Data             Height
Data scale            100.0 nm
```

**Figure 2.6:** AFM image of a pentacene film deposited onto an HMDS coated $SiO_2$ surface at 60 °C. The lamellar structure of the islands is clearly visible.

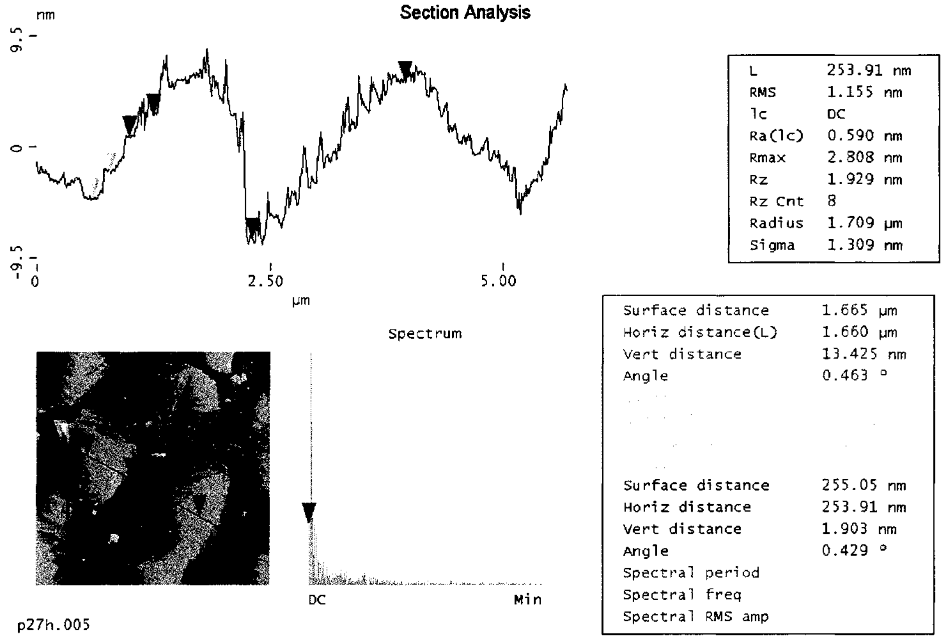

| | |
|---|---|
| L | 253.91 nm |
| RMS | 1.155 nm |
| lc | DC |
| Ra(lc) | 0.590 nm |
| Rmax | 2.808 nm |
| Rz | 1.929 nm |
| Rz Cnt | 8 |
| Radius | 1.709 µm |
| Sigma | 1.309 nm |

| | |
|---|---|
| Surface distance | 1.665 µm |
| Horiz distance(L) | 1.660 µm |
| Vert distance | 13.425 nm |
| Angle | 0.463 ° |
| Surface distance | 255.05 nm |
| Horiz distance | 253.91 nm |
| Vert distance | 1.903 nm |
| Angle | 0.429 ° |
| Spectral period | |
| Spectral freq | |
| Spectral RMS amp | |

**Figure 2.7:** Sectional analysis of the pentacene film shown in Figure 2.6.

system involving the growth of tetracene on an oil-covered surface.[63] Silicon dioxide is a particularly suitable substrate for surface modification using self assembled monolayers to promote the growth of pentacene and other materials, and will be discussed in greater detail in Chapter 5.[61,64-70]

Schreiber has outlined issues which are specific to organic materials which can contribute to different growth behaviour:[57]

1. Organic molecules have more internal degrees of freedom compared to atomic species used in the growth of inorganic films.
2. The interaction potential (molecule-molecule and molecule-substrate) is generally lower compared to the case of atomic adsorbates, and van der Waals interactions are more significant.
3. The size of the molecules and their unit cells are much larger than that of (typical) inorganic substrates such as silicon.

The orientational and vibrational degrees of freedom are not taken into account in conventional growth models but could be the source of new phenomena during growth such as the change in molecular orientation. In addition, transitions during growth could occur where the molecular orientation changes with respect to the surface.

The lower interaction potential implies that the response of the system to strain is different than that of an atomic system. It is thought that more strain could be accommodated in molecular systems and the build up of strain would lead to a critical thickness before the growth mode changes. This type of growth has been discussed in terms of van der Waals epitaxy, where physisorption involving only van der Waals bonding dominates, and quasi epitaxy, where the substrate and film are incommensurate over any substantial lattice length scale.[71] Due to the importance of van der Waals interactions, the temperature at which the material is evaporated and the temperature at which the substrate is held are much lower than in inorganic epitaxial growth. However, the total interaction energy of a molecule could be substantial and comparable to that of chemisorbing atomic adsorbates.[57] Moreover, there are usually no dangling bonds present on the organic surface, which results in lower surface energies when compared to inorganic surfaces.

## 2.3 Electronic Properties of Organic Molecules and Polymers

### 2.3.1 Configuration Coordinate Diagrams

Electronic transitions are usually illustrated using a configuration coordinate diagram. An example is shown in Figure 2.8. When a neutral molecule is excited or ionized, a change in the configuration occurs within the molecule to accommodate the additional energy of the excitation or excess charge. This change in conformation is represented by a change in the configuration coordinate $r$, and it is usually depicted in the diagram by a shift to higher $r$ values on the $x$ axis and a shift to higher energy, on the $y$ axis. In the diagram, $S_0$ and $S_1$ represent the ground and excited states of the molecule, respectively. In each state, the first three vibronic levels are shown, with the vibrational probability functions. A direct vertical transition from a ground state vibrational level, denoted $a_i$, to an excited state vibrational level, $a_j$*, and similarly a direct vertical transition from the ground state of the excited molecular state $c_0{}^*$ to a molecular ground state vibrational level $c_i$, are known as Frank-Condon transitions. The probability of an electronic transition between two states depends on the overlap between the vibrational wavefunctions of the initial and final states. If we assume that the wavefunctions of the initial and final vibrational states are given by $\xi_n$ and $\xi_m$, respectively, then the Frank-Condon factor is written as:

$$\left|S_{mn}\right|^2 = \left|\left\langle \xi_m \middle| \xi_n \right\rangle\right|^2 . \tag{2}$$

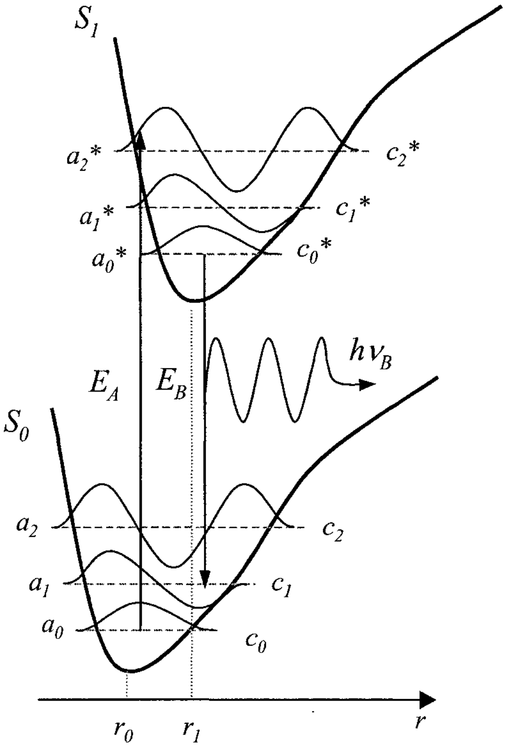

**Figure 2.8:** The configuration coordinate diagram. The symbols are defined in the text.

The transition from the vibrational ground state of one electronic level to the first vibrationally excited state of another electronic level is known as a 0-1 transition.

A molecule in a vibrationally excited state will undergo radiationless relaxation to the lowest vibrational state, occurring on timescales approaching 0.1 ps.[2,72] Radiative emission occurs from the lowest vibrational level of the excited state to some vibrational level of the electronic ground state. These transitions can be observed in the optical absorption and emission spectra which usually exhibit mirror symmetry, with the emission spectra showing a red shift, also known as a Stokes shift. The oscillator strength of each of the vibrational peaks is highly dependent on the change in equilibrium configuration coordinate between the ground and excited state, $\Delta r_i$, or the amount of structural relaxation that occurs in the excited state. The amount of relaxation can be described by the Huang-Rhys parameter $S_i$:[2]

$$S_i = \frac{\frac{1}{2} M\omega_i^2 \left(\Delta r_i\right)^2}{\hbar\omega_i} \tag{3}$$

where $\omega_i$ is the phonon frequency and $M$ is the reduced mass for the mode $r_i$. The Huang-Rhys parameter gives the energy of relaxation in the units of the phonon energy.

### 2.3.2 Molecular Energy Levels

When a molecule is part of a condensed phase of identical molecules, additional intermolecular forces alter the ionization energy and electron binding energy as depicted in Figure 2.9. A major factor in this alteration is the stabilizing effect of the polarization energy of the positive and negative ions in the crystal which is qualitatively comparable to the solvation energy of ions in solution.

In 1957, Lyons proposed the energy diagram shown in Figure 2.9, which illustrated the energy level shifts when a molecule in vacuum is condensed into a crystal.[73] The ionization potential, $I_g$, is the energy required to remove an electron from the highest filled valence level of a neutral molecule. In a crystal, the electron originates from the valence level and the polarization energy of the resultant hole, $P_h$, lowers the total energy needed for ionization from $I_g$ to $I_c$, where $I_c$ is the ionization energy of the crystal which corresponds to the highest valence level. The valence level in a crystal shifts up towards the vacuum level because it is easier to ionize a neutral crystal molecule when the remaining positive charge is stabilized by its polarization energy $P_h$.

The energy released when an electron enters the crystal is called the electron affinity and is denoted $A_c$. According to Figure 2.9, a single molecule with an excess electron transforms into a crystal molecule by gaining the polarization energy $P_e$. This corresponds to the energy of the lowest conduction level. The conduction level is lowered because it is more difficult to extract an excess electron to the vacuum level because the original ion is more stable in the crystal environment. The energy separating the first conduction level and the valence level is known as the band gap energy, $E_g$. This is the energy released when the positive and negative carriers in their lowest energy states recombine inside the crystal. $E_g$ is also the least amount of energy required to produce an uncorrelated pair of carriers inside the crystal. In molecules,

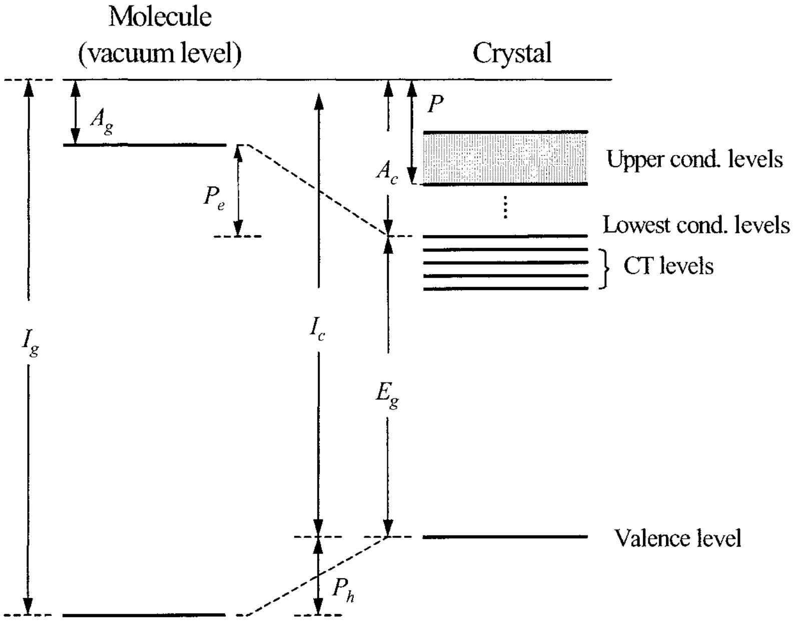

**Figure 2.9:** Energy levels of an isolated molecule and of a crystal. The vacuum level is used as the reference level. The parent molecular states are linked to the crystal states via dashed lines. The symbols are defined in the text. Adapted from Pope and Swenberg (reference 1).

the conduction and valence levels are also known as the lowest unoccupied molecular orbital (LUMO) and highest occupied molecular orbital (HOMO) levels.

Although the terms valence and conduction levels are used in this discussion, they do not carry the same interpretation as in conventional inorganic semiconductors. The carriers in these states are not delocalized in the same sense as they are in silicon, for example. In fact, at room temperature the carriers are highly localized in molecular crystals and the traditional one-electron band picture is inadequate for the explanation of their conducting properties due to large electronic polarization effects. The existence of a large polarization energy in itself is not a barrier to the transfer of a carrier between neighboring sites, but it is the relative magnitude of the polarization energy compared to the nearest neighbor site which determines the ease of carrier transfer. If the intermolecular interaction energy is smaller than the polarization energy, then the carrier will tend to be localized. In wide band materials such as silicon and germanium, the polarization energy is smaller than the intermolecular interaction energy, so carrier transfer between nearest neighbors occurs with ease.

In the model proposed by Lyons there is a distinct gap between the lowest conduction level and the higher conducting levels. Silinsh, however, proposed that the conducting levels form a continuum and that there is a large density of free carriers states from the lowest conduction level up to the highest level.[74] This is indicated by the dots in the gap predicted by Lyons' model. Silinsh noted that there was no convincing evidence of any forbidden energy region for electrons of energy greater than $E_c$ or of holes with energy less than $E_v$. Silinsh proposed that the ultimate relaxed state of a trap-free polyacene molecule with an excess electron is a negative ion, and similarly for an excess hole results in a positive ion. The normal conduction of the electron and hole involves the movement of these charges from one relaxed state to another though the crystal, with a mobility determined by the energy of interaction between the neighboring molecules. The binding energy of the relaxed excess carrier is comprised of lattice, vibronic and electronic polarizations and is referred to as $E_c$ for electrons and $E_v$ for holes in Figure 2.10 . As the excess kinetic energy of the electron or hole increases, it can move so rapidly that the lattice and vibronic polarization time scales become too long to exert any effect on the carrier and the polarization energies can be neglected when $E_c^o$ is reached. As the carrier acquires additional energy and approaches the free carrier state, it begins

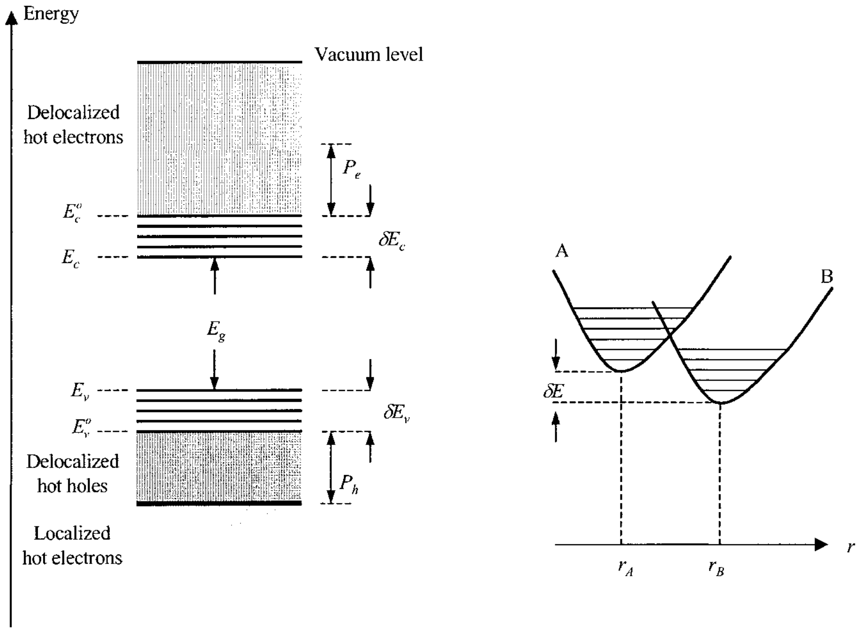

(a) (b)

**Figure 2.10:** (a) Energy level diagram for carriers in an ideal polyacene molecular crystal. (b) Configuration coordinate diagram representing the relaxation resulting from vibronic and lattice polarizations. State A represents either a hole or electron after the effects of electronic polarization have been included. State B includes all of the polarization terms. Adapted from Pope and Swenberg (reference 1).

to lose its electronic polarization energy. The energy interval from $E_c$ to the vacuum level is approximately equal to the polarization energy $P$. For kinetic energies higher than $P_e$ the electron will not experience any difficulty in moving from one molecule to another until it loses energy by some scattering process. However, for very hot (energetic) holes the core electrons lie in discrete energy levels that do not overlap with neighboring molecules. These energetic holes represent localized states. The polarization energy $\delta E_c$ ($\delta E_v$) includes both the energy gained by the carriers as a result of the intramolecular reorganization of the atoms (vibronic polarization) and intermolecular reorganization (lattice polarization). The existence of two distinct regions of electrons is supported by the observations of several groups in which groups of fast electrons (1-3 eV) and slow electrons (0.3-0.4 eV) are clearly distinguishable.[75-78]

### 2.3.3 Electronic Structure

*Molecular Orbitals*

The shape of the molecule's backbone primarily defines the overall shape of the molecule. In straight chain saturated hydrocarbons, the carbon atoms are $sp^3$ hybridized with the hybrid orbitals pointing towards the corners of the tetrahedron. In an alkene, the carbon atoms participating in the double bond are $sp^2$ hybridized. The overlap of the $sp^2$ hybrid orbitals between the two carbon atoms produces a $\sigma$ bond along the C-C axis. Each carbon atom also possesses an unhybridized pure *p* orbital. These overlap sideways to produce a $\pi$ bond which has its electron density concentrated above and below the bond axis. Because of the geometry of the $sp^2$ hybrids and the restriction that the un-hybridized p orbitals must overlap in the π bond, a planar configuration of atoms with approximately 120° bond angles is formed.[79] Figure 2.11 illustrates $sp^3$ and $sp^2$ hybridization.

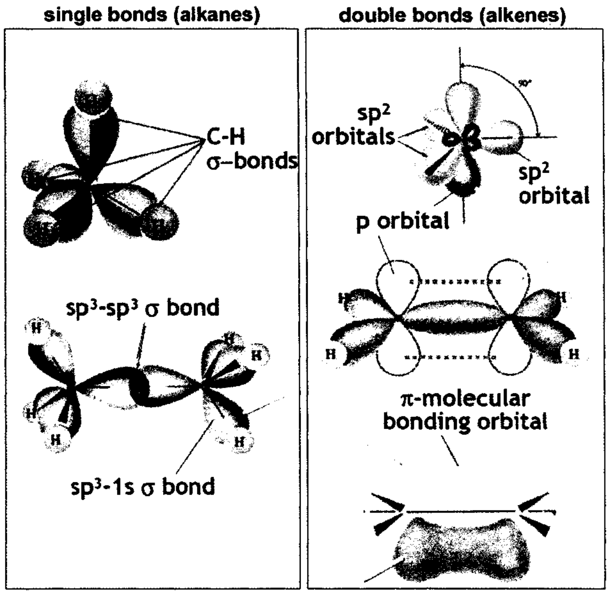

**Figure 2.11:** Diagram depicting $sp^3$ hybridization (left) and $sp^2$ hybridization (right). Original reference unknown.

The electronic states that are of interest are derived from the hybridization of p orbitals in carbon atoms in an $sp^2$-p configuration. The hybridized $sp^2$ orbitals generate the σ bonds which form the backbone of the molecule. The σ bonds require very high energies for electronic excitations or charged states. The effects from the σ bonds are usually neglected. The excitations of interest are formed in the p orbitals which are involved in π bonding.[1,2,80,81]

Many of the conjugated materials used in OLEDs and OFETs contain phenylene (benzene) moieties, shown in Figure 2.12. It is instructive to examine its molecular orbitals. The solid straight lines in the molecular structure represent the σ bonds formed from the $sp^2$ hybridized orbitals of carbon and the s orbitals of hydrogen. The $p_z$ orbitals of the carbon atoms are orthogonal to the plane of the page, and the spacing between the carbon atoms is such that there is an overlap between neighboring $p_z$ orbitals. These overlapping orbitals form π bonds, shown in Figure 2.11. The π bond creates a delocalized electron

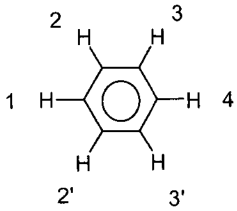

**Figure 2.12:** Chemical structure of benzene.

density above and below the plane of the carbon atoms, with no electron density in the nodal plane coinciding with the plane of the molecule. The delocalized structure is denoted by a circle within the benzene ring (as shown in Figure 2.12) and is referred to as a resonance structure. The delocalized π bonds enhance the stability of the benzene molecule compared to the case of a fixed alternation of localized single and double bonds (ie. a non-resonance structure).

Materials containing resonance structures belong to a class of compounds known as conjugated aromatic hydrocarbons. The term conjugated refers to the periodic alternating sequence of single and double bonds in the molecule. Benzene, anthracene, tetracene (also called napthlacene), pentacene, etc. are all aromatic hydrocarbons and are collectively known as polyacenes, or acenes, and their structures are shown in Figure 2.13. These molecules are generally planar while in the electronic ground state but can become non-planar when in an excited state. The general chemical stability of these molecules also decreases as the number of carbon atoms increase. For example, pentacene can oxidize in air in the absence of light while benzene and anthracene do not.

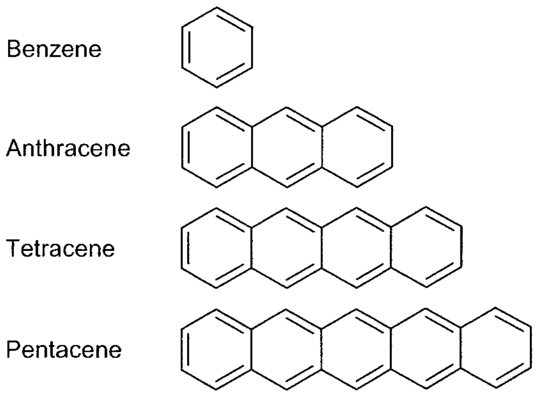

**Figure 2.13:** Molecular structure of benzene and three other acenes which have been used in OLEDs or OFETs.

The π electrons are in the highest energy occupied orbitals and are the most easily excited. Since the lowest energy vacant orbitals are also π orbitals, the electronic transitions from the filled to the unfilled levels are referred to as π-π* transitions. The position of the molecular energy levels, the optical absorption and fluorescence spectra, and relative transition intensities can be accounted for by using simplified wave functions for the molecule.

### *Born-Oppenheimer Approximation*

A major simplification can be made by assuming that the change in the distance between the nuclei is almost negligible over the time period required to effect an electronic transition. This is the basis of the Born-Oppenheimer (B-O) approximation.

In principle, all of the macroscopic properties of a system can be determined if the wavefunction of the system is known. The wavefunction can be obtained by solving the Schrödinger equation,

$$H\psi = E\psi, \qquad (3)$$

where $H$ is the Hamiltonian operator, $E$ is the energy and $\psi$ is the wavefunction. For molecules, $H$ is the sum of several operators including the electronic energy operator $H_E$, a combined nuclear kinetic and potential energy operator $H_N$, and nuclear-electronic interaction operator $H_{NE}$. Therefore $\psi$ is a function of the electronic coordinates $\boldsymbol{r}_i$ and the nuclear coordinates $\boldsymbol{r}_k$.

The electronic transition probability $F$ is given by Fermi's Golden Rule:

$$F = \left\langle \psi_i \middle| \vec{\mu} \middle| \psi_f \right\rangle, \qquad (4)$$

where $\psi_i$ and $\psi_f$ are the initial and final wavefunctions, respectively, and the dipole moment operator is given by:

$$\vec{\mu} = q\sum \vec{r}_j \ , \tag{5}$$

where $q$ is the electronic charge and $\vec{r}_j$ is the distance to the $j^{th}$ electron.

The electronic wavefunctions can be further expressed as a product of the space ($\Phi$) and spin (S) components, and the wavefunction describing nuclear vibrations ($\Theta$):

$$\psi_m = \Theta_m S_m \Phi_m \ . \tag{6}$$

Fermi's Golden Rule can then be expressed in the following manner:

$$F = \langle \Theta_i | \Theta_f \rangle \langle S_i | S_f \rangle \langle \Phi_i | \vec{\mu} | \Phi_f \rangle \ . \tag{7}$$

If any of the terms in Equation (7) are zero then the electronic transition from state $i$ to state $f$ is forbidden. In addition, spin selection rules require that spin be conserved ($\Delta S = 0$) during a radiative electronic transition. This implies that singlet to triplet and triplet to singlet radiative transitions are forbidden.

Most formulations of molecular electronic states deal with vibronic motion. Rotational energies are relatively small and their contributions to vibronic transitions only appear in the fine structure of the transition. The treatment of vibronic transitions is generally performed within the framework of the adiabatic B-O approximation. This approximation makes use of the fact that there is a large difference between the nuclear and electronic masses, thus the electrons are assumed to respond instantaneously (~$10^{-15}$seconds) to any configuration change of the nuclei (~$10^{-13}$ seconds). For any given electronic state, it is assumed that the positions of the nuclei can be changed and that the potential energy for the configuration of nuclei can be described in the form of a surface. The approximation is termed adiabatic because the movement of the relative positions of the nuclei is considered a measure of the work on the shape of the molecule with no accompanying loss or gain in electronic energy through the aid of a radiation field.[1] However, even if the adiabatic approximation is valid, the nuclear wavefunctions do not describe the harmonic-oscillator states, and their functional form depends on the electronic states. Since the electronic and nuclear vibrational wavefunctions are decoupled, it will break down near degeneracies. It also does not explain forbidden transitions in the absorption and luminescence spectra which arise from spin-orbit coupling.

### *Molecular Orbital Theory and Linear Combination of Atomic Orbitals*

Molecular orbital (MO) theories of varying degrees of mathematical complexity have been developed and MO wavefunctions based on linear combination of atomic orbitals (LCAO) have been used extensively. Reasonable agreement between theory and experiment is obtained when the atomic orbitals are approximated by suitable self-consistent wavefunctions.[1] In the simplest MO treatment of polycyclic aromatic hydrocarbons, in which there are no carbon atoms that belong to more than two rings and all carbon atoms fall on the perimeter of the molecule, the electrons are divided into two sets, those forming the σ bonds and those forming the π bonds. The molecular electronic wave function can be separated into the σ and π components:

$$\psi = \psi_\sigma \psi_\pi . \qquad (8)$$

The σ bonds, along with the nuclei, form a fixed potential in which the π electrons move. Most optical transitions correspond to transitions of the π electrons, denoted as $\pi \rightarrow \pi^*$, in which only $\psi_\pi$ changes. The LCAO method of approximating MO's for the π electrons is motivated by the expectation that when a given electron is in the vicinity of a particular nucleus, its wavefunction will be similar to what it would be in the valence orbital of that atom. Therefore a wavefunction of a π molecular orbital in the LCAO approximation can be written as a summation over all atoms in the molecule:

$$\psi_\pi = \sum_{l=1}^{N} a_l \phi_l , \tag{9}$$

where $\phi_l$ represents the atomic orbital of the $l^{\text{th}}$ atom and the $a_l$ coefficients are determined by minimizing the total energy of the system. The result is $N$ molecular wavefunctions with their respective $a_l$ coefficient and each accommodating two electrons of opposite spin, by the Pauli exclusion principle. Filling the lowest *N/2* levels gives the ground state wave functions of the system:

$$\psi_\pi(ground) = \psi_1 \alpha_1 \psi_1 \beta_1 \ldots \psi_{N/2} \alpha_{N/2} \psi_{N/2} \beta_{N/2} , \tag{10}$$

where the $\psi_l$ terms are the functions of the form given by Equation 9 and are listed in order of increasing energy, $\alpha_l$ and $\beta_l$ denote electron spin functions for the up and down orientations, respectively. When the molecule is in its ground state, the unfilled MO's are called antibonding MO's while bonding MO's are those which are occupied. Excited states are formed by promoting one of the bonding electrons to an unfilled antibonding MO.

### *The Su, Schrieffer, and Heeger (SSH) Formulation*

In moving from small molecules to polymers it is possible to describe the electronic structure within the framework of the molecular orbital description previously discussed or use the formalism of band theory as applied to a one-dimensional periodic chain. The crossover between molecular orbital theory and band theory has been a source of much debate. It is generally accepted that electron-phonon and electron-electron interactions are visible in the optical spectra of conjugated molecules and that these effects lead to the localization of excited electronic states on the polymer chain. Depending on the symmetry of the polymer chain and the charge on the excitation, these states are commonly referred to as solitons, polarons, bipolarons, or excitons, which will be discussed later.

Trans-polyacetylene is an ideal material for modeling the electronic properties of an infinite one-dimensional chain. Trans-polyacetylene has two equivalent structures with the same energy, shown in Figure 2.14, and is referred to as a degenerate ground state polymer. The band structure of trans-polyacetylene has been studied by numerous groups[82-85] and the most widely used model is the one proposed by Su, Schrieffer, and Heeger (SSH);[86,87] it involves a tight-binding calculation for a polymer chain with cyclic boundary conditions and neglects electron-electron interactions. The polymer chain is represented using a ball and stick model with the σ bond connecting neighbouring carbon atoms with an effective spring constant $K$. Electron-phonon interactions are considered by introducing a nearest neighbour overlap integral into the Hamiltonian. This is expanded linearly about the equilibrium separation of neighbouring atoms, $t = t_o + \alpha(u_n - u_{n+1})$, where $u_n$ is the displacement of site $n$, and the σ electrons are parameterized through the force constant for the bonds, $K$. The SSH Hamiltonian is written as:

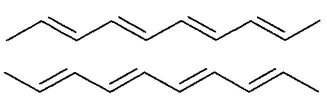

**Figure 2.14:** Two isomers of trans-polyacetylene.

$$H = -\sum_n \left[t_o + \alpha\left(u_n - u_{n+1}\right)\right]\left(c_n^+ c_{n+1} + c_{n+1}^+ c_n\right) + \frac{1}{2M}\sum_n p_n^2 + \frac{K}{2}\sum_n \left(u_n - u_{n+1}\right)^2 \quad . \qquad (11)$$

The first term gives the kinetic energy of the π electrons ($c_n$ and $c_n^+$ are annihilation and creation operators at site *n*), the second term represents the kinetic energy of the lattice with $p_n$ being the momentum of the atom at site *n*, and the third term representing the σ bond strain energy. The π electron system of trans polyacetylene can be considered to be an example of a one-dimensional, half-filled electron band, and the bond dimerization that is found for the ground state of the chain can therefore be considered the result of a Peierls distortion (a lattice distortion resulting in the creation of an energy gap) of the regular chain.[82,88] This creates an energy gap in the dispersion curve at $k = \pi/2a$, where *a* is the unit cell length before dimerization, shown in Figure 2.15a with the reduced zone shown in Figure 2.15b.[2] The gap energy of 2Δ is determined by the dimensionless electron-phonon coupling constant, λ through the relation:[89]

$$\Delta = 8t_o \exp\left[-\left(1 + 1/2\lambda\right)\right], \qquad (12)$$

where λ is related to the parameters in the SSH Hamiltonian through:

$$\lambda = \frac{2\alpha^2}{\pi t_o K}. \qquad (13)$$

Using experimental values of 1.7 eV for the band gap and 12 eV for the bandwidth gives a value for λ of 0.2, which is larger than can be attributed to electron-phonon coupling alone.[89] It is believed that the enhanced bond dimerization is due to the effects of the on-site Coulomb repulsion energy $U_o$. Baeriswyl and Maki have shown that when $U_o < 4t$, bond dimerization is enhanced.[90] Despite the clear evidence for the importance of Coulomb interactions and their role in determining the properties of conjugated molecules, the SSH model and its derivatives are still widely used.[91]

The trans isomer of polyacetylene is special amongst other polymers due to its ground

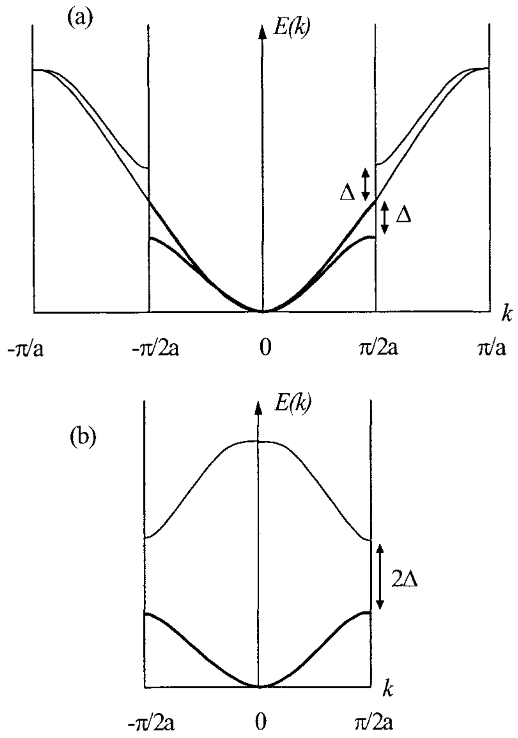

**Figure 2.15:** (a) The extended-zone band structure of trans-polyacetylene before and after dimerization. (b) The reduced zone scheme after dimerization showing the energy gap 2Δ. Occupied states are denoted by dark lines while unoccupied states are denoted by light lines.

state symmetry with respect to bond alternation. Most polymers have a nondegenerate ground state, meaning that there is a preferred bond alternation sequence. A parameter which accounts for the ground state degeneracy of polyacetylene was added to the SSH formulation by Brazovskii and Kirova.[92] The modification introduced an intrinsic contribution to the gap parameters, $\Delta_i$, which is added to the Peierls contribution.

The majority of polymers used in organic electronic devices are formed by the coupling of aromatic rings such as thiophene and phenylene. In these materials, the π-π* gap is usually significantly larger than that of trans-polyacetylene so that the contribution from the intrinsic gap is larger than from the Peierls mechanism. In this situation, it is more realistic to begin with the molecular orbitals of the appropriate moieties and build the electronic structure by introducing nearest neighbour interactions between the moieties.

When a polymer chain with Peierls distortion is excited, phase kinks, or solitons, are formed. Su and Rice have shown that solitons in polyacetylene take the form of bond alternation defects, shown in Figure 2.16.[83,86,87] Although the solitons are shown to be localized on specific carbon sites, Su has demonstrated that the solitons are in fact delocalized over 10 to 15 carbon sites.[86,87]

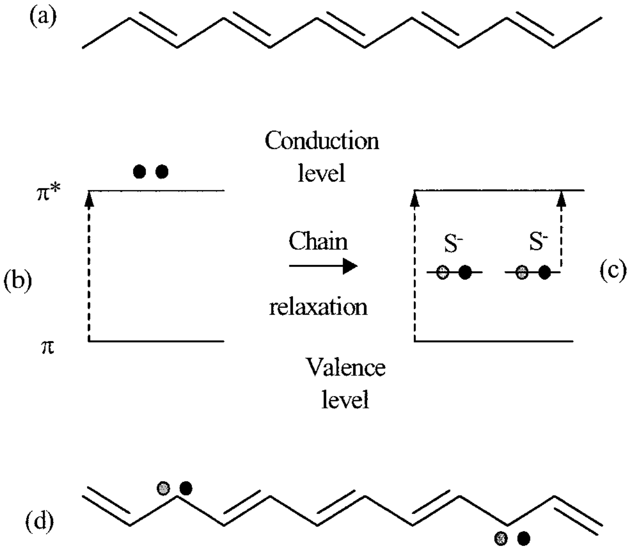

**Figure 2.16:** (a) Ground state of polyacetylene and (b) the corresponding band structure with two excess electrons in the conduction level, (c) the band structure after the chain has relaxed and formed a polaron level within the band gap and (d) the relaxed chain after the introduction of two excess electrons. After Greenham and Friend (reference 2).

Figure 2.16a depicts an undistorted trans-polyacetylene chain in the ground state with the corresponding band diagram in Figure 2.16b. The π-π* optical transition is denoted by a vertical arrow. If two electrons are introduced into the conduction band, the chain will relax into the state shown in Figure 2.16d, with the bond alternation phase reversed between the two solitons. These solitons have non-bonding π states within the energy gap which are created from a doubly occupied valence band state and an empty conduction band state. These two states are doubly occupied, as shown in Figure 2.16c, and each carry a negative charge. New optical transitions can therefore occur from the soliton levels to the conduction band levels. The analogous situation exists for positive charges which are introduced into the chain as well.

In polymers with a non-degenerate ground state, the two variations in bond alternation do not have equivalent energies. PPV is such a material, as shown in Figure 2.17. In this case, solitons cannot be formed because they are not stable. The charged excitations in nondegenerate ground state polymers are referred to as polarons or bipolarons.[93] Like solitons, these charged excitations represent localized charges on the polymer chain with a localized rearrangement of bond alternation. They may also be considered as a confined soliton pair where the nonbonding mid-gap soliton states form bonding and antibonding combinations producing two gap states which are symmetric about the mid-gap. Figure 2.18 shows the energy level diagrams for positively and negatively charged polarons and bipolarons as well as the energy levels for a singlet exciton.[2] The energy levels formed in the gap can be occupied by 0, 1, 2, 3, or 4 electrons yielding a positive bipolaron ($bp^{2+}$), positive polaron ($p^+$), a polaron exciton (singlet exciton), negative polaron ($p^-$), or a negative bipolaron ($bp^{2-}$), respectively.

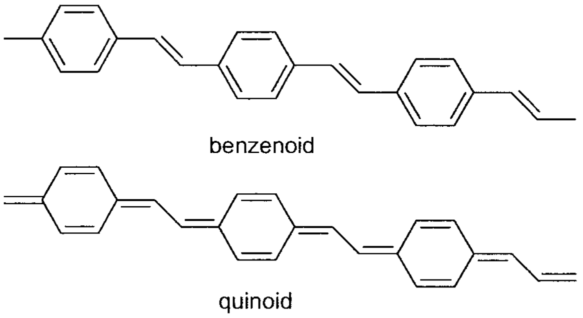

**Figure 2.17:** Benzenoid and quinoid isomers of PPV. The benzenoid isomer has a lower binding energy and is more stable than the quinoid isomer.

Positive polarons and bipolarons can also generate new optical absorption features which have an energy less than the energy gap of the material. Referring to Figure 2.18, bipolarons can exhibit up to four additional transitions from the valence level to the lower or upper bipolaron level ($\Delta$-$\omega$ or $\Delta$+$\omega$, respectively) and from the lower polaron level to the upper

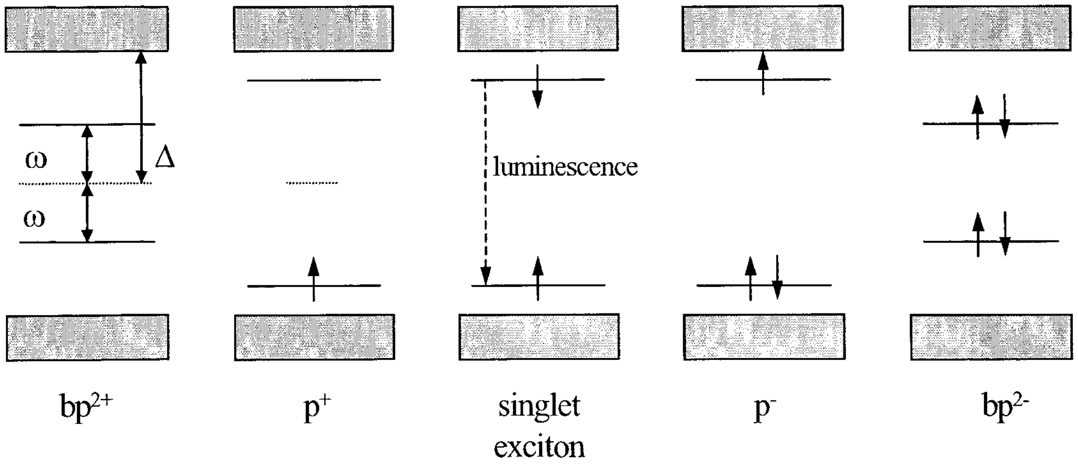

**Figure 2.18:** Polaron, bipolaron, and singlet exciton energy levels in a non-degenerate ground state polymer with an energy gap of $2\Delta$. After Greenham and Friend (reference 2).

polaron level or conduction level ($2\omega$ or $\Delta+\omega$, repsectively) with two of the transitions being degenerate. This degeneracy and asymmetric positioning of the bands about the mid-gap level is inconsistent with predictions made by the noninteracting electron continuum model (a modified SSH model).[92,94]

More advanced quantum chemical calculations have been used to describe the electronic structure of polymers and small molecules, in both the ground state and excited states and show good agreement with experimental observations.[95-99] These results provide confirmation that the simpler tight binding and Hückel methods which are the basis for the SSH formulation are useful; their failure is usually due to neglecting electron-electron interactions. For example, while it is predicted that the energy of the photons emitted by luminescence pathways should be equal to the energy spacing between two bipolaron levels, experimental photoinduced absorption measurements indicate that the energy of the emitted photons occurs at a higher energy.[100] Other groups have incorporated electron-electron interactions[101-103] and other symmetry-breaking effects[104,105] into the SSH framework but the importance of these contributions is still a source of uncertainty.

## 2.4 Conduction Methods in Non-Crystalline Solids

### 2.4.1 Applicability of the Band Model

In the preceding discussion, we assumed that the organic materials were in the form of single crystals and that the application of band theory to explain charge conduction was valid. Several groups have observed band-like transport in pentacene[106] and naphthalene[107,108] and treated theoretically by several groups.[109-111] Warta and Karl reported on hole mobilities in naphthalene single crystals of 400 $cm^2/Vs$ at 10 K using time of flight measurements.[38]

However, the approximations employed in band theory usually consists of the use of a one-electron potential and electron-lattice interactions are treated as small perturbations.[36] Ioffe has shown that semiconductors with a mobility of less than 100 $cm^2/Vs$ have a mean free path which is less than the wavelength of thermal electrons.[112,113] Under these conditions, the latter assumption no longer remains valid due to the increased effect of electron-lattice coupling. Another phenomenon which is cannot be explained by band theory is the increase in electrical conductivities in a number of molecular crystals upon melting.[36] If the number of carriers remains constant during the phase change, the loss of well-ordered crystal structure would be expected to lower the mobility of the carriers. While this has been observed for some materials, the opposite has been observed in others.[36,114] It has been shown by McCubbin that the loss of structure upon melting must lead to the broadening of the energy bands and to the formation of new energy levels within the band gap of the solid.[115] The new levels constitute shallow traps and would lower the recombination rate between electrons and holes which would lead to an increase in the conductivity.

### 2.4.2 Tunneling Models

Tunneling is a quantum mechanical phenomenon where an electron (or hole) passes through a potential energy barrier without acquiring enough energy to pass over the top of the barrier. This type of behaviour has been used to explain the transfer of charge from one molecule to a neighboring molecule.[1,36,116,117] The probability of a carrier tunneling from one potential well to the next increases with the height of the energy level involved. This model assumed that the tunneling action occurs when a electron in a $\pi$ molecular orbital on one molecule is excited from the ground state.

While the tunneling model has had success in predicting the magnitude of carrier mobility,[118,119] it fails to explain two important items: the negative temperature dependence of mobility and the difference between electron and hole mobilities.[120,121]

### 2.4.3 Hopping Models

In contrast to tunneling through the potential barrier which separates neighbouring molecules, a carrier can pass over the potential barrier. This process, shown in Figure 2.19, is referred to as hopping and the carrier is usually polaronic in nature.[36] The necessary conditions for hopping arise from restrictions on the mean free path $L$. When $L$ is comparable to or smaller than the lattice spacing, scattering effects make the application of band theory invalid. The hopping model also emphasizes the molecular character of the conduction states while the band model, in contrast, emphasizes the collective character of the conduction states.

Hopping theory was further developed by Mott and Davis to variable range hopping (VRH).[122] The optimum hopping distance is written as:

$$R = \left[\frac{2}{3}\pi\alpha N\left(E_F\right)k_B T\right]^{-\frac{1}{4}} \quad , \qquad (14)$$

where $\alpha$ is the inverse distance over which the carrier's wavefunction decays to $1/e$ of its original value, $N(E_F)$ is the density of states at the Fermi level, $k_B$ is the Boltzmann constant and $T$ is the temperature. Equation (14) is the hopping distance for a three-dimensional system and has a $T^{1/4}$ temperature dependence. For two- and one-dimensional systems there are $T^{1/3}$ and $T^{1/2}$ temperature dependencies, respectively. The origin of the term variable range hopping stems from the stipulation that the carrier is not restricted to hop to the nearest neighbor. In other hopping models, such as the Miller-Abrahams formalism, the distance that a carrier can hop is restricted to site that depends on the temperature $T$.[1] In the VRH model, the

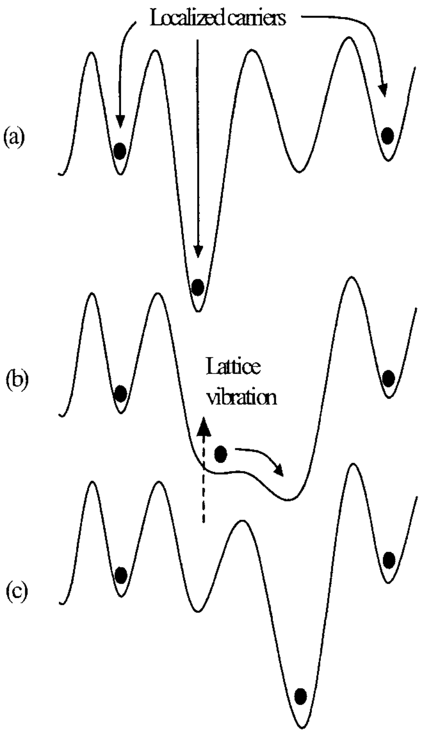

**Figure 2.19:** A schematic view of electrical conduction via hopping. (a) carriers are localized in potential wells. (b) a lattice vibration modifies the local potential allowing a previously trapped carrier to move to another site.(c) the final state after the lattice vibration has been dissipated showing the motion of a carrier from one site to another.

optimal hopping distance is an inverse function of temperature. The physical interpretation of this dependence may be described as when the temperature decreases the probability of hopping decreases, so the volume of available sites must be increased in order to optimize the probability of finding a suitable transport route, thus increasing $R$. The probability per unit time of such a hop is proportional to $\exp(-T^{-1/4})$ and therefore decreases with decreasing temperature. VRH theory predicts a conductivity of the form:

$$\sigma = 2\left[\frac{9}{8}\frac{N(E_F)}{\pi\alpha k_B T}\right]^{\frac{1}{2}} \nu_{ph} \exp\left[-\left(\frac{T_o}{T}\right)^{\frac{1}{4}}\right], \tag{15}$$

where $T_o$ is a characteristic temperature, $\nu_{ph}$ is the average phonon frequency, and the density of states is assumed to be constant.

The hopping properties of polarons have a strong temperature dependence. For temperatures below some critical temperature ($T_c$, or the Debye temperature) the polarons tunnel through narrow bands. When the temperature is above $T_c$ the polaronic band collapses and transport occurs via hopping.[93] The shape of the drift mobility as a function of reciprocal temperature is shown in Figure 2.20. The transition from band-type transport to hopping transport was first reported by Schein and co-workers in 1978 in naphthalene.[123]

Polarons can be classified as small or large, depending on the size of the polaron binding energy. This is defined as the energy gain of an infinitely slow carrier owing to the polarization and distortion of the lattice. In a large polaron, the binding energy is smaller than the conduction or valence bandwidth. The converse is true for small polarons, which are typically encountered in organic materials.

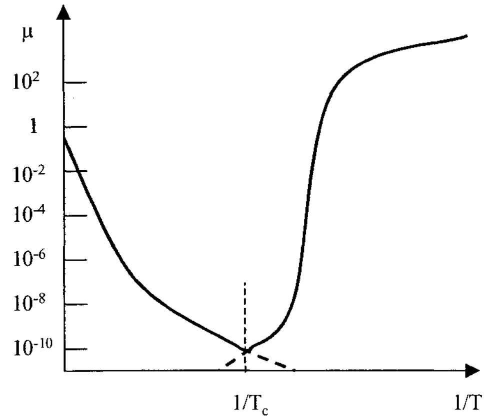

| $T > T_c$ | $T < T_c$ |
|---|---|
| Phonon-assisted hopping | Small polaron band |
| $\lambda \approx a$ | $\lambda > a$ |
| No correlation between initial and final phonon states | Phonon states remain unchanged during intermolecular transitions |

**Figure 2.20:** Drift mobility μ in a small polaron conductor as a function of reciprocal temperature. The critical temperature $T_c$ separates the hopping conduction regime from the band conduction regime. After Pope and Swenberg (reference 1).

The theory of small polarons was first proposed by Yamashita and Kurosawa to explain the small observed mobility in transition metal oxides.[124] Holstein has extensively developed the theory of small polarons.[125]

There is still no definitive evidence supporting the existence of small polaron band conduction in some important families of organic semiconductors such as thiophene polymers and oligomers.[126] It is thought that because the small polaron band width is extremely narrow, the small polaron band model cannot be regarded as suitable when impurities are present to a sufficient degree.

## 2.5 Relevance to OFETs

This chapter has reviewed important physical properties of organic semiconductors. Various techniques which are used to deposit the materials have been presented. Some of the issues which distinguish the growth behaviour of organic materials from inorganic materials was summarized. The concept of the configuration coordinate diagram was introduced and a discussion of the electronic properties of organic semiconductors was presented. Reference will be made to these concepts in Chapters 7 and 8. The Born-Oppenheimer approximation was introduced and is used as a fundamental tool in the modeling results presented in Chapter 7.

Polarons and solitons were introduced and their role in charge transport and electronic structure was outlined. Conduction methods in polycrystalline and amorphous organic solids were discussed in terms of quantum mechanical tunneling and variable range hopping.

## 2.6 References

[1] M. Pope and C. E. Swenberg, *Electronic Processes in Organic Crystals and Polymers*, Second ed. (Oxford University Press, New York, 1999).

[2] N. C. Greenham and R. H. Friend, in *Solid State Physics: Advances in Research and Applications*; *Vol. 49*, edited by H. Ehrenreich and F. Spaepen (Academic Press, San Diego, 1995), p. 1-149.

[3] C. W. Tang and S. A. Van Slyke, Appl. Phys. Lett. **51,** 913 (1987).

[4] C. W. Tang, S. A. Van Slyke, and C. H. Chen, J. Appl. Phys. **65,** 3610 (1989).

[5] J. H. Burroughes, D. D. C. Bradley, A. R. Brown, R. N. Marks, K. Mackay, R. H. Friend, P. L. Burns, and A. B. Holmes, Nature **347,** 539 (1990).

[6] C. D. Dimitrakopoulos, S. Purushothaman, J. Kymissis, A. Callegari, and J. M. Shaw, Science **283,** 822 (1999).

[7] S. F. Nelson, Y.-Y. Lin, D. J. Gundlach, and T. N. Jackson, Appl. Phys. Lett. **72,** 1854 (1998).

[8] D. J. Gundlach, Y. Y. Lin, T. N. Jackson, S. F. Nelson, and D. G. Schlom, IEEE Electron Device Lett. **18,** 87 (1997).

[9] C. H. M. Maree, R. A. Weller, L. C. Feldman, K. Pakbaz, and H. W. H. Lee, J. Appl. Phys. **84,** 4013 (1998).

[10] Y. Agari, M. Shimada, and A. Ueda, Polymer **38,** 2649 (1997).

[11] H. Klauk, M. Halik, U. Zschieschang, G. Schmid, W. Radlik, and W. Weber, J. Appl. Phys. **92,** 5259 (2002).

[12] D. Knipp, R. A. Street, B. Krusor, and R. Aptr, J. Non-Cryst. Solids **299-302,** 1042 (2002).

[13] M. Shtein, J. Mapel, J. B. Benziger, and S. R. Forrest, Appl. Phys. Lett. **81,** 268 (2002).

[14] C. J. Drury, C. M. J. Mutsaers, C. M. Hart, M. Matters, and D. M. deLeeuw, Appl. Phys. Lett. **73,** 108 (1998).

[15] H. Sirringhaus, N. Tessler, and R. H. Friend, Science **280,** 1741 (1998).

[16] A. R. Brown, C. P. Jarrett, D. M. de Leeuw, and M. Matters, Synth. Met. **88,** 37 (1997).

[17] A. Assadi, C. Svensson, M. Willander, and O. Inganäs, Appl. Phys. Lett. **53,** 195 (1988).

[18] Z. Bao, A. Dodabalapur, and A. J. Lovinger, Appl. Phys. Lett. **69,** 4108 (1996).

[19] H. Sirringhaus, R. J. Wilson, R. H. Friend, M. Inbasekaran, W. Wu, E. P. Woo, M. Grell, and D. D. C. Bradley, Appl. Phys. Lett. **77,** 406 (2000).

[20] A. Afzali, C. D. Dimitrakopoulos, and T. L. Breen, J. Am. Chem. Soc. **12,** 8812 (2002).

[21] R. W. I. de Boer, M. E. Gershenson, A. F. Morpurgo, and V. Podzorov, Phys. Stat. Sol. A. **201,** 1302 (2004).

[22] J. Yamaguchi, K. Itaka, T. Hayakawa, K. Arai, M. Yamashiro, S. Yaginuma, and H. Koinuma, Macromol. Rapid Commun. **25,** 334 (2004).

[23] G. B. Blanchet, C. R. Fincher, and I. Malajovich, J. Appl. Phys. **94,** 6181 (2003).

[24] A. J. Salih, J. M. Marshall, and J. M. Maud, J. Non-Cryst. Solids **230 B,** 1240 (1998).

[25] C. Hong, H. B. Chae, K. H. Lee, S. K. Ahn, C. K. Kim, T. W. Kim, N. I. Cho, and S. O. Kim, Thin Solid Films **409,** 37 (2002).

[26] L. D. Wang and H. S. Kwok, Thin Solid Films **363,** 58 (2000).

[27] J. G. Laquindanum, H. E. Katz, and A. J. Lovinger, J. Amer. Chem. Soc. **120,** 664 (1998).

[28] C. D. Dimitrakopoulos, A. Afzali, B. Furman, J. Kymissis, and S. Purushothaman, Synth. Met. **89,** 193 (1997).

[29] C. Kloc, P. G. Simpkins, T. Siegrist, and R. A. Laudise, J. Cryst. Growth **182,** 416 (1997).

[30] R. A. Laudise, C. Kloc, P. G. Simpkins, and T. Siegrist, J. Cryst. Growth **187,** 449 (1998).

[31] R. W. I. de Boer, T. M. Klapwijk, and A. F. Morpurgo, Appl. Phys. Lett. **83,** 4345 (2003).

[32] V. Podzorov, V. M. Pudalov, and M. E. Gershenson, Appl. Phys. Lett. **82,** 1739 (2003).

[33] V. Podzorov, S. E. Sysoev, E. Loginova, V. M. Pudalov, and M. E. Gershenson, Appl. Phys. Lett. **83,** 3504 (2003).

[34] R. Dabestani, M. Nelson, and M. E. Sigman, Photochem. Photobiol. **64,** 80 (2996).

[35] R. Farchioni and G. Grosso, *Organic Electronic Materials* (Springer-Verlag, Berlin, 2001).

[36] F. Gutmann and L. E. Lyons, *Organic Semiconductors* (Robert E. Krieger Publishing Company, Malabar,

1981).

[37] N. Karl, in *Crystals: Growth, Properties and Applications*; *Vol. 4* (Springer-Verlag, Berlin, 1980), p. 1.

[38] W. Warta and N. Karl, Phys. Rev. B **32,** 1172 (1985).

[39] S. Narioka, H. Ishii, D. Yoshimura, M. Sei, Y. Ouchi, K. Seki, S. Hasegawa, T. Miyazaki, Y. Harima, and K. Yamashita, Appl. Phys. Lett. **67,** 1899 (1995).

[40] A. Rajagopal, C. I. Wu, and A. Kahn, J. Appl. Phys. **83,** 2649 (1996).

[41] Y. Park, V. Choong, E. Ettedgui, Y. Gao, B. R. Hsieh, T. Wehrmeister, and K. Müllen, Appl. Phys. Lett. **69,** 1080 (1996).

[42] R. Schlaf, B. A. Parkinson, P. A. Lee, K. W. Nebesny, and N. R. Armstrong, Appl. Phys. Lett. **73,** 1026 (1998).

[43] S. T. Lee, X. Y. Hou, M. G. Mason, and C. W. Tang, Appl. Phys. Lett. **74,** 670 (1998).

[44] T. Kugler, W. R. Salaneck, H. Rost, and A. B. Holmes, Chem. Phys. Lett. **310,** 391 (1999).

[45] S. C. Veenstra, U. Stalmach, V. V. Krasnikov, G. Hadziioannou, H. T. Jonkman, A. Heeres, and G. A. Sawatzky, Appl. Phys. Lett. **76,** 2253 (2000).

[46] P. G. Schroeder, C. B. France, J. B. Park, and B. A. Parkinson, J. Phys. Chem. B **107,** 2253 (2003).

[47] I. G. Hill, A. J. Mäkinen, and Z. H. Kafafi, Appl. Phys. Lett. **77,** 1825 (2000).

[48] N. J. Watkins, L. Yan, and Y. Gao, Appl. Phys. Lett. **80,** 4384 (2002).

[49] H. Peisert and M. Knupfer, Phys. Stat. Sol. A. **201,** 1055 (2004).

[50] H. Ishii, N. Hayashi, E. Ito, Y. Washizu, K. Sugi, Y. Kimura, M. Niwano, Y. Ouchi, and K. Seki, Phys. Stat. Sol. A. **201,** 1075 (2004).

[51] M. Iwamoto, A. Fukuda, and E. Ito, J. Appl. Phys. **75,** 1607 (1994).

[52] N. Hayashi, H. Ishii, Y. Ouchi, and K. Seki, J. Appl. Phys. **92,** 3784 (2002).

[53] R. B. Campbell, J. M. Robertson, and J. Trottier, Acta Cryst. **14,** 705 (1961).

[54] C. D. Dimitrakopoulos, A. R. Brown, and A. Pomp, J. Apply. Phys. **80,** 2501 (1996).

[55] T. Jentzsch, H. J. Juepner, K. W. Brzezinka, and A. Lau, Thin Solid Films **315,** 273 (1998).

[56] C. D. Dimitrakopoulos and D. J. Mascaro, IBM J. Res. & Dev. **45,** 11 (2001).

57 F. Schreiber, Phys. Stat. Sol. A. **201,** 1037 (2004).

58 J. A. Venables, G. D. T. Spiller, and M. Hanbucken, Rep. Prog. Phys. **47,** 399 (1984).

59 R. Ruiz, B. NIckel, N. Koch, L. C. Feldman, R. Haglund Jr., A. Kahn, F. Family, and G. Scoles, Phys. Rev. Lett. **91,** 136102 (2003).

60 F.-J. Meyer zu Heringdorf, M. C. Reuter, and R. M. Tromp, Nature **412,** 517 (2001).

61 Y.-Y. Lin, D. J. Gundlach, S. F. Nelson, and T. N. Jackson, IEEE Trans. Electron Devices **44,** 125 (1997).

62 K. Shankar and T. N. Jackson, J. Mater. Res. **19,** 2003 (2004).

63 M. Voigt, S. Dorfsfeld, A. Volz, and M. Sokolowski, Phys. Rev. Lett. **65,** 026103 (2003).

64 F. Schreiber, Prog. Surf. Sci. **65,** 151 (2000).

65 F. Schreiber, J. Phys.: Condens. Matter **16,** R881 (2004).

66 A. Salleo and R. A. Street, J. Appl. Phys. **94,** 471 (2003).

67 T. C. Gorjanc, I. Lévesque, and M. D'Iorio, J. Vac. Sci. Technol. B. **22,** 760 (2004).

68 A. Salleo, M. L. Chabinyc, M. S. Yang, and R. A. Street, Appl. Phys. Lett. **81,** 4383 (2002).

69 D. Knipp, R. A. Street, A. Vökel, and J. Ho, J. Appl. Phys. **93,** 347 (2003).

70 T. C. Gorjanc, I. Lévesque, and M. D'Iorio, Appl. Phys. Lett. **84,** 930 (2004).

71 S. R. Forrest, Chem. Rev. **87,** 1793 (1997).

72 L. E. Lyons, J. Chem. Soc., 5001 (1957).

73 E. A. Silinsh, *Organic Molecular Crystals* (Springer-Verlag, Berlin, 1980).

74 A. N. Terenin and F. I. Vilesov, in *Advances in Photochemistry*; *Vol. 2* (Interscience, New York, 1964).

75 F. I. Vilesov and A. N. Terenin, Dokl. Akad. Nauk SSSR **133,** 1060 (1960).

76 F. I. Vilesov and A. N. Terenin, Dokl. Akad. Nauk SSSR **134,** 71 (1960).

77 B. L. Kurbatov and F. I. Vilesov, Dokl. Akad. Nauk SSSR **141,** 1343 (1961).

78 J. E. Brady and G. E. Humiston, *General Chemistry: Principles and Structure*, Second ed. (John Wiley & Sons, Toronto, 1978).

79 P. M. Borsenberger and D. S. Weiss, *Organic Photoreceptors for Xerography* (Marcel Dekker, New York, 1998).

[80] L. J. Rothberg and A. J. Lovinger, J. Mater. Research. **11,** 3174 (1996).

[81] H. C. Longuet-Higgins and L. Salem, Proc. Roy. Soc. London **A521,** 172 (1959).

[82] M. J. Rice, Phys. Lett. **71A,** 152 (1979).

[83] A. J. Heeger, S. Kivelson, J. R. Schrieffer, and W.-P. Su, Rev. Mod. Phys. **60,** 781 (1988).

[84] J. F. Lennard-Jones, Proc. Roy. Soc. London **A158,** 280 (1937).

[85] W.-P. Su, J. R. Schrieffer, and A. J. Heeger, Phys. Rev. Lett. **42,** 1698 (1979).

[86] W.-P. Su, J. R. Schrieffer, and A. J. Heeger, Phys. Rev. B. **22,** 2099 (1980).

[87] R. Peierls, *Quantum Theory of Solids* (Clarendon Press, Oxford, 1955).

[88] D. Baeriswyl, D. K. Campbell, and S. Mazumdar, in *Conjugated Conducting Polymers*; *Vol. 102*, edited by H. Kiess (Springer-Verlag, Berlin, 1992), p. 7.

[89] D. Baeriswyl and K. Maki, Phys. Rev. B. **31,** 6633 (1985).

[90] H. Takayama, Y. R. Lin-Liu, and K. Maki, Phys. Rev. B. **21,** 2388 (1980).

[91] S. A. Brazovskii and N. N. Kirova, JEPT Lett. **33,** 4 (1981).

[92] A. S. Alexandrov and N. Mott, *Polarons and Bipolarons* (World Scientific, New Jersey, 1995).

[93] K. Fesser, A. R. Bishop, and D. K. Campbell, Phys. Rev. B **27,** 4804 (1983).

[94] J. L. Brédas, in *Handbook of Conducting Polymers*; *Vol. 2*, edited by T. A. Skotheim (Marcel Dekker, New York, 1986), p. 859.

[95] J. L. Brédas, R. R. Chance, and R. Silbey, Phys. Rev. B **26,** 5843 (1982).

[96] J. L. Brédas, B. Thémans, J. G. Fripiat, J. M. André, and R. R. Chance, Phys. Rev. B **29,** 6761 (1984).

[97] J. L. Brédas and G. B. Street, Acc. Chem. Res. **18,** 309 (1985).

[98] P. Bröms, M. Fahlman, K. Z. Xing, W. R. Salaneck, P. Dannetun, J. Cornil, D. A. dos Santos, J. L. Brédas, S. Moratti, A. B. Holmes, and R. H. Friend, Synth. Met. **67,** 93 (1994).

[99] R. H. Friend, D. D. C. Bradley, and P. D. Townsend, J. Phys. D **20,** 1367 (1987).

[100] U. Sum, K. Fesser, and H. Büttner, Solid State Commin. **61,** 607 (1987).

[101] M. Gabrowski, D. Home, and J. R. Schrieffer, Phys. Rev. B **31,** 7850 (1985).

[102] M. Sasai and H. Fukutome, Prog. Theor. Phys. **73,** 1 (1985).

[103] U. Sum, K. Fesser, and H. Büttner, Phys. Rev. B **38,** 6166 (1988).

[104] P. L. Danielson and R. C. Ball, J. Physique **46,** 1611 (1985).

[105] O. Ostroverkhova, D. G. Cooke, S. Shcherbyna, R. F. Egerton, F. Hegmann, R. R. Tykwinski, and J. E. Anthony, Phys. Rev. B., 035204 (2005).

[106] W. Graupner, G. Cerullo, G. Lanzani, M. Nisoli, E. J. W. List, G. Leising, and S. De Silvestri, Phys. Rev. Lett. **81,** 3259 (1998).

[107] P. B. Miranda, D. Moses, and A. J. Heeger, Phys. Rev. B. **64,** 081201 (2001).

[108] K. Hannewald and P. A. Bobbert, Appl. Phys. Lett. **85,** 1535 (2004).

[109] V. M. Kenkre and P. E. Parris, Phys. Rev. B. **65,** 205104 (2002).

[110] R. Kersting, U. Lemmer, M. Deussen, H. J. Bakker, R. F. Mahrt, H. Kurz, V. I. Arkhipov, H. Bässler, and E. O. Göbel, Phys. Rev. Lett. **73,** 1440 (1994).

[111] A. F. Ioffe, Phys. Chem. Solids **8,** 6 (1959).

[112] A. F. Ioffe, Can. J. Phys. **34,** 1342 (1956).

[113] G. D. Thaxton, R. C. Jarnagin, and M. Silver, J. Phys. Chem. **66,** 2461 (1962).

[114] W. L. McCubbin, Trans. Faraday Soc. **59,** 769 (1963).

[115] D. D. Eley, G. D. Parfitt, M. J. Perry, and D. H. Taysum, Trans. Faraday Soc. **49,** 79 (1953).

[116] D. D. Eley and G. D. Parfitt, Trans. Faraday Soc. **51,** 1529 (1955).

[117] D. D. Eley, J. Polymer Sci. C. **17,** 73 (1967).

[118] D. D. Eley and M. R. Willis, in *Symposium on Electrical Conductivity in Organic Solids*, edited by H. Kallmann and M. Silver (Wiley Interscience, New York, 1961), p. 257.

[119] R. A. Keller and H. E. Rast, J. Chem. Phys. **36,** 2640 (1962).

[120] R. H. Tredgold, Proc. Phys. Soc. (London) **80,** 807 (1962).

[121] N. F. Mott and E. A. Davis, *Electronic Processes in Non-Crystalline Materials* (Clarendon Press, Oxford, 1979).

[122] L. B. Schein, C. B. Duke, and A. R. McGhue, Phys. Rev. Lett. **40,** 197 (1978).

[123] J. Yamashita and T. Kurosawa, J. Phys. Chem. Solids **5,** 34 (1958).

[124] T. Holstein, Ann. Phys. **8**, 343 (1959).

[125] G. Horowitz and P. Delannoy, in *Handbook of Oligo- and Polythiophenes*, edited by D. Fichou (Wiley-VCH, Toronto, 1999), p. 283.

# Chapter 3
# Optical Properties of Organic Semiconductors

## 3.1 Introduction

The optical properties of organic materials are unique when compared to inorganic elements and compounds. To change the optical properties in crystalline inorganic semiconductors, it is necessary to vary parameters such as strain, mole fractions, and doping to adjust the colour over a small wavelength range. In organic materials, the optical and electrical properties can be changed by simply modifying a functional group on the molecule. This allows molecules to be engineered to possess the desired optical properties.

In this Chapter, the concept of optical transitions and selection rules as applied to organic molecules will be reviewed. The configuration coordinate diagram will be introduced and its relation to the absorption and emission spectra of organic molecules will be explained. The different types of excitons and their roles in organic molecules will be outlined and we will conclude the chapter with some remarks regarding energy transfer mechanisms.

## 3.2 Optical Properties

### 3.2.1 Background

The Born-Oppenheimer approximation was used in the previous chapter to separate the wavefunction of the molecule into the electronic, vibrational, and rotational components. For a given electronic state, the associated vibrational levels are labeled 0, 1, 2... in order of increasing energy. A transition referred to as $0 \rightarrow 2$ indicates a transition from a given electronic ground state in its 0th vibrational mode to an electronic state in its second vibrational state. Figure 3.1 shows a diagram of the vibronic energy levels and their transitions. Usually electronic transition energies are in the ultraviolet or visible portion of the electromagnetic spectrum , the vibrational energies in the near infrared portion of the spectrum and the rotational energies are in the far infrared.[1]

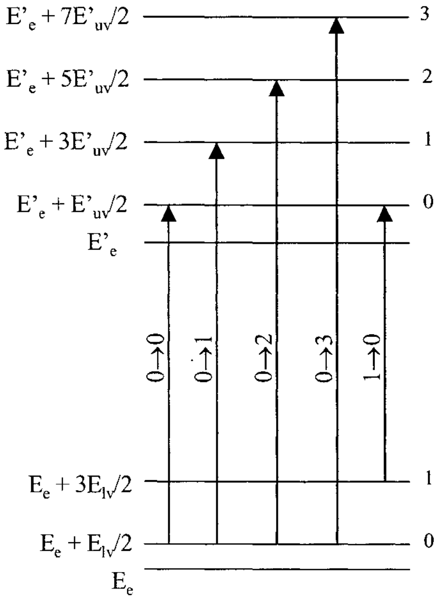

**Figure 3.1:** Vibronic absorption transitions. The vibrational levels are numbered in order of increasing energy. The 1→0 transition is known as a “hot band’ transition.

The usual convention for referring to electronic transitions is taken after Birks.[2] The states are denoted by subscripts *lm* and *un*, which denote the $m^{th}$ vibrational level of the $l^{th}$ electronic state and the $n^{th}$ vibrational level of the $u^{th}$ electronic state, respectively. The absorption rate of light is indicated by the parameter $B_{lm,un}$. There are two possible emission processes: spontaneous emission and stimulated emission. Spontaneous emission is a random process and determines the normal radiative lifetime of the excited state and the rate constant is denoted by $A_{un,lm}$. The rate of spontaneous emission is denoted $B_{un,lm}$. These parameters are more commonly referred to as Einstein coefficients.[3] The total probability of transitions to all vibronic levels of an upper π electronic state $u$ from the lowest vibrational state of a lower state $l$ is written as:[1]

$$B_{lu} = \sum_{n} B_{l0,un} = \frac{2303c}{hn_{o}N} \int \frac{\alpha(\nu)}{\nu} d\nu, \qquad (1)$$

where $c$ is the speed of light, $h$ is Planck's constant, $n_o$ is the refractive index of the medium, $N$ is Avogadro's number and $\alpha(\nu)$ is the absorption coefficient as a function of the photon frequency $\nu$. The integration in Equation 1 is over the entire frequency range and is summed over all possible vibrational states of level $l$. Figure 3.2 shows the shape of the absorption function $\alpha(\nu)$ as a function of frequency $\nu$. The peaks in the absorption spectrum correspond to vibronic transitions as defined in Figure 3.1. The shaded area under the curve in Figure 3.2 represents the value of Equation 1 after it has been integrated.

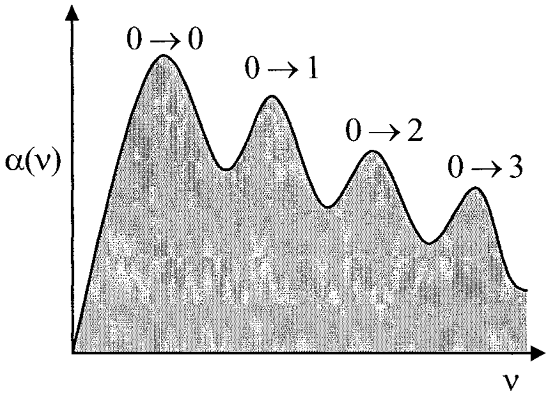

**Figure 3.2:** The absorption coefficient as a function of the frequency $\nu$. The transitions are from the ground state vibronic state to an excited state vibronic level, denoted above the peaks. The integration of Equation (1) is represented by the shaded portion under the curve.

### 3.2.2 Selection Rules

The wavefunction of a molecule can be written as:

$$\psi_t = \psi_e \psi_v \psi_r , \tag{2}$$

where the $t$, $e$, $v$, and $r$ subscripts refer to the total wavefunction, and the electronic, vibrational, and rotational components of the wavefunction, respectively, within the adiabatic Born-Oppenheimer formulation. The probability of exciting the molecule is:

$$R_{lu}^2 \propto \left| \left\langle \psi_u \middle| \vec{\mu} \middle| \psi_l \right\rangle \right|^2 , \tag{3}$$

where the subscripts refer to the initial and final states and $\mu$ is the dipole moment operator. As mentioned in Chapter 2, the electronic wavefunction can be further separated into two components which are only dependent on position or spin and a rotational component. If it is assumed that the position and spin components do not interact and that the rotational contribution is negligible, Equation 3 can be re-written in the following form:

$$R_{lu}^2 \propto \left| \langle \psi'_{el} | \vec{\mu} | \psi'_{eu} \rangle \right|^2 \left| \langle \chi_{vl} | \chi_{vu} \rangle \right|^2 \left| \langle \psi_{sl} | \psi_{su} \rangle \right|^2 . \tag{4}$$

The vibrational wavefunctions are represented by $\chi$ and the middle term is known as the Frank-Condon factor, discussed in Chapter 2, and $l$ and $u$ represent initial and final states. The last term represents the spin wavefunction of the initial and final states. The dipole moment operator $\mu$ is only present in the term containing the electronic wavefunctions because the nuclei cannot respond rapidly enough to optical frequencies and the spin is not affected by electric fields. If any of the values in Equation 4 is zero, then the transition probability is zero and the transition would be forbidden.

There are several factors which influence the absorption coefficient. Consider the first term which contains the dipole moment operator. Dipole allowed transitions are those for which the transition moment,

$$T_{lu} = \langle \psi_l | \vec{\mu} | \psi_u \rangle , \tag{5}$$

is not equal to zero. When $T_{lu} = 0$ then it is said that the transition $l \rightarrow u$ is dipole forbidden. Due to the nature of the dipole operator, $T_{lu}$ is zero unless $l$ and $u$ have opposite symmetry with respect to the inversion operator.

If we consider the vibrational degrees of freedom, the transition probability can be written as:

$$T_{lm,un} = T_{lu}\langle \chi_{lm} | \chi_{um} \rangle, \tag{6}$$

where $T_{lu}$ is the purely electronic amplitude defined in Equation 5 evaluated at the equilibrium position of the nuclei, and $\chi$ represents the vibrational wavefunctions.

Figure 3.3 shows the configuration coordinate diagram for a ground (*l*) and excited (*u*) electronic state. Vertical transitions which occur at time scales lower than the reaction time for nuclei are referred to as Frank-Condon transitions and is denoted by transition a. Once in an excited vibrational state in the upper electronic manifold, the carrier undergoes a radiationless

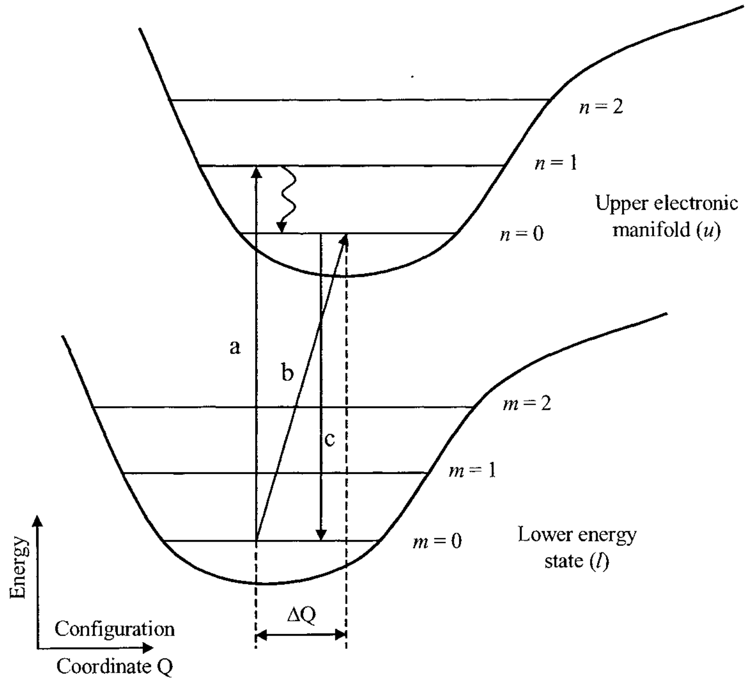

**Figure 3.3:** The configuration coordinate diagram for lower (*l*) and upper (*u*) electronic states. Transition a represents a vertical Frank-Condon transition. Transition b represents a zero-phonon transition. Transition c indicates fluorescence emission from *u* to *l*. The wavy line is radiationless decay from an excited vibrational level to the lowest vibrational state in the upper electronic manifold. ΔQ is the change in configuration coordinate of the two states. After Pope and Swenberg (reference 1).

relaxation to the vibrational ground state of the upper manifold, usually the $n = 0$ state. Once the system has relaxed to the $n = 0$ state, the electron can return to the electronic ground state by emitting a photon, indicated by transition c, or by other processes of decay. The emitted photon is characterized by having a longer wavelength than that of the photon involved in the excitation process. The redshift of the emission maximum compared to the fundamental absorption maximum is known as the Stokes shift and is illustrated in Figure 3.4.[1] This figure also illustrates the mirror symmetry between the fundamental absorption band and the vibrational structure in the fluorescence band.

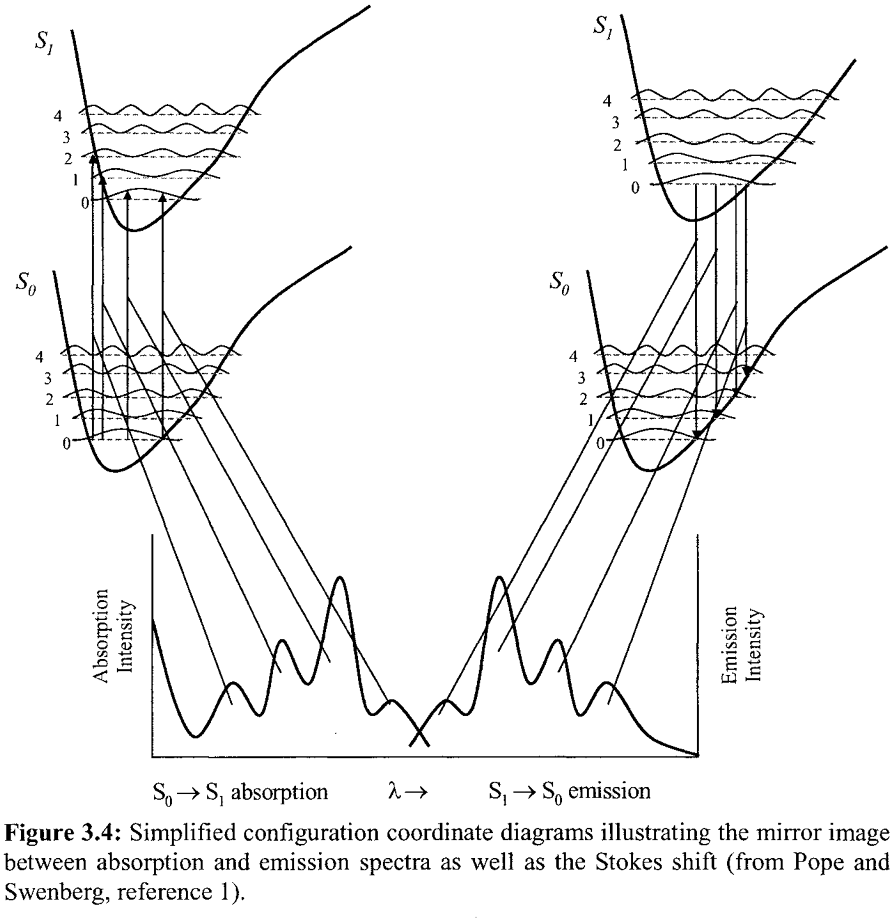

**Figure 3.4:** Simplified configuration coordinate diagrams illustrating the mirror image between absorption and emission spectra as well as the Stokes shift (from Pope and Swenberg, reference 1).

From Equation 4, it can be seen that there are also spin selection rules which contribute to the transition probability. Only states with the same spin quantum number $S$ can combine with each other. Thus, neglecting spin-orbit effects, transitions from the singlet state to the triplet state are forbidden. In practice, there is some small spin-orbit coupling which does occur and the transition rates between states of different multiplicity are typically $10^3$-$10^5$ times slower than same state transitions.[1]

### 3.2.3 Excitons

*Introduction*

Organic molecules have a plethora of excited states, especially in unsaturated molecules (molecules with double or triple carbon-carbon bonds), which leads to a rich absorption spectrum compared to inorganic crystals. Electrons which are optically excited remain localized within a few molecular spacings from the excitation site and usually form charge transfer or Frenkel excitons.

The concept of excitons was briefly introduced in Chapter 2 in the discussion of polarons and bipolarons. An exciton can be considered as a bound electron-hole pair and can be classified as either a Frenkel exciton if the electron-hole pair is localized onto one molecular site, a Wannier exciton if the electron-hole pair is extended over many molecular sites, or as a charge transfer (CT) exciton if the electron hole pair extends over only a few adjacent molecular sites. Figure 3.5 illustrates the different types of excitons.[4] In organic materials, excitons are usually Frenkel or CT types.[1,4]

A Frenkel exciton is a bound electron-hole pair that is localized on a single molecule

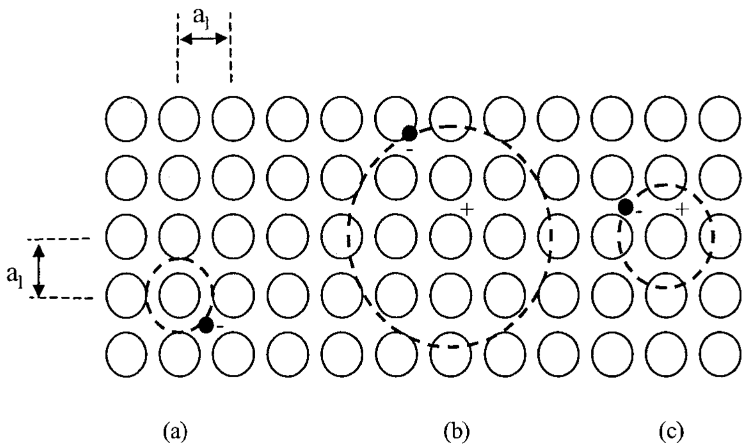

**Figure 3.5:** Schematic diagram of (a) Frenkel, (b) Wannier, and (c) charge transfer (CT) excitons.

whereas a CT exciton consists of an electron which is correlated with a hole on a neighboring molecular site. CT excitons resemble Wannier more than Frenkel excitons. Bounds and Siebrand have suggested that all but the lowest level CT states can be treated as Wannier excitons in anthracene.[5]

Optical transitions of Wannier excitons in a solid resemble the Rydberg transitions in a hydrogen atom. The modified Rydberg levels form a series defined by:

$$E = E_g - \frac{G}{n^2}, \tag{7}$$

where $n = 1, 2, \ldots$, $E_g$ is the band gap energy of the material, and $G$ is the binding energy of the exciton.

In organic materials Wannier excitons do not exist due to the small exciton radius compared to the molecular spacing, high effective masses (since the intermolecular contacts are not large) and relatively low permitivities. It should be noted, however, that in some cases such as PPV the effective mass for motion along the polymer chain is relatively low ($m_{\parallel} = 0.0421\ m_e$,

$m_{\perp} = 2.66m_e$).[6,7]

*CT Excitons*

When a CT exciton is created, the excited electron is transferred to the nearest or next-nearest neighbouring molecular site, but still remains correlated with the hole on the original molecular site. These entities were originally termed ionic states, but are now referred to as CT excitons.[8] CT excitons may be considered as distorted Wannier excitons due to the anisotropic nature of molecular crystals. CT excitons can also be mobile (delocalized) or trapped. CT states were predicted by Lyons to lie below the conduction (LUMO) band with energies,

$$E_{CT} = I_g - A_g - P_{eh}(r) - C(r), \tag{8}$$

where $I_g$ is the molecular ionization potential, $A_g$ is the molecular electron affinity, $P_{eh}(r)$ is the polarization energy of an electron-hole pair separated by a distance $r$, and $C(r)$ is the coulombic energy of the two molecules (separated by a distance $r$) on which the electron and hole reside on.

Ewing and Kearns have predicted that the oscillator strength of optical transitions in neutral crystals to a CT state are extremely weak and are estimated to be of the order of $10^{-4}$.[9] Another factor which contributes to the difficulty in observing CT states is that CT transitions occur in the same spectral region as those for Frenkel excitons, which are extremely strong. Tanaka has reported CT transitions between 3.1-3.5 eV in α-perylene crystals,[10] 3.36 eV for a CT transition in 9,10-dichloroanthracene by Tanaka and Shibata[11] and confirmed by Abbi and Hanson.[12] Pope, Burgos, and Giachino have reported on the observation of CT excitons in tetracene crystals and placed $E_{CT}$ = 2.9 eV based on other experimental data.[13] More recent reports indicate that this CT exciton may be in fact a trapped CT exciton. Sebastian *et al* have measured CT exciton levels using electroabsorption spectroscopy on a polycrystalline tetracene film.[14] The values of $E_{CT}$ found by Sebastian *et al* agree with those of Pope *et al* when proper account is taken for the different values of $E_g$ used in each report.

### *Singlet and Triplet Excitons*

In a free molecule, both singlet (S = 0) and triplet (S = 1) states can occur. The triplet state has a lower energy than its corresponding singlet state. Triplet excitons in crystals of anthracene, naphthalene, and biphenyl have been treated by several groups,[15-17] however phosphorescence is not observed from perfect homo-molecular crystals even though phosphorescence might be visible while dissolved in solution. Phosphorescence can be observed in blended thin films where a guest molecule is mixed with a host material.[18,19] Recently, OLEDs have been fabricated using materials which break the dipole forbidden optical decay of triplet excitons to create highly efficient OLEDs.[20-22]

Figure 3.6 illustrates the various processes which are possible when an electron is excited from the ground state by the absorption of a photon. The decay pathways can be either radiative (solid lines) or non radiative (dashed lines).

If the absorbed photon excited the electron from the ground state to some vibrational level in the excited singlet state (process 1), it will decay via phonon emission to the ground state of the excited singlet (process 2). Process 2 typically occurs on time scales approaching $10^{-13}$ seconds.[23] Once the electron is in the lowest vibronic state of the excited singlet state, one of three processes can occur: radiative decay to a vibronic level in the ground state (process 7),

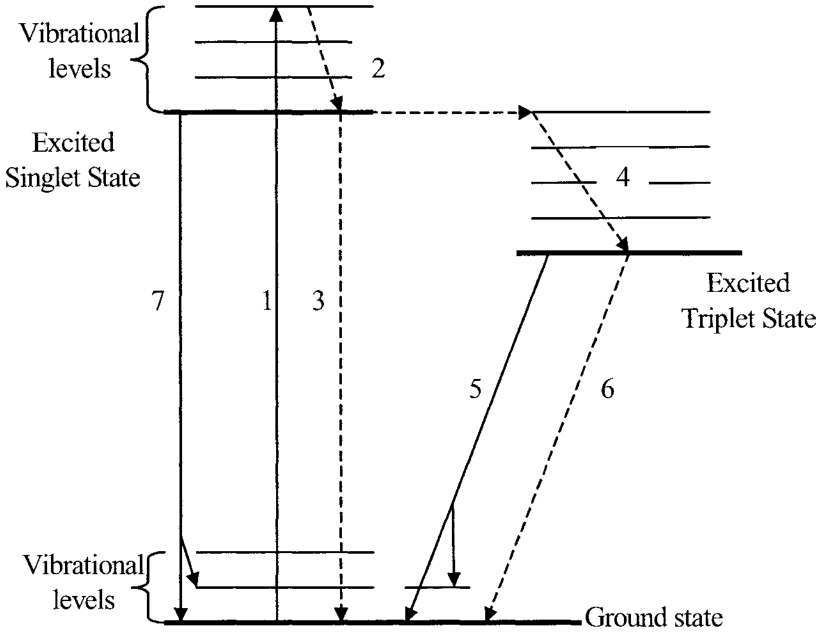

**Figure 3.6:** Transitions in optical materials when light is absorbed (1) and the various radiative (5,7) and non-radiative (2,3,4,6) decay pathways.

non-radiative decay to the ground state (process 3), or inter-system crossing (process 4) in which the electron will decay from the singlet ground state to a vibronic level in the triplet and proceed to decay to the ground state of the triplet.

Non-radiative transitions in electronic and vibronic states have been discussed in detail by Robinson and Frosch.[24-26] A typical example is that even a small 0.001 meV interaction between singlet and triplet states corresponds to a rate constant of the order of $10^7$ $sec^{-1}$. The observed rapid rate of intersystem crossing (process 4) may be explained as well as the relatively slow rate of triplet quenching (process 6).

Radiative transitions occur when an excited state is sufficiently long lived. Process 7 represents the fluorescence emission from a molecule and has a lifetime of approximately $10^{-8}$ sec, while process 5 has a lifetime of approximately $10^{-2}$ sec and is responsible for phosphorescence in the molecule. The transfer of the excitation in a molecular crystal by exciton motion usually occurs after process 2 has taken place.

### 3.2.4 Energy Transfer Mechanisms

There are two fundamental non-excitonic energy transfer mechanisms which are possible. The first is the reabsorption of fluorescence at another position within the crystal. Usually fluorescence emitted by a host crystal is only very weakly reabsorbed. Ferguson has shown, however, that reabsorption is inadequate to explain the fluorescence from tetracene molecules in an anthracene host.[27,28]

The second type of energy transfer is that proposed by Förster and involves the transfer of energy from a donor molecule to an acceptor molecule.[29] This process is known as resonant transfer or Förster energy transfer. Energy transfer is usually accomplished by the reabsorption of fluorescence from the donor (D) molecule by the acceptor (A) molecule and can occur at fairly large distances - typically more than 100 Å from the site of fluorescence. The net effect of this process is to increase the apparent lifetime of the singlet state because the fluorescence creates another exciton instead of exiting the medium and can be as large as a factor of two.[1]

Förster energy transfer depends on the overlap between the absorption spectrum of the acceptor and the fluorescence spectrum of the donor, shown as the shaded portion of Figure 3.7. Perrin[30] and Perrin[31] have defined the transfer rate at which energy passes from the donor to the acceptor as:

$$K_{D\to A} = \frac{4|J|}{\hbar} \propto \frac{1}{R^3}, \tag{9}$$

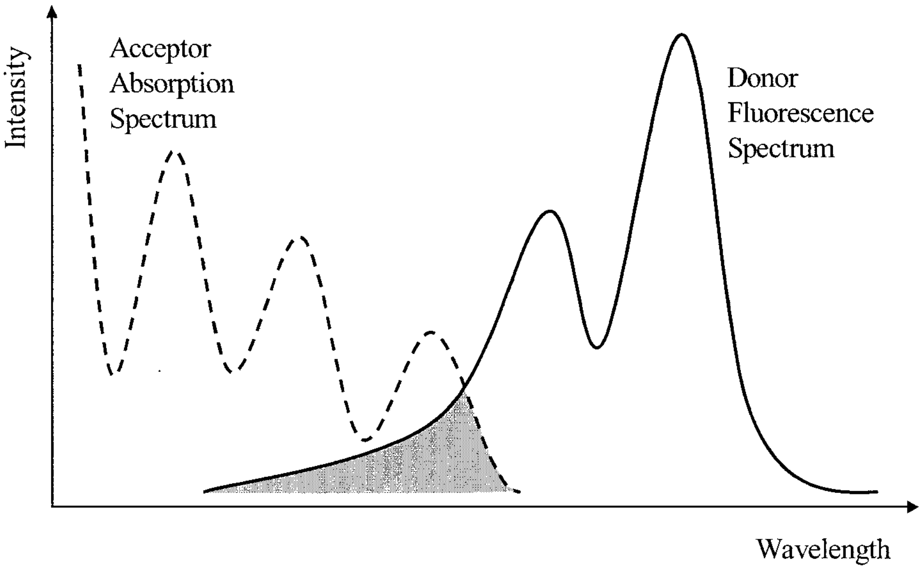

**Figure 3.7:** The overlap of the acceptor molecule's absorption spectrum with the donor molecule's fluorescence spectrum. A non-zero overlap, denoted by the shaded area, is required for long range Förster energy transfer.

where $R$ is the mean separation between donor and acceptor molecules and $J$ is the strength of the interaction between the donor and acceptor which, for dipole interaction, has an $R^{-3}$ dependence. The condition placed on Equation 9 in order to remain valid is that the acceptor state lifetime must be much longer than $\hbar|J|^{-1}$. If $|J|$ is much greater than the width of a single vibronic level ($\Delta E$), Equation 9 is obtained multiplied by the $0 \rightarrow 0$ Franck-Condon factor.[32] More commonly, if $\Delta E > |J|$ the transfer rate is then expressed as:[33]

$$K_{D \rightarrow A} = \frac{1}{\tau_D} \frac{1}{R^6} \left( \frac{3}{4\pi} \int \frac{c^4}{\omega^4 n_o^4} F_D(\omega) \sigma_A(\omega) d\omega \right), \tag{10}$$

where $F_D(\omega)$ is the normalized fluorescence emission spectrum, $\sigma_A(\omega)$ is the normalized acceptor absorption cross section per cm$^2$, $n_o$ is the index of refraction, $c$ is the speed of light, $\tau_D$ is the natural lifetime of the donor in the absence of quenching, and $\omega$ is the frequency. Knox has proposed a classical derivation of Equation 10 which fully accounts for the $R^{-6}$ dependence.[34]

## 3.3 Application to OLEDs

A simple method to alter the emission colour of an OLED takes advantage of Förster energy transfer. A suitable laser dye, such as DCM or Coumarin 540, is doped into a host material such as Alq.[35] The emission spectrum of Alq overlaps the absorption spectrum of the dye and energy is transferred.[36]

The presence of a large Stokes shift is also of technological importance because the materials are essentially transparent to the EL-generated light. The obvious benefit to having an OLED that does not re-absorb it's own light is a device with a higher external quantum efficiency. Another major benefit of the large Stokes shift is that OFETs can be used in the driving circuitry for a transparent OLED-based display as minimal amounts of visible light will be absorbed by the driving circuitry, resulting in an almost transparent display.

## 3.4 References

[1] M. Pope and C. E. Swenberg, *Electronic Processes in Organic Crystals and Polymers*, Second ed. (Oxford University Press, New York, 1999).

[2] J. B. Birks, *Photophysics of Aromatic Molecules* (Wiley, New York, 1970).

[3] F. L. Pedrotti and L. S. Pedrotti, *Introduction to Optics, Second Edition* (Prentice Hall, New Jersey, 1993).

[4] S. R. Forrest, Chem. Rev. **87,** 1793 (1997).

[5] P. J. Bounds and W. Siebrand, Chem. Phys. Lett. **75,** 144 (1980).

[6] N. C. Greenham and R. H. Friend, in *Solid State Physics: Advances in Research and Applications*; *Vol. 49*, edited by H. Ehrenreich and F. Spaepen (Academic Press, Toronto, 1995).

[7] P. Gommes da Costa and E. M. Conwell, Phys. Rev. B **48,** 1993 (1993).

[8] L. E. Lyons, Aust. J. Chem. **10,** 365 (1967).

[9] J. J. Ewing and D. R. Kearns, J. Chem. Phys. **44,** 3139 (1966).

[10] J. Tanaka, Bull. Chem. Soc. Japan **41,** 34 (1963).

[11] J. Tanaka and M. Shibata, Bull. Chem. Soc. Japan **41,** 34 (1968).

[12] S. C. Abbi and D. M. Hanson, J. Chem. Phys. **60,** 319 (1974).

[13] M. Pope, J. Burgos, and J. Giachino, J. Chem. Phys. **43,** 3367 (1965).

[14] L. Sebastian, G. Weiser, and H. Bässler, Chem. Phys. **61,** 125 (1981).

[15] S. Choi, J. Jortner, S. A. Rice, and R. Silbey, J. Chem. Phys. **41,** 3294 (1964).

[16] R. S. Berry, J. Jortner, J. C. Mackie, E. S. Pysh, and S. A. Rice, J. Chem. Phys. **42,** 1535 (1965).

[17] R. Silbey, J. Jortner, M. Vala Jr., and S. A. Rice, J. Chem. Phys. **42,** 2948 (1965).

[18] N. K. Chaudhuri and M. A. El-Sayed, J. Chem. Phys. **43,** 3423 (1965).

[19] J. Tanaka and S. Iwata, in *Third Organic Crystal Symposium,* Chicago, Ill., 1965, p. Paper No. 11.

[20] M. A. Baldo, M. E. Thompson, and S. R. Forrest, Nature **403,** 750 (2000).

[21] S. Tokito, J. Photopolymer Tech. Sci. **17,** 307 (2004).

[22] J. Kido, in *The International Conference on the Science and Technology of Synthetic Metals*, Wollongong,

Australia, 2004 (University of Wollongong, Intelligent Polymer Research Institute), p. 167.

[23] F. Gutmann and L. E. Lyons, *Organic Semiconductors* (Robert E. Krieger Publishing Company, Florida, 1981).

[24] G. W. Robinson and R. P. Frosch, J. Chem. Phys. **38,** 1187 (1963).

[25] G. W. Robinson and R. P. Frosch, J. Chem. Phys. **37,** 1962 (1962).

[26] G. W. Robinson, R. P. Frosch, and M. Gouterman, J. Chem. Phys. **36,** 2846 (1962).

[27] J. Ferguson, Australlian J. Chem. **9,** 172 (1956).

[28] J. Ferguson, Australlian J. Chem. **9,** 160 (1956).

[29] T. Förster, Discussions Faraday Soc. **27,** 7 (1959).

[30] J. Perrin, C. R. Acad. Sci. (Paris) **184,** 1097 (1927).

[31] F. Perrin, Ann. Chim. Physique **17,** 283 (1932).

[32] T. Förster, Ann. Phys. **2,** 66 (1948).

[33] T. Förster, in *Modern Quantum Chemistry, Part 2: Action of Light and Organic Molecules*, edited by O. Sinanoglu (Academic Press, New York, 1965).

[34] R. S. Knox, in *Bioenergetics of Photosynthesis*, edited by Govindjee (Academic Press, New York).

[35] C. W. Tang, S. A. Van Slyke, and C. H. Chen, J. Appl. Phys. **65,** 3610 (1989).

[36] J. Lam, T. C. Gorjanc, Y. Tao, and M. D'Iorio, J. Vac. Sci. Technol. A **18,** 593 (2000).

# Chapter 4

# Physics of Organic Electronic and Photonic Devices

## 4.1 Introduction

The two most widely studied organic devices are organic light emitting diodes (OLEDs) and organic field effect transistors (OFETs). An OLED consists of a thin film of luminescent organic material with appropriate electrodes on either side. One electrode serves to inject holes and the other to inject electrons which traverse the film, form excitons, and recombine to generate light. OFETs are usually three terminal devices comprising a gate electrode, a gate dielectric, source and drain electrodes, and a thin organic film which is in contact with the source and drain electrodes and electrically isolated from the gate electrode by the gate dielectric. When a bias is applied to the source and drain electrodes, charges are injected into the organic film and current flows between the two contacts. The source-drain current is modulated by the voltage applied to the gate electrode, thus giving rise to the field effect. The current that flows between the source and drain electrodes is in the plane of the film, contrary to OLEDs where the current flows perpendicular to the film.

The active layers in organic electronic and photonic devices are usually unintentionally doped and semi-insulating. Unlike their inorganic semiconductor equivalents, p- and n-type doping of organic materials suitable for bipolar devices have not reached the same level of maturity, however, doped conducting organic materials, such as acid doped polymers, have electrical properties which are similar to low conductivity metals and have been used as electrodes in OLEDs.

The performance of organic photonic and electronic devices has improved dramatically since their first introduction and a wide range of new products are now available in the consumer electronic market.[1-4]

OLEDs have been reported with current efficiencies of 50-70 cd/A and with external quantum efficiencies of 22% (internal quantum efficiency greater than 100%) by using "multi photon emission" device structures.[5] These efficiencies compare favorably with other display technologies which typically possess luminous efficiencies of the order of 5 lm/W.[6]

The progress of OFETs has not been as rapid as for OLEDs, but are now beginning to achieve performance levels which are suitable for applications in driving circuitry.[7-14] p-type OFETs with field effect mobilities in excess of 1 cm$^2$/Vs have been reported,[14] while n-type OFETs as well as CMOS circuitry based on OFETs have also been reported.[15]

This chapter will commence with a review of metal-organic contacts and related injection phenomena. Some techniques which are used to engineer the Schottky barrier height will be summarized. The effect of space charges and their effect on electrical current will be reviewed. The concept of the metal-oxide-semiconductor diode and field effect transistor are introduced and the theory of operation is summarized. The OFET is then discussed in terms of inorganic FET theory and the uniqueness of the OFET is emphasized: the formation of the conduction layer, contact resistance effects, gate bias dependent mobility. The OLED is introduced and device geometries are discussed. Common materials which are used in OLEDs are summarized and the electrical properties of OLEDs are detailed.

## 4.2 Metal-Organic Electrical Contacts

### 4.2.1 Neutral Contacts

The most elementary metal-semiconductor junctions are referred to as neutral contacts. In this case, the contact does not generate a built-in electric field or space charge region. The energy levels of both the metal and semiconductor align without bending, otherwise known as the flat band condition. A neutral contact will form when the work function of the metal exactly matches the Fermi level of the semiconductor. The probability of an electron flowing from the semiconductor to the metal is equal to that of the electron flowing in the reverse direction, hence there is no net current flow and no space charge region is created. Figure 4.1 depicts the energy level diagram for a neutral contact. If a DC bias is applied between the two electrodes, as shown in Figure 4.1c, the cathode can supply a maximum electron density $n_o$ through a thermionic emission process to maintain the current flow within the semiconductor. The current

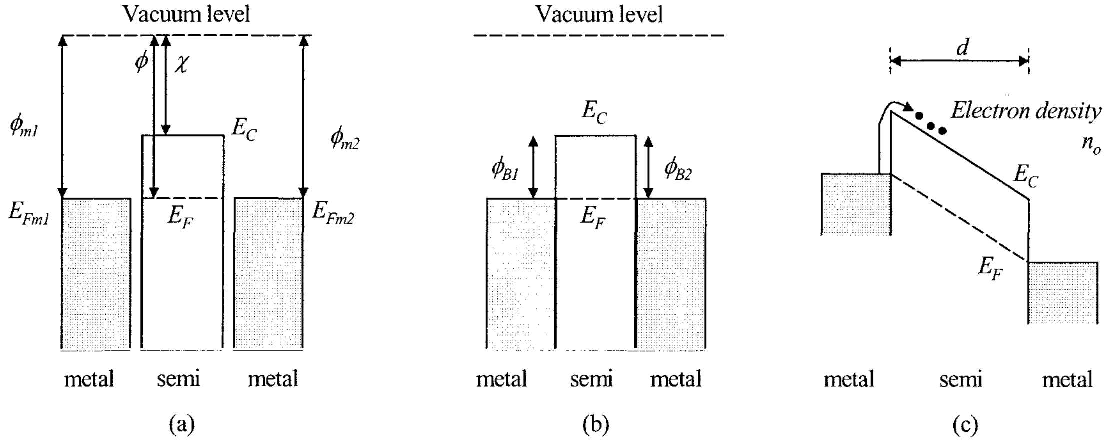

**Figure 4.1:** Energy level diagram of a neutral contact (a) before intimate contact, (b) after intimate contact, and (c) after intimate contact with a bias V applied. $\phi_{B1} = \phi_{M1} - \chi$ and $\phi_{B2} = \phi_{M2} - \chi$ where $\phi_B$ is the built-in potential of the contact.

density recorded at the anode can be written as:

$$J = qn_o\mu\frac{V}{d}, \qquad (1)$$

which is Ohm's law. The contact is said to be ohmic if certain conditions are held: (i) a uniform electric field exists throughout the semiconductor (no band bending), (ii) the mobility $\mu$ is independent of the electric field for low current levels (ie. minimal Joule heating effects), (iii) the current draw through the semiconductor is less than the saturated thermionic emission current from the cathode. When the current draw is greater than the thermionic emission current, the contact ceases being ohmic and tends to become a Schottky contact.

### 4.2.2 Ohmic Contacts

An ohmic contact between a metal and a semiconductor has minimal resistance when compared to the bulk semiconductor. This implies that the free carrier density in the vicinity of the contact is greater than in the bulk. Referring to the contact as ohmic is a misnomer because the current-voltage relationship is not linear.

There are two methods by which an ohmic contact can be formed. The first is the matching of the work function of the metal ($\phi_m$) and the Fermi level of the semiconductor ($\phi$). The details are listed in Table 4.1 and the energy level diagram is shown in Figure 4.2. The other technique is to dope the semiconductor surface heavily near the contact area to make the potential barrier thin enough

**Table 4.1:** Criteria for forming an ohmic contact with a metal and a semiconductor (doped, intrinsic) or insulator.

| Condition | Carrier | Semiconductor Type |
|---|---|---|
| $\phi_m < \phi_s$ | electron | n-type |
| $\phi_m < \phi$ | electron | intrinsic, insulator |
| $\phi_m > \phi_s$ | hole | p-type |
| $\phi_m > \phi$ | hole | intrinsic, insulator |

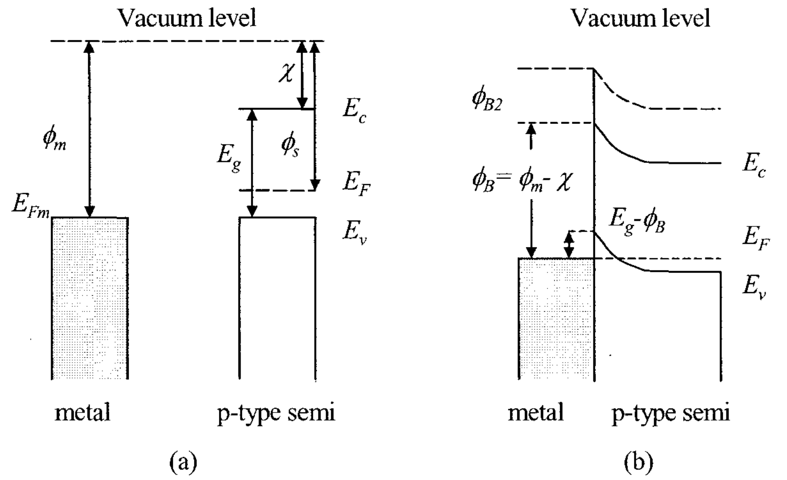

**Figure 4.2:** Energy level diagram for an ohmic contact to a p-type semiconductor (a) before and (b) after contact.

for efficient quantum mechanical tunneling to occur. This method is usually employed when an ohmic contact to a wide band-gap semiconductor is required. There are no metals that exist which have a low enough work function to minimize the energy barrier.

Even though the semiconductor may be intrinsic, the concentration of free carriers injected by the ohmic contact is much greater than the thermally generated carriers within the semiconductor. This transforms the semiconductor into an extrinsic semiconductor and the conduction mechanism is space charge limited (SCL), which is discussed in detail in Section 4.2.8.

### 4.2.3 Schottky Contacts

A Schottky barrier is formed when there is a large difference in the work function of the metal and the energy level into which the carriers are being injected. Figure 4.3 shows hole and

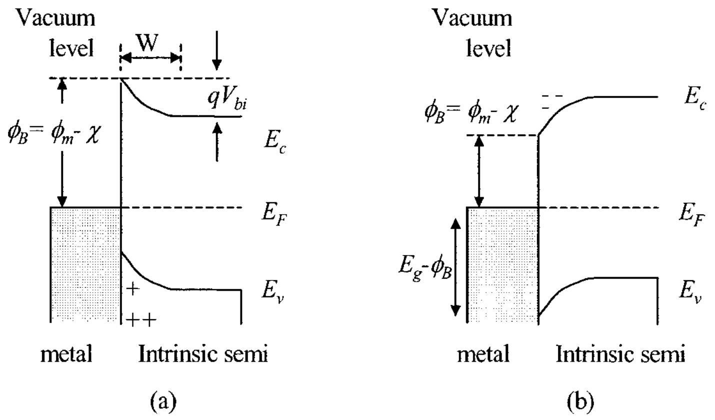

**Figure 4.3**: (a) Electron and (b) hole blocking contacts for a metal-intrinsic semiconductor interface.

electron blocking Schottky contacts for a metal-intrinsic semiconductor interface.

For a Schottky contact, the work function of the metal must be sufficiently higher (lower) than the Fermi level of the semiconductor to be an electron (hole) blocking contact. When this condition is met, electrons (holes) will flow from the semiconductor to the metal, leaving a positive (negative) space charge region in the semiconductor. This space charge region is also known as the depletion region and is characterized by its width, denoted by W. The depletion width for an abrupt metal-semiconductor junction can be written as:[16]

$$W = \sqrt{\frac{2\varepsilon_S}{qN_D}\left(V_{bi} - V - \frac{kT}{q}\right)}\ , \qquad (2)$$

where $qN_D$ is the charge density, $\varepsilon_s$ is the dielectric constant of the semiconductor, and $V_{bi}$ is the built in voltage of the contact. The barrier height $\phi_B$ is the energy that the carrier must have to pass from the metal into the semiconductor. If there are traps present in the semiconductor, it is the density of traps which determines the amount of band bending, and thus the width of the depletion region.[17] For a shallow trap density of $N_t$ at an energy $E_t$ below the conduction band, the width of the depletion region is approximated by:[18]

$$W = \frac{\pi}{2}\sqrt{\frac{2kT\varepsilon_s}{q^2 N_t}}\exp\left[\frac{\frac{1}{2}E_g - E_t}{2kT}\right], \tag{3}$$

In metal-organic contacts, there is a qualitative difference in the observed Schottky energy barriers compared to metal-inorganic semiconductors.[19-21]

### 4.2.4 Thermionic Emission

The theory of thermionic emission was originally proposed in 1942 by Bethe.[22] This theory assumes that the barrier height is much larger than $kT$, that the device is in thermal equilibrium, and that the existence of a net current flow does not affect the thermal equilibrium. Due to these assumptions, the shape of the barrier is of no consequence and the current flow depends only on the barrier height. The current density for thermionic emission over a triangular barrier of height $\phi_B$ is given by:[16,18]

$$J = \frac{4\pi q k^2 m^*}{h^3} T^2 \exp\left[-\frac{\phi_B}{kT}\right] = A_1^* T^2 \exp\left[-\frac{\phi_B}{kT}\right], \tag{4}$$

where $A_l^*$ is the effective Richardson constant and $m^*$ is the effective mass of an electron.

The field dependence is given by the image force lowering of the barrier height: when an electron is placed at a distance $x$ from a metal surface, a positive charge is induced on the surface of the metal. This effect is shown in Figure 4.4. The potential due to the force between the charges is given by:

$$V = \frac{q^2}{16\pi\varepsilon_s x}. \qquad (5)$$

When the effect of the applied electric field $F$ is superimposed on the image force, a field dependent lowering of the barrier is obtained, which is given by:

$$\Delta\phi = \sqrt{\frac{q^3 F}{4\pi\varepsilon_o}}. \qquad (6)$$

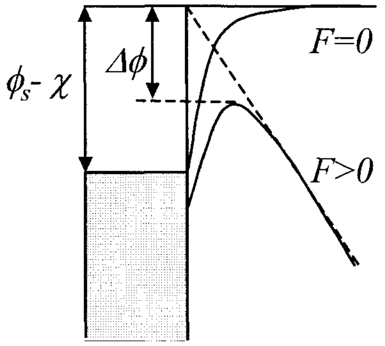

**Figure 4.4:** Image force lowering of the barrier height. For an applied electric field F the barrier height is reduced by $\Delta\phi$.

A Schottky barrier under a bias $V$, experiences a barrier lowering of:

$$\Delta\phi = \left[\frac{q^6(qV - \phi_B)N_D}{2(8\pi)^2\varepsilon_s^3}\right]^{1/4}, \qquad (7)$$

When the semiconductor has a lower mobility, it is necessary to take into account the diffusion of carriers within the barrier region. The effective Richardson constant $A_1^*$ is replaced by $A_2^*$ which is a function of the electric field $F$, temperature $T$, and mobility $\mu$. A full treatment is given by Kao and Hwang.[23] In the high field limit of an intrinsic semiconductor, we have:

$$\frac{A_2^*}{A_1^*} = \mu(2m^*)^{1/2}\left[4\varepsilon_s\left(\frac{F}{q}\right)^3\right]^{1/4} \exp\left[-\frac{\phi_B}{kT}\right], \qquad (8)$$

and for a Schottky barrier in the high field, low mobility limit, the ratio of the two effective Richardson constants is given by:

$$\frac{A_2^*}{A_1^*} = \frac{\left(\dfrac{2\pi m^*}{kT}\right)^{1/2}}{\int_{x_m}^{W} \dfrac{q}{\mu kT} \exp\left[-\dfrac{\phi_B - \psi}{kT}\right] dx}, \tag{9}$$

where $x_m$ is the position of the maximum barrier height taking into account image force barrier height lowering. $\psi$ represents the energy difference between the quasi-Fermi level energy and the energy of the electrons in the conduction band.

### 4.2.5 Field (Tunneling) Emission

Carriers can be injected via quantum mechanical tunneling through the barrier at low temperatures or when a high electric field is applied across a junction with a small barrier height.[23] The tunneling rate through a triangular barrier at low temperatures is given by:[18]

$$J = \frac{A_1^* T^2}{\phi_B} \left(\frac{qF}{\alpha kT}\right)^2 \exp\left[-\frac{2\alpha\phi_B^{3/2}}{3qF}\right], \tag{10}$$

where

$$\alpha = \frac{4\pi\sqrt{2m^*}}{h}, \tag{11}$$

where the symbols have the same meaning as above. Equation 10 is commonly written as:[16]

$$J = J_s\left(\exp\left[\frac{qV}{kT}\right] - 1\right), \tag{12}$$

where $J_s$ is the saturation current.

The tunneling characteristics are usually analyzed using a Fowler-Nordheim plot in which $\log(J/F^2)$ is plotted as a function of $F^{-1}$ to give a straight line. From the slope of the line the barrier height can be deduced. For a Schottky barrier, the tunneling rate is given by:[18]

$$J = A_1^* T^2 \left(\frac{E_{00}}{kT}\right)^2 \frac{\phi_B + qV}{\phi_B} \exp\left[-\frac{2\phi_B^{3/2}}{3E_{00}\sqrt{\phi_B + qV}}\right], \tag{13}$$

where

$$E_{00} = \frac{2q}{\alpha}\left(\frac{N_D}{2\varepsilon_s}\right)^{1/2}. \tag{14}$$

The field emission current is insensitive to temperature but has a strong dependence on the applied electric field. Since the tunneling rate is also strongly dependent on the width of the barrier, thermal excitations can substantially increase the tunneling current. In the case of a Schottky barrier, the current can be written as:[16]

$$J = J_s\left(\exp\left[\frac{qV}{nkT}\right] - 1\right) \approx J_s \exp\left[\frac{qV}{nkT}\right] \quad \text{for} \quad V >> \frac{kT}{q}, \tag{15}$$

where $J_s$ is a constant at low doping levels and $n$ is known as the ideality factor and is approximately equal to 1 at low doping levels and high temperatures.[16,18]

### 4.2.6 Characterization of the Barrier Height and Built In Potential

The built in potential and barrier heights can be measured by using electroabsorption (EA) measurements and internal photoemission spectroscopy (IPS), respectively.[24] The EA response, or differential transmittance ($-\Delta T/T$), of the organic film at a given photon energy is proportional to the imaginary part of the nonlinear susceptibility, $\mathrm{Im}\chi^{(3)}(h\nu)$, and the square of the electric field. In the experiment, a metal-organic-metal diode structure is used and a static DC electric field is applied across the two electrodes with a superimposed AC component of the form:

$$E = E_{DC} + E_{AC}\cos(\Omega t) \ , \tag{16}$$

where $E_{AC}$ is the amplitude of the AC component. The EA response at the fundamental frequency is written as:[25,26]

$$-\frac{\Delta T}{T}(h\nu;\Omega) \propto \operatorname{Im}\chi^{(3)}(h\nu)\left(2E_{AC}E_{DC}\right)\cos(\Omega t), \tag{17}$$

and the EA response at the second harmonic of the AC frequency is written as:

$$-\frac{\Delta T}{T}(h\nu,2\Omega) \propto \operatorname{Im}\chi^{(3)}(h\nu)\left(E_{AC}^{2}/2\right)\cos(2\Omega t). \tag{18}$$

If the DC component of the electric field is null, then the response is only modulated by the AC component. The DC field is comprised of the built in potential and the applied DC bias. The magnitude of the built in potential can be determined by applying an external DC bias and monitoring the EA signal at the fundamental frequency of the AC bias. When the applied DC bias is equal to the built in potential but with opposite sign, the total DC field in the semiconductor is zero and the total differential transmittance falls to zero as well. An alternate approach would be to measure the ratio of the differential transmittance at the fundamental and second harmonic frequencies of the AC signal in the absence of a DC bias.

The absorbance and the EA signal are shown in Figure 4.5a for the fundamental and second harmonic of the applied AC bias. The magnitude of the EA signal, when measured at the fundamental frequency, depends on the size of the DC bias, as depicted in the upper panel.

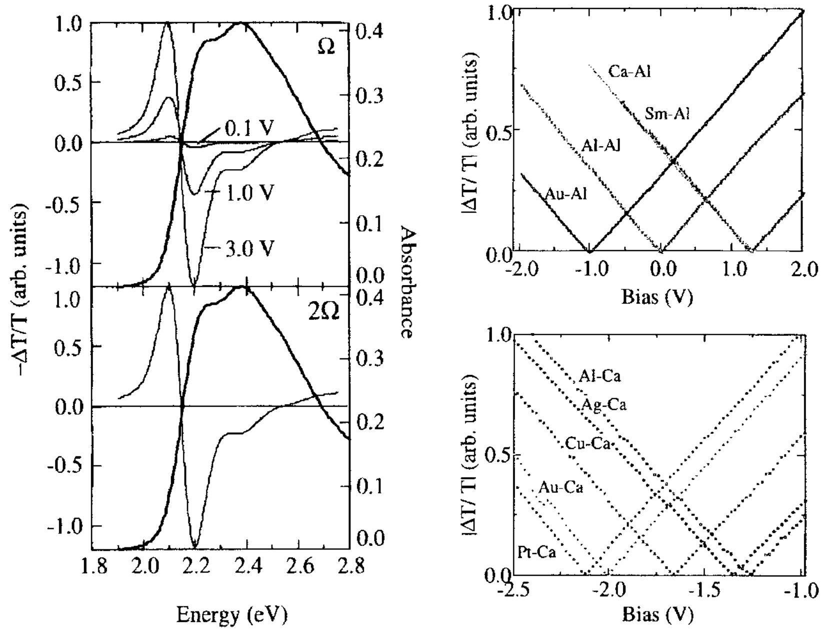

(a) (b)

**Figure 4.5:** (a) Absorbance (dark line) EA signal (light lines) as a function of photon energy for an Al/MEH-PPV/AL structure the fundamental (upper) and second harmonic (lower) frequency of the applied AC signal. The three EA signals in the upper panel denote different applied DC biases. (b) The magnitude of the differential transmittance at 2.1 eV as a function of DC bias for metal/MEH-PPV/Al (upper) and metal/MEH-PPV/Ca (lower) structures. Data from Campbell and Smith (reference 24).

In this case, because the device is symmetrical (Al/MEH-PPV/Al) there is no built in potential and the EA signal vanishes when the DC bias falls to zero. When the magnitude of the EA signal is plotted as a function of the applied DC bias, as shown in Figure 4.5b, the point where the EA signal is nullified corresponds to the built in potential of the device. The DC bias is stated with respect to Al or Ca metal, respectively.

In order to perform EA spectroscopy, Im$\chi^{(3)}$(hν) must be large enough to yield significant absorption changes. Unfortunately, this fundamental prerequisite is not satisfied for all organic materials, such as Alq.[24] In this case, a measurement of the photocurrent as a function of bias is used to determine the built in potential. The photocurrent signal changes sign when the applied bias reverses the sign of the electric field in the material and is nullified when the applied bias cancels the built in field.

IPS is a sensitive technique in which the individual Schottky energy barriers are measured rather than the difference between them.[27] However, IPS only works for a limited range of Schottky barrier heights in organic materials. Optically generated hot electrons or holes in a metal contact generate a photocurrent as they traverse the metal-semiconductor interface. The photocurrent yield $\eta$ is written as:[24]

$$\eta \propto \left(h\nu - \phi_B\right)^2, \qquad (19)$$

where $\phi_B$ is the Schottky barrier and $h\nu$ is the photon energy. The Schottky barrier is obtained by extrapolating $\eta$ to zero as a function of photon energy.

Figure 4.6 illustrates the typical spectra obtained from IPS measurements. In (a) the device, Al/MEH-PPV/Ca, is biased to collect electrons, while in (b) the device structures are

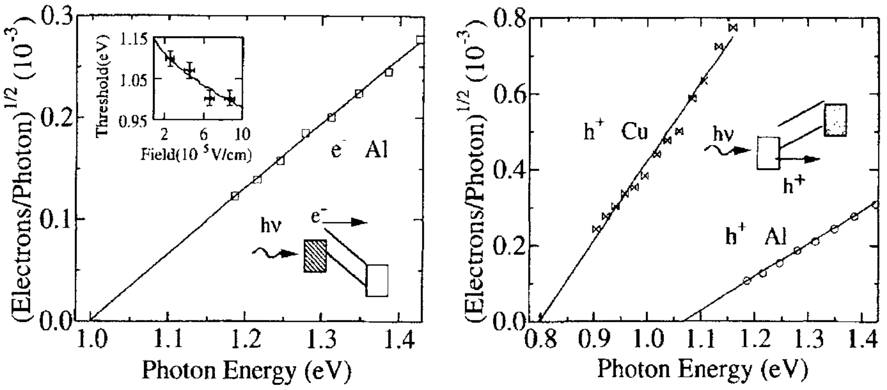

(a) (b)

**Figure 4.6:** IPS spectra for (a) Al/MEH-PPV/Ca, (b) Al/MEH-PPV/Ca and Cu/MEH-PPV/Ca structures biased to collect (a) electrons and (b) holes. After Campbell and Smith (reference 24).

Al/MEH-PPV/Ca and Cu/MEH-PPV/Ca and are biased to collect holes.

In fully depleted organic materials, IPS can be used to determine both the electron and hole Schottky barrier heights in the same structure by simply changing the bias direction. This is in contrast to inorganic semiconductors where an n/p-type sample must be used to measure the electron/hole Schottky barrier height. This allows a more accurate determination due to the minimization of inconsistencies between different devices.

### 4.2.7 Engineering the Schottky Barrier

In order to have efficient carrier injection into the organic material the Schottky barrier must be minimized. Some materials, such as MEH-PPV, have energy levels which are almost equal to the work functions of common metals and display excellent injection characteristics, however, the metals used for electron injection, such as calcium, are usually very reactive. For other materials such as Alq, there is no metal which will provide a near ohmic contact for electron injection. A common method to tailor the Schottky barrier is to modify the interfacial region using self assembled monolayers (SAMs). The details of SAMs will be discussed in greater detail in Chapter 5, but a general overview of the mechanism of barrier height control will be presented here.

Ideally, the interface would be modified in such a way that would preclude the use of reactive, low work function metals.[28-31] By forming a SAM of polar molecules on a metal surface, the work function can be modified by the dipole layer created by the SAM. A general overview of how the SAM dipole layer effects the work function is shown in Figure 4.7. A plain, un-treated metal-organic contact with a Schottky barrier height $\phi_B$ is shown in Figure 4.7a. In Figure 4.7b the SAM dipole layer is oriented such that the negative dipole is oriented towards the surface, decreasing the Schottky barrier height. In Figure 4.7c, the dipole orientation is reversed and the negative dipole is oriented away from the surface increasing the Schottky barrier height. It has been shown that SAMs of different dipole moments can significantly effect the work function of a metal.[28] Three SAMs were used by Campbell *et al* to show how the work function of silver can be modified: $CH_3(CH_2)_9SH$ [$CH_3$ SAM], $NH_2(CH_2)_{10}SH$ [$NH_2$ SAM], and $CF_3(CF_2)_7(CH_2)_2SH$ [$CF_3$ SAM]. The thiol moiety reacts and binds with the surface of a group 1B metal to form the SAM. The chemical structure of the $CH_3$ SAM is shown in Figure 4.8a and has a calculated dipole moment of 2.24 D.

A Kelvin probe was used to measure the change in the potential of the pristine Ag surface and the modified Ag surfaces. The details of the Kelvin probe technique can be found elsewhere.[32] In Figure 4.8b the Kelvin probe current is plotted as a function of the applied bias

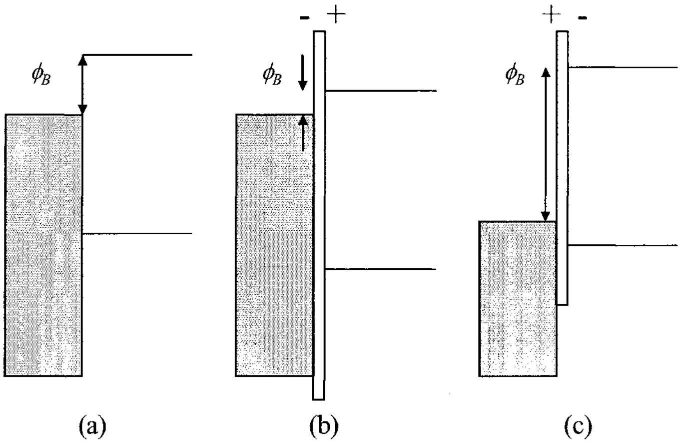

**Figure 4.7**: Schematic energy level diagram of a metal-organic interface: (a) plain interface, (b) and (c) SAM dipole layer which decreases or increases the Schottky energy barrier $\phi_B$, respectively. Adapted from Campbell and Smith (reference 24).

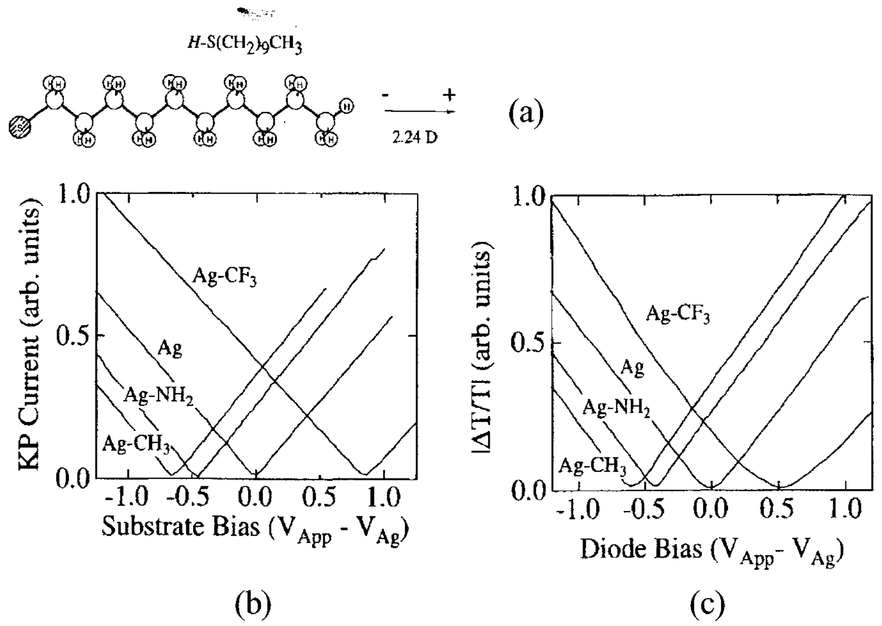

**Figure 4.8:** (a) chemical structure of the $CH_3$ SAM with a calculated dipole moment of 2.24D. (b) the Kelvin probe current as a function of substrate bias for a pristine Ag surface and dipole-modified Ag surfaces. The surface potential shifts due to the presence of a surface dipole. (c) EA signal for an Ag/MEH-PPV/Ca structure with bare Ag and dipole modified Ag electrodes. Data from Campbell and Smith (reference 24).

relative to the pristine Ag surface. The $CH_3$, $NH_2$, and $CF_3$ SAMs shift the surface potential by -0.70 V, -0.45 V, and 0.85 V, respectively. The positive shift increases the effective work function of Ag while the negative shifts serve to decrease the effective work function of Ag. The shift in surface potential can be written as:

$$\Delta\theta = N\left(\frac{\mu_{mol}}{\varepsilon} + \mu_{Ag^+S^-}\right), \qquad (20)$$

where $N$ is the density of molecules, $\mu_{mol}$ is the dipole moment of the molecule, $\mu_{Ag+S-}$ is the screened dipole moment of the $Ag^+S^-$ bond, and $\varepsilon$ is the static dielectric constant. $N$ is assumed to be between 3-5x$10^{14}$ $cm^{-2}$ and $\varepsilon$ between 2 and 3. The screened dipole moment is assumed to be the same for all three SAMs and the molecular dipole moments were calculated using quantum chemical techniques to be 2.24 D, 1.77 D, -1.69 D for $CH_3$, $NH_2$, and $CF_3$, respectively.[24] The EA response as a function of the diode bias relative to the pristine Ag surface is shown in Figure 4.8c. By using different SAM dipole layers the Schottky barrier can be tuned over a range greater than 1 eV.

## 4.3 Space Charge Limited Current

Space charge limited (SCL) current is the predominant mechanism found in OLEDs. These currents are independent of the mechanism of carrier generation and only depend on the transport and trapping of the carriers within the materials. As mentioned in Section 4.2.2, ohmic contacts display a linear I-V relationship at low electric fields and become highly non-linear at high electric fields. This behaviour is primarily due to two effects: the large concentration of charge carriers within the material between the electrodes which constitute a space charge and the existence of traps within the material.[33] The traps may be due to any number of sources: defects, impurities, or other defects which give rise to highly localized energy levels within the energy gap, shown in Figure 4.9. If the trapping center carries a net positive (negative) charge, then it will act as an electron (hole) trap. Traps are characterized as deep or shallow. In Figure 4.9, $T_1$ and $T_2$ are shallow traps with an energy difference between the bottom of the trap level and the bottom of the conduction band of less than $kT$. When this difference is large compared to $kT$ then the traps are characterized as deep.

As the applied electric field increases, the amount of injected carriers increases and the shallow traps are filled and a space charge is generated. This space charge is different from that which is generated by a large concentration of injected carriers in the material: the space charge due to the presence of traps is immobile compared to the excess non-trapped carriers.

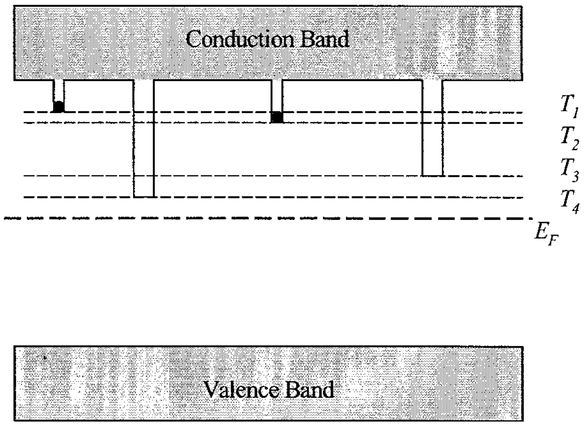

**Figure 4.9:** Energy diagram of an organic semiconductor with traps. $T_1$ and $T_2$ are referred to as shallow traps while $T_3$ and $T_4$ are deep traps and are empty.

The general shape of the current-voltage characteristics is depicted in Figure 4.10. At low voltages there is negligible injection from the contacts and the current obeys Ohm's law (region *AB'* or *AB*):

$$J_{\Omega} = q\mu n_o \frac{V}{d}, \tag{21}$$

where $\mu$ is the field-independent mobility, $q$ is the electronic charge, $d$ is the electrode separation, $\varepsilon$ is the permittivity of the organic material, and $n_o$ is the thermally generated background free charge carrier density. This region is often difficult to observe experimentally due to the extremely low currents involved. In the trap-free limit, the current becomes space charge limited at the voltage corresponding to *B'*. The concentration of free carriers injected from the electrodes becomes considerably greater than the concentration of the thermally generated majority carriers present in the material. Child's law is obeyed and there is a $V^2$ dependence:[34-37]

$$J_{SCL} = \frac{9}{8}\mu\varepsilon\frac{V^2}{d^3}, \tag{22}$$

and the current follows the *B'DE* line.

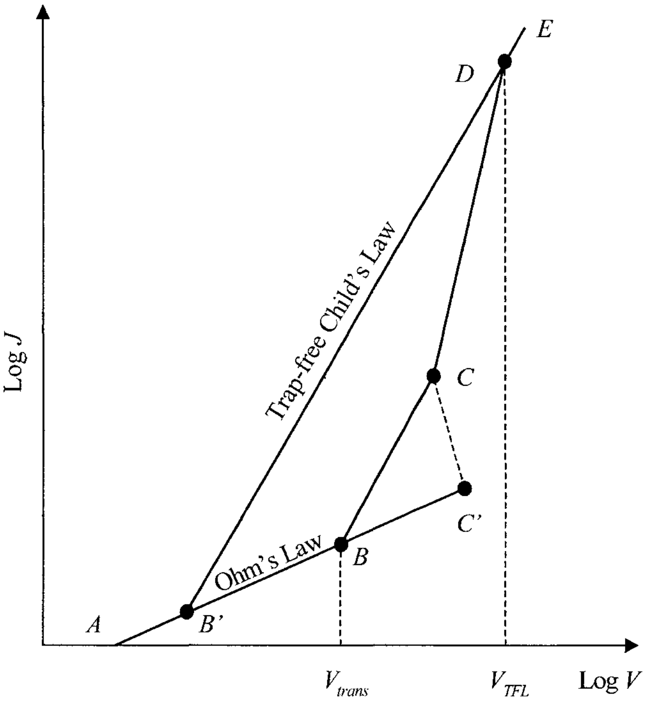

**Figure 4.10:** Logarithmic current density-voltage characteristics for solids containing traps. Most of the AB region is experimentally inaccessible due to the extremely low currents.

If there are shallow traps present, only a fraction of the injected carriers will be free while the remainder are immobilized by the traps. Assuming steady state conditions, the fraction of the total space charge which remains free is expressed as $\theta$.[33]

$$\theta = \frac{N_c}{N_t}\exp\left[-\frac{E_t}{kT}\right], \quad (23)$$

where $N_c$ is the concentration of free carriers injected into the conduction band and $N_t$ is the concentration of shallow traps at an energy level $E_t$ below the bottom of the conduction level. Equation 22 may still be used to describe the system, however, the mobility $\mu$ is now replaced with the effective mobility $\mu = \mu_o\theta$, where $\mu_o$ is the free carrier mobility.

In real solids, there is a distribution of shallow and deep traps and Equation 23 is not expected to be voltage independent and that the SCL current will increase at a rate higher than that predicted by Child's Law. As carriers are injected into the conduction level, the Fermi level rises towards the bottom of the conduction level. At a certain point, labeled $V_{trans}$, the current becomes non-ohmic and rises proportional to $V^n$. The Fermi level is still near the equilibrium position and the concentration of injected free carriers is greater than the concentration of majority carriers at equilibrium. When the voltage is increased past $V_{trans}$ the Fermi level begins to rise significantly. The transition voltage is defined as:[33]

$$V_{trans} = \frac{qn_{co}d^2}{2\varepsilon\varepsilon_o}, \tag{24}$$

where $n_{co}$ is the equilibrium majority carrier concentration. As the voltage is increased past point *C*, the Fermi level begins to overlap some of the deep trap levels and $\theta$ becomes voltage dependent. At this point, any injected carriers must go into the conduction band as all of the traps are filled and the current rises proportional to $V^n$ with $n > 2$. This is represented by the *CD* region in Figure 4.10. Point *D* corresponds to the trap free limit, or $V_{TFL}$ and is defined as:

$$V_{TFL} = \frac{qd^2N_t}{2\varepsilon}. \tag{25}$$

When the voltage is less than $V_{TFL}$, the excess charges are stored in the traps. When the voltage exceeds $V_{TFL}$, all of the traps are filled and they no longer contribute to the overall current and the overall current behaviour reverts back to Child's Law, represented by region *DE* in Figure 4.10, since the material can be considered "trap-free."

Mark and Helfrich have shown that the current in the *CD* region of Figure 4.10 can be written as:[38]

$$I = N_o\mu q^{L-1}\left[\frac{\varepsilon L}{H(L+1)}\right]^L\left[\frac{2L+1}{L+1}\right]^{L+1}\left[\frac{V^{L+1}}{d^{2L+1}}\right], \tag{26}$$

where $N_o$ is the effective density of states in the valence band at room temperature, and $L = T_c/T$. $T_c$ is the characteristic temperature of the trap distribution and is always larger than $T$. The energy $kT_c$ represents the distance of the mean trapping level above the top of the valence band.

Using Equation 26, $V_{trans}$ can be written as:[38]

$$V_{trans} = \frac{n_o q d^2}{\varepsilon}\left(\frac{n_o}{N_o}\right)\left(\frac{N_t}{n_o}\right)^{L}\left[\frac{9}{8}\left(\frac{L+1}{L}\right)^{L}\left(\frac{L+1}{2L+1}\right)^{L+1}\right]^{1/L-1}. \qquad (27)$$

## 4.4 The Field Effect Transistor

### 4.4.1 Introduction

The metal-oxide-semiconductor (MOS) transistor is a four terminal device in which the lateral current flow is controlled by an externally applied vertical electric field. A typical MOS transistor is shown in Figure 4.11. The four terminals are designated as the source, drain, gate, and substrate. In most cases, the effect of the substrate is neglected and the MOS transistor is considered to be a three-terminal device. With no voltage applied to the gate, the two opposing *pn* junctions between the drain and the source prevent current flow in either direction. When a positive voltage is applied to the gate with respect to the substrate, a mobile negative charge is induced in the semiconductor below the oxide-semiconductor interface. The negative carriers create a conduction channel between the source and the drain. Since the current is controlled by the vertical and lateral electric fields, this type of device is also known as a field effect transistor (FET). For the device structure in Figure 4.11, the gate electrode is insulated from the channel so that no current may pass through

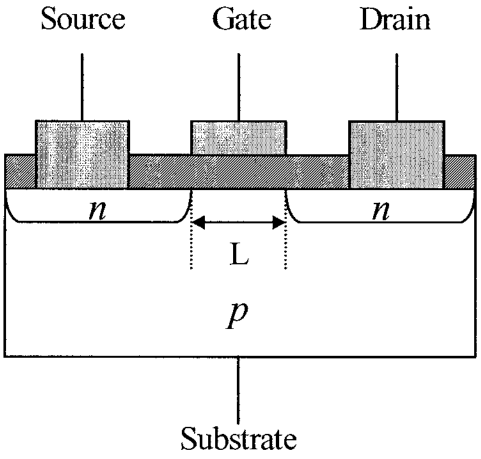

**Figure 4.11:** An *n*-channel MOS transistor.

the dielectric into the gate electrode. This type of device is also known as an insulated-gate field effect transistor, or IGFET.

### 4.4.2 Metal-Oxide-Semiconductor (MOS) Diodes

The MOS diode is the most useful device in the study of semiconductor surfaces and interfaces. The first MOS structure was proposed as a voltage-variable capacitor in 1959 by Moll[39] and by Pfann and Garrett.[40] Its characteristics were later analyzed by Frankl[41] and Lindner.[42]

The energy diagram for the metal, oxide, and semiconductor as isolated components is shown in Figure 4.12a. In order to simplify the analysis, the energy bands are assumed to be flat and the work functions are assumed to be identical for all three parts. As the three materials are brought into intimate contact their Fermi levels align, as shown in Figure 4.12b. Again, the emphasis is that this is an idealized structure in which the energy bands remain flat because the

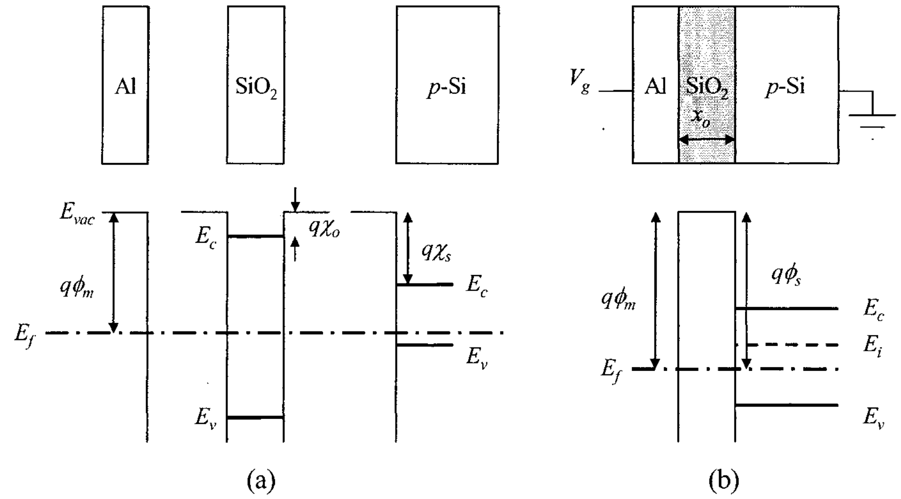

**Figure 4.12:** The MOS capacitor: structure and idealized energy band diagram (a) before contact and (b) after contact. The vertical energy axis is not drawn to scale.

work functions are assumed to be the same so that there is no charge transfer on contact. We also assume that there is no charge present inside the dielectric or at either dielectric interface. These assumptions eliminate any localized space-charge regions and built-in potential differences. These effects will be addressed later.

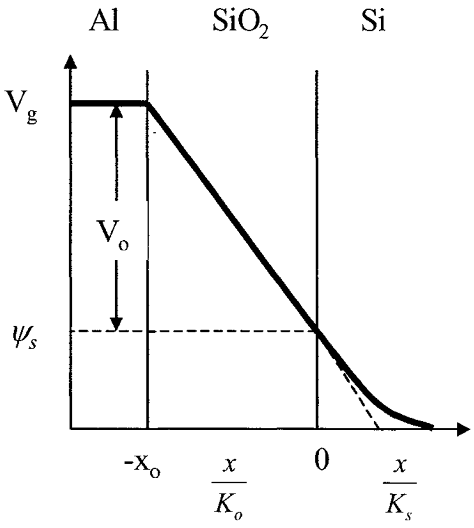

**Figure 4.13:** The potential distribution in a MOS structure with applied voltage $V_g$. $K_o$ and $K_s$ are the dielectric constants of the oxide and semiconductor, respectively. The silicon layer in this device is *p*-type.

When a voltage is applied across the MOS capacitor, an electric field $E_o$ is generated between the gate and the substrate. As a result, carriers are displaced towards the interfaces creating two space charge regions. Figure 4.13 shows the potential distribution inside a MOS structure with an applied voltage $V_g$. The abscissa has been scaled with the dielectric constant to avoid discontinuities at the interfaces. The penetration of the electric field into the semiconductor produces a potential barrier beneath the surface. The depth of this penetration is inversely proportional to the doping density. By assuming that there is a negligible voltage drop in the metal plate, the applied voltage $V_g$ is distributed between the voltage across the oxide layer, $V_o$, and the surface potential, $\psi_s$:

$$V_g = V_o + \psi_s . \tag{28}$$

Using the bulk semiconductor as the reference, $\psi_s$ corresponds to the potential at the Si-

$SiO_2$ interface. The electric field that exists in the semiconductor modifies the band structure and creates a space-charge region below the surface. Depending on the magnitude and polarity of the applied voltage, there are three surface conditions which can arise: carrier accumulation; carrier depletion; and carrier inversion.

Carrier accumulation occurs when the hole density below the semiconductor surface is greater than the equilibrium hole density in the bulk. This condition is attained by applying a negative voltage to the metal electrode. The resulting negative surface potential $\psi_s$ produces an upward bending of the energy bands as shown in Figure 4.14. Since the Fermi energy remains constant, the band bending results in a larger $E_f - E_i$ difference near the surface. As a result, holes accumulate near the surface and the surface conductivity is increased.

When a small positive voltage is applied to the gate, the surface potential is positive and the Fermi level is now further away from the valence band edge. This results in a smaller $E_f - E_i$ difference and the energy bands bend down, as shown in Figure 4.15, and holes are depleted from the interface region. This in turn produces a space charge region consisting of stationary acceptor ions.

If a large enough positive voltage is applied to the gate, the energy bands will be bent enough such that the midgap energy $E_i$ will cross the Fermi energy near

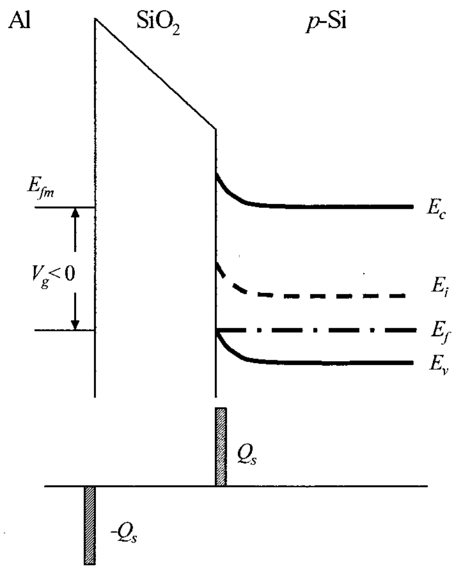

**Figure 4.14:** Energy band diagram for a p-channel MOS operating in the accumulation region.

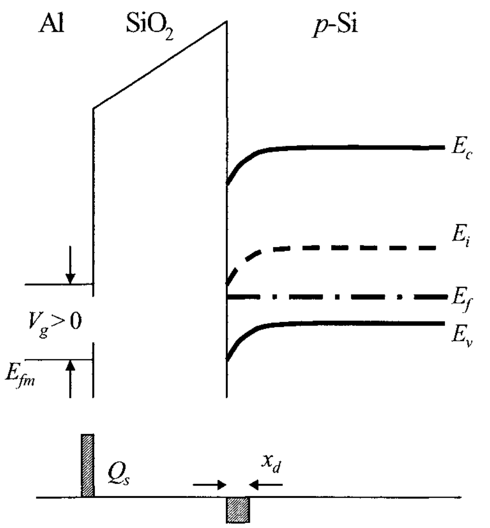

**Figure 4.15:** Energy band diagram for a $p$-channel MOS operating in the depletion region.

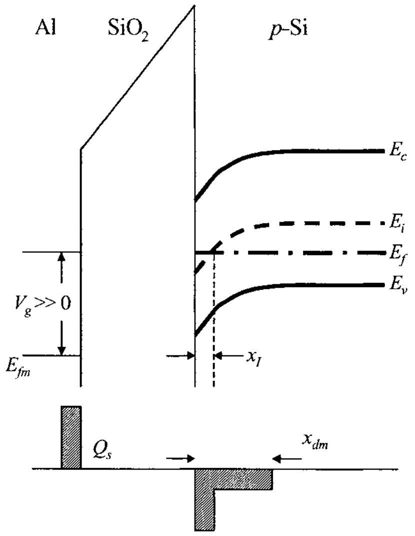

**Figure 4.16:** Energy band diagram for a $p$-channel MOS operating in the inversion region.

the surface. When this happens, the device is said to be operating in the inversion region. The inversion layer has an electron density which is greater than the hole density. As illustrated in Figure 4.16, the semiconductor to the right of $x_I$ remains $p$-type while the region between the interface and $x_I$ is $n$-type. This produces an induced $pn$ junction.

In practice, the energy levels exhibit bending in the absence of an applied gate voltage due to differences in work functions, charges in the gate dielectric, and surface states, as shown in Figure 4.17. When the layers are brought into intimate contact, band bending occurs in the semiconductor in order to satisfy the requirement of a constant Fermi level under thermal equilibrium (see Figure 4.17b). The difference between the modified work functions of the metal and the semiconductor is the gate voltage necessary to nullify the built in electric field within the semiconductor:

$$V_{g1} = \phi'_{ms} = \phi'_m - \phi'_s . \tag{29}$$

This is known as the flat band condition and is shown in Figure 4.17c.

The necessary voltage is also influenced by charges residing within the oxide layer. A negative gate voltage is needed to lower the electric field distribution until the charge is reduced to zero at the semiconductor surface.

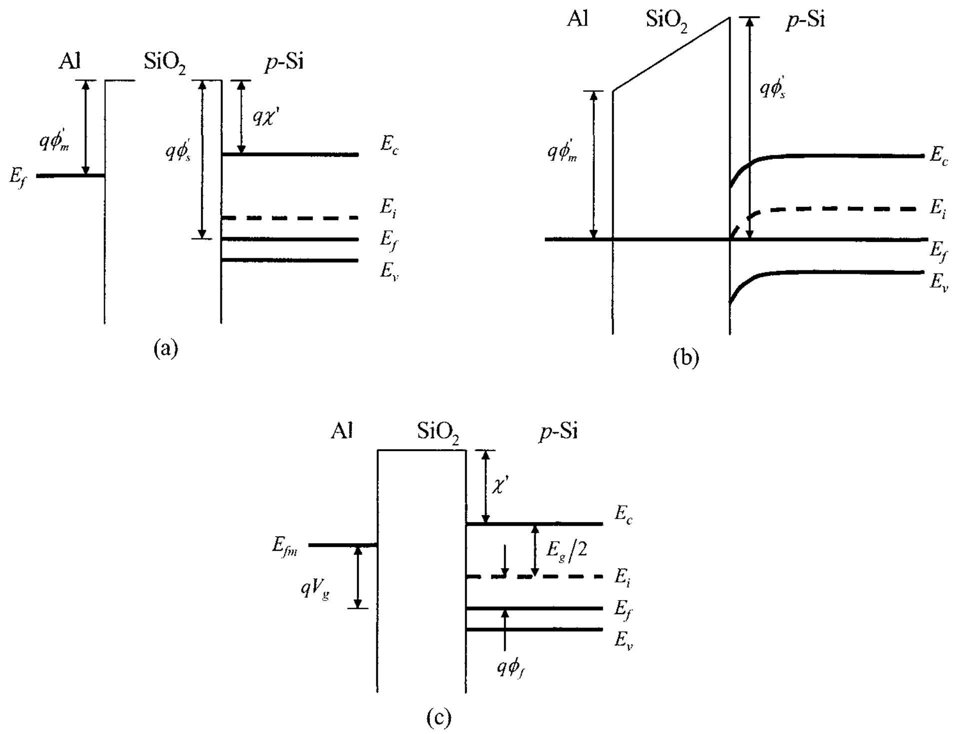

**Figure 4.17:** Energy band diagrams for a MOS structure (a) before contact, (b) after contact at $V_g$=0, and (c) with $V_g = -V_{FB} = q(\phi_m' - \phi_s')$.

### 4.4.3 The MOS Field Effect Transistor (MOSFET)

A simplified cross-sectional structure of a MOSFET is shown in Figure 4.11. A more detailed diagram is shown in Figure 4.18. For this device model, the substrate and source

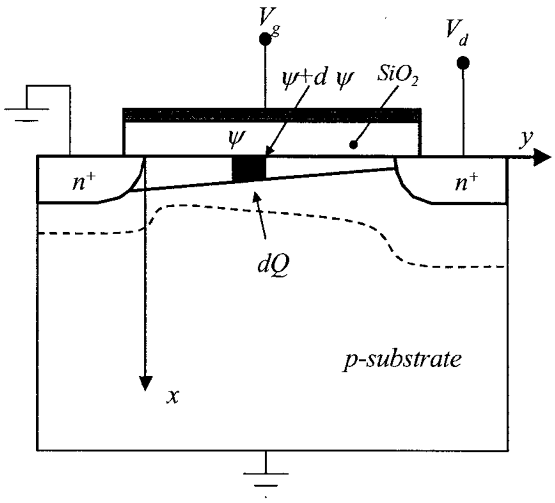

**Figure 4.18:** A detailed cross sectional schematic of an *n*-channel MOSFET.

electrodes are grounded. MOSFETs have two characteristic regions of operation in static mode: linear and saturation. At low drain voltages the source-drain current-voltage characteristics are ohmic and linear. At high drain voltages, the drain currents saturates and remains essentially constant with increasing drain voltage.

*The Linear Regime*

For our analysis, we shall assume that the vertical and lateral electric fields are independent of each other. In Figure 4.18 the electric field in the $x$ direction induces an inversion layer whereas the electric field in the $y$ direction produces a drain current flowing along the semiconductor surface.

Let us consider a small section at $y$ of the transistor shown in Figure 4.18 under the condition that the gate voltage is greater than the threshold voltage so that significant amounts of mobile carriers are induced in the inversion layer. The relationship between the mobile charge $Q_I$ and the gate voltage is given by Equation 30 if we assume the channel voltage is zero. As a result of the drain-source bias, a potential $\psi$ is established at $y$ and the induced channel charge is modified to be:

$$Q_I = -C_o\left(V_g - V_T - \psi\right). \tag{30}$$

The transport equation for electrons can be written as:

$$I_d = W\mu_n Q_I E_y \tag{31}$$

where $I_d$ is the drain current, $W$ is the depletion layer width, $\mu_n$ is the electron mobility, and $E_y$ is the y component of the electric field. If we substitute $E_y = -d\psi/dy$ and $Q_I$, and integrate from $y = 0$ to $L$ (the distance between the source and drain) and from $\psi = 0$ to $V_d$ we get:

$$I_d = C_o\mu_n \frac{W}{L}\left\{ \begin{aligned} &\left(V_g - \phi'_{ms} - \phi_{si} + \frac{Q_o}{C_o} - \frac{V_d}{2}\right)V_d \\ &- \frac{2}{3}\frac{\sqrt{2qK_s\varepsilon_o N_a}}{C_o}\left[\left(V_d + \phi_{si}\right)^{3/2} - \phi_{si}^{3/2}\right] \end{aligned} \right\}. \tag{32}$$

If we assume that the threshold voltage is independent of the potential $\psi$, Equation 32 reduces to the equation describing a MOSFET operating in the linear regime:

$$I_d = C_o\mu_n \frac{W}{L}\left[\left(V_g - V_t\right)V_d - \tfrac{1}{2}V_d^2\right], \tag{33}$$

or, if $V_d << (V_g - V_t)$,

$$I_d \approx C_o\mu_n \frac{W}{L}\left(V_g - V_t\right)V_d. \tag{34}$$

The channel conductance $g_D$ and the transconductance $g_m$ can be written as

$$g_D \equiv \left.\frac{\partial I_d}{\partial V_d}\right|_{V_g = const} = \frac{W}{L}\mu_n C_o\left(V_g - V_t\right) \tag{35}$$

$$g_m \equiv \left.\frac{\partial I_d}{\partial V_g}\right|_{V_d = const} = \frac{W}{L}\mu_n C_o V_d \tag{36}$$

*The Saturation Regime*

When the drain voltage is increased so that $V_d >> V_g$ the inversion layer will disappear on the drain side of the channel. The channel is then said to be pinched off and further increases of the drain voltage will not significantly increase the drain current.

The condition for the onset of current saturation is given by setting $Q_l$ equal to zero in Equation 30. Therefore,

$$V_{ds} = \psi = V_g - V_t, \tag{37}$$

where $V_{ds}$ is the saturation drain voltage which is equal to $\psi$ for the channel adjacent to the drain. Substituting Equation 37 into Equation 33 we get:

$$I_{ds} = \frac{\mu_n C_o W}{2L}\left(V_g - V_t\right)^2, \tag{38}$$

which is valid at the onset of saturation.

## 4.5 Application of MOSFET Principles to OFETs

### 4.5.1 OFET Geometries

There are two fundamental designs for an organic field effect transistor (OFET). The bottom contact (BC) design, in which the source and drain are buried beneath the organic layer or the top contact (TC) design if the source and drain electrodes are deposited on top of the organic layer. Of these two structures, there are some possible variations, which are shown in Figure 4.19. Here, the clear boxes represent the substrate which in principle can be anything compatible with the processing steps required to fabricate the devices. The black boxes represent electrical contacts: either metals or highly doped silicon. The light grey regions represent dielectric material. For TC devices, the structure shown in Figure 4.19c is the most common structure reported in the literature consisting of a heavily doped Si substrate with a pre-grown thermal $SiO_2$ layer. In principle the $SiO_2$ dielectric could be replaced by any suitably smooth, insulating material such as silicon nitride or an organic dielectric. The geometry shown in Figure 4.19a is the least desirable due to the necessity of depositing a dielectric on top of the organic layer. High quality inorganic dielectrics require energetic deposition techniques to form pinhole free films and may damage the underlying organic layer. Conversely, if an organic dielectric is being deposited, the solvents used during spin casting may damage the

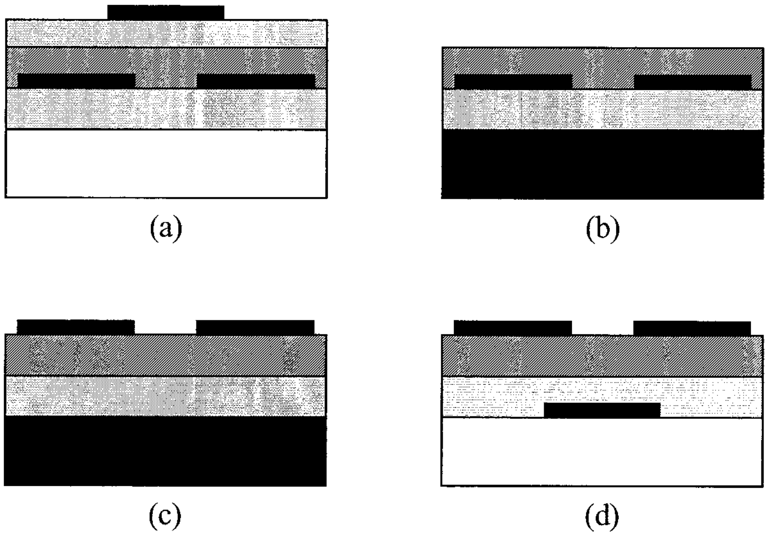

**Figure 4.19:** The different possible geometries for an OFET: (a) and (b) are referred to as bottom contact geometries with the source and drain electrodes below the organic layer and the gate dielectric and electrode (a) on top or (b) below the organic layer. (c) and (d) are referred to as top contact devices with the gate dielectric and electrode below the organic layer and the source and drain on top of the organic layer. The black layers indicate electrodes, light grey indicates a dielectric, the hashed region represents the organic layer and the horizontal line pattern in (d) indicates an organic or inorganic dielectric.

active organic layer as well. In our discussion of BC devices, we shall not consider the structure in Figure 4.19a in our discussion.

The BC device geometry uses conventional microfabrication techniques to define the features. The chief advantage to this approach is that the feature size is only limited by current state of the art lithographic technology. If an electron beam writer was used, the transistor channels could have been made as small as 10 nm. After all of the microfabrication steps have been completed, the organic semiconductor can be deposited on top of the structure after which no further processing can be performed due to the organic semiconductor's sensitivity to solvents and temperature extremes. However, there are several disadvantages to this type of device structure. Although exaggerated in Figure 4.19, the thickness of the organic semiconductor is typically between 200 Å and 600 Å thick, which is about an order of magnitude smaller than the thickness of the patterned source and drain electrodes. This means that the cross section of the organic film which is available for electrical injection is small: 300 $\mu m^2$ for a film 300 Å thick and a channel length of 1000 Å. Comparing this to a typical top contact device with a 300 Å thick film and a 100 μm wide electrode, the surface area in which injection occurs is almost three orders of magnitude higher at 200,000 $\mu m^2$. The second disadvantage to the bottom contact design is because of the need for spin coating of polymers onto the substrate. The resulting film is essentially a conformal coating and unless mechanically removed around the gate and active device area, there will be current leakage between the source/drain electrodes and the gate electrode, which will decrease the performance of the device.

The TC design simplifies the fabrication process at the expense of feature size. To fabricate a TC device, the organic material is deposited onto the entire surface and then electrodes are deposited using a shadow mask. For the devices used in this study, the structure shown in Figure 4.19c was used primarily. The entire substrate acted as the gate electrode and contact was made from the back side of the chip. As with the bottom contact devices, organic material must be mechanically removed around the perimeter of the active area of the devices to minimize leakage currents.

### 4.5.2 Mode of Operation

OFETs are accumulation mode devices. In the typical *p*-type OFET when a negative bias is applied to the gate electrode a positive charge is induced at the organic-dielectric interface and a conducting channel is formed, allowing a current to flow between the source and drain electrodes. At low drain voltages, the OFET will operate in the linear regime. At high drain voltages the OFET will enter the saturation regime where the current is independent of the drain voltage.

It is widely accepted that conjugated organic molecules tend to orient themselves with their long axis parallel to each other and form layers.[43] It has been established that charge transport in conjugated organic materials is favored in the direction parallel to the layers, as demonstrated in sexithiophene[44,45] and pentacene transistors.[46,47] The thickness of the accumulation layer which is formed in the organic material is $\sqrt{2}L_D$ where $L_D$ is the Debye length and is defined by:[43]

$$L_D = \frac{\sqrt{2}kT\varepsilon_s}{qC_iV_G}. \tag{39}$$

The Debye length typically has a value between 0.1 and 1 nm, which is less than the length of the organic molecule. Therefore, it is often stated that the majority of charge conduction occurs within the first monolayer next to the semiconductor-dielectric interface.[48] The charge density distribution does, however, extend into subsequent monolayers, but it has been shown by Tanase *et al* that the contribution of this is negligible, especially in amorphous films.[49] Horowitz has shown that, for a lamellar polycrystalline film, most of the charge density is localized within the first monolayer only at high gate voltages.[43] At low gate voltages, the charge present in the first layer is strongly dependent on the thickness of the film. Figure 4.20 illustrates the charge density in the organic film as a function of layer number for films of various thicknesses. As the films become thicker, the charge density in the first layer decreases. This implies that the mobility would decrease at a high gate bias because the monolayers next to the dielectric interface may be influenced by surface defects. Similarly, it can be predicted that as the thickness of the organic film is increased the mobility should increase as well. This effect has been observed in sexithiophene and pentacene OFETs.[50,51]

### 4.5.3 Contact Resistance

As the performance of OFETs increases, the channel resistance becomes small compared to the contact resistance and becomes the limiting factor to improving device performance. Horowitz has proposed accounting for the contact resistance in the linear regime of the channel conductance by replacing $V_d$ by $V_d$ - $R_c I_d$ where $R_c$ is the contact resistance. Therefore, the

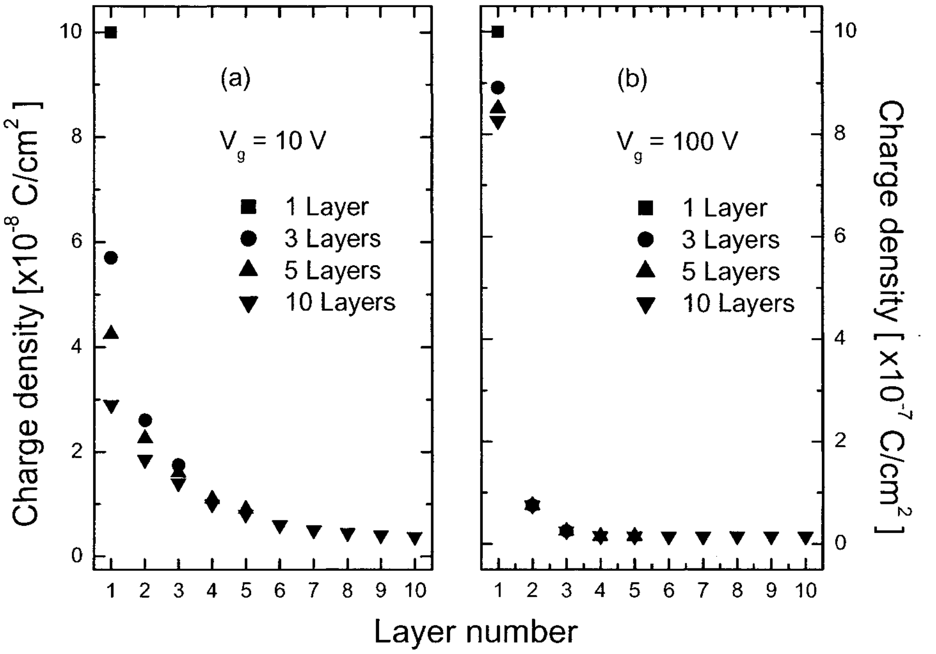

**Figure 4.20:** The charge density in each layer for films of various thicknesses at a gate voltage of (a) 10 V and (b) 100 V. Data from Horowitz (reference 43).

conductance (Equation 35) may be rewritten as:[43,52]

$$g_D = \left( \frac{1}{(W/L)C_i\mu(V_g - V_t)} + R_c \right)^{-1} . \qquad (40)$$

This analysis assumes a constant resistance and a mobility which is dependent on the gate voltage. Street and Salleo, however, assumed a constant mobility and reported a non-ohmic contact resistance which had a slight gate voltage dependence.[53]

Other methods which allow access to the contact resistance include the use of an atomic force microscope tip to map the potential across the transistor channel.[54,55] These results confirm that the contact resistance depends on the nature of the injecting electrode and the energy level mismatch. The contact resistance also displays a strong gate bias dependence.[56] Other groups have pursued the more traditional transfer line method (TLM) to extract the contact resistance.[57-59] This method consists of measuring the resistance of the channel for various channel lengths. The linear relationship is extrapolated to zero channel length and the contact resistance can be determined. However, this technique requires the fabrication of many devices and the assumption of identical contacts in all devices cannot be made. The ideal technique to measure the contact resistance is via a four-point probe technique where the voltage drop between the source and drain electrodes can be measured. This technique has been used successfully on single crystal devices.[60,61]

### 4.5.4 Gate Voltage Dependent Mobility

The main evidence which indicates that the mobility has a gate voltage dependence comes from the deviations of the data from a straight line in the linear regime ($I_d$ vs $V_g$) and the saturation regime ($I_d^{1/2}$ vs $V_g$). It is believed that in organic semiconductors, the gate voltage dependence arises from charge density dependence. This may be predicted by charge transport models based on hopping in an exponential distribution of traps.[62] In polycrystalline films, most of the defects are located at the grain boundaries. In this case the approach is slightly different: the film is divided into high (the grains) and low (the grain boundaries) conductivity regions. The dimensions of the grains are assumed to be much larger than the dimensions of the grain boundaries. Knipp *et al* have studied the effect of mobility as a function of grain size in pentacene OFETs.[63] They reported that the mobility depended greatly on the nature of the surface on which the pentacene was deposited. Interestingly, they also found that when the $SiO_2$ dielectric surface was treated with a silane agent (OTS, discussed in detail in Chapter 5), the grain size decreased but the mobility increased. It is thought that, when pentacene is deposited on an OTS covered surface, the majority of the grains adopt the bulk phase structure rather than the thin film phase structure.[43] In addition, Gundlach *et al* have demonstrated that when pentacene is deposited onto an OTS-treated surface, the molecules tend to grow more vertically compared to bare $SiO_2$ where the growth is more horizontal (ie. two dimensional). This is related to the majority of the charge conduction being localized in the first layer of the organic and the importance of a well ordered organic layer at the interface.[64]

### 4.5.5 Charge Transport in OFETs

Vissenberg and Matters have proposed a variable range hopping transport mechanism with an exponential distribution of traps and a thermally activated mobility that varies with gate voltage according to a power law.[62] This model has its foundations in the multiple trapping and release (MTR) model originally developed by Le Comber and Spear to explain transport in hydrogenated amorphous silicon.[65] It assumes that charge transport occurs in delocalized bands and is limited by a distribution of traps near the band, but makes no assumptions on the type of transport mechanism in the band.[66] Although this model has successfully explained the behaviour in the early devices based on polycrystalline conjugated molecules, it does not account for the temperature independent mobility that has been observed in pentacene[14] and oligothiophenes[52,67] OFETs.

Street *et al* have proposed a trapping model as opposed to a grain boundary model to explain the hole transport mechanisms in pentacene OFETs.[68] The Levinson model, originally proposed for CdSe transistors, was used in the analysis of pentacene OFETs:[69]

$$\begin{aligned} I_D &= \mu_o V_d C_i \frac{W}{L} V_g \exp\left[ - \frac{E_B}{kT} \right] \\ &= \mu_o V_d C_i \frac{W}{L} V_g \exp\left[ - \frac{s}{V_g} \right] \end{aligned}, \tag{41}$$

with

$$s = \frac{q^3 N_t^2 t}{8 \varepsilon k T C_i}, \tag{42}$$

where $t$ is the thickness of the semiconducting layer, $\varepsilon$ is the dielectric constant of the semiconductor, $N_t$ is the trap density, $E_b$ is the barrier height, and $\mu_o$ is the trap free mobility. The parameter $s$ is determined from the Levinson plot of $\ln(I_d/V_d)$ as a function of $1/V_g$. The thermally activated mobility is given by:

$$\mu = \mu_o \exp\left[ - \frac{E_B}{kT} \right] = \mu_o \exp\left[ - \frac{s}{V_g} \right], \tag{43}$$

where $\mu_o$ is the trap free mobility. Wang and co-workers[70] also performed this analysis on pentacene devices and have achieved results which are consistent with those reported in the literature.[71]

## 4.6 The Organic Light Emitting Diode

### 4.6.1 Introduction

The first study of electroluminescence in organic materials was documented in 1963 by

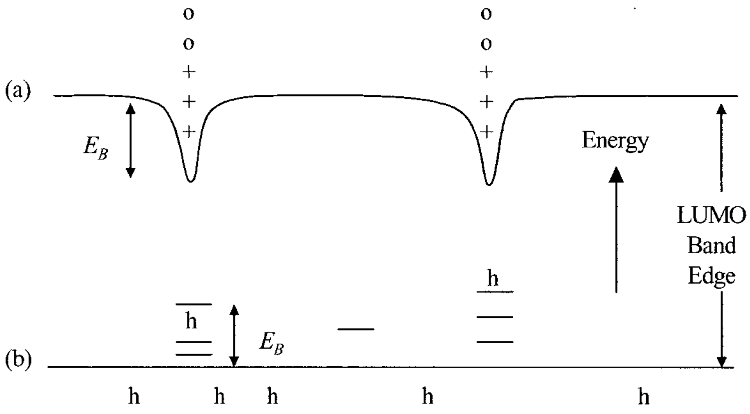

**Figure 4.21:** Energy level diagram comparing the (a) potential barrier (grain boundary) model and (b) trap model for the LUMO energy level. The activation energy $E_B$ is shown for each case.

Pope, Kallmann, and Magnante.[72] A thin film of single crystal anthracene was subjected to a high voltage and a faint glow was observed. Throughout the late 1960s and 1970s, electroluminescence in organic materials was studied intensively.[72-87] This work was abandoned because of the extremely high voltages (several hundred volts), low conductivity, and great difficulty in growing large, high quality organic molecular crystals.

In 1987, Tang and Van Slyke published results on an organic electroluminescent diode based on 8-hydroxyquinolate aluminum (Alq) , which exhibited efficient production of green light at low voltages[88] and in 1989 they demonstrated EL with dye-doped Alq.[89]

Since these pivotal articles were published, research into organic light emitting diodes (OLEDs) has increased exponentially and there are now commercial products which are already incorporating full colour OLED displays.[90-92] Device efficiency has increased dramatically in the span of only two decades to the point where it is comparable to inorganic devices which are a more mature technology.[93]

One of the great advantages that OLEDs possess over other forms of solid state lighting is the ease in which the colour may be controlled. By changing the conjugation length of the molecule or by adding functional groups, the wavelength of the emitted light can be controlled. See, for example, Braun and Heeger,[94] Tao *et al*,[95] Zhang *et al*,[96] and other recent reviews.[90,91,97]

OLEDs consist of one or more organic layers sandwiched between charge injecting electrodes. Due to the imbalance in electron and hole conductivities, the most common OLED structure is based on the multi layer structure, although there are some materials, such as PPV, which can form efficient single layer devices due to minimal energy barrier between its LUMO level and the work function of calcium. The typical multi layer device consists of a hole transporting material and an electron transporting material which form a *pn* junction, with recombination occurring in one of the two materials. The single layer device will be considered first followed by the multi layer device.

### 4.6.2 Single Layer OLEDs

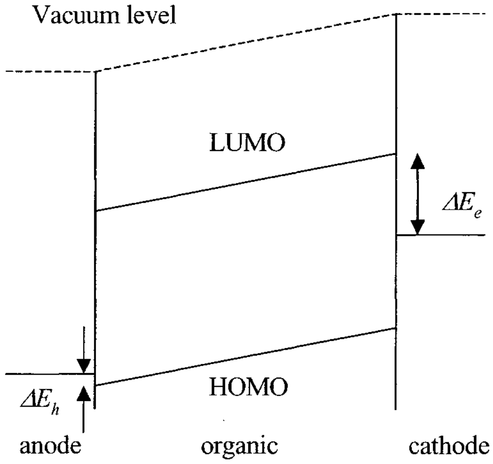

**Figure 4.22:** Energy level diagram of a single layer OLED. The anode is typically ITO and the cathode is a low work function metal.

The single layer OLED geometry is shown in Figure 4.22. The anode is a transparent conducting oxide such a indium tin oxide (ITO) or a thin, semi-transparent metal such as gold. The cathode is a low work function metal such as Ca, Mg, a Mg:Ag alloy or Al. The electrodes are chosen such that the injection barriers are as low as possible. Matching the anode work function with the HOMO energy is relatively easy to achieve, however matching the cathode work function with the LUMO energy is more difficult because there are very few metals with work functions low enough to make a good contact without oxidizing readily in air and water. Table 4.2 summarizes the HOMO and LUMO levels of some of the more common organic materials used in OLEDs (and OFETs) as well as the work functions of common metals used for electrical contacts.

The injected electrons and holes migrate from their respective injection electrodes and form excitons within the organic film. The excitons can be either singlet or triplet with only the singlet excitons generating light in a "classical" OLED. Both types of excitons generate light in some of the more exotic phosphorescent-based OLEDs.

Marks and co-workers have studied the J-V characteristics for single layer PPV diodes in detail for different electrode materials and temperatures.[98] They have shown that the current density has a power law dependence at low voltages which is attributed to space charge limited

**Table 4.2:** HOMO and LUMO energy levels for various organic semiconductors and work function energies of common metals used in OLEDs and OFETs. PEDOT is a synthetic metal.

| Organic Material | LUMO [eV] | HOMO [eV] | $E_g$ [eV] | Metal | Work Function (approx.) [eV] |
|---|---|---|---|---|---|
| Alq | 2.9 | 5.7 | 2.8 | Ca | 2.9 |
| TPD | 2.4 | 5.4 | 3.0 | Mg | 3.7 |
| PPV | 2.5 | 5.0 | 2.5 | Ag | 4.3 |
| MEH-PPV | 2.8 | 4.9 | 2.1 | Al | 4.2 |
| Pentacene | 2.4 | 4.9 | 2.5 | ITO | 4.6-4.9 |
| CuPc | 2.7 | 4.8 | 2.1 | Au | 5.1 |
| NPB | 1.8 | 5.2 | 3.4 | Pt | 5.4 |
| 8H-BBEP | 3.3 | 6.0 | 2.7 | Cr | 4.4 |

current with a significant amount of trapping.

Parker has studied single carrier devices based on MEH-PPV. In these devices, the anodes and cathodes are fabricated with the same material, allowing only holes or electrons to be injected into the organic material.[99] The electrical data was analyzed using Fowler-Nordheim tunneling through a triangular barrier and assuming that the device was operating in the flat band regime. This requires that there be negligible space charge present within the device and that the doping concentration is low enough that the width of any Schottky barriers formed are significantly greater than the thickness of the device. The calculated barrier heights were in agreement with those predicted by the electrode work functions and there was no temperature dependence observed. The lack of temperature dependence was a strong indication that tunneling was the predominant injection mechanism. When devices with hole and electron injecting electrodes were studied, the total current was significantly greater than the sum of the equivalent currents in the single carrier devices. This implies that space charge effects play a significant role in limiting current, contradicting the assumptions made by the Fowler-Nordheim model. Even though the barrier heights extracted from the Fowler-Nordheim plots are in agreement with the expected values, the observed currents are still several orders of magnitude lower than those predicted by Fowler-Nordheim theory in Equation 10.

Karg, Rieß and co-workers have proposed a Schottky barrier model for the operation of single layer PPV devices with ITO and Al electrodes.[100-103] Using Equation 15, they were able to achieve good fits to the data between 1 and 2 V with values of $n$ between 1.8 and 2.4 (compared to $n = 1$ for the ideal case). However when the internal resistance of the diode was taken into account, better fits were obtained over a larger voltage range; there is still some controversy over the validity of this assumption.

### 4.6.3 Multi Layer OLEDs

Most organic materials do not possess all of the attributes required to realize single layer devices. Therefore, multiple materials are employed for different tasks such as hole transport, electron transport and emission. In the seminal paper by Tang and Van Slyke on the development of the first practical OLED, the devices were based on a heterostructure geometry, shown in Figure 4.23.[88] In this type of device, the same considerations were made for matching the work function of the injecting electrode with the HOMO or LUMO level depending on hole or electron injection. Holes are injected into the "preferentially p-type" hole transport layer, or

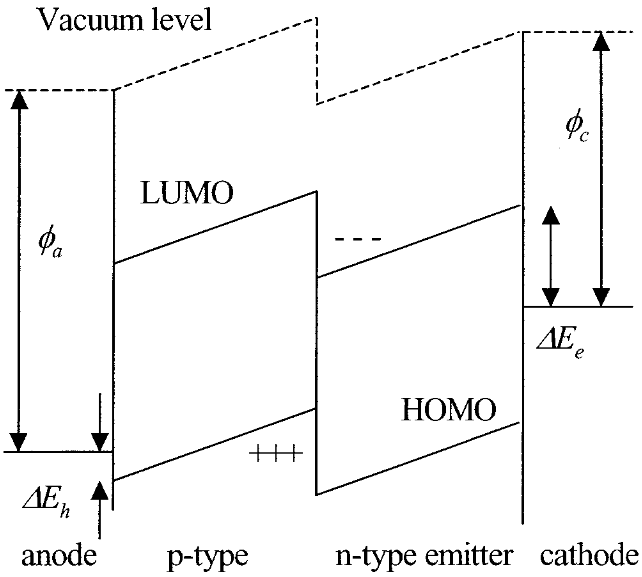

**Figure 4.23:** Energy level diagram for a heterostructure OLED. $\phi_a$ and $\phi_c$ denote the work functions of the anode and cathode, respectively.

HTL, and electrons are injected into a material which is still p-type, but has a higher electron mobility compared to the HTL. This layer is called the electron transport layer, or ETL. Under the influence of the applied electric field, the carriers migrate towards the interface between the two materials and form excitons which recombine and emit light. By analyzing the light generated by electroluminescence (EL) and comparing it to the fluorescence (PL) spectra of both HTL and ETL layers, it has been shown that the excitons annihilate within the ETL as the EL and PL spectra are almost identical.[104]

### 4.6.4 Materials

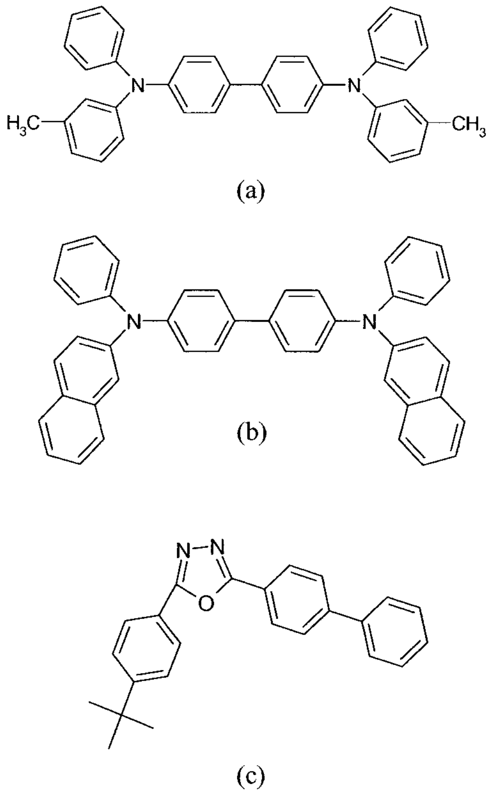

**Figure 4.24:** Some typical OLED materials: (a) TPD and (b) NPB are hole transport materials while (c) Bu-PBD is an electron transport material, however it is not fluorescent.

The first generation bi-layer OLED used TPD [N,N'-diphenyl-N,N'-bis(3-methylphenyl) benzadine] as the HTL. Unfortunately, while TPD displayed excellent hole transfer characteristics in OLEDs, its glass temperature was only 65°C, making it unsuitable for practical applications. NPB [4,4-bis(1-naphthyl phenylamino)biphenyl] quickly replaced TPD as the preferred HTL due to its superior film forming properties and higher glass temperature of 98°C.[105] Today there are myriads of new high performance HTL materials available with glass temperatures in excess of 100°C exhibiting lower threshold voltages ( < 2.5 V) and higher luminous efficiencies.[106-108] Bu-PBD [2-(4-biphenyl)-5-(4-tert-butylphenyl)1,3,4-oxidiazole] was used as an electron transporting layer.[109,110]

Alq is an electron transport material and emitter that was used in the first generation of OLEDs.[88] It emits at 530 nm and has excellent film forming properties. The colour of the emitted light can be changed by changing the metal atom by other group 3A metals,[111] modifying the ligands,[108] or by using entirely new materials.[112]

Another technique used to shift the emission colour is by doping the material in which recombination would normally occur with a fluorescent laser dye such as coumarin or DCM.[89,113] Energy is transferred from the excited host material to the dye via Förster energy transfer and re-emitted at a longer wavelength. For example, Alq doped with 1% DCM will shift the emission wavelength from 530 nm to 590 nm.[114]

### 4.6.5 Injection Enhancement Layers

Additional layers may be inserted at the anode/HTL and cathode/ETL interfaces. It has been reported that inserting a thin (<200 Å) layer of copper phthalocyanine (or other suitable material) between the ITO and HTL substantially improves device performance.[105,115,116] This has been attributed to several factors: passivation of the ITO surface producing a smoother interface; a graded energy barrier between the ITO and HTL; and better adhesion of the organic HTL onto the substrate producing superior quality films. At the cathode/ETL interface a thin 5-10 Å layer of LiF[117-123] or $Al_2O_3$[124,125] can be deposited prior to the deposition of the Al cathode and has been shown to dramatically increase the device efficiency.

## 4.7 Context of This Thesis

The two novel oligomers studied in this work were used in OFETs and OLEDs. The OFETs were analyzed in terms of the MOSFET theory for the saturation regime and by applying the analysis originally proposed by Levinson for CdSe TFTs. Important parameters such as the hole field effect mobility, threshold voltage, on/off ratio, subthreshold slope, grain boundary trap state density, trap energy, and trap-free mobility values were obtained. A relationship was established between the structure of the thin film and the observed electrical properties and methods to further improve the performance of the OFETs was proposed.

Single and multi layer OLEDs were used to characterize BBEP and 8H-BBEP. In the multi layer devices, various configurations were used including using the oligomers as the ETL, HTL, and emitter. The current-luminance-voltage characteristics were measured for all of the OLEDs tested. A green/blue light was observed from all of the OLEDs fabricated with BBEP or 8H-BBEP. Child's law was obeyed in the OLEDs at lower voltages and trapped charge limited current dominated at higher voltages.

## 4.8 References

[1] J. R. Sheats, H. Antoniadis, M. Hueschen, W. Leonard, J. Miller, R. Moon, D. Roitman, and A. Stocking, Science **273,** 884 (1996).

[2] D. B. Roitman, H. Antoniadis, J. R. Sheats, and F. Pourmirzaie, Laser Focus World **34,** 163 (1998).

[3] P. E. Burrows, G. Gu, V. Bulovic, Z. Shen, S. R. Forrest, and M. E. Thompson, IEEE Trans. Elec. Device **44,** 1188 (1997).

[4] R. H. Friend, R. W. Gymer, A. B. Holmes, J. H. Burroughes, R. N. Marks, C. Taliani, D. D. C. Bradley, D. A. DosSantos, J. L. Bredas, and M. Logdlund, Nature **397,** 121 (1999).

[5] J. Kido, in *The International Conference on the Science and Technology of Synthetic Metals*, University of Wollongong, Australia, 2004.

[6] S. Matsumoto, in *Electronic Display Devices*, edited by S. Matsumoto (John Wiley & Sons, New York, 1990).

[7] H. Sirringhaus, N. Tessler, and R. H. Friend, Science **280,** 1741 (1998).

[8] H. Sirringhaus, P. J. Brown, R. H. Friend, M. M. Nielsen, K. Bechgaard, B. M. W. Langeveld Voss, A. J. H. Spiering, R. A. J. Jannssen, and E. W. Meijer, Nature **401,** 685 (1999).

[9] Z. Bao, A. Dodabalapur, and A. J. Lovinger, Appl. Phys. Lett. **69,** 4108 (1996).

[10] Z. Bao, A. J. Lovinger, and A. Dodabalapur, Appl. Phys. Lett. **69,** 3066 (1996).

[11] A. Dodabalapur, Z. Bao, A. Makhija, J. G. Laquidanum, V. R. Raju, Y. Feng, H. E. Katz, and J. Rogers, Appl. Phys. Lett. **73,** 142 (1998).

[12] R. Hajlaoui, G. Horowitz, F. Garnier, A. ArceBrouchet, L. Laigre, A. El Kassmi, R. Demanze, and F. Kouki, Adv. Mater. **9,** 389 (1997).

[13] C. J. Drury, C. M. J. Mutsaers, C. M. Hart, M. Matters, and D. M. deLeeuw, Appl. Phys. Lett. **73,** 108 (1998).

[14] S. F. Nelson, Y.-Y. Lin, D. J. Gundlach, and T. N. Jackson, Appl. Phys. Lett. **72,** 1854 (1998).

[15] Y.-Y. Lin, A. Dodabalapur, R. Sarpeshkar, Z. Bao, W. Li, K. Baldwin, V. R. Raju, and H. E. Katz, Appl.

Phys. Lett. **74,** 2714 (1999).

16 S. M. Sze, *Physics of Semiconductor Devices*, Second ed. (John Wiley & Sons, Toronto, 1981).

17 J. G. Simmons, J. Phys. Chem. Solids **32,** 1987 (1971).

18 N. C. Greenham and R. H. Friend, in *Solid State Physics: Advances in Research and Applications*; *Vol. 49*, edited by H. Ehrenreich and F. Spaepen (Academic Press, Toronto, 1995).

19 X. Wei, A. S. Jeglinski, and Z. V. Vardeny, Synth. Met. **85,** 1215 (1997).

20 G. G. Malliaras, J. R. Salem, P. J. Brock, and J. C. Scott, J. Appl. Phys. **84,** 1583 (1998).

21 I. D. Parker, J. Appl. Phys. **75,** 1656 (1994).

22 H. A. Bethe, MIT Radiat. Lab. Rep., 43-12 (1942).

23 K. C. Kao and W. Hwang, *Electrical Transport in Solids With Particular Reference to Organic Semiconductors* (Pergamon Press, Toronto, 1981).

24 I. H. Campbell and D. L. Smith, in *Solid State Physics: Advances in Research and Applications*; *Vol. 55*, edited by H. Ehrenreich and F. Spaepen (Academic Press, New York, 2001).

25 F. H. Pollak and H. Shen, Mater. Sci. and Eng. **R10,** 275 (1993).

26 H. Shen and M. Dutta, J. Appl. Phys. **78,** 2151 (1995).

27 R. Williams, in *Semiconductors and Semimetals*; *Vol. 6*, edited by R. K. Willardson and A. C. Beer (Academic Press, New York, 1970).

28 I. H. Campbell, S. Rubin, T. A. Zawodzinkski, J. D. Kress, R. L. Martin, D. L. Smith, N. N. Barashkov, and J. P. Ferraris, Phys. Rev. B. **54,** R14321 (1996).

29 I. H. Campbell, J. D. Kress, R. N. Marks, D. L. Smith, N. N. Barashkov, and J. P. Ferraris, Appl. Phys. Lett. **71,** 3528 (1997).

30 F. Nuesch, Y. Li, and L. J. Rothberg, Appl. Phys. Lett. **75,** 1799 (1999).

31 F. Nuesch, F. Rotzinger, L. SiAhmed, and L. Zuppiroli, Chem. Phys. Lett. **288,** 861 (1998).

32 D. P. Woodruff and T. A. Delchar, *Modern Techniques of Surface Science*, Second ed. (Cambridge University Press, New York, 1994).

33 F. Gutmann and L. E. Lyons, *Organic Semiconductors* (Robert E. Krieger Publishing Company, Malabar,

1981).

[34] N. F. Mott and R. W. Gurney, *Electronic Processes in Ionic Crystals* (Clarendon Press, Oxford, 1940).

[35] M. A. Lampert, A. Rose, and R. W. Smith, Phys. Rev. **103,** 1648 (1956).

[36] M. A. Lampert, A. Rose, and R. W. Smith, Phys. Chem. Solids **8,** 464 (1959).

[37] A. Rose, Phys. Rev. **97,** 1538 (1955).

[38] P. Mark and W. Helfrich, J. Appl. Phys. **33,** 205 (1962).

[39] J. L. Moll, Wescon. Conv. Rec. **Pt. 3.,** 32 (1959).

[40] W. G. Pfann and C. G. B. Garrett, Proc. IRE **47,** 2011 (1959).

[41] D. R. Frankl, Solid State Electron. **2,** 71 (1961).

[42] R. Lindner, Bell Syst. Tech. J. **41,** 803 (1962).

[43] G. Horowitz, J. Mater. Res. **19,** 1946 (2004).

[44] B. Servet, G. Horowitz, S. Ries, O. Lagorsse, P. Alnot, A. Yassar, F. Deloffre, P. Srivastava, R. Hajlaoui, P. Lang, and F. Garnier, Chem. Mater. **6,** 1809 (1994).

[45] F. Garnier, A. Yassar, R. Hajlaoui, G. Horowitz, T. A. Delchar, B. Servet, S. Ries, and P. Alnot, J. Am. Chem. Soc. **115,** 8716 (1993).

[46] T. Minakata, I. Nagoya, and M. Ozaki, J. Appl. Phys. **69,** 7354 (1991).

[47] C. D. Dimitrakopoulos, A. R. Brown, and A. Pomp, J. Appl. Phys. **80,** 2501 (1996).

[48] A. Dodabalapur, L. Torsi, and H. E. Katz, Science **268,** 270 (1995).

[49] C. Tanase, E. J. Meijer, P. W. M. Blom, and D. M. de Leeuw, Org. Elecon. **4,** 33 (2003).

[50] E. L. Granstrom and C. D. Frisbie, J. Phys. Chem. B. **103,** 8842 (1999).

[51] M. Kiguchi, M. Nakayama, K. Fujiwara, K. Ueno, T. Shimada, and K. Saiki, Jpn. J. Appl. Phys. 2 **42,** L1408 (2003).

[52] G. Horowitz, M. E. Hajlaoui, and R. Hajlaoui, J. Appl. Phys. **87,** 4456 (2000).

[53] R. A. Street and A. Salleo, Appl. Phys. Lett. **81,** 2887 (2002).

[54] K. Sheshadri and C. D. Frisbie, Appl. Phys. Lett. **78,** 993 (2001).

[55] L. Burgi, H. Sirringhaus, and R. H. Friend, Appl. Phys. Lett. **80,** 2913 (2002).

[56] L. Burgi, T. J. Richards, and R. H. Friend, J. Appl. Phys. **94,** 6129 (2003).

[57] P. V. Necliudov, M. S. Shur, D. J. Gundlach, and T. N. Jackson, Solid-State Electron. **47,** 259 (2003).

[58] H. Klauk, G. Schmid, W. Radlik, W. Weber, L. Zhou, C. D. Sheraw, J. A. Nichols, and T. N. Jackson, Solid-State Electron. **47,** 297 (2003).

[59] E. J. Meijer, G. H. Gelinck, E. van Veenendaal, B. H. Huisman, D. M. de Leeuw, and T. M. Klapwijk, Appl. Phys. Lett. **82,** 4576 (2003).

[60] V. Podzorov, V. M. Pudalov, and M. E. Gershenson, Appl. Phys. Lett. **82,** 1739 (2003).

[61] J. Takeya, C. Goldman, S. Haas, K. P. Pernstich, B. Ketterer, and B. Batlogg, J. Appl. Phys. **94,** 5800 (2003).

[62] M. C. J. M. Vissenberg and M. Matters, Phys. Rev. B. **57,** 12964 (1998).

[63] D. Knipp, R. A. Street, A. Völkel, and J. Ho, J. Appl. Phys. **93,** 347 (2003).

[64] D. J. Gundlach, C. C. Kuo, C. D. Sheraw, J. A. Nichols, and T. N. Jackson, Proc. SPIE **3366,** 54 (2001).

[65] P. G. Le Comber and W. E. Spear, Phys. Rev. Lett. **25,** 509 (1970).

[66] G. Horowitz, R. Hajlaoui, and P. Delannoy, J. Phys. III France **5,** 355 (1995).

[67] G. Horowitz, R. Hajlaoui, R. Bourguiga, and M. E. Hajlaoui, Synth. Met. **101,** 401 (1999).

[68] R. A. Street, D. Knipp, and A. R. Völkel, Appl. Phys. Lett. **80,** 1658 (2002).

[69] J. Levinson, F. R. Shepherd, P. J. Scanlon, W. D. Westwood, G. Este, and M. Rider, J. Appl. Phys. **53,** 1193 (1982).

[70] Y.-W. Wang, H.-L. Cheng, Y.-K. Wang, T.-H. Hu, J.-C. Ho, C.-C. Lee, T.-F. Lei, and C.-F. Yeh, Thin Solid Films **467,** 215 (2004).

[71] S. Verlaak, V. Arkhipov, and P. Heremans, Appl. Phys. Lett. **82,** 745 (2003).

[72] M. Pope, H. Kallmann, and P. Magnante, J. Chem. Phys. **38,** 2540 (1963).

[73] D. F. Williams and M. Schadt, Solid State Comm. **7,** 1 (1969).

[74] M. I. Brodzeli, I. A. Eligulashvili, E. L. Kertsman, G. A. Nakashidze, and L. D. Rozenshtein, Fizika i Tekhnika Poluprovodnikov (Translation in: Soviet Physics Semiconductors) **4,** 954 (1970).

[75] G. J. Hoytink, Discussions of the Faraday Society **45,** 14 (1968).

[76] D. F. Williams and M. Schadt, Proceedings of the IEEE **58,** 476 (1970).

[77] D. F. Williams and M. Schadt, J. Chem. Phys. **53,** 3480 (1970).

[78] I. Granacher, M. Schadt, and E. Baldinger, in *Proceedings of the international conference on luminescence.*, Akademiai Kiado, Budapest, Hungary, 1968, p. 1915.

[79] J. Dresner, RCA Rev. **30,** 322 (1969).

[80] A. M. Zvyagintsev, V. I. Steblin, and G. S. Chilaya, Zhurnal Prikladnoi Spektroskopii **13,** 165 (1970).

[81] M. Kawabe, K. Masuda, and -. S. Namba, Jap. J. Appl. Phys. **10,** 527 (1971).

[82] A. G. Gol'dman, M. V. Kurik, Y. I. Vertsimakha, and B. N. Korol'ko, Zhurnal Prikladnoi Spektroskopii **14,** 235 (1971).

[83] M. Wittmer and I. Zschokke-Granacher, Helvetica Physica Acta **46,** 405 (1973).

[84] N. I. Wakayama, N. Wakayama, and D. F. Williams, Molecular Crystals and Liquid Crystals **26,** 275 (1974).

[85] J. Gonzalez-Basurto and -. Z. Burshtein, Molecular Crystals and Liquid Crystals **31,** 211 (1975).

[86] J. Kalinowski, J. Godlewski, and R. Signerski, Molecular Crystals and Liquid Crystals **1976,** 247 (1976).

[87] W. Helfrich and W. G. Schneider, Phys. Rev. Lett. **14,** 229 (1965).

[88] C. W. Tang and S. A. Van Slyke, Appl. Phys. Lett. **51,** 913 (1987).

[89] C. W. Tang, S. A. Van Slyke, and C. H. Chen, J. Appl. Phys. **65,** 3610 (1989).

[90] J. Kalinowski, J. Phys. D.: Appl. Phys. **32,** R179 (1999).

[91] A. Kraft, C. Grimsdale, and A. B. Holmes, Angew. Chem. Int. Ed. **37,** 402 (1998).

[92] L. J. Rothberg and A. J. Lovinger, J. Mater. Res. **11,** 3174 (1996).

[93] J. M. Shaw and P. F. Seidler, IBM J. Res. & Dev. **45,** 3 (2001).

[94] D. Braun and A. J. Heeger, Appl. Phys. Lett. **58,** 1982 (1991).

[95] Y. Tao, A. Donat-Bouillud, M. D'Iorio, J. Lam, T. C. Gorjanc, C. Py, and M. S. Wong, Synth. Met. **111-112,** 417 (2000).

[96] C. Zhang, S. Hoger, K. Pakbaz, F. Wudl, and A. J. Heeger, J. Electron. Mater. **22,** 413 (1993).

[97] M. D'Iorio and Y. Tao, in *Molecular Nanoelectronics*, edited by M. A. Reed and T. Lee (American

Scientific Publishers, Stevenson Ranch, 2003).

[98] R. N. Marks, D. D. C. Bradley, R. W. Jackson, P. L. Burn, and A. B. Holmes, Synth. Met. **55-57,** 4128 (1992).

[99] I. D. Parker, J. Appl. Phys. **75,** 1656 (1993).

[100] S. Karg, W. Riess, V. Dyakonov, and M. Schwoerer, Synth. Met. **54,** 427 (1993).

[101] S. Karg, W. Riess, M. Meier, and M. Schwoerer, Synth. Met. **55-57,** 4186 (1993).

[102] J. Gmeiner, S. Karg, W. Reiß, P. Strohriegl, and M. Schwoerer, Acta Polymer **44,** 201 (1993).

[103] W. Reiß, S. Karg, V. Dyakonov, M. Meier, and M. Schwoerer, J. Lumin. **60-61,** 906 (1994).

[104] A. R. Brown, D. D. C. Bradley, J. H. Burroughes, R. H. Friend, N. C. Greenham, P. L. Burn, A. B. Holmes, and A. Kraft, Appl. Phys. Lett. **61,** 2793 (1992).

[105] S. A. Van Slyke, C. H. Chen, and C. W. Tang, Appl. Phys. Lett. **69,** 2160 (1996).

[106] S. Tokito, H. Tanaka, A. Okada, and Y. Taga, Appl. Phys. Lett. **69,** 878 (1996).

[107] Y. Shirota, Y. Kuwabara, H. Inada, T. Wakimoto, H. Nakada, Y. Yonemoto, S. Kawami, and K. Imai, Appl. Phys. Lett. **65,** 807 (1994).

[108] Z. H. Kafafi, H. Murata, L. C. Picciolo, H. Mattoussi, C. D. Merritt, Y. Iizumi, and J. Kido, Pure Appl. Chem. **71,** 2085 (1999).

[109] C. Adachi, T. Tsutsui, and S. Saito, Appl. Phys. Lett. **55,** 1489 (1989).

[110] A. Schmidt, M. L. Anderson, and N. R. Armstrong, J. Appl. Phys. **78,** 5619 (1995).

[111] P. E. Burrows, L. S. Sapochak, D. M. McCarty, and S. R. Forrest, Appl. Phys. Lett. **64,** 2718 (1994).

[112] C. H. Chen, J. Shi, and C. W. Tang, Macromol. Symp. **125,** 1 (1997).

[113] J. Shi and C. W. Tang, Appl. Phys. Lett. **70,** 1665 (1997).

[114] J. Lam, T. C. Gorjanc, Y. Tao, and M. D'Iorio, J. Vac. Sci. Technol. A. **18,** 593 (2000).

[115] J. Blochwitz, M. Pfeiffer, T. Fritz, and K. Leo, Appl. Phys. Lett. **73,** 3202 (1998).

[116] X. Zhou, M. Pfeiffer, J. Blochwitz, A. Werner, A. Nollau, T. Fritz, and K. Leo, Appl. Phys. Lett. **69,** 878 (2001).

[117] A. Donat-Bouillud, I. Levesque, Y. Tao, M. D'Iorio, S. Beaupre, P. Blondin, M. Ranger, J. Bouchard, and

M. Leclerc, Chem. Mater. **12,** 1931 (2000).

118 Z. H. Lu, R. S. Khangura, M. W. C. Dharma-wardana, M. Z. Zgierski, and D. Ritchie, Appl. Phys. Lett. **85,** 323 (2004).

119 R. M. Montereali, S. Gambino, S. Loreti, S. Gagliardi, A. Pace, G. Baldacchini, and F. Michelotti, Synth. Met. **143,** 171 (2004).

120 W. J. Song, S. K. So, K. W. Wong, W. K. Choi, and L. L. Cao, Appl. Surf. Sci. **228,** 373 (2004).

121 A. Uddin, C. B. Lee, X. Hu, and T. K. S. Wong, Appl. Phys. A. **78,** 401 (2004).

122 T. Mori, H. Fujikawa, S. Tokito, and Y. Taga, Appl. Phys. Lett. **73,** 2763 (1998).

123 D. Yoshimura, T. Yokoyama, E. Ito, H. Ishii, Y. Ouchi, S. Hasegawa, and K. Seki, Synth. Met. **102,** 1145 (1999).

124 F. Li, H. Tang, J. Anderegg, and J. Shinar, Appl. Phys. Lett. **70,** 1233 (1997).

125 H. Tang, F. Li, and J. Shinar, Appl. Phys. Lett. **71,** 2560 (1997).

# Chapter 5
# Self Assembled Monolayers

## 5.1 Introduction

Self assembled monolayers (SAMs) have their origins in Langmuir-Blodgett film technology where highly ordered films of large polar molecules are deposited onto flat surfaces.[1] The first recorded preparation of a self assembled molecular monolayer was in 1946 by Zisman *et al* by adsorbing a surfactant onto a clean metal surface.[2] Due to the absence of appropriate analytical surface characterization tools, this publication received minimal attention. Interest was rekindled in the 1960s in Kuhn's laboratory where chlorosilane derivatives were reacted with glass surfaces to form hydrophobic substrates. The first report of a self assembled monolayer of *n*-octadecyltrichlorosilane ($C_{18}H_{37}SiCl_3$, denoted OTS-18) on a silica surface was reported by Sagiv in 1980.[3]

The formation of monolayers of surfactant molecules onto solid surfaces is an example of the general phenomenon of self assembly, which is a predominant force in nature. In recent years, chemistry and physics have converged from their respective traditional research disciplines into a powerful interdisciplinary area in part because of the opportunities and lucrative promises of the "bottom up" nanotechnology approach.

In contrast to ultrathin films made by molecular beam epitaxy or chemical vapour deposition techniques, highly ordered SAMs can incorporate a wide range of groups both in the alkyl chain and at head and tail ends. Due to their dense and stable structure, SAMs have tremendous potential in other applications such as anti-corrosion coatings, wear coatings, and other biologically-compatible applications.

The ability to tailor the head and tail groups of the constituent molecules make SAMs excellent systems for a more fundamental understanding of phenomena affected by competing intermolecular, molecular-substrate, and molecular-solvent interactions such as ordering and growth, wetting, adhesion, and lubrication. Figure 5.1 illustrates the basic mechanics of SAM formation. A substrate is immersed in a solution containing the surface-active material (Figure 5.1a and 5.1b) for a time ranging from seconds to hours, depending on the type of SAM. The resulting SAM is shown in Figure 5.1c, with an expanded view in Figure 5.1d, illustrating the details of the SAM: the inter-molecular interactions, the bonding sites, and the structure.

In this thesis, three different types of SAMs were used; hexamethyldisilazane (HMDS), OTS-18, and *n*-octyltrichlorosilane, referred to as OTS-8. HMDS was deposited from the

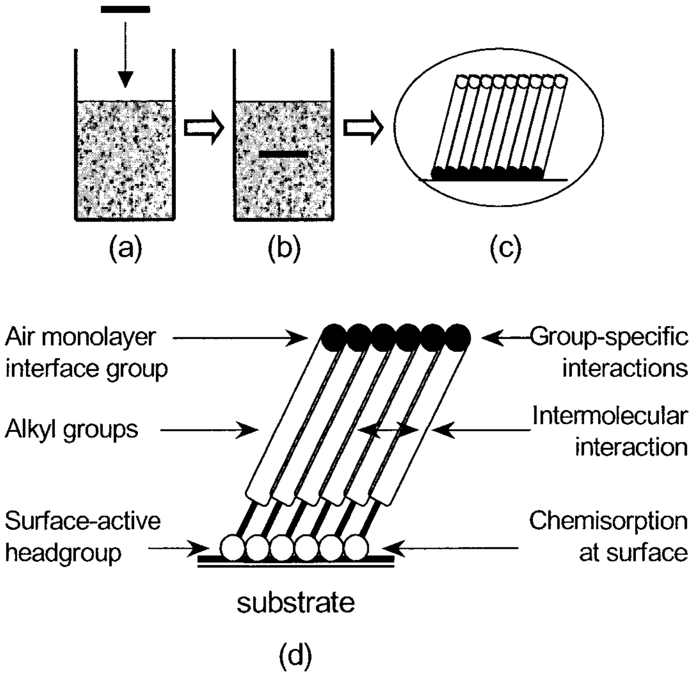

**Figure 5.1:** Self assembled monolayers are formed spontaneously by immersing a substrate into a solution of the surface-active material under controlled conditions.

vapour phase in vacuum. OTS-18 SAMs were deposited from solution and OTS-8 SAMs were deposited from both solution and vapour phase. In the following sections an introduction to $SiO_2$ surface conductivity will be presented followed by a discussion of HMDS and OTS and their reaction mechanisms with $SiO_2$, and concluded by presenting an overview of the use of SAMs within the context of OFETs.

## 5.2 The Application of SAMs to OFETs

The majority of OFETs reported in the literature use $SiO_2$ as the gate dielectric but there have been reports of other dielectrics used, such as $Si_3N_4$, $Al_2O_3$, and organic dielectrics.[4-14] Unlike epitaxial techniques which grow lattice matched or strained systems, depositing amorphous or polycrystaline organic films onto an inorganic substrate can present problems such as adhesion, interface roughness and defects, wettability, and small grain size. These issues arise most often from the poor adhesion of organic materials to inorganic materials. One alternative is to use an organic gate dielectric given the better adhesion of organic materials to organic materials. However, issues such as swelling, surface roughness, or lack of stability at elevated temperatures can affect device performance. Inserting a buffer layer, such as a SAM, between the inorganic dielectric and the organic semiconductor is another method to both increase the wettability of the organic on the dielectric and to engineer the properties of the interface.[10,15-17] By controlling the chemical properties of the surface, the interactions between the organic semiconducting molecules and the dielectric surface are also changed. In some systems, forming a SAM will reduce the surface energy of the dielectric film, allowing the organic molecules to rearrange themselves into a more thermodynamically favorable configuration on the surface, thus promoting the growth of larger grains.[16] In other systems, SAMs with long alkyl chains can interact with alkyl chains on the organic molecules (if present) and induce the molecule to be oriented in various directions such as parallel to the surface or perpendicular to it, illustrated in Figure 5.2.[15,18] The orientation of the molecule with respect to the surface plays an important role in the performance of an OFET due to the amount of $\pi$-$\pi^*$ orbital overlap and whether the charge conduction occurs parallel or perpendicular to the backbone of the molecule.

As discussed earlier, using SAMs such as HMDS can lower the surface conductivity of the dielectric. Since most OFETs operate as normally off devices, minimizing the off current is crucial to increase the on/off ratio and improve overall transistor performance. By forming a non-polar SAM, built-in electric fields which might be present at the interface can be reduced. Boulas and co-workers have estimated the HOMO-LUMO gap in SAMs with 12, 16, and 18 carbon alkyl chains between 9.2 and 9.9 eV ± 0.3 eV.[19] Using a tight binding approximation, theoretical values of ~11 eV and ~12 eV were obtained for 18 and 10 carbon membered alkyl chains, respectively.

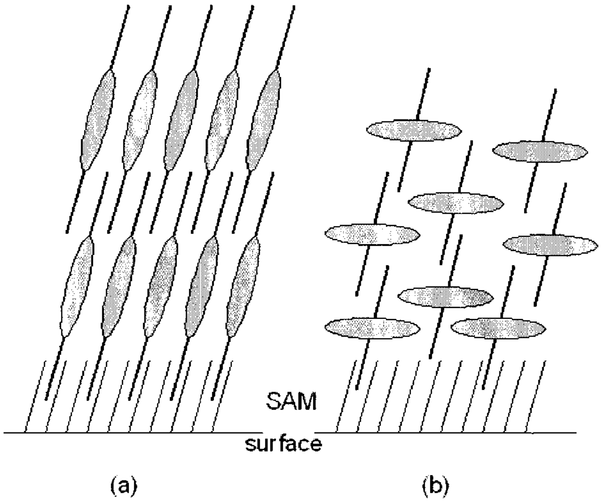

**Figure 5.2:** Possible orientations of the organic semiconductor backbone with respect to the surface due to the SAM: (a) perpendicular (with a 10-20° tilt angle) and (b) parallel to the surface. The diagrams are not drawn to scale.

A SAM can be used to repair surface defects and to passivate the dielectric surface prior to the deposition of the organic semiconductor. Kiguchi *et al* have shown that the thickness of the accumulation layer in OFETs can be of the order of 9-50 Å, depending on the organic semiconductor being used.[20] Consider, for example, an $SiO_2$ surface with a root mean square, or RMS, roughness in the range of 10-20 Å. This RMS roughness is approximately the same order of magnitude as the thickness of the accumulation layer which is formed during device operation. A rough interface such as this promotes a disordered film as well as the scattering and trapping of charge carriers, therefore decreasing the mobility of charges in the organic material and substantially increasing the threshold voltage in these OFETs. Consider now the same $SiO_2$ dielectric, but with a SAM on the surface. A SAM can slightly reduce the effective RMS roughness of the dielectric surface, leading to a smoother interface. Wang and Leiberman[21] have demonstrated that SAMs of OTS-18 which are formed under dry conditions

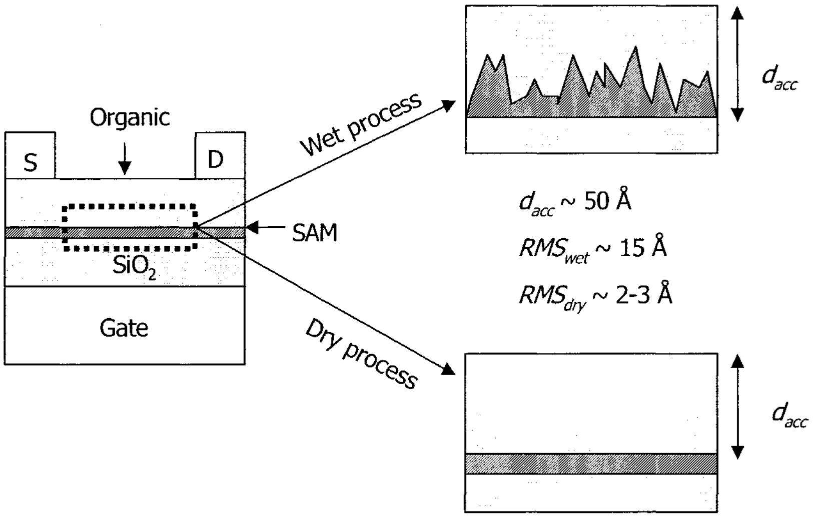

**Figure 5.3:** Expanded view of the organic-SAM-dielectric interfacial region (not to scale). The SAM using the wet process results in a very high RMS roughness of approximately 15 Å while the SAM formed using the dry process produces a much smoother film with an RMS roughness of 2-3 Å.

are ultra-smooth, with an RMS roughness of 2-3 Å while those SAMs formed under wet conditions have an RMS roughness in the range of 15 Å. This is large enough to contribute to carrier scattering and trapping in the interfacial region. A diagram is shown in Figure 5.3 illustrating the difference between a rough interface and a smooth interface in the context of an OFET, further emphasizing the importance of a smooth dielectric-organic interface.

## 5.3 $SiO_2$ Surface Conductivity

In addition to the surface composition, the surface conductivity at the $SiO_2$-air interface is sensitive to a number of parameters such as cleaning solvents, relative atmospheric humidity, and surface silanol concentration. The surface conductivity of the $SiO_2$ dielectric is of great importance in the operation of the OFET. A high surface conductivity will result in a large leakage current when there is no gate voltage applied to the device. Shockley *et al* have shown that mobile charges at an oxide-air interface can move due to an applied lateral electric field.[22] They reported that the surface conductivity strongly depends on the partial pressure of polar gases, such as water vapour, in the surrounding ambient air.

There are two types of water vapour adsorption that can occur in sequence at the $SiO_2$-air interface. Water is chemisorbed onto the surface converting siloxanes to vicinal silanols and the physisorption of water occurs at the surface silanol groups through hydrogen bonding. Awakuni and Calderwood have investigated how the surface conductivity is affected by monolayers of water on $SiO_2$ and Teflon surfaces.[23] The reported results can be modeled very well by using Brunauer, Emmet, and Teller's (BET) adsorption theory. BET theory assumes that a statistical distribution of surface regions occurs comprising of areas without any adsorbed molecules and with one or more monolayers present. The coverage ratio $R_c$, defined as the relative portion of the surface covered with one or more monolayers, can be written as a function of the relative humidity:[24]

$$R_c = \frac{Ch}{1+(C-1)h} \quad , \tag{1}$$

where $h$ is the relative humidity and $C$ is a dimensionless constant between 0.01 and 0.06.[24-26] Equation 1 is only valid for an untreated $SiO_2$ surface.

Castagne[24] and Martin[27] have both studied the mechanism of surface conductivity of quartz glass. Their results indicate that it is impossible to determine whether the measured conductivity is predominantly electronic or ionic in nature, assuming that the adsorbed layer of water is continuous. According to Equation 1, using $C = 0.05$, the coverage ratio $R_c$ is much smaller than unity for most values of $h$. For example, $R_c = 0.83$, 0.13, and 0.047 when the relative humidity $h = 0.99$, 0.75 and 0.50, respectively. This indicates that adsorption occurs in island-type spots with bare regions isolating the islands. Castagne and co-workers have used this assumption to describe the surface conductivity by applying BET theory and a hopping electron model.[24] The model assumes that the surface conductivity is determined by the hopping of electrons between adsorbed spots across the bare regions. They proposed that the surface conductivity of $SiO_2$ is a function of the relative humidity and takes the following form:

$$\sigma = \sigma_o \exp\left[-\alpha\sqrt{\frac{1-h}{Ch}}\right], \tag{2}$$

where $\sigma_o$ is the surface conductivity at 100% relative humidity and $\alpha$ is a constant which depends on the electron mass, the diameter of the adsorbed spots and the energy of electrons on the $SiO_2$ surface. Equation 2 can also be expressed in terms of the coverage ratio $R_c$ by using Equation 1:

$$\sigma = \sigma_o \exp\left[ - \alpha\sqrt{\frac{1 - R_c}{R_c}} \right]. \tag{3}$$

With these results, Voorthuyzen *et al* have measured the surface conductivity of plain, uncleaned $SiO_2$ to be approximately $10^{-10}$ S using an open-gate FET structure.[26] They have also reported that there are two possible methods in which the surface conductivity of $SiO_2$ may be reduced: through cleaning of the surface and through chemical surface modification.

The cleaning of an oxide surface by rinsing it with an appropriate solution is the most elementary method. It has been suggested that using solvents with a low dipole moment and low dissociation constant would lower the surface conductivity.[22] Indeed, even rinsing the sample with deionized (DI) water in which the ionic impurity level is extremely low can yield a decrease in the surface conductivity. This has been demonstrated by Voorthuyzen and *et. al.* where the surface conductivity was decreased by approximately two orders of magnitude.[26]

The constituent particles which make up bulk silica can be regarded as polymers of silicic acid, consisting of interlinked $SiO_4$ tetrahedra. At the surface, the structure terminates in either a siloxane group with the oxygen at the surface or in one of several forms of silanol, shown in Figure 5.4. Silanols are classified into three categories; isolated groups, or free silanols, shown in Figure 5.4a, vicinal, or bridged silanols, shown in Figure 5.4b, and geminal silanols shown in Figure 5.4c. In free silanols, the surface silicon atom has three bonds into the

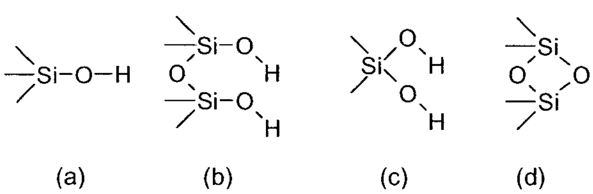

**Figure 5.4:** Types of surface silanols: (a) isolated, (b) vicinal and (c) geminal. A siloxane group is shown in (d).

bulk structure while the fourth bond is attached to a single surface hydroxyl group. Vicinal silanols consist of two single silanol groups attached to different silicon atoms, but are close enough to experience hydrogen bonding between the hydroxyl functional groups. Geminal silanols are composed of two hydroxyl groups that are attached to the same silicon atom. These hydroxyl groups are too close to each other to permit hydrogen bonding effects, whereas in the free silanols the hydroxyl groups are too far apart.[28] These three different silanol species are identifiable by their unique infrared and $^{29}$Si NMR properties,[29] however, their effects on the surface conductivity are indistinguishable.

Because most OFETs are relatively low current devices, minimizing the off state currents is extremely important. The effect of different cleaning processes on the contact angle of $SiO_2$ was studied. While the contact angle technique does not give us a direct measure of the surface conductivity, it does allow for a qualitative examination of the hydophobicity of the surface (through surface tension), which is directly affected by the number of polar species (such as silanols) present. The surface conductivity will increase with an increase in the concentration of polar species present on the surface. Table 5.1 summarizes the measured contact angles (the error in the contact angle goniometer is ±3°) of $SiO_2$ surfaces which have undergone various cleaning processes. Attempts were made to characterize the surfaces using XPS, but because the samples were exposed to ambient atmosphere the surface became contaminated and it was difficult to see any difference from sample to sample. The results of the cleaning processes are discussed in order of descending contact angle (i.e. increasing surface conductivity).

The bare $SiO_2$ was used "as received," with no additional cleaning steps aside from passing a strong flow of dry $N_2$ across the surface to remove any dust particles. A contact angle of 30° was measured and served as a baseline for comparison. The most basic cleaning process used was acetone, hot isopropyl alcohol, and DI water for 5-10 minutes per step (hereafter referred to as solvent cleaning). The surface did not show any difference in contact angles compared to the as-received $SiO_2$ surface. Next, the solvent cleaning was followed by either a 10 minute soak in a piranha acid solution or a 10 minute exposure in the UV-$O_3$ photoreactor. Both of these processes yielded approximately the same contact angles between 29° and 30°. The solvent cleaning followed by a 1 hour soak in the piranha acid did show a marginal decrease in the contact angle to 26°. This was attributed to the growth of a thin chemical oxide on the surface which probably possessed a higher than stoichiometric amount of oxygen. The solvent

**Table 5.1:** Measured contact angle for various $SiO_2$ surface treatments. A/I/W refers to acetone, isopropyl alcohol and water cleaning.

| Treatment | Contact Angle |
|---|---|
| Bare $SiO_2$ | 30° |
| A/I/W (solv) | 30° |
| solv + 10 min Piranha | 30° |
| solv + 10 min UV-$O_3$ | 29° |
| solv + 1 hour Piranha | 26° |
| solv + 3 min Ar/$O_2$ plasma | 9° |
| solv + RCA 1&2 | 7° |
| solv + 1h UV-$O_3$ | 6° |
| solv + RCA 1&2 +1h UV-$O_3$ | 3° |

cleaning followed by a 1 hour UV-$O_3$ exposure resulted in a contact angle of 6°. This drastic decrease in the contact angle was attributed to a large increase in the concentration of surface silanols generated by the UV-$O_3$ process.

Solvent cleaning followed by exposure to an argon/oxygen plasma was attempted. The Ar:$O_2$ ratio was fixed at 120:30 sccm with an rf power of 200 W with the reflected power at 9 W. The samples were placed in the plasma for 3 minutes and showed a substantial decrease in the contact angle.

Finally, a two-stage RCA cleaning process was used which resulted in a contact angle of 7°. The same RCA process followed by a 1 hour UV-$O_3$ exposure resulted in the lowest contact angle of 3°, which was at the limit of detection of the goniometer. No other attempted process was able to reach contact angles this low.

Atomic force microscopy (AFM) was performed on the silanol-terminated samples to ensure that the initial surface was smooth. The process involving solvent cleaning, RCA 1&2, and a 1 hour UV-$O_3$ exposure was used for all substrates prior to any SAM processing. The AFM image shown in Figure 5.5 verifies that the $SiO_2$ surface is extremely smooth with an RMS roughness of 2.26 Å for a 1 $\mu m^2$ area. The smoothness of the surface on which the organic semiconductor will be deposited on is of critical importance in OFET performance, and will be discussed in greater detail in subsequent sections.

## 5.4 Chemical Modification of the $SiO_2$ Surface

We have shown that by using simple beaker chemistry and an UV-$O_3$ exposure we can substantially decrease the contact angle which implies that the $SiO_2$ has a relatively high surface conductivity. In order to decrease the surface conductivity, the polar surface must be converted into a non-polar surface. Chemically modifying a surface to alter the surface conductivity is a well known technique.[30,31] By using various silanizing agents which react with the surface silanols, the surface conductivity can be decreased by four orders of magnitude, summarized in Table 5.2.[26]

From Equation 3, the number of surface silanol groups which were passivated can be estimated. Using the results of Castagne,[24] Voorthuyzen has estimated that $R_c = 0.05$ and 0.03 for HMDS and DCDMS deposited via a liquid phase reaction at 75 °C, respectively. This infers that 95% and 97% of the surface silanols have been replaced by the respective silane agent. Van den Berg has also estimated that 90 to 99% of the original silanol groups have been replaced by silane agents.[31] These results also agree with those of Ponjeé and co-workers who correlated water contact angles and HMDS surface coverage using time of flight secondary ion mass spectroscopy (TOF-SIMS).[32,33] A steady increase in the contact angle with respect to surface coverage was observed, with a plateau forming at a surface coverage of approximately 90%. Due to the size of the methyl moieties, steric hindrance is thought to prevent the substitution of all surface silanols with silanes. However, compared to alkyl-based silanes, the steric effects are smaller and thus a higher number of surface silanols may be substituted.

In the selection of a chemical modification process, there are two important parameters which must be taken into account: the desired coating morphology and the scale on which the modification has to be performed. The coating morphology includes layer thickness, the modification density, the orientation of the surface molecules, and the interaction of the coating

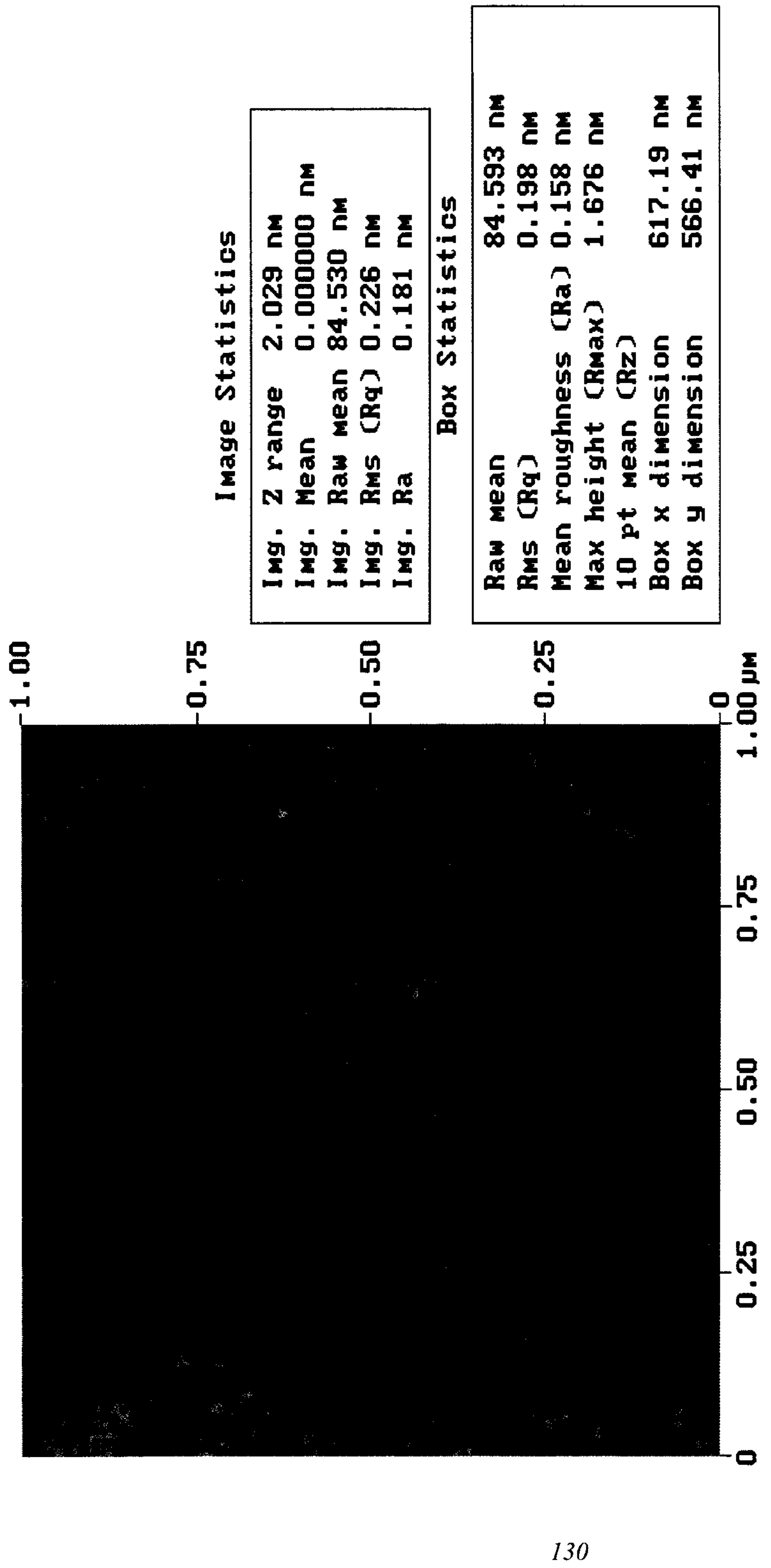

```
Image Statistics

Img. Z range    2.029 nm
Img. Mean       0.000000 nm
Img. Raw mean   84.530 nm
Img. Rms (Rq)   0.226 nm
Img. Ra         0.181 nm

Box Statistics

Raw mean                84.593 nm
Rms (Rq)                0.198 nm
Mean roughness (Ra)     0.158 nm
Max height (Rmax)       1.676 nm
10 pt mean (Rz)
Box x dimension         617.19 nm
Box y dimension         566.41 nm
```

**Figure 5.5:** AFM of a clean $SiO_2$ surface using solvents, RCA 1&2, and a 1 hour UV-$O_3$ exposure. The RMS roughness for the entire 1 $\mu m^2$ area is 2.26 Å.

**Table 5.2:** Surface conductivity as a result of various cleaning and chemical modifications of the $SiO_2$ surface. Data from Reference 8.

| Compound | Surface Conductivity |
|---|---|
| Plain $SiO_2$ | $10^{-10}$ S |
| $H_2O$ rinsed $SiO_2$ | $10^{-12}$ S |
| hexamethydisilazane (HMDS) | $10^{-15}$ S |
| dichlorodimethylsilane (DCDMS) | $10^{-16}$ S |
| trimethoxyvinylsilane (TMVS) | $10^{-14}$ S |
| triethoxymethylsilane (TEMS) | $2.5 \times 10^{-14}$ S |

layer with the surface and any film that will be deposited onto it. These criteria will be discussed in each of the following sections as they apply to either hexamethyldisilazane or trichlorosilane-based surface treatments.

## 5.5 Hexamethyldisilazane (HMDS)

HMDS has been used in photolithography for many years as a priming agent to aid in the processing of materials such as $SiO_2$. When used in such an application, HMDS prevents the delamination of photoresist from the substrate during development or undercutting during wet etching by preventing the alkaline or acidic solutions from penetrating into the interface between the substrate and the photoresist.[32] Due to this effect, HMDS is often, although incorrectly, referred to as an adhesion promoter whereas, in fact, it has been shown that HMDS actually decreases the mechanical adhesion due to the non-reactive, low surface energy trimethylsilyl terminated surface.[33,34] The silanol-terminated surface is heated in a vacuum oven and then exposed to HMDS vapours. This reaction will break the HMDS molecule in half and

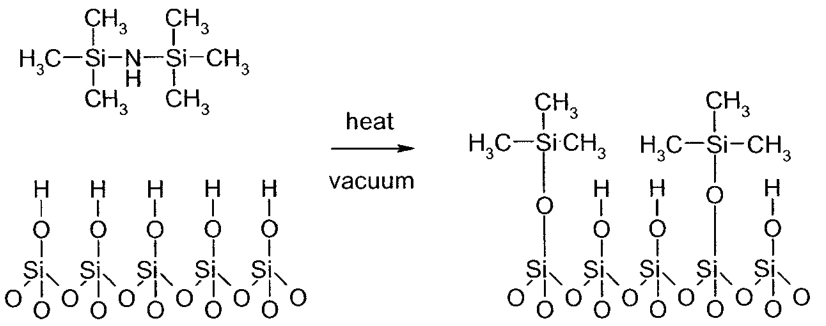

**Figure 5.6:** Reaction mechanism of HMDS with a silanol-terminated $SiO_2$ surface.

react with the surface silanols resulting in the formation of non-polar trimethylsilyl groups on the surface. The reaction mechanism is shown in Figure 5.6.

A critical factor in achieving a high surface coverage is the hydroxyl density on the surface. Michielsen *et al* have performed a thorough study on the adhesion of trimethylsilyl compounds on silicon substrates.[32] They have correlated contact angle measurements with the

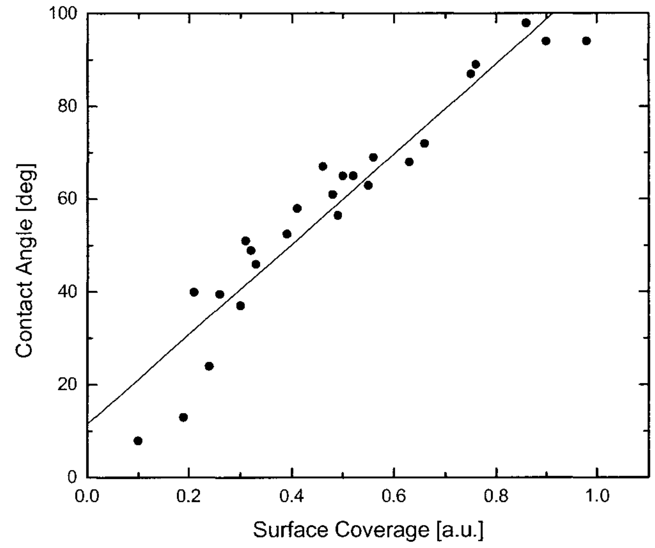

**Figure 5.7:** Advancing contact angle as a function of trimethylsilyl surface coverage as measured by TOF-SIMS. The straight line is to guide the eye. Adapted from reference 32.

relative surface coverage of trimethylsilyl groups using TOF SIMS. The data from reference 14 is presented in Figure 5.7. It is apparent that there is a nearly linear relationship between the surface coverage and the contact angle for trimethylsilyl terminated surfaces.

Immediately after HMDS coating, the samples were rinsed with water and contact angle measurements were performed as a function of the exposure time to HMDS vapours. These measurements were made with samples that underwent different surface cleaning processes with the exception of the Ar/$O_2$ processed sample where only a 12 minute HMDS exposure was performed. The data points presented in Figure 5.8 represent the average values of 10 measurements performed on a single sample. The contact angles are quoted with an uncertainty of ±3°. The results were reproducible on different samples fabricated using the same recipe.

From the trends in Figure 5.8, there did not seem to be any noticeable difference between

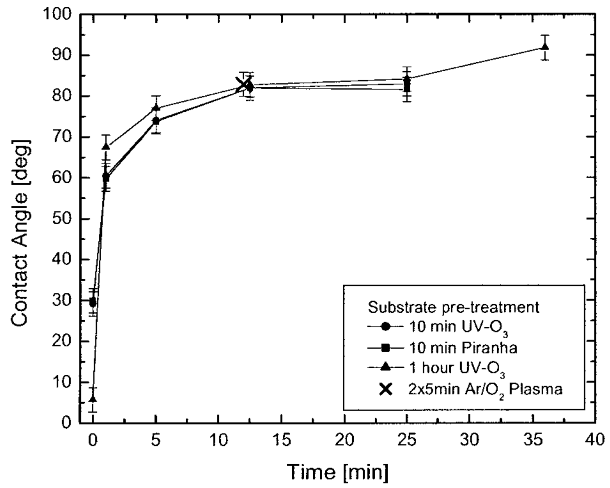

**Figure 5.8:** Contact angle as a function of exposure time to HMDS vapours at 136 °C for four different substrate cleaning processes. Only one measurement was made for the Ar/$O_2$ plasma cleaned sample. The 10 minute UV-$O_3$ and 10 minute piranha curves overlap almost perfectly.

**Table 5.3:** t-test results comparing HMDS samples fabricated using different surface preparation techniques.

| Exposure Time | Cleaning Process | t | p (%) | Exposure Time | Cleaning Process | t | p (%) |
|---|---|---|---|---|---|---|---|
| 1 min | P = O10 | 1.0 | 36 | 12 min | P = O10 | 0.0 | 100 |
| | P ≠ O60 | 10.5 | 4.4 x$10^{-5}$ | | P = O60 | 1.7 | 12 |
| | O10 ≠ O60 | 18.7 | 1.1 x$10^{-7}$ | | O10 = O60 | 1.8 | 11 |
| 5 min | P = O10 | 0.3 | 80 | 25 min | P ≠ O10 | 5.2 | 4 x $10^{-1}$ |
| | P ≠ O60 | 7.3 | 1.6 x$10^{-3}$ | | P ≠ O60 | 10.8 | 1.6 x$10^{-5}$ |
| | O10 ≠ O60 | 3.5 | 5 x $10^{-1}$ | | O10 ≠ O60 | 5.3 | 2 x $10^{-1}$ |

= denotes that the mean values are not significantly different.
≠ denotes that the mean values are significantly different.
P: 10 minute piranha, O10: 10 min UV-$O_3$, O60: 60 min UV-$O_3$

the 10 minute UV-$O_3$ and piranha treated samples until 25 minutes of exposure was reached, where the 10 minute UV-$O_3$ sample showed a slightly higher contact angle. This was verified by applying a two population student t-test on the measured contact angles using a significance level of 0.05. The results are summarized in Table 5.3. The one hour UV-$O_3$ treated substrates displayed a slightly higher contact angle for 1, 5, and 25 minute exposures but were not found to have significantly different contact angles for 12 minute exposures. The Ar/$O_2$ treated sample showed similar contact angles for 12 minute exposures (t-test results $t = 0.19674$ and $p = 84.568\%$ when compared to the 1 hour UV-$O_3$ samples), but was not used due the design of the Ar/$O_2$ plasma chamber which did not accommodate more than 4 samples for simultaneous processing, and hence large batches could not be processed.

Figure 5.9 shows images from the contact angle goniometer of a water droplet on a bare $SiO_2$ surface (Figure 5.9a) and HMDS-treated surface. The surface treatment outlined in Recipe C.2 was used with a 1 hour UV-$O_3$ exposure and 1, 5, and 12 minutes HMDS exposures (Figure 5.9b-d).

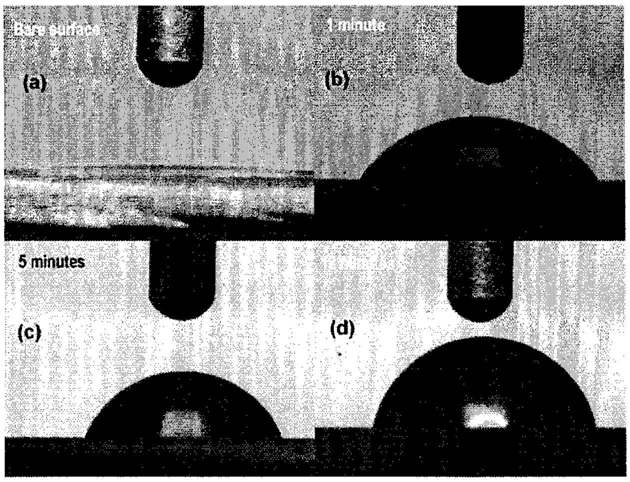

**Figure 5.9:** Images from the contact angle goniometer showing the evolution of the shape of the water droplet with increasing HMDS exposure time.

The initial contact angle was very low; typically 3°. An exposure time of one minute increased the contact angle to approximately 70°. After about 10 minutes, the contact angle reached a quasi plateau in the range of 80-85°. Longer exposures did increase the contact angle, but due to the nature of the oven used to deposit HMDS, exposures longer than 12 minutes required a complete repeat of the coating cycle. Figure 5.10 compares the surface morphology between the 1 and 12 minute samples. The RMS roughness decreased from 2.77 Å to 2.40 Å when the exposure time was increased, but still remained slightly higher than the RMS roughness of the bare $SiO_2$ surface shown in Figure 5.5. This smoothing effect is expected due to the increased surface coverage of the trimethylsilyl groups on the surface.

## 5.6 Trichlorosilanes

Chlorosilane-, alkoxysilane-, and aminosilane-based SAMs require hydroxylated surfaces as substrates for their formation. The driving mechanism for this self assembly is the *in situ* formation of polysiloxane, which is connected to surface silanol groups via Si-O-Si bonds. Substrates on which these types of monolayers have been formed include silicon dioxide,[1,35-38] aluminum oxide,[39,40] quartz,[41-43] glass,[35] mica,[44-46] zinc selenide,[35,40] germanium oxide,[35] and gold.[47-49] In particular, OTS-18 has been studied extensively.[38,39,50-54] Figure 5.11 shows the chemical structure of OTS-8 and OTS-18.

Although SAMs are formed using simple beaker chemistry, the formation of high quality SAMs is not trivial. There are many parameters which affect the structure of the film, perhaps the most important being the water content in both the solution and in the atmosphere.[21,37,38,55,56] Water can act as a catalyst to polymerize the OTS molecules in the solution which results in clusters of polymerized OTS islands being deposited on the surface.[21,43,57]

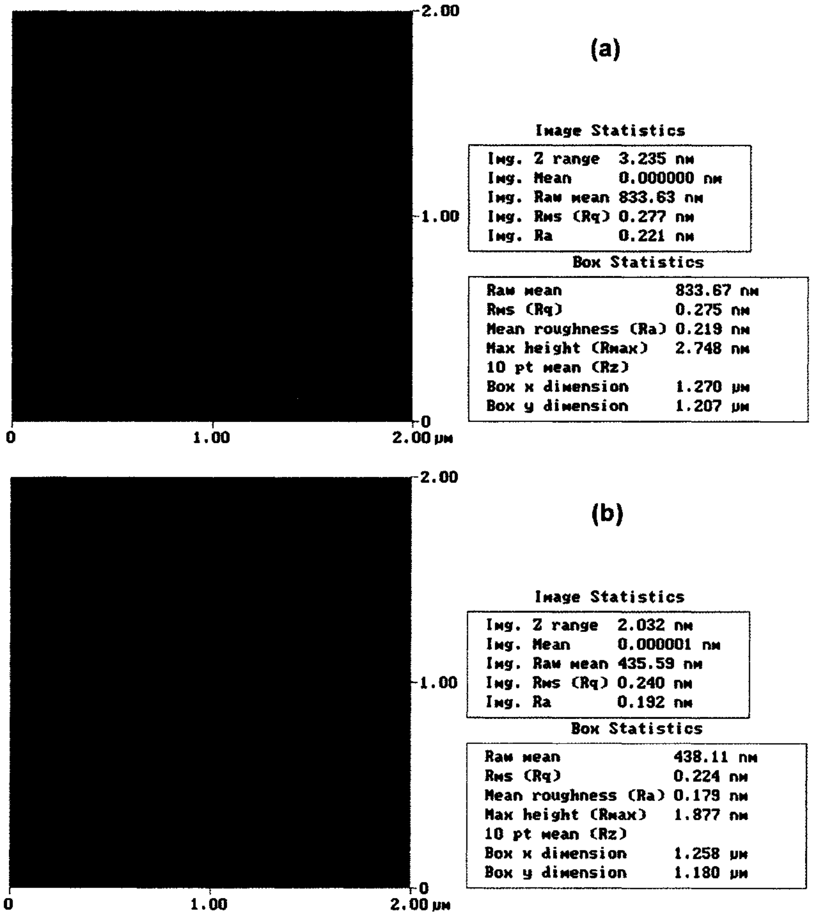

(a)

Image Statistics

| | |
|---|---|
| Img. Z range | 3.235 nm |
| Img. Mean | 0.000000 nm |
| Img. Raw mean | 833.63 nm |
| Img. Rms (Rq) | 0.277 nm |
| Img. Ra | 0.221 nm |

Box Statistics

| | |
|---|---|
| Raw mean | 833.67 nm |
| Rms (Rq) | 0.275 nm |
| Mean roughness (Ra) | 0.219 nm |
| Max height (Rmax) | 2.748 nm |
| 10 pt mean (Rz) | |
| Box x dimension | 1.270 µm |
| Box y dimension | 1.207 µm |

(b)

Image Statistics

| | |
|---|---|
| Img. Z range | 2.032 nm |
| Img. Mean | 0.000001 nm |
| Img. Raw mean | 435.59 nm |
| Img. Rms (Rq) | 0.240 nm |
| Img. Ra | 0.192 nm |

Box Statistics

| | |
|---|---|
| Raw mean | 438.11 nm |
| Rms (Rq) | 0.224 nm |
| Mean roughness (Ra) | 0.179 nm |
| Max height (Rmax) | 1.877 nm |
| 10 pt mean (Rz) | |
| Box x dimension | 1.258 µm |
| Box y dimension | 1.180 µm |

**Figure 5.10:** AFM images of an $SiO_2$ surface exposed to HMDS vapours for (a) 1 minute and (b) 12 minutes. The RMS roughness decreased from 2.77 Å to 2.40 Å.

Wang and Lieberman have performed a detailed study on the growth mechanisms of OTS-18.[21] By comparison, there exists almost no information in the literature on the study of OTS-8 SAMs but, in principle, the SAM formation process should be identical to the OTS-18 process, with possibly a shorter time needed for a complete SAM to form due to the shorter alkyl chain which reduces steric effects between molecules. In their work, the effect of water content in the solvent on the quality of OTS-18 SAMs was examined and a reaction mechanism was proposed which explains the formation of OTS SAMs. Figure 5.12 shows the proposed reaction process under dry and wet conditions. Under dry solvent

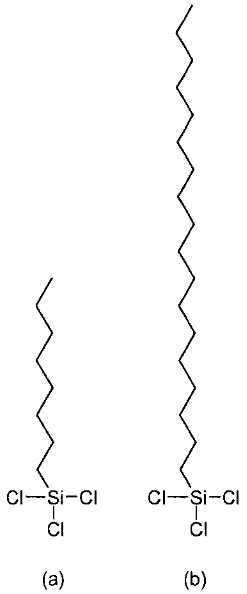

**Figure 5.11:** Chemical structures of (a) OTS-8 and (b) OTS-18.

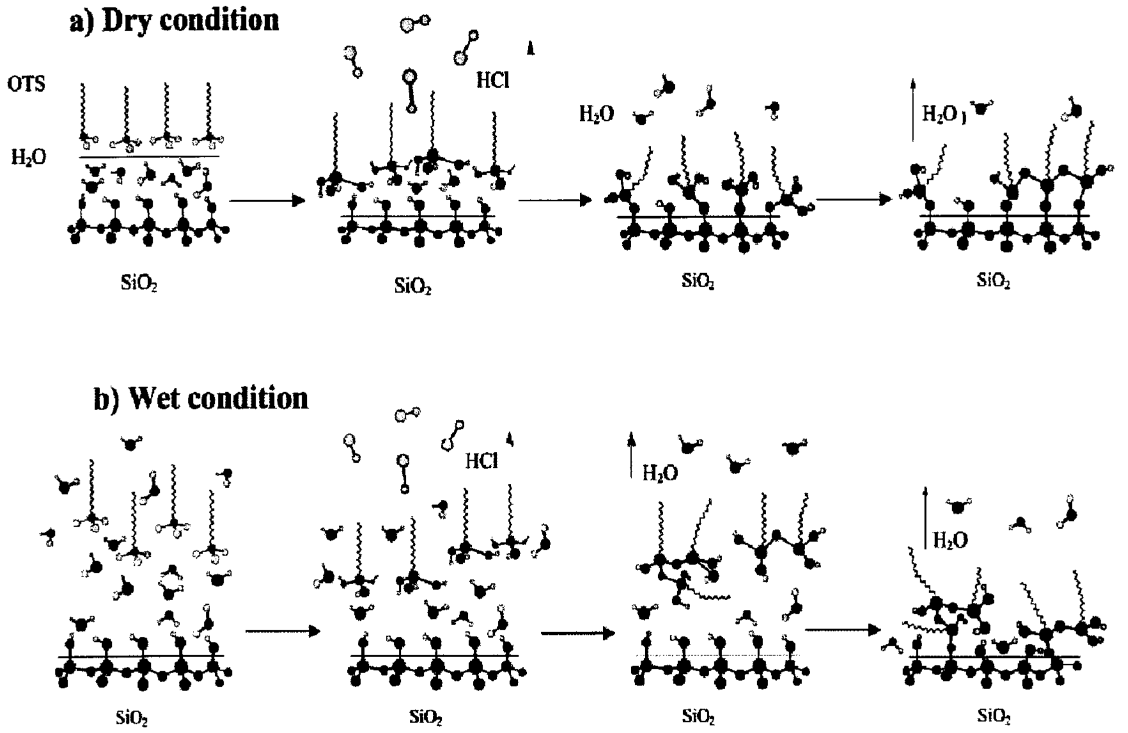

**Figure 5.12:** Proposed reaction mechanism of OTS-18 with an $SiO_2$ surface under (a) dry solvent conditions and (b) wet solvent conditions ($H_2O$ concentration > 50 mM). From Wang and Lieberman (reference 21).

conditions, there is a monolayer of water which is hydrogen bonded to the silanol terminated surface. The water molecules hydrolyze the OTS molecule to form a tri-silanol structure with hydrochloric acid produced as a byproduct. The central OTS silanol reacts with the surface silanol to form a siloxane bridge and OTS molecules cross-link to form a poly-siloxane bridge across the surface. Since the only water present in the solution is localized to the surface reaction site, the polymerization reaction is strictly under control.

Wasserman *et al* have shown an empirical relationship between the number of carbons in the alkyl chain and the film thickness, given by:

$$d = 1.26(n - 1) + 4.78, \tag{4}$$

where $d$ is measured in Å and $n$ is the number of carbons in the alkyl chain.[38] This equation is valid for hydrocarbon chains oriented perpendicular to the solid substrate and extended in their all-trans conformation. Using Equation 4, the thickness of an OTS-18 SAM is approximately 26 Å and for an OTS-8 SAM, approximately 13.5 Å. Experimental measurements of the thickness of the SAMs are in agreement with the values generated by Equation 4. Films deposited by Langmuir-Blodget techniques are oriented perpendicular to the surface with a tilt angle of about 10 ± 2° from the normal[58] or 15-17° on chemisorbed films.[59]

In contrast, when there is excess water present in the solution, the OTS molecules are hydrolyzed far away from the surface whereas, under dry conditions, the hydrolysis reaction occurs in very close proximity to the surface. When the hydrolysis reaction occurs far from the surface, the OTS molecules will cross link with themselves *before* bonding with the surface silanols and produce clusters of cross-linked OTS molecules. When these clusters bond to the surface, they will produce a very rough layer of OTS. Although the morphology of the wet and dry processes are very different, contact angle measurements cannot distinguish between these two films as it is a macroscopic property. However, AFM imagining can show the difference in film structures. Figure 5.13a shows an ultra smooth OTS-18 film while the cross-linked OTS-18 islands are clearly visible in Figure 5.13b.

Brzoska *et al* have shown that the quality of the OTS SAM is dependent on the temperature of formation.[53] Furthermore, they have demonstrated that there exists a critical temperature, $T_c$, below which densely packed, high quality SAMs are obtained with minimal

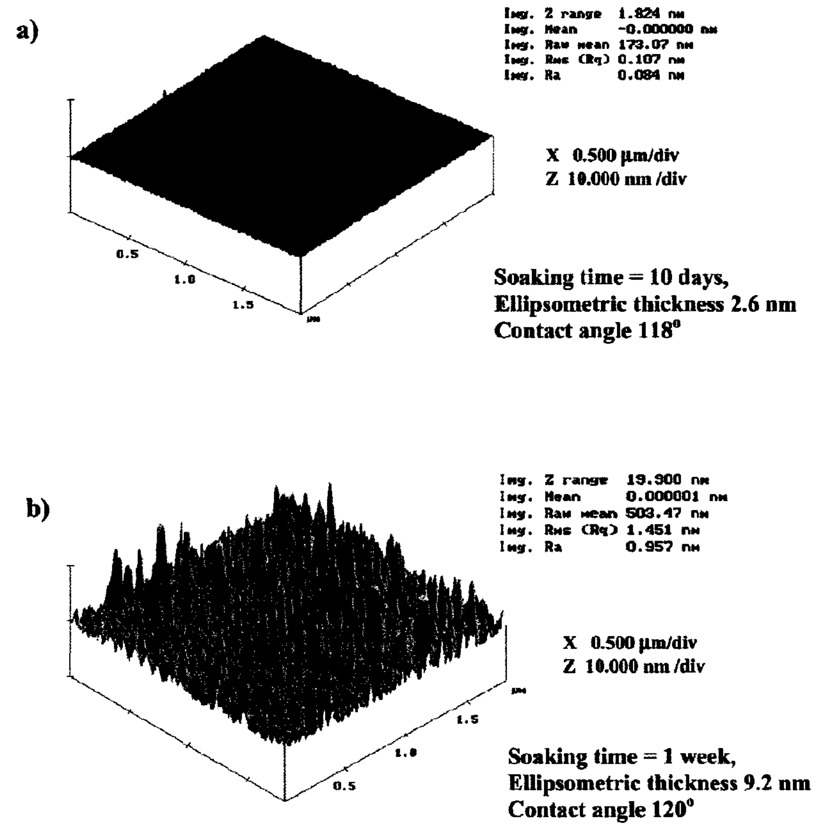

**Figure 5.13:** AFM images of (a) dry and (b) wet process OTS-18 SAMs. From Wang and Lieberman (reference 21).

hysteresis effects between the advancing and receding contact angles. This critical temperature is an intrinsic property of the tricholorosilane which is used. From reference 35, $T_c$ for OTS-18 is approximately 24 ± 2 °C and for OTS-8 it is extrapolated to be approximately -7 ± 1 °C. While the OTS-8 SAMs used in this thesis were deposited at room temperature, no significant hysteresis effects were observed. In addition, other groups have reported on OTS-8 SAM formation at elevated temperatures and did not observe any degradation in device performance.[60]

In the case of OTS-18, the SAMs were formed from the liquid phase. An $n =$ 5mM solution was made using a 4:1 volume ratio of Isopar-G and chloroform ($CHCl_3$). The density of OTS-18 was $\rho_{OTS\text{-}18} = 0.984$ g/mL and the molecular weight was $m_{OTS\text{-}18} = 387.93$ g/mol.[61] The volume of OTS-18 needed to make the 5mM solution, $V_{OTS\text{-}18}$, was calculated using:

$$V_{OTS-18} = \frac{n\rho_{OTS-18}}{m_{OTS-18}} V_{solvent}, \tag{5}$$

In addition to 4:1 Isopar-G/$CHCl_3$, hexane was also tried as a solvent, but the final SAMs displayed some variation across the same sample and from sample to sample, as can be seen by the noticeably larger error bars in Figure 5.14. The progression of the shape of the water droplets on OTS-18 treated samples as a function of time is shown in Figure 5.15. The curves in Figure 5.14a show the contact angle as a function of soak time for a 2 mM solution in hexane (open points) and 4:1 Isopar-G/ $CHCl_3$ (solid points) solutions. The solutions using hexane show an overall larger contact angle for a given soak time. The Isopar-G/$CHCl_3$ samples showed an initial sharp increase in the contact angle, but then decreased dramatically, giving less than 100° as a maximum contact angle, even after 144 hours whereas hexane showed a

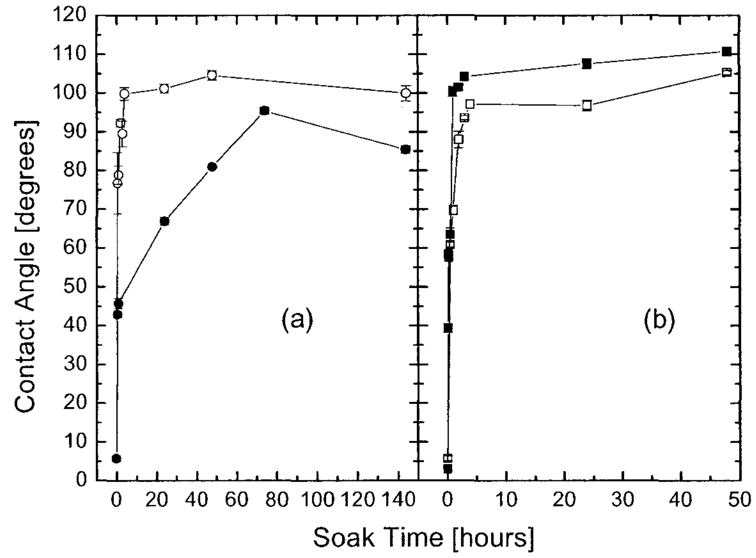

**Figure 5.14:** Advancing contact angle of water on OTS-18 SAMs from an (a) 2 mM and (b) 5 mM solutions. SAMs formed from hexane are shown as open data points while those formed from 4:1 Isopar-G/CHCl$_3$ are shown as solid data points.

maximum of almost 105° after only 48 hours. Figure 5.14b shows the same data, but using a 5 mM solution. In this case, the samples formed from the Isopar-G/CHCl$_3$ solutions displayed higher contact angles and more consistency between measurements, producing a contact angle exceeding 110° after only 48 hours. However, the samples soaked in the hexane solution had a contact angle of 105° after 48 hours, as in the 2 mM samples. This is a strong indication that the polar nature of CHCl$_3$ plays a role in the formation of high quality SAMs of OTS-18 as both hexane and Isopar-G are non-polar hydrocarbon solvents. All of the OTS-18 modified samples discussed hereafter were soaked for 24 hours in a 5 mM 4:1 Isopar-G/CHCl$_3$ solution.

Using the OTS-18 SAM parameters, films of OTS-8 were also formed on SiO$_2$. 5 mM solutions were prepared in 4:1 Isopar-G/CHCl$_3$. The material parameters were $\rho_{OTS\text{-}8} = 1.075$ g/mL and $m_{OTS\text{-}8} = 247.67$ g/mol.[61] Based on the experimental data from OTS-18 in hexane,

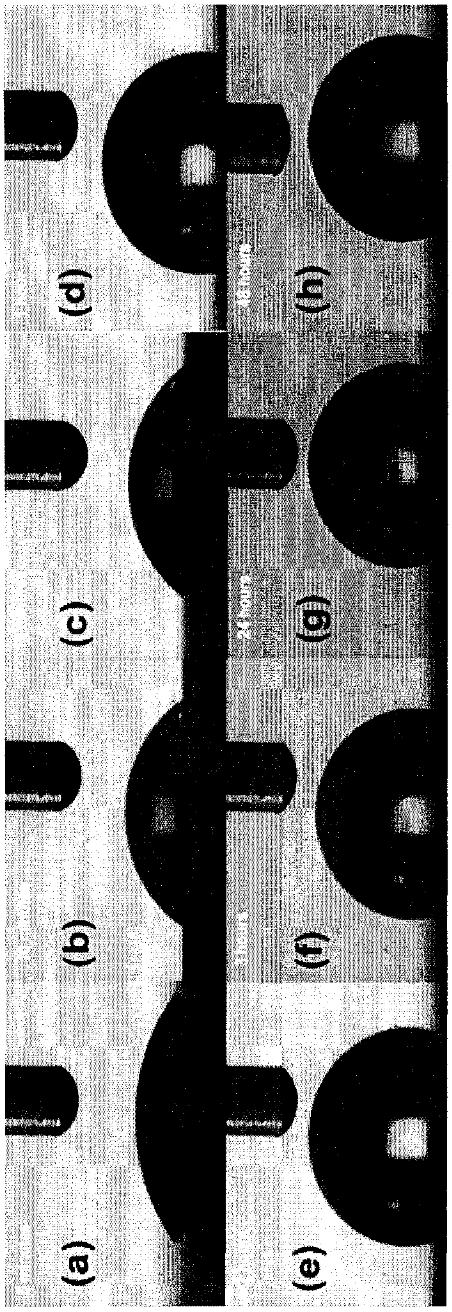

**Figure 5.15:** Images from the contact angle goniometer showing the evolution of the advancing contact angle of a water droplet on an $SiO_2$ surface soaked in a 5 mM OTS-18 solution for (a) 5 minutes, (b) 10 minutes, (c) 15 minutes, (d) 1 hour, (e) 2 hours, (f) 3 hours, (g) 24 hours, and (h) 48 hours.

only the 4:1 Isopar-G/$CHCl_3$ solvent was used to form the OTS-8 SAMs. The advancing contact angle as a function of soak time curve is shown in Figure 5.16. This curve displays the expected shape reaching a quasi-plateau after about 8 hours in solution with contact angles

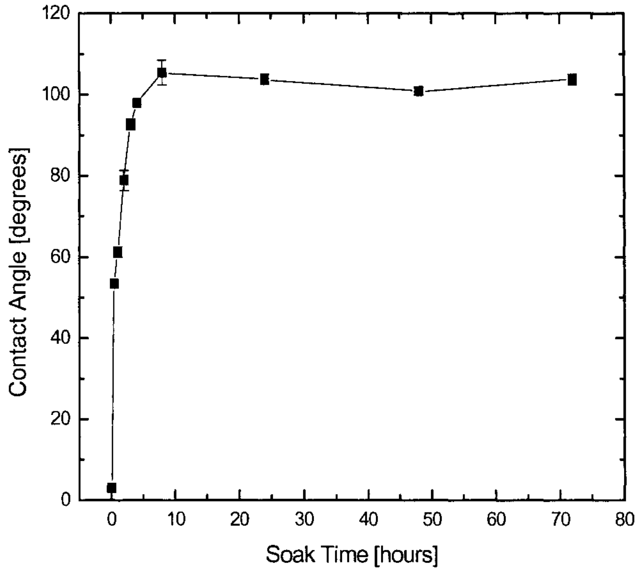

**Figure 5.16:** Advancing water contact angle as a function of soak time in a 5 mM OTS-8 solution in 4:1 Isopar-G/$CHCl_3$.

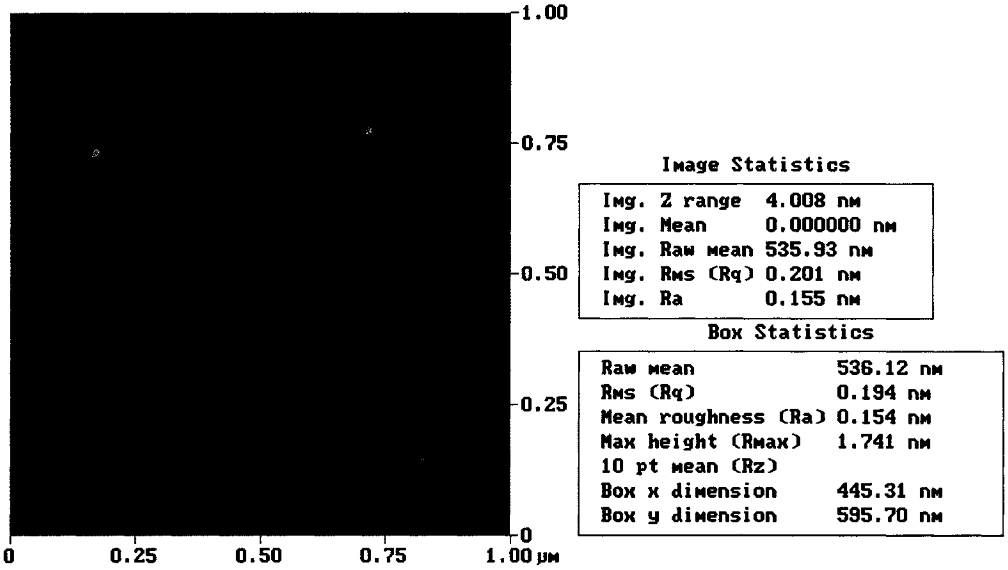

```
Image Statistics
Img. Z range    4.008 nm
Img. Mean       0.000000 nm
Img. Raw mean   535.93 nm
Img. Rms (Rq)   0.201 nm
Img. Ra         0.155 nm
Box Statistics
Raw mean                 536.12 nm
Rms (Rq)                 0.194 nm
Mean roughness (Ra)      0.154 nm
Max height (Rmax)        1.741 nm
10 pt mean (Rz)
Box x dimension          445.31 nm
Box y dimension          595.70 nm
```

**Figure 5.17:** AFM of an OTS-8 SAM on $SiO_2$ soaked for 24 hours in a 5 mM solution of 4:1 Isopar-G/$CHCl_3$. The RMS roughness was 2.01 Å.

between 100° and 105°. For all subsequent samples, a 24 soak in 5 mM OTS-8 in 4:1 Isopar-G/$CHCl_3$ has been used.

AFM imaging of OTS-18 and OTS-8 samples indicated that the surface topologies are flat. A typical AFM is depicted in Figure 5.17 for a 5 mM OTS-8 SAM on an $SiO_2$ surface. The RMS roughness of the entire $1 \mu m^2$ area was 2.01 Å with a local RMS roughness of less than 1.94 Å. These RMS values were lower than those of the HMDS films, and even smoother than the bare $SiO_2$ surfaces, indicating that the dielectric-organic interface should be as smooth as possible.

## 5.7 References

[1] R. Maoz and J. Sagiv, J. Colloid Interface Sci. **100,** 465 (1984).

[2] W. C. Bigelow, D. L. Pickett, and W. A. Zisman, J. Colloid Interface Sci. **1,** 513 (1946).

[3] J. Sagiv, J. Am. Chem. Soc. **102,** 92 (1980).

[4] B. K. Crone, A. Dodabalapur, R. Sarpeshkar, R. W. Filas, Y.-Y. Lin, Z. Bao, J. H. O'Neil, W. Li, and H. E. Katz, J. Appl. Phys. **89,** 5125 (2001).

[5] T. Kawase, H. Sirringhaus, R. H. Friend, and T. Shimoda, Adv. Mater. **13,** 1601 (2001).

[6] C. D. Dimitrakopoulous, S. Purushothaman, J. Kymissis, A. Callegari, and J. M. Shaw, Science **283,** 822 (1999).

[7] J. Xue and S. R. Forrest, Appl. Phys. Lett. **79,** 3714 (2001).

[8] K. S. Narayan and N. Kumar, Appl. Phys. Lett. **79,** 1891 (2001).

[9] D. Knipp, R. A. Street, B. Krusor, R. Apte, and J. Ho, J. Non-Cryst. Solids Part B **299,** 1042 (2002).

[10] D. Knipp, R. A. Street, A. Vökel, and J. Ho, J. Appl. Phys. **93,** 347 (2003).

[11] D. Knipp, R. A. Street, and A. R. Vökel, Appl. Phys. Lett. **82,** 3907 (2003).

[12] Y. Iino, Y. Inoue, Y. Fujisaki, H. Fujikake, H. Sato, M. Kawakita, S. Tokito, and H. Kikuchi, Jap. J. Appl. Phys.Part 1 **42,** 299 (2003).

[13] F. Eder, H. Klauk, M. Halik, U. Zschieschang, G. Schmid, and C. Dehm, Appl. Phys. Lett. **84,** 2673 (2004).

[14] J. Lee, J. H. Kim, and S. Im, J. Appl. Phys. **95,** 3733 (2004).

[15] A. Salleo, M. L. Chabinyc, M. S. Yang, and R. A. Street, Appl. Phys. Lett. **81,** 4383 (2002).

[16] Y.-Y. Lin, D. J. Gundlach, S. F. Nelson, and T. N. Jackson, IEEE Trans. Electron Dev. **44,** 1325 (1997).

[17] A. Salleo and R. A. Street, J. Appl. Phys. **94,** 471 (2003).

[18] M. Halik, H. Klauk, U. Zschieschang, G. Schmid, S. Ponomarenko, S. Kirchmeyer, and W. Weber, Adv. Mater. **15,** 917 (2003).

[19] C. Boulas, J. V. Davidovits, F. Rondelez, and D. Vuillaume, Phys. Rev. Lett. **76,** 4797 (1996).

[20] M. Kiguchi, M. Nakayama, K. Fujiwara, K. Ueno, T. Shimada, and K. Saiki, Jpn. J. Appl. Phys. Part 2 **42,** L1408 (2003).

[21] Y. Wang and M. Lieberman, Langmuir **19,** 1159 (2003).

[22] W. Shockley, W. W. Hooper, H. J. Queisser, and W. Schroen, Surface Sci. **2,** 227 (1964).

[23] Y. Awakuni and J. H. Calderwood, J. Phys. D (Appl. Phys.) **5,** 1038 (1972).

[24] R. Castagne, P. Hesto, and A. Vapaille, Thin Solid Films **17,** 253 (1973).

[25] G. J. Young, J. Colloid. Sci. **13,** 67 (1958).

[26] J. A. Voorthuyzen, K. Keskin, and P. Bergveld, Surface Sci. **187,** 201 (1987).

[27] A. D. Martin and K. J. McLean, J. Appl. Phys. **48,** 2950 (1977).

[28] A. V. Kiselev and V. I. Lygin, *Infrared Spectra of Surface Compounds* (John Wiley & Sons, New York, 1975).

[29] T. I. Suratwala, M. L. Hanna, E. L. Miller, P. K. Whitman, I. M. Thomas, P. R. Ehrmann, R. S. Maxwell, and A. K. Burnham, J. Non-Cryst. Solids **316,** 349 (2003).

[30] L. Bousse, N. F. de Rooij, and P. Bergveld, IEEE Trans. Electron Dev. **ED-30,** 1263 (1983).

[31] A. van den Berg, P. Bergveld, D. N. Reinhoudt, and E. R. Sudholter, Sensors and Actuators **8,** 129 (1985).

[32] M. C. B. A. Michielsen, V. B. Marriott, J. J. Ponjeé, H. van der Wel, F. J. Touwslager, and J. A. H. M. Moonen, Microelectronic Engineering **11,** 475 (1990).

[33] J. J. Ponjeé, V. B. Marriott, M. C. B. A. Michielsen, F. J. Touwslager, P. N. T. van Velzen, and H. van der Wel, J. Vac. Sci. Technol. B **8,** 463 (1990).

[34] H. Yanazawa, Colloids Surf. **9,** 133 (1984).

[35] J. Gum and J. Sagiv, J. Colloid Interface Sci. **112,** 457 (1986).

[36] J. D. Le Grange, J. L. Markham, and C. R. Kurjian, Langmuir **9,** 1749 (1993).

[37] P. Silberzan, L. Léger, D. Ausserré, and J. J. Benattar, Langmuir **7,** 1647 (1991).

[38] S. R. Wasserman, Y.-T. Tao, and J. M. Whitesides, Langmuir **5,** 1074 (1989).

[39] N. Tillman, A. Ulman, J. S. Schildkraut, and T. L. Penner, J. Am. Chem. Soc. **110,** 6136 (1988).

[40] J. Gum, R. Iscovici, and J. Sagiv, J. Colloid Interface Sci. **101,** 201 (1984).

[41] K. Mathauser and C. W. Frank, Langmuir **9,** 3446 (1993).

[42] K. Mathauser and C. W. Frank, Langmuir **9,** 3002 (1993).

[43] S. Brandriss and S. Margel, Langmuir **9,** 1232 (1993).

[44] D. K. Schwartz, S. Steinberg, J. Israelachvili, and J. A. N. Zasadzinski, Science **69,** 3554 (1992).

[45] G. Carson and S. Granick, J. Appl. Polym. Sci. **37,** 2767 (1989).

[46] C. R. Kessel and S. Granick, Langmuir **7,** 532 (1991).

[47] I. Rubinstein, E. Sabatani, R. Maoz, and J. Sagiv, Electroanal. Chem. **219,** 365 (1987).

[48] I. Rubinstein, E. Sabatani, R. Maoz, and J. Sagiv, Proc. Electrochem. Soc. **86,** 175 (1986).

[49] H. O. Finklea, L. R. Robinson, A. Blackburn, B. Richter, D. L. Allara, and T. Bright, Langmuir **2,** 239 (1986).

[50] K. Biebaum, M. Grunze, A. A. Baski, L. F. Chi, W. Schrepp, and H. Fuchs, Langmuir **10,** 4367 (1995).

[51] L. Netzer, R. Iscovici, and J. Sagiv, Thin Solid Films **100,** 67 (1983).

[52] A. G. Lambert, D. J. Neivandt, R. A. McAloney, and R. B. Davies, Langmuir **16,** 8377 (2000).

[53] J. B. Brzoska, I. B. Azouz, and F. Rondelez, Langmuir **10,** 4367 (1994).

[54] N. Tillman, A. Ulman, and T. L. Penner, Langmuir **5,** 101 (1989).

[55] C. P. Tripp and M. L. Hair, Langmuir **8,** 1120 (1992).

[56] D. L. Angst and G. W. Simmons, Langmuir **7,** 2236 (1991).

[57] T. Vallant, H. Brummer, U. Mayer, H. Hoffmann, T. Leitner, R. Resch, and G. Friedbacher, J. Phys. Chem. B. **102,** 7190 (1998).

[58] D. L. Allara, A. N. Parikh, and F. Rondelez, Langmuir **11,** 2357 (1995).

[59] A. Takahara, K. Kojio, and T. Kajiyama, Ultramicroscopy **91,** 203 (2002).

[60] B. Ong, private communication (2003).

[61] *Aldrich Handbook of Fine Chemicals and Laboratory Equipment* (Sigma-Aldrich Fine Chemicals, 2003-2004).

# Chapter 6
# Experimental Techniques

## 6.1 General Information

Silicon substrates were purchased from MEMC Electronic Materials Inc. and SQI Inc. Soda lime glass substrates that were pre-coated with indium tin oxide (ITO) were bought from Thin Film Devices Inc. and Colorado Concept Coating Inc. Solvents, acids and bases were supplied by Honeywell, ARCH Chemicals Inc., Air Products Electronic Chemicals, EM Science, Fisher Scientific, and Exxon-Mobil Chemicals. All solvents, acids and bases were pre-filtered through 0.2 μm filters and were semiconductor grade with the exception of Isopar-G, chloroform (HPLC grade), and hexanes (reagent grade) which was a mixture of n-hexane, 2-methylpentane, 3-methylpentane and melthycyclopentane. The photoresists and developers were supplied by Shipley Company L.L.C and Microchem. Hexamethyldisilazane (HMDS) was purchased from Ashland Chemical (semiconductor grade) and the trichlorosilanes were purchased from Aldrich.

All of the processing was performed in a class 1000 clean room. All of the wet chemistry was carried out in laminar flow benches that were rated at less than class 100. The actual particle count readings were below the limit of the detector (10 particles over 1 μm in diameter per cubic foot of air).

## 6.2 Material Purification

The semiconducting organic materials were purified at least once in a custom made

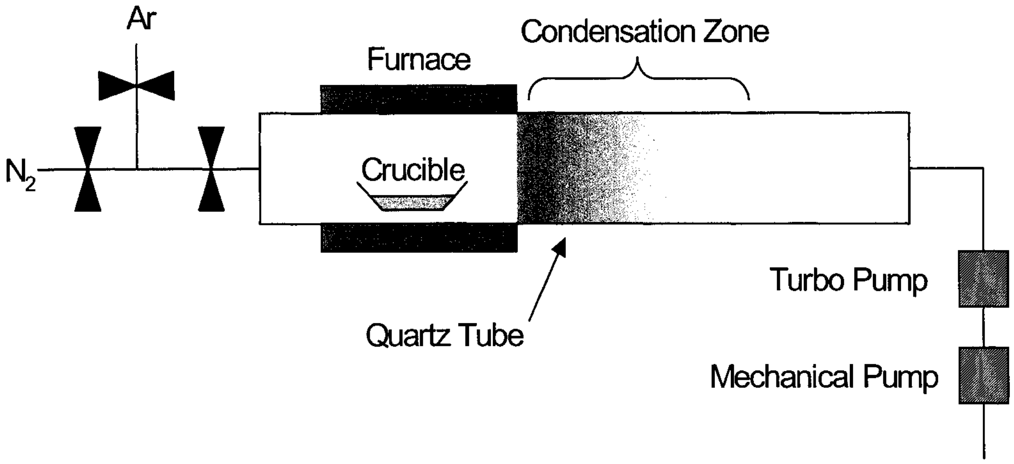

**Figure 6.1:** Vapour train sublimation apparatus. A purge gas is injected from the end opposite the vacuum pumps to aid in the separation of the organic vapours. When the vapours exit the section of the glass tube inside the furnace, there is a temperature gradient and the vapours condense according to their molecular weight. The inner tube is not shown for the sake of clarity.

vapour train sublimation apparatus (see Figure 6.1) before devices were made.

The vapour train sublimation system consisted of a 1 meter long quartz tube with vacuum mounting flanges on each end. Another quartz tube of slightly shorter length and smaller diameter was cut into 7cm segments and placed inside the outer tube to facilitate the recovery of the purified material and cleaning of the glassware. The inner tube and glass crucible were first cleaned with acetone and isopropyl alcohol. The glassware was placed in a large oven and baked at approximately 550°C to remove any residual organic materials. The glassware was subsequently rinsed with acetone and isopropyl alcohol and blown dry with $N_2$ gas to remove any carbon residue. The material to be purified was placed in the crucible and the glassware was loaded into the outer tube.

A base pressure between $10^{-6}$ and $10^{-7}$ torr was achieved by using a mechanical pump and a turbo molecular pump. The furnace was controlled using an Omega temperature control unit equipped with a K-type thermocouple. The furnace was set to 100°C for about an hour to allow the organic material to outgas and to remove very light impurities. As the temperature of the furnace was slowly increased, ultra pure argon was bled into the quartz tube from the end opposite the pumps until the pressure was between 30 and 50 mTorr. When the material was heated a few degrees above its sublimation temperature, impurities with a lower sublimation temperature were vapourized and removed from the system by the argon gas flow. The desired material was sublimed and condensed in the tube just outside of the furnace due to a sudden drop in temperature. The impurities with a higher sublimation temperature remained in the quartz crucible inside the furnace. When the sublimation was finished, the furnace was shut off and allowed to cool to room temperature. The purge gas was turned off and the system was vented. The inner quartz tube segments were removed and small spatulas were used to recover the purified organic material from the inside of the tubes. The organic materials were typically passed through the purification system at least twice before they were used in any devices.

## 6.3 Organic Field Effect Transistor Fabrication

### 6.3.1 Substrate Preparation

Boron doped *p*-type (100) Si wafers with a resistivity less than 20 Ωcm and either a 600 nm or a 300 nm layer of thermal $SiO_2$ were used for all the OFET and XRD samples.

Due to the thermal $SiO_2$ growth process, both sides of the Si wafer were covered in $SiO_2$. Since electrical contact to the substrate was made via the backside, the thermal oxide must be removed from the unpolished side of the chip in order to minimize the voltage drop across the gate. Recipe B.1 was used to remove the oxide from the back surface (see Appendix B for the recipe details).

The samples were then cleaned using an industry standard cleaning process to remove contaminants from Si surfaces. The cleaning involved a two step process: one removes any organic contaminants and the second removes any heavy metallic and ionic impurities. The organic cleaning solution consisted of a 100:2:2 mixture of $H_2O$:$H_2O_2$:$NH_4OH$ at 80°C. The ionic cleaning solution consisted of a 100:2:2 mixture of $H_2O$:$H_2O_2$:HCl at 80°C. This process is more commonly referred to as RCA cleaning, and is outlined in Recipe B.2.

When the samples were removed from the cascade, they were dried under a strong $N_2$ flow. The substrates were then placed in a Plasma-Preen II-862 oxygen plasma descum unit for 3 minutes to remove any residual organic materials which may not have been removed during wet cleaning and stored in DI water until needed.

### 6.3.2 Device Fabrication

A heavily doped *p*-type silicon substrate with a dense thermal $SiO_2$ layer was used as the gate and gate dielectric, respectively. The silicon substrate formed the gate electrode and the thermal oxide acted as the gate dielectric. Figure 6.2 shows a cross-sectional view of the top contact device structure. The top electrodes were gold, a high

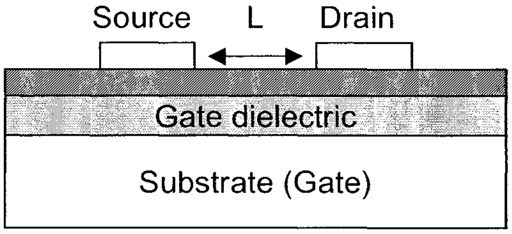

**Figure 6.2:** Top contact OFET geometry. The substrate was heavily doped *p*-type Si, the gate dielectric was thermal $SiO_2$, the source and drain were thermally evaporated gold, and the dashed area represents the organic semiconductor. L denotes the channel length.

work function metal. The organic material around the perimeter of the active area was mechanically removed to minimize leakage currents.

Two basic types of bottom contact devices were made; interdigitated and linear electrodes, shown in Figure 6.3 and Figure 6.4. By using interdigitated electrodes, the effective channel width to length ratio was increased to 200:1, 800:1 and 1400:1. A thin wetting layer of titanium was used to promote the adhesion of gold onto $SiO_2$. Before testing the devices, the organic material around the gate contact pad and the perimeter of the active area was removed with the probing station tips to reduce leakage currents.

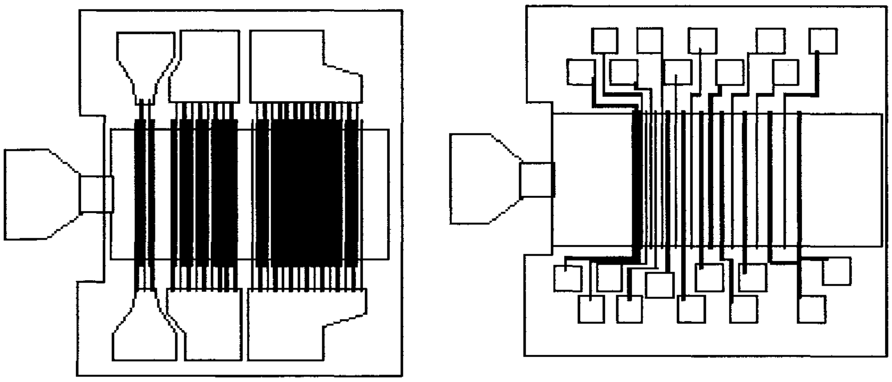

**Figure 6.3:** Top view of the various electrode configurations used in the bottom contact transistor design. The device on the left has interdigitated electrodes with effective width to length ratio of 200:1, 800:1 and 1400:1. The device on the right has width to length ratios between 10:1and 200:1.

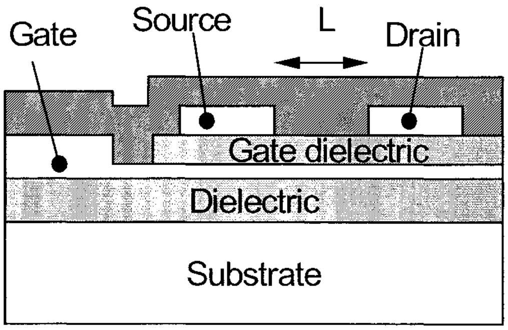

**Figure 6.4:** Cross sectional view of the bottom contact device. The dashed portion represents the organic semiconductor.

An Edwards Auto 306 Coater was used for evaporating organic materials and metals. The base pressure of the system was typically 1-2x$10^{-7}$ torr. During the sublimation of the organic materials the pressure increased to approximately 4-5x$10^{-7}$ torr. The samples were mounted on an anodized aluminum stage using metal clips. The stage was equipped with a ceramic mounting mechanism which provided good thermal isolation of the aluminum portion of the stage and the rest of the chamber. A schematic drawing of the chamber is shown in Figure 6.5.

The substrate heating system consisted of four 20 watt halogen light bulbs mounted between the rear of the stage and a reflector. The power sent to the light bulbs was modulated by an Omega CAL 9900 temperature controller. Two thermocouples were used to calibrate the system; one was mounted in a hole drilled into the side of the stage while the other was mounted on the outside of the reflector housing. The temperature of the stage was monitored at various reflector housing temperatures as a function of time. It was found that after about two hours, the stage was within 5 °C of the reflector housing. Therefore, the temperature that was monitored

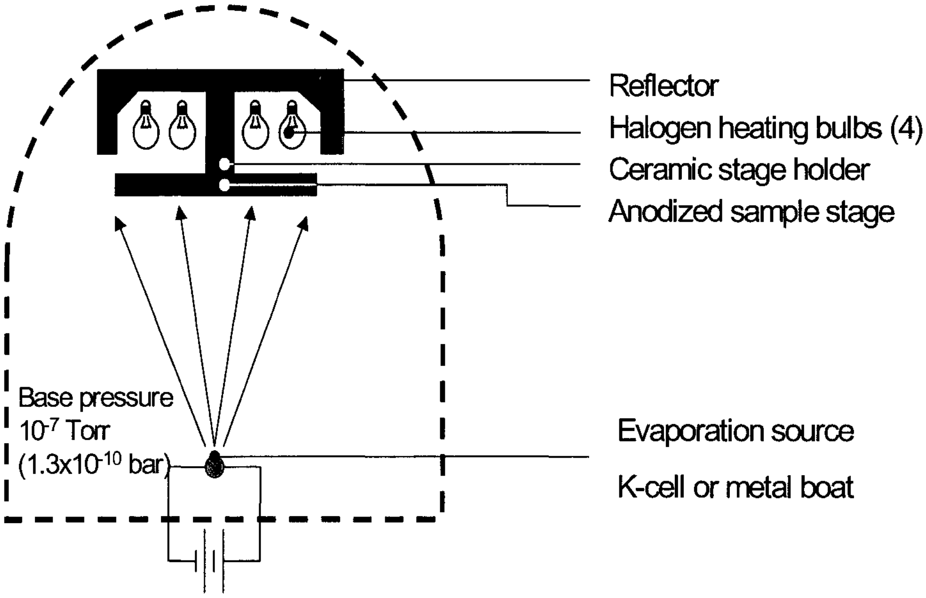

**Figure 6.5:** Diagram of the Edwards Auto 306 Coater deposition chamber.

was that of the reflector housing, not the stage. This allowed the stage to be rotated while organic materials were being deposited to provide a more uniform film across the samples. The calibration curve between the reflector and stage temperatures is shown in Figure 6.6. A water-cooled quartz crystal film thickness monitor was mounted as close to the stage as possible to give an accurate estimate of the actual thickness of the evaporated film.

The organic materials were placed in PBN crucibles and inserted into a Kurt J. Lesker Knudsen cell mounted slightly off-center at the base of the chamber. The Knudsen cell was controlled by a Kurt J. Lesker LTE Power Controller operating in manual mode with a resolution of 0.1°C. The typical deposition rates were between 0.1 Å/s and 0.3 Å/s and organic film thicknesses were 300 Å using a density of 1.2 g/cm$^3$ and an acoustic impedance of 6.0 x

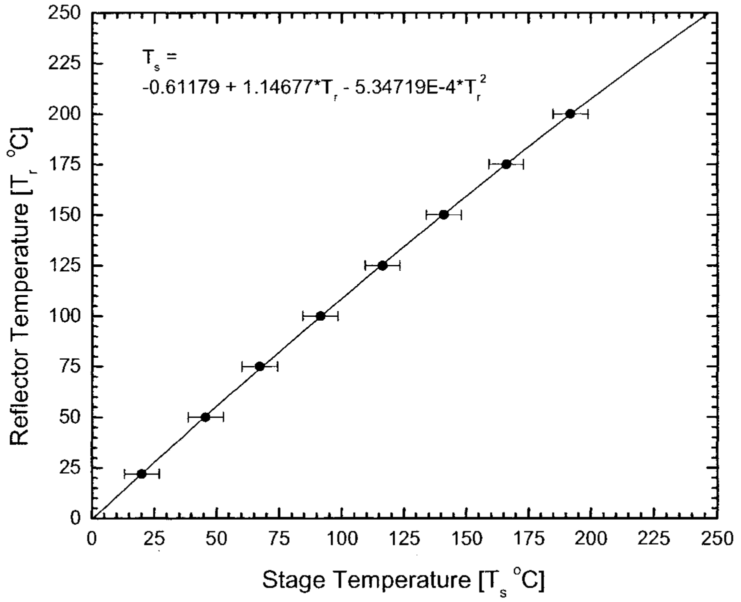

**Figure 6.6:** Temperature calibration of the measured reflector temperature and the sample stage temperature.

$10^5$ cm$^2$ g$^{-1}$ sec$^{-1}$ .

The source and drain in the top contact OFETs were defined by using TEM grids as shadow masks (purchased from SPI and Ernest Fullum Inc.) Depending on which grid was used, channel width to length ratios were between 4:1 and 58:1. The samples were mounted on the sample stage with clips and the TEM grids were placed on the surface and held in place with clips. The stage was loaded into the Edwards Auto 306 Coater with a few gold shots in a molybdenum boat. The top gold contact pads were deposited at a rate between 4 and 7 Å/sec and were approximately 700 - 1000 Å thick.

Bottom contact OFETs used standard photolithographic techniques to pattern the desired features. The photoresists were exposed using a Karl Suss MJB 3 mask aligner with a lateral resolution of ± 0.1 μm on the alignment stage. The samples were exposed to UV light from a mercury short arc lamp with a power density of 12.5 mW/cm$^2$. The photomask which was used to pattern the samples was designed as part of this work and manufactured by ADTEK Photomask. The mask consisted of a soda lime glass substrate with a chromium film which was patterned according to the specified design. The portion of the photoresist that was exposed to UV light was chemically changed so that it could be readily removed by the developer. Figure 6.7 shows a generic overview of the liftoff and etching process.

A bi-layer photoresist process was used to ensure that the sidewalls of the electrodes would be vertical and that delamination would not occur as it does with a single layer lift-off. The process is outlined in Recipe B.3. LOR-5a is a PMGI-based photoresist that does not require UV exposure and is etched by the developer. A Ti/Au/Ti stack (50Å/1000Å/50Å, respectively) was deposited by e-beam evaporation. The samples were then placed in a hot n-methyl pyrrolidinone (NMP) bath to remove the photoresist and leave the patterned metal on the surface. A summary of the process and resulting features is shown in Figure 6.8. The reasons and merit of this process is discussed in detail in the Appendix.

After the gate electrode was patterned, a dense conformal $SiO_2$ layer was deposited using a Plasma-Therm model 790 plasma-enhanced chemical vapour deposition (PECVD) system. Silane ($SiH_4$), nitrogen and nitrous oxide ($N_2O$) gasses were used in the growth of the $SiO_2$

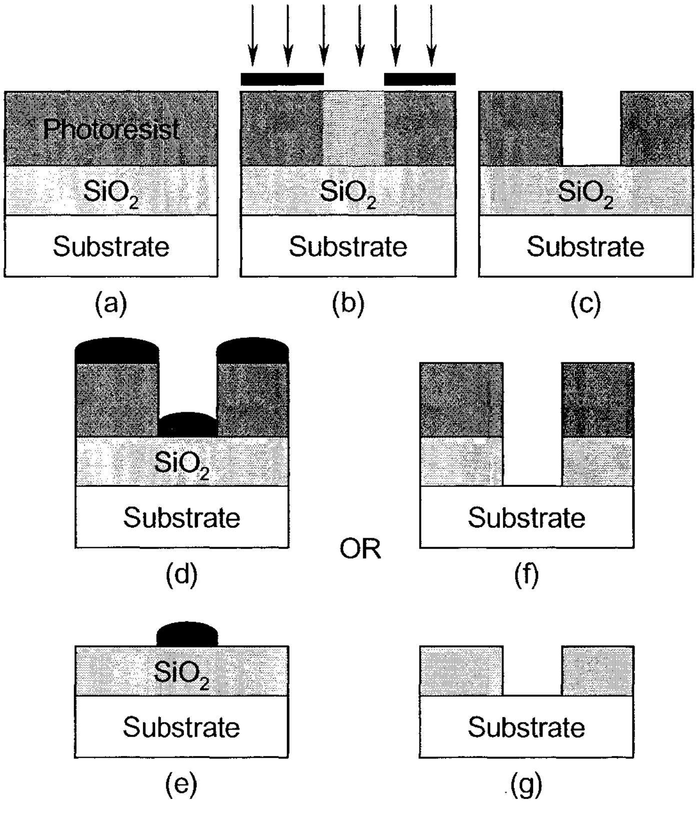

**Figure 6.7:** Basic steps involved in photolithography. (a) spinning the photoresist, (b) patterning and exposing the photoresist and, (c) developing. (d) and (e) show the steps involved in metallization while (f) and (g) show the steps involved in etching.

layer. The substrates were held at approximately 400°C and the growth rate was about 2.5 nm/min with a total film thickness of about 2000Å. The resulting samples were patterned using the process outlined in Recipe B.4.

Upon completion, $SiO_2$ remained only over a portion of the gate electrode. Recipe B.3 was followed again with a different photomask to define the source and drain electrodes comprised of a 50Å Ti/1000Å Au stack. The completed samples were stored in a $N_2$ dry box until needed.

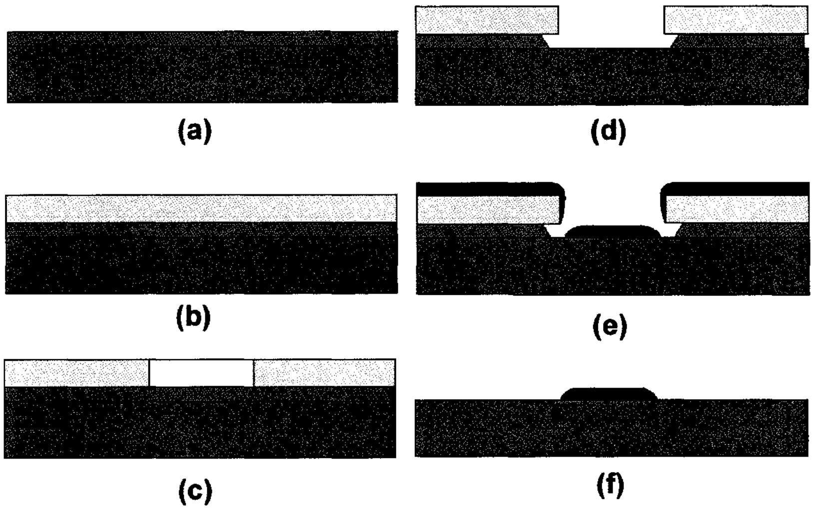

**Figure 6.8:** Bi-layer photoresist process: coat (a) LOR-5a and (b) s1813 photoresist, (c) expose s1813, (d) develop resist to create undercut, (e) deposit metal, and (f) lift-off.

### 6.3.3 Surface Modification

The $SiO_2$ surface preparation was common to all three schemes. It was critical that the $SiO_2$ surface be completely clean and free from water, oil and other contaminants. Thus all glassware and tweezers were thoroughly cleaned, degreased and dried prior to use. Teflon tweezers were used to handle the samples and were cleaned in chloroform, hexane, acetone and isopropyl alcohol. After the samples had been cleaned as outlined above, two different methods, dry and wet, were used to prepare the surface for the self assembled monolayer deposition. The principle behind both process was the same: to prepare a fresh, hydroxyl-terminated, hydrophilic $SiO_2$ surface. In the dry process, the samples were placed in a UVP Inc. PR-100 UV-Ozone photoreactor for 1 hour. The wet process consisted of soaking the samples in a piranha acid solution (4:1 $H_2SO_4$:30% $H_2O_2$) for 1 hour and then rinsing with copious amounts of DI water. Both of these techniques eliminated all organic residue on the sample and form a freshly oxidized layer on the surface.

*Hexamethydisilazane (HMDS)*

HMDS was deposited onto the samples from the vapour phase using two different experimental configurations; a custom-built vapour priming oven and a commercially available priming system. The chemical structure of HMDS is shown in Figure 6.9a. A diagram of the HMDS priming system is depicted in Figure 6.10. While two different apparatuses were used, the operating principles were identical and involved three main steps; dehydration, priming, and flushing. The samples were placed into the vacuum oven and the system was

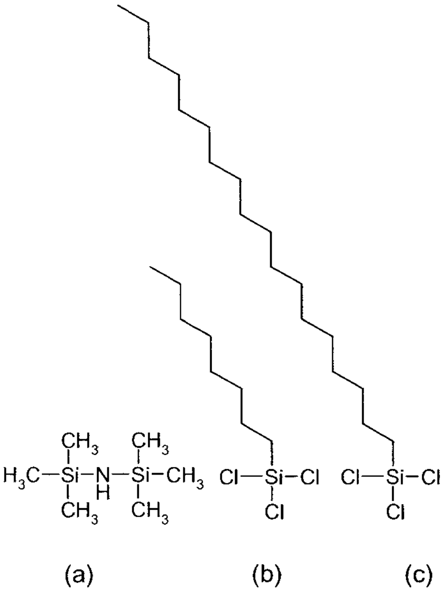

**Figure 6.9:** Chemical structures of (a) HMDS, (b) OTS-8 and (c) OTS-18.

pumped to a base pressure between 550 mTorr and 1000 mTorr at temperatures between 135°C and 150°C (valves B and D closed, A and C open). The system was pumped for 2 minutes and then backfilled with dry $N_2$ three times (closing valve C and opening valve D). This process was used to dehydrate the samples and to remove any moisture that may be on the surface. The samples were then baked in an ambient $N_2$ atmosphere for 5 minutes and again for another 5 minutes between 550 mTorr and 1000 mTorr. Valve A was then closed and valve B was opened along with valve C to allow HMDS vapours to enter the vacuum oven. Since the vapour pressure of HMDS was approximately 6 Torr, the vapours were drawn into the chamber due to the pressure differential. When the specified time for vapour priming had been reached, valve B was closed and valve A was opened. The baking and purging cycle was repeated four times to remove residual HMDS and ammonia gas from the vacuum oven. The samples were removed from the oven, rinsed in DI water, dried with $N_2$, and stored until needed in a dry nitrogen storage box.

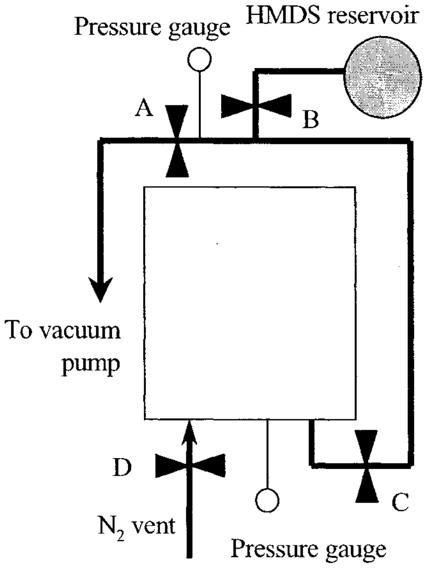

**Figure 6.10:** Diagram of the HMDS vapour priming system.

*Trichlorosilanes*

Two different trichlorosilanes were used to modify the $SiO_2$ surfaces: *n*-octyltrichlorosilane (OTS-8, Figure 6.9b) and *n*-octadecyltrichlorosilane (OTS-18, Figure 6.9c).

Unless specified, the generic term OTS shall be used to refer to both OTS-8 and OTS-18 since the properties are virtually identical. OTS monolayers were deposited onto the $SiO_2$ surfaces from the liquid phase. A 4:1 mixture of Isopar-G and chloroform was used to make solutions with concentrations ranging from 0.5mM to 40mM. The Isopar series of solvents are synthetic hydrocarbon fluids made by the oligomerization of $C_3$ to $C_5$ hydrocarbons derived from crude oil fractionation and cracking operations. Isopar-G, in particular, is a solution of $C_{10}$ and $C_{11}$ isoparaffins. They also possess other desirable properties such as high purity, low odor, low toxicity, low surface tension and a high compatibility with plastics. Solvents were first mixed and then passed through a column of activated alumina under an argon flow to reduce the water content of the solvents. The recovered solvents were immediately placed inside a glove box which had a nitrogen over pressure and a relative humidity level below the measurable range of the analog hydrometer inside (less than 1% relative humidity).

OTS was added to the solvents using a Clonepette dispenser and then agitated. The samples were placed into plastic cups and the OTS solution was added. The soaking time ranged between 5 minutes and 2 weeks. After soaking, the samples were rinsed with copious amounts of chloroform and placed in a clean container with fresh chloroform and placed in an ultrasonic cleaner for 2-5 minutes. Once more, the samples were rinsed with chloroform and dried with nitrogen, rinsed for another 2-5 minutes in DI water in an ultrasonic cleaner, dried with nitrogen, and placed into a dry nitrogen storage box for at least 24 hours prior to use.

## 6.4 Organic Light Emitting Diode Fabrication

### 6.4.1 Substrate Patterning

ITO on glass substrates were cleaned using detergent, acetone, isopropyl alcohol and finally rinsed with copious amounts of DI water. The ITO anodes were patterned according to Recipe B.5. After the anode was defined, a photoresist spacer layer was patterned using Recipe B.6. This was used to define the size of the segments (approximately 1x5 mm$^2$) in the OLED. When completed, the substrates were ready for the deposition of the organic materials. Figure 6.11 shows the cross sectional and top view of the patterned substrate.

The photoresist spacer layer serves several functions. It acts as a dielectric buffer between the anode and the cathode, eliminating short circuits within the device. It also acts as an integrated shadow mask, allowing the organic materials to only come into direct contact with the ITO in the selected regions. The cathode makes contact to the two designated electrodes patterned in the ITO shown in the top right and bottom left of Figure 6.11a, denoted with a "-"

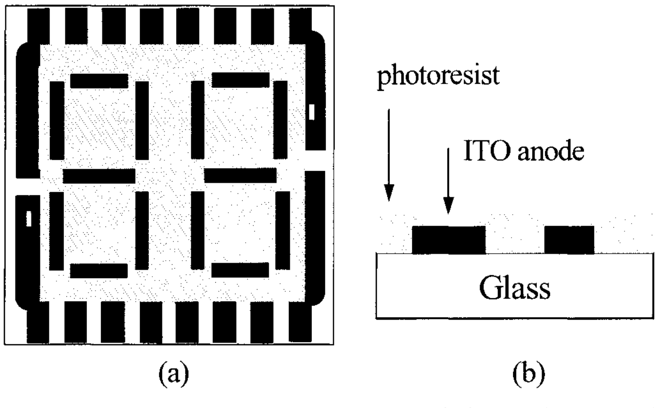

**Figure 6.11:** (a) Top and (b) cross sectional view of the pattered ITO substrates. The blue boxes in (a) denote the openings in the photoresist where the active area of the OLED will be.

patterned into the electrode. When the substrates were patterned, they were placed into sample boxes and stored in a dry $N_2$ box until needed.

### 6.4.2 Organic and Metal Deposition

The substrates were mounted onto a sample stage using a frame that covered the exposed ITO electrodes along the two edges. The stage was mounted inside the Edwards Auto 306 Coater with a movable shadow mask frame. The shadow mask frame was used to define the area where the organic materials would be deposited, typically a small square just large enough to cover all 14 segments of the display, but not the exposed ITO contacts which will be used to make contact to the cathode. When the shadow mask was removed, all of the newly deposited organic material along with the cathode pass through contacts would be covered with the cathode material.

The final device structure is shown in Figure 6.12. The hole transport layer, NPB or TPD, was sublimed from a molybdenum boat using resistive heating. The electron transport layer/emitter layer was either BBEP or 8H-BBEP and was deposited at room temperature using

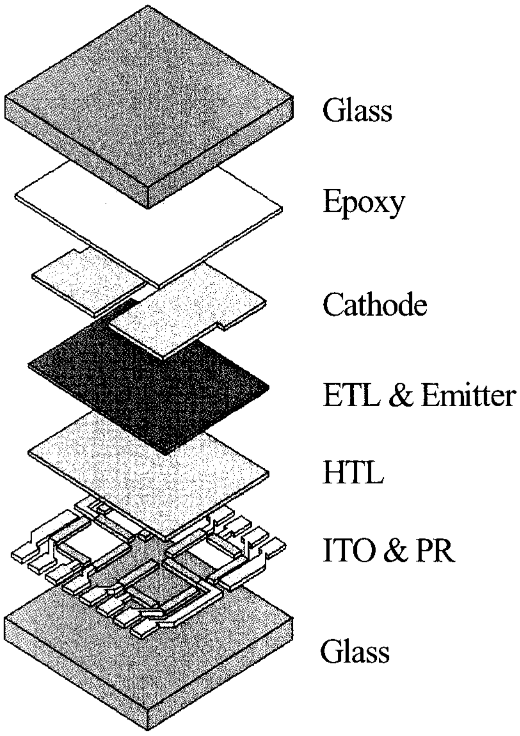

**Figure 6.12:** OLED structure. PR: photoresist, HTL: hole transport layer, ETL: electron transport layer. The photoresist layer is not explicitly shown for the sake of clarity.

either a K-cell or covered tantalum boat. Depending on the sample, the deposition rates of the organics were between 1 Å/sec and 20 Å/sec and the thickness of the films was between 500 Å and 600 Å. Aluminum was used as the cathode and was evaporated from a tungsten wire basket at a rate between 5 Å/sec and 7 Å/sec with a final thickness between 1000 Å and 1500 Å. The more elaborate devices structures also incorporate thin (~10 Å) layers of copper phthalocyanine (CuPc) between the ITO and the hole transport layer or lithium fluoride (LiF) between the cathode and the electron transport layer to enhance carrier injection. Both of these were evaporated from a tungsten boat using resistive heating.

Once the deposition was complete, the devices were removed from the chamber via a pass-through port directly into a nitrogen-filled glove box. This ensured that the device was exposed to minimal amounts of oxygen and humidity. A UV-curable epoxy was spread over the aluminum layer and a piece of glass was carefully placed over it to minimize the amount of bubbles that might be trapped in the epoxy. The sample was then placed under a UV lamp to cure the epoxy and was then removed from the glove box for characterization.

## 6.5 Characterization Techniques

### 6.5.1 Contact Angle

The contact angle is defined as the angle between the liquid-vapour interface and the liquid-solid interface at the solid-liquid-vapour contact point, as shown in Figure 6.13. Contact

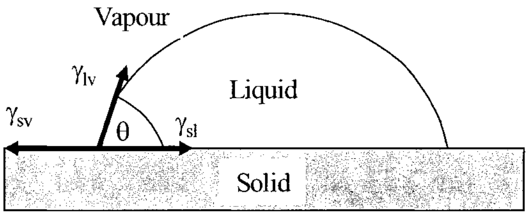

**Figure 6.13:** Diagram of contact angle measurement and interpretation.

angle measurements were performed using a FTÅ200 contact angle measurement system (manufactured by First Ten Ångstroms). The apparatus consisted of a video camera with a macro lens to view the droplets along the surface of the sample, which was front and back lit. The drops were dispensed from a syringe attached to a motor which accurately controlled how much liquid was ejected (typically 1-10 μL). In principle any solvent could have been used for the contact angle measurements, but only DI water was used in our experiments. All contact angle measurements were performed in ambient atmosphere and no attempt was made to control the relative humidity. All of the contact angles recorded were "advancing" contact angles (ie. the water was spreading out over the surface). "Receding" contact angles were not measured (ie. the water was being retracted and the volume of the droplet was decreasing).

### 6.5.2 Physical Characterization Techniques

Atomic force microscopy was performed using a Digital Instruments Dimension 3000 AFM in tapping mode.

A Hitachi SEM 2600 cold field emission SEM was used for imaging. This SEM is unique because it has two different detectors designed to detect different secondary electrons and combine the signal from both detectors to generate clearer higher resolution images.

XRD on thin film samples was performed using a Philips 1710 and a Scintag X2 for powder samples using Cu Kα X-rays with a wavelength of 1.54 Å. Thin film and powder samples were scanned from $2\theta = 1.5°$ to $50°$. The sample were between 3 $cm^2$ and 9 $cm^2$ in size. The thin film XRD samples were grown concurrently with the OFET samples to ensure that the growth conditions were identical. The thickness of the films was between 300 Å and 400 Å.

### 6.5.3 Chemical Characterization Techniques

Differential scanning calorimetry (DSC) measurements were performed using a TA Instruments DSC2920. Samples of BBEP and 8H-BBEP were placed into sealed pans and heated/cooled at a rate of 10 °C/minute.

Electrochemical measurements were performed on a Solartron 1285 potentiostat. The electrolyte was 0.1M $tBuNH_4PF_6$ in acetonitrile and a silver wire was used as the reference electrode. The system was calibrated using ferrocene. The solids were solubilized/suspended in chloroform and deposited on a platinum electrode.

### 6.5.4 Electrical Characterization Techniques

All of the OFETs were characterized using a 4-point probing station connected to a Hewlett-Packard 4155a or an Agilent 4155c Semiconductor Parameter Analyzer. These units consisted of five independent source measurement units (SMUs) which could be programmed to perform various tasks such as sweeping voltages and measuring currents. For the devices used in this study, three of the four probes were used: one for applying a voltage onto the gate electrode, one for sweeping the voltage on the drain and the third to provide the ground on the source electrode, shown in Figure 6.14. The substrate was placed on an electrically insulating pad which was situated on the grounded sample stage.

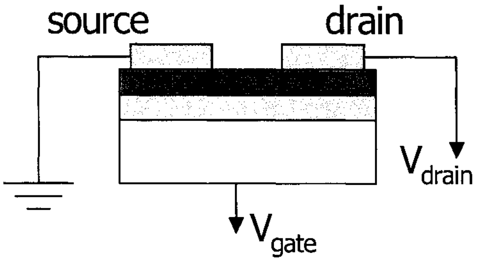

**Figure 6.14**: Scheme for electrical characterization of TC-OFETs.

The top contact devices required some extra preparation steps. Thin copper plates were cut to approximately 2.5 cm x 5 cm and sanded to remove any surface oxidation and contaminants. A coaxial cable was soldered onto one end of the copper plate which was connected to the SMU which controlled the gate voltage. The sample was then mounted onto the copper plate using conducting silver paint and allowed to cure or double sided conducting carbon tape. The sample was then placed on an insulating ceramic plate and affixed to the sample stage in the probing station. By applying a voltage on the entire copper plate, the substrate became charged as well and acted as the gate electrode. Source and drain contacts were made as mentioned above. Prior to all electrical characterization, the organic materials around the perimeter of the device were mechanically removed to minimize leakage current to the gate electrode and fringing of the electric field at the edge of the electrodes.

The current-voltage characteristics of the OLEDs were measured with a Keithley model 2400 SMU which was controlled by data acquisition software written in Microsoft Visual Basic 6.0 as part of this work. A Keithley 238 high current SMU was used to drive the OLEDs for the electroluminescent measurements. The OLEDs were mounted on a custom built frame and placed in front of the optical measuring instruments. Pins on the frame made contact to the electrodes on the OLED when properly aligned and allow easy selection of the OLED segments to be turned on or off.

### 6.5.5 Optical Characterization Techniques

The organic materials to be studied were deposited onto quartz or sapphire substrates that were cleaned using acetone, isopropyl alcohol and DI water. The substrates were baked at 550°C for several hours and then blown off with $N_2$. Absorption measurements were performed on a Varian Cary 50 Bio UV-Visible spectrophotometer operating in transmission mode. Fluorescence excitation measurements were performed on a Jobin Yvon-Spex Fluorlog 3 model FL3-12 with a xenon arc lamp. The samples were placed at an angle of about 40° with respect to the incident beam to minimize any pump beam artefacts in the detected light. The electroluminescence spectra were measured with a Photo Research PR-650 spectrophotometer equipped with a CCD detector array. The luminance of the OLEDs was measured by both the PR-650 and a Minolta LS-110 handheld luminance meter. The LS-110 was integrated with a Keithley 2400 SMU to allow real-time current-voltage-luminance measurements. The PR-650 was connected to a different computer to measure the EL spectra of the OLEDs that were driven by the Keithley 238 SMU. All of the equipment was mounted on an optical bench and the alignment was adjusted to attain the maximum signal each time. The data acquisition software that controls the PR-650 spectrophotometer, the Keithley 2400, and the Minolta LS-110 luminance meter was written by the author in Microsoft Visual Basic 6.0 as part of this work.

# Chapter 7
# Computational Techniques

## 7.1 Overview

The quantum chemistry calculations used in the *Hyperchem*[1] modeling package are based on the semi-empirical PM3 algorithm[2] for the geometry optimizations and Zindo/S algorithm.[3] The latter has been specifically parametrized to reproduce UV-visible absorption spectra. The Zindo algorithm was developed by Zerner and is modeled from the INDO (intermediate neglect of differential overlap) method. Both of these methods solve the Schrödinger equation to describe the electronic properties of atoms and molecules. Some of the approximations used by these methods are: only considering the valence electrons, neglecting the interaction integral for certain interactions by using standard non-optimized electron orbitals basis functions, and using empirically obtained parameters.

For geometric optimization, the Pollack-Ribiere conjugated gradient method was used with an RMS gradient of 0.001 kcal/(mol Å). The initial geometry was determined by theoretical bond lengths and torsion angles.

The UV-visible spectra, HOMO and LUMO energy levels and orbitals were calculated after the molecule's structure had been optimized. A single point calculation using a singly excited configuration interaction was used with 10 or 25 filled/empty orbitals for BBEP and 8H-BBEP, respectively.

## 7.2 Structure Optimization and Energy Calculations of BBEP

BBEP and 8H-BBEP consist of two basic moieties, phenylene (benzene) and vinylene (butene). 8H-BBEP has two alkane groups at the α and α' positions. These moieties are depicted in Figure 7.1. Two forms of the vinylene moiety were possible: cis and trans, shown in Figure 7.1b and c. In the trans conformation, the hydrogen atoms are on opposing sides of the double bonded carbons while in the cis conformation the hydrogens are on the same side. Therefore BBEP and 8H-BBEP molecules can be in one of three conformations: trans-trans, cis-trans, and cis-cis. The significance of the conformation of the vinylene bond greatly impacts the overall structure of the molecule. If the vinylene moieties are in the trans-trans conformation, the molecule tends to be linear with some torsion in the biphenyl moieties. If there are combinations of the cis conformation, the molecule will develop twists and kinks in the backbone, reducing the packing density.

In the trans-trans conformation, two geometries were used: the symmetric "$U_{tt}$" and anti-symmetric "$Z_{tt}$" conformations, shown in Figure 7.2a and b. The extra phenyl rings have been omitted for clarity. For the cis-cis conformation there were two orientations, shown in Figure

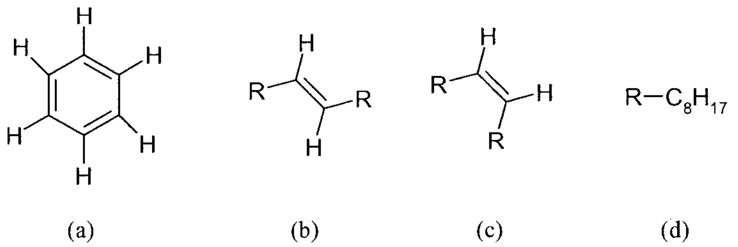

**Figure 7.1:** Different moieties which form the building blocks for BBEP and 8H-BBEP: (a) phenylene (benzene), (b) trans vinylene, (c) cis vinylene, and (d) $C_nH_{2n+1}$ alkane with n=8. In (b)-(d) the -R group denotes the bonding location to the rest of the molecule

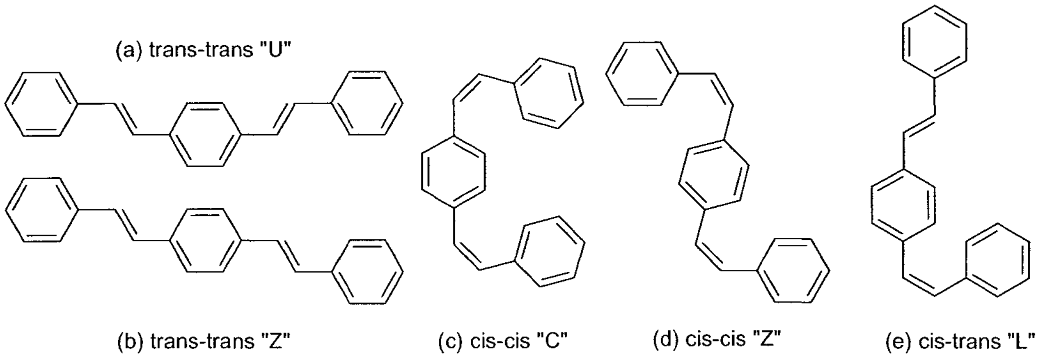

(a) trans-trans "U"

(b) trans-trans "Z" (c) cis-cis "C" (d) cis-cis "Z" (e) cis-trans "L"

**Figure 7.2:** The various conformations of the PPV backbone: trans-trans (a) symmetric "U" and (b) anti-symmetric "Z", cis-cis (c) symmetric "C" and (d) anti-symmetric "Z", and (e) cis-trans "L". The extra phenyl ring on each end has been omitted for clarity.

7.2c ("$C_{cc}$" conformation) and d ("$Z_{cc}$" conformation). For the cis-trans isomer only one conformation was used because the energy differences between the two were negligible.

Table 7.1 summarizes the results of these calculations. The binding energies determined by the PM3 geometry optimization indicate that the trans-trans isomers are the most stable and the cis-cis isomer as the least. Depending on the conformation, the HOMO energy levels calculated with the Zindo/S algorithm indicate energies between -6.94 eV and -7.43 eV. While

**Table 7.1:** Binding energy, HOMO and LUMO energies and molecular length for BBEP.

| Structure | | $E_b$ [kcal/mol] | HOMO [eV] | LUMO [eV] | $d_{CC}$ [Å] | $d_{HH}$ [Å] |
|---|---|---|---|---|---|---|
| trans-trans | $U_{tt}$ | -7019.0242 | -6.94 | -0.55 | 24.3 | 26.5 |
| | $Z_{tt}$ | -7019.0295 | -6.94 | -0.55 | 24.4 | 26.6 |
| cis-cis | $Z_{cc}$ | | | | [a] | [a] |
| | $C_{cc}$ | -7010.6666 | -7.43 | +0.06 | | |
| cis-trans | $L_{ct}$ | -7013.8075 | -7.21 | -0.23 | 17.7 | 18.1 |

[a] molecule was not planar

**Table 7.2:** Binding energy, HOMO and LUMO energies and molecular length for BBEP.

| Material | HOMO [a] [eV] | HOMO [b] [eV] | Difference [eV] |
|---|---|---|---|
| TPD | -5.42 | -6.87 | 1.45 |
| NPB | -5.10 | -6.87 | 1.77 |
| TTA | -5.85 | -6.92 | 1.07 |

[a] Accepted values

the calculated values are 1-1.5 eV larger in magnitude than those obtained experimentally, we are only concerned with the changes in the energy level when comparing one conformation to another. When compared to other materials such as TTA, NPB, and TPD, the calculated HOMO energies are usually about 1-2 eV larger in magnitude than the experimentally determined values. Some results are summarized in Table 7.2. The energy levels also shift as the molecule passes from the gas phase (calculations) to the solid state (experimental). This effect is discussed in Chapter 2.3.

Figure 7.3 to Figure 7.5 show the HOMO and LUMO orbitals for the trans-trans, cis-trans, and cis-cis conformations, respectively. The light and dark wireframes represent orbitals of the same phase.

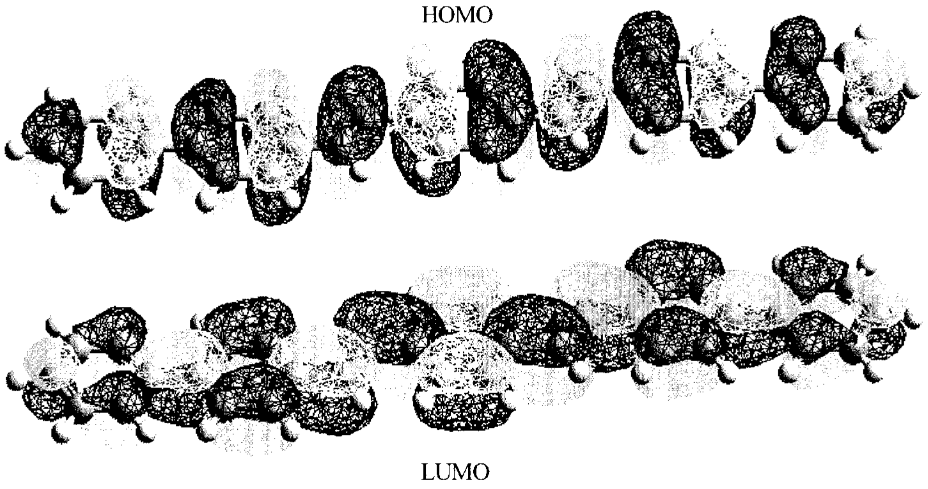

**Figure 7.3:** The HOMO and LUMO orbitals for the trans-trans conformation of BBEP.

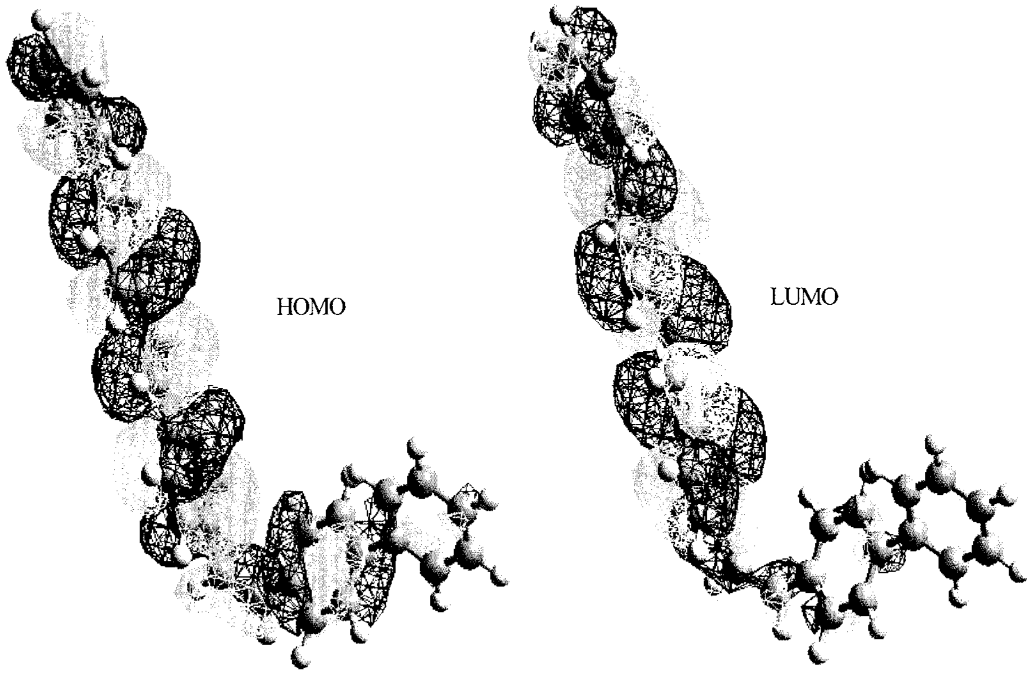

**Figure 7.4:** The HOMO and LUMO orbitals for the cis-trans conformation of BBEP.

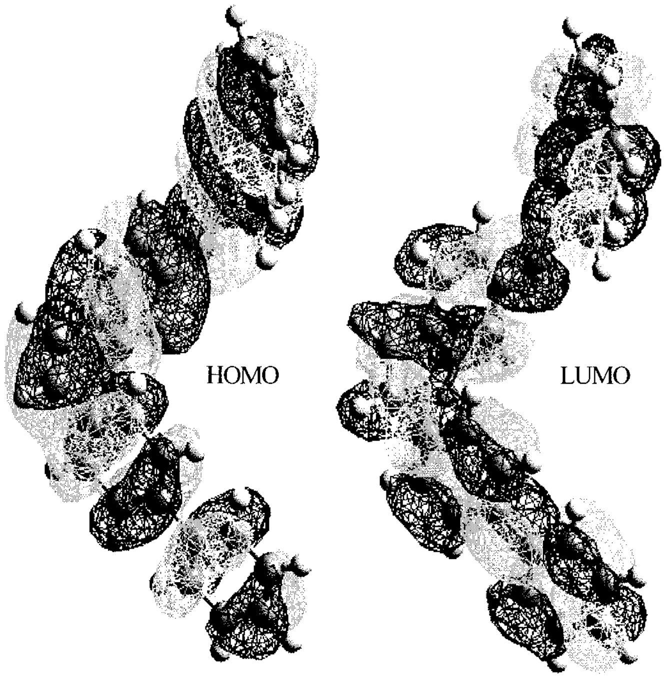

**Figure 7.5:** The HOMO and LUMO orbitals for the cis-cis conformation of BBEP.

Even though the binding energies of the cis-trans conformation dictate that it is more stable than the cis-cis conformation, it is obvious that the conjugation of the backbone has been broken in the cis-trans conformation at the cis vinylene linkage. The shortening of the conjugation length is detrimental to the molecule's ability to conduct electrons or holes. The trans-trans and cis-cis conformations are fully conjugated along the length of the backbone and indicate a great deal of overlap in the orbitals.

## 7.3 Structure Optimization and Energy Calculations of 8H-BBEP

8H-BBEP has essentially the same structure as BBEP but with two alkyl chains attached at the $\alpha$ and $\alpha'$ positions. The orientation of the alkyl chains will affect the shape of the molecule and the structure of the film. The trans-trans conformation of 8H-BBEP was used with the alkyl chains oriented symmetrically and anti-symmetrically. This was attempted in the cis-cis and cis-trans conformations but the alkyl chains always reverted to a single preferred orientation. The structures are illustrated in Figure 7.6. The relative orientation of the alkyl chains does not seem to affect the electronic properties, but can affect the packing. The chains will be tilted off of the long axis of the backbone. The manner in which both chains are tilted will affect the length of the molecule and their packing density.

The binding, HOMO and LUMO energies, and molecular lengths are summarized in Table 7.3. All of the different trans-trans conformations have slightly different binding energies. They all have identical HOMO and LUMO energies of -6.86 eV and -0.55 eV. The cis-trans and cis-cis conformations have binding energies approximately 4.0 and 8.5 kcal/mol

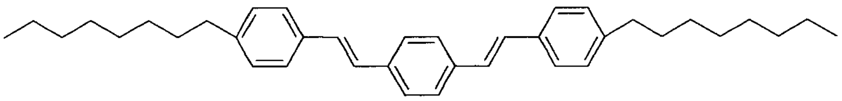

(a) trans-trans "U"

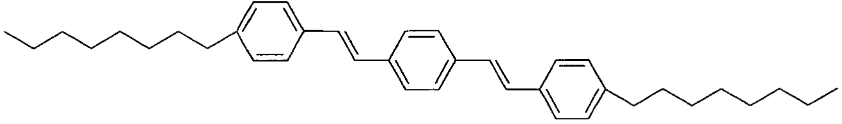

(b) trans-trans "Z"

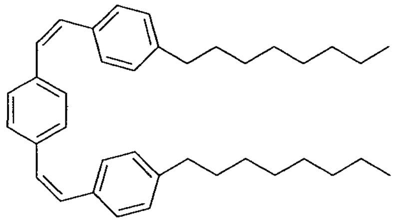

(c) cis-cis "C"

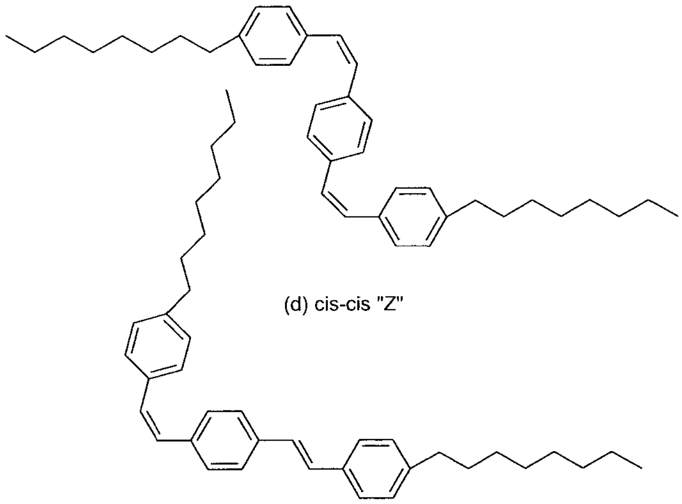

(d) cis-cis "Z"

(e) cis-trans

**Figure 7.6:** The different conformations of 8H-BBEP (a) and (b) are trans-trans, (c) and (d) are cis-cis and (e) is cis-trans. The extra phenyl ring has been omitted for clarity.

higher, respectively. The HOMO energies were also deeper at -7.10 eV (cis-trans) and -7.54 eV (cis-cis), compared to -6.86 eV for the trans-trans conformation. Figure 7.7 to Figure 7.10 illustrates the molecular orbitals for the various conformations. Only one is shown for trans-

trans since all of the molecules are virtually identical.

**Table 7.3:** Binding energy (PM3), HOMO and LUMO energies (Zindo/S), and molecular length calculations for 8H-BBEP.

| Structure | | $E_b$ [kcal/mol] | HOMO [eV] | LUMO [eV] | $d_{CC}$ [Å] | $d_{HH}$ [Å] |
|---|---|---|---|---|---|---|
| trans-trans | $U_{tt,s}$ | -11513.7558 | -6.86 | -0.55 | 41.5 | 43.7 |
| | $U_{tt,a}$ | -11513.7476 | -6.86 | -0.55 | 42.1 | 44.2 |
| | $Z_{tt,s}$ | -11513.7509 | -6.86 | -0.55 | 40.7 | 42.9 |
| | $Z_{tt,a}$ | -11513.7417 | -6.86 | -0.55 | 41.8 | 44.0 |
| cis-cis | $C_{cc}{}^{a}$ | - | - | - | - | - |
| | $Z_{cc}$ | -11505.0443 | -7.54 | +0.32 | 37.1 | 39.1 |
| cis-trans | | -11509.7079 | -7.10 | -0.24 | 32.0 | 33.4 |

[a] Calculation did not converge

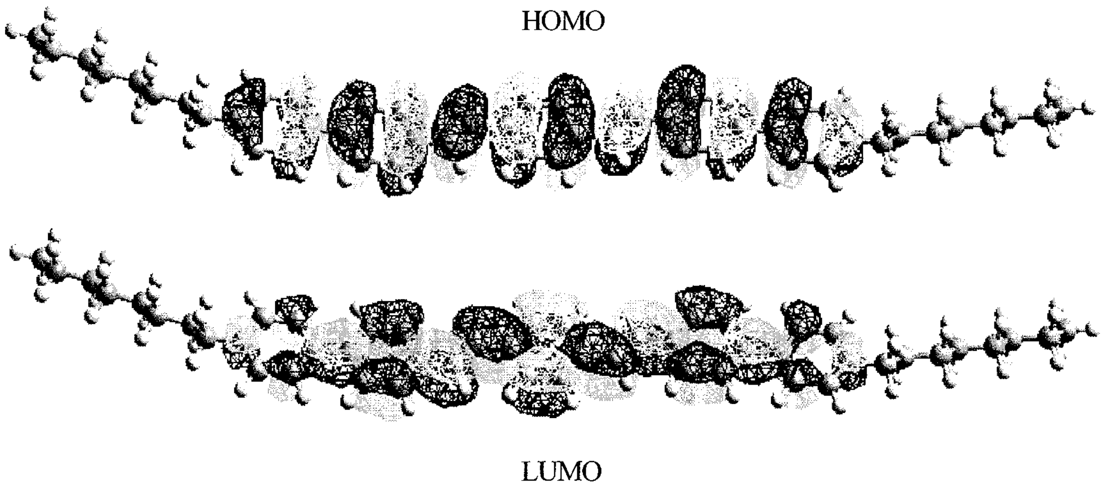

**Figure 7.7:** The HOMO and LUMO orbitals for the trans-trans conformation of 8H-BBEP.

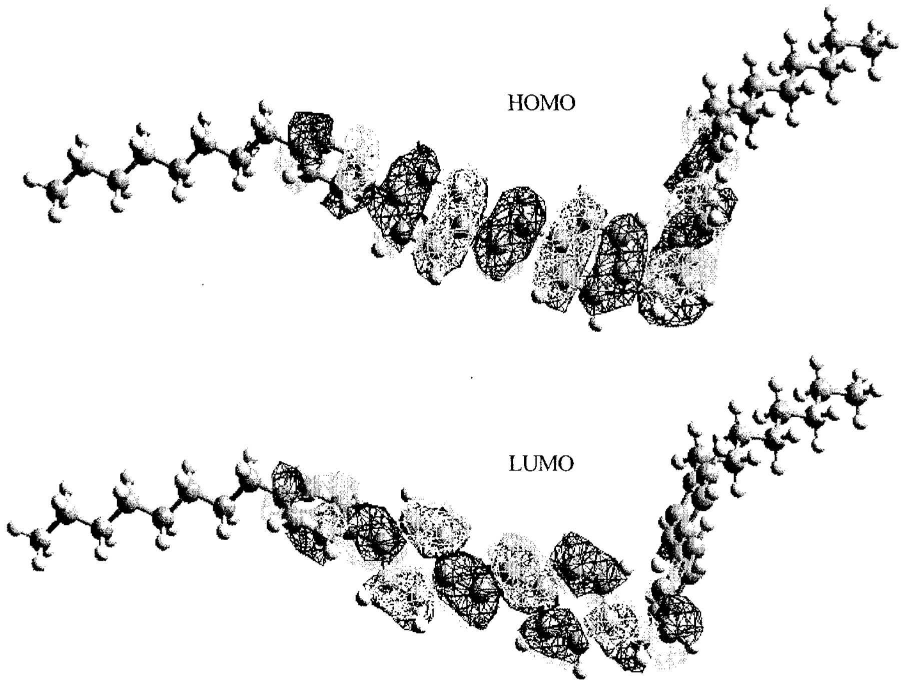

**Figure 7.8:** The HOMO and LUMO orbitals for the cis-trans conformation of 8H-BBEP. Note that the $\pi$-$\pi^*$ conjugation is broken at the cis linkage in the LUMO.

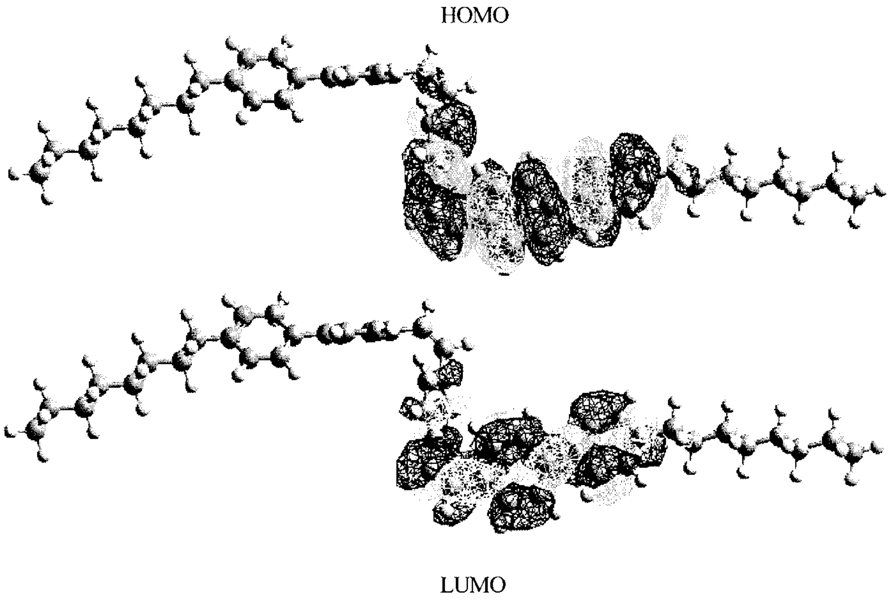

**Figure 7.9:** The HOMO and LUMO orbitals for the "Z" cis-cis conformation. Note that the $\pi$-$\pi^*$ conjugation is broken at the cis linkage in the HOMO and LUMO.

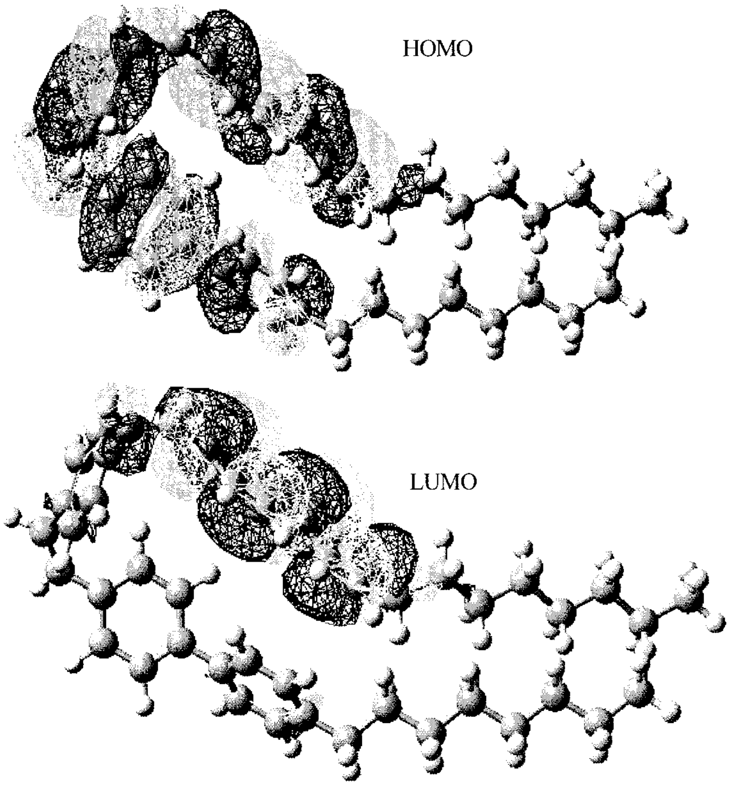

**Figure 7.10:** The HOMO and LUMO orbitals for the "C" cis-cis conformation. Note that the $\pi$-$\pi^*$ conjugation is broken at the cis linkage in the LUMO. This calculation did not converge.

The most stable and the most desirable form of 8H-BBEP is the trans-trans conformation due to it's planarity and abundance of $\pi$ orbitals. The cis-trans and cis-cis conformations are undesirable because of the kinks induced by the cis linkages. They decrease the conjugation length of the molecule by creating a non-planar backbone that is not conducive to dense packing in a thin film and the orbitals are localized onto a small portion of the entire molecule.

Therefore it is desirable to employ a synthesis route which will selectively create only the trans-trans conformations of BBEP and 8H-BBEP.

## 7.4 References

[1] HyperChem, 7.0 ed. (Hypercube, Inc., 1115 NW 4th Street, Gainesville, Florida 32601, USA).

[2] J. J. P. Stewart, J. Comput. Chem. **10,** 210 (1989).

[3] M. C. Zerner, in *Rev. Comp. Chem.*; *Vol. 2* (VCH, New York, 1991), p. 313.

# Chapter 8
# Results and Discussion

## 8.1 Overview

In this chapter we shall present the experimental findings of this thesis. We begin by presenting physical and chemical properties of BBEP and 8H-BBEP: differential scanning calorimetry was used to measure the melting points of the materials and cyclic voltammetry allowed us to measure the oxidation potential and calculate the HOMO level of the materials. The LUMO energy levels were determined by the optical bandgap energy. The optical absorption and emission measurements are presented next and compared to the calculated values found in Chapter 7. The structural data is then presented, including x-ray diffraction spectra, scanning electron micrographs and atomic force micrographs which examine the microstructure of the materials. These results will be compared with the modeling results from Chapter 7.

Organic LEDs were fabricated to allow the study of optical processes in these materials. The current-voltage-luminance data for a variety of OLEDs based on BBEP and 8H-BBEP will be presented.

The OFET results are then presented. The effect of substrate surface treatment and substrate temperature during film growth on device parameters such as mobility, threshold voltage, sub-threshold slope, and frequency response are summarized. The performance and operating mechanisms of TC and BC geometry OFETs are compared. Finally, the structure-property relationships between the molecular and film structures and the field effect mobility are discussed.

## 8.2 Chemical Characterization

### 8.2.1 Differential Scanning Calorimetry (DSC)

The DSC scans were performed on BBEP and 8H-BBEP using heating and cooling modes. The DSC spectra are shown in Figure 8.1 and the results are summarized in Table 8.1.[1,2] On the first heating scan BBEP showed two melting points at 200.7 °C and 373.0 °C and a crystallization point at 328.3 °C. This is consistent with the starting powder consisting of two different solid phases of BBEP, α and β, with the α-phase having a lower melting point than the β-phase. As the temperature is increased the α-phase melts and re-crystallized into the β-phase. The β-phase then melts at 373.0 °C. In the first cooling scan, BBEP re-crystallizes at 365 °C into the β-phase. In the second heating scan, only the β-phase melting and re-crystallization points were observed.

The heating scans of 8H-BBEP also displayed two melting points at approximately 122 °C and 367 °C, consistent again with two phases, α and β (which do not necessarily have the same crystal structure as those for BBEP). On the first cooling scan, the 8H-BBEP re-crystallized at approximately 363 °C and showed a minor crystallization peak at approximately 216 °C. The peaks at 122 °C and at 216 °C are characteristic of a reversible liquid crystal (LC) phase transition, which is to be expected from a material

**Table 8.1:** Summary of DSC results for BBEP and 8H-BBEP.

| Material | Scan | $T_{m1}$ [°C] | $T_{m2}$ [°C] | $T_{c,heating}$ [°C] | $T_{c1,cooling}$ [°C] | $T_{c2,heating}$ [°C] |
|---|---|---|---|---|---|---|
| BBEP | 1 | 200.7 | 373.0 | 328.3 | 365.0 | - |
| | 2 | - | 372.1 | - | 366.6 | - |
| 8H-BBEP | 1 | 122.4 | 367.5 | - | 363.2 | 216.0 |
| | 2 | 122.7 | 366.2 | - | [a] | - |

[a] unable to measure due to decomposition of material.

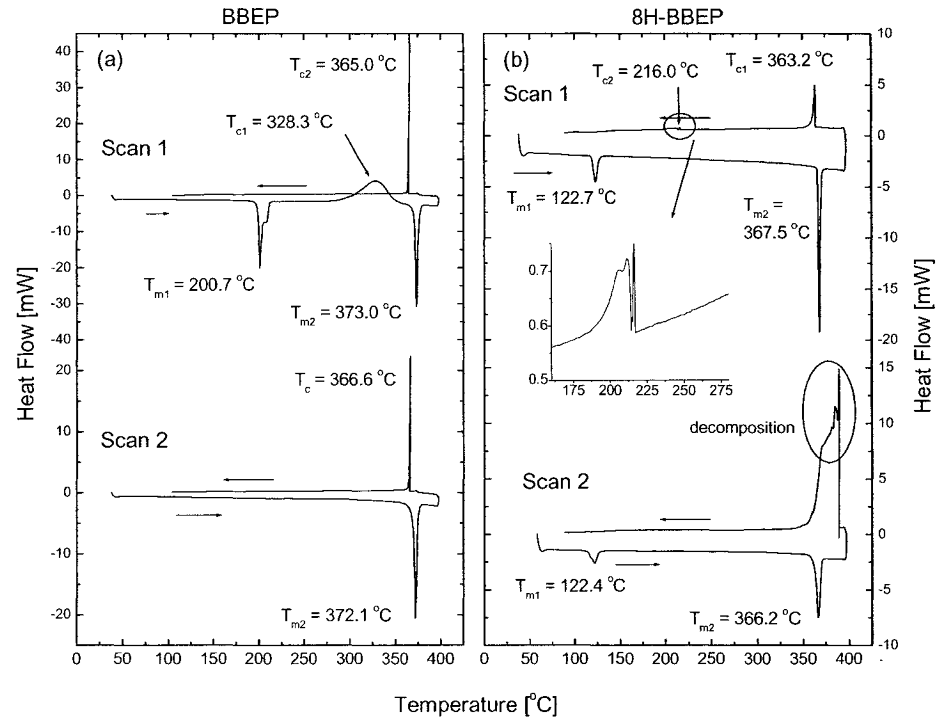

**Figure 8.1:** Heating and cooling curves for (a) BBEP and (b) 8H-BBEP. $T_m$ denotes a melting temperature and $T_c$ denotes a crystallization temperature. The peak in (b) between 115°C and 135°C denotes a liquid crystal phase transition. The inset in (b) shows the reversible liquid crystal crystallization peak between 200°C and 225°C in scan 1.

containing long alkyl chains such as this one. The LC phase is a macroscopic property of the material. When the material is in the LC phase, the macroscopic grains or needles have the ability to move and re-arrange themselves in a more energetically favourable fashion. The LC phase is not a crystalline state - it is comprised of macroscopic particles, which may be crystalline at the microscopic level, and have some sort of long-range order in their packing arrangement.

In the second heating scan, both melting points were observed again, but at the end of the scan, the material showed signs of decomposition, causing the feature seen in the second scan of Figure 8.1b at about 375 °C.

### 8.2.2 Cyclic Voltammetry

Samples of each material were suspended in chloroform and dropped onto a platinum electrode where the solvent was allowed to evaporate. The platinum electrode was placed in an electrochemical cell containing a 0.1 M solution of tetrabutylammonium hexafluorophosphate (TBuAPF$_6$) in acetonitrile (CH$_3$CN) as the electrolyte. Ferrocene was added to calibrate the electrochemical cell. The cyclic voltammetry curves with ferrocene are shown in Figure 8.2a and c. Figure 8.2b and d show the cyclic voltammetry curves for BBEP

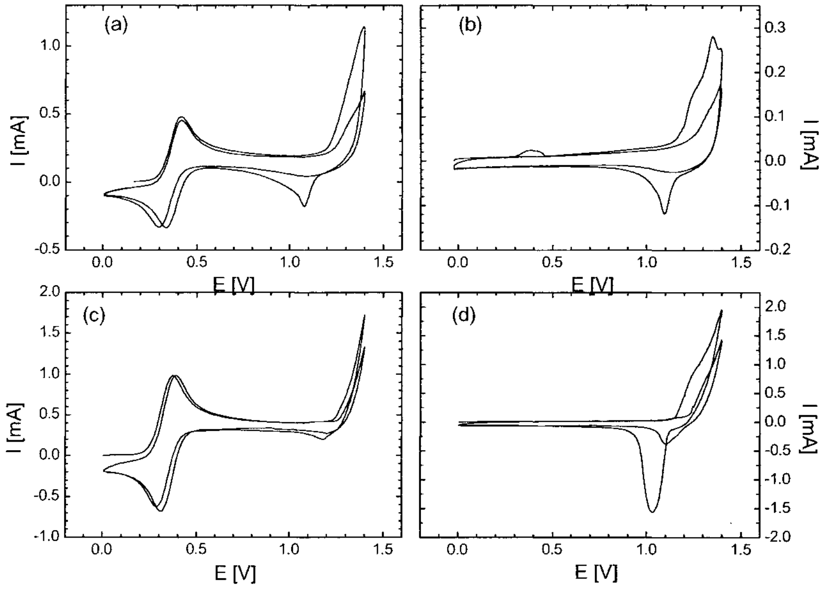

**Figure 8.2:** Cyclic voltammetry of BBEP (a) with and (b) without ferrocene and for 8H-BBEP (c) with and (d) without ferrocene.

**Table 8.2:** Summary of the electrochemical data extracted from the cyclic voltammetry data. SCE refers to a saturated calomel electrode. All values have an uncertainty of ±0.1 V or eV, respectively.

| Material | $E_{ox}$ [vs SCE, V] | $E_{ox}$ [vs NHE, V] | HOMO [eV] | LUMO [eV] | $E_g$ [eV] |
|---|---|---|---|---|---|
| BBEP | 1.2 | 1.5 | 5.9 | 3.4 | 2.5 |
| 8H-BBEP | 1.3 | 1.6 | 6.0 | 3.3 | 2.7 |

and 8H-BBEP. The electrochemical data is summarized in Table 8.2.[1] The oxidation potential of the materials were measured against a saturated calomel electrode (SCE).The SCE was calibrated against ferrocene and a potential of 0.34 V was obtained. The oxidation potential of ferrocene with respect to a normal hydrogen electrode (NHE) is 0.68 V,[3] and it is known that the HOMO energy level of a NHE is -4.5 eV.[4,5] The oxidation values found with respect to a SCE were adjusted by 0.34 V to give the oxidation potential with respect to NHE and the HOMO energy level was then calculated.

## 8.3 Optical Absorption and Emission Spectroscopy of BBEP and 8H-BBEP

### 8.3.1 BBEP

The UV-visible absorption and photoluminescence spectra for BBEP deposited at a substrate temperature of 20°C, 50°C, 75°C, 100°C and 175°C are shown in Figure 8.3. Each spectrum was normalized with respect to itself and then layered with the other spectra. The emission spectra display a low wavelength shoulder around 447 nm with the main emission peak at about 470 nm. The absorption peaks are at 202, 225, 265, and 310 nm with a small shoulder at 284 nm. The features seen below 300 nm are from the individual transitions on the benzene rings while the oscillations in the absorption tail above 310 nm are a result of the conjugated nature of the molecule. The absorption peak associated with the structure of the molecule is at 310 nm. The peak positions were invariant with temperature, but became somewhat less defined with increasing temperature, with a larger background. The sample deposited at 175°C (only 5-10°C below the Knudsen cell temperature) showed very poor film characteristics that were visible to the eye while no material adhered to the OFET samples at all. It is suspected that the material underwent decomposition.

The emission peak is red shifted by more than 150 nm from the absorption maximum of 310 nm. This is in agreement with experimental evidence from Colaneri *et al* where they

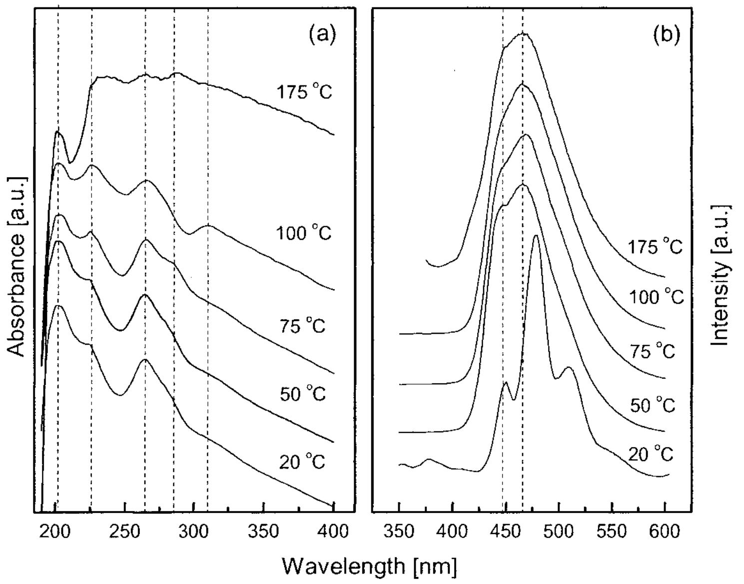

**Figure 8.3:** (a) Absorption and (b) emission spectra for BBEP deposited at various substrate temperatures. The emission spectra were obtained by using an excitation pump at 310 nm, corresponding to the absorption maximum of the molecule. Each spectrum was normalized with respect to itself and tiled.

showed that the main absorption peak is at approximately 330 nm (3.75 eV) while the central emission peak is at approximately 495 nm (2.5 eV) giving a redshift of 165 nm for a molecule similar to BBEP.[6]

The calculated absorption spectrum of all BBEP configurations (trans-trans, cis-trans, and cis-cis) is shown in Figure 8.5 using a Zindo/S semi-empirical calculation. The peaks in the calculated

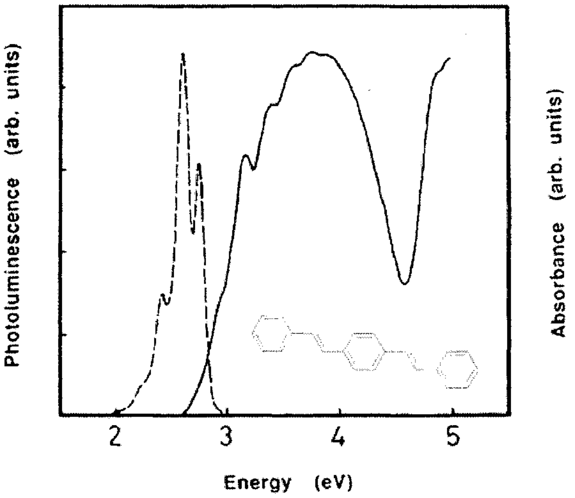

**Figure 8.4:** Photoluminescence (dashed) and absorption (solid) spectra for distyrylbenzene, shown in the inset. After Colaneri *et al* (reference 6).

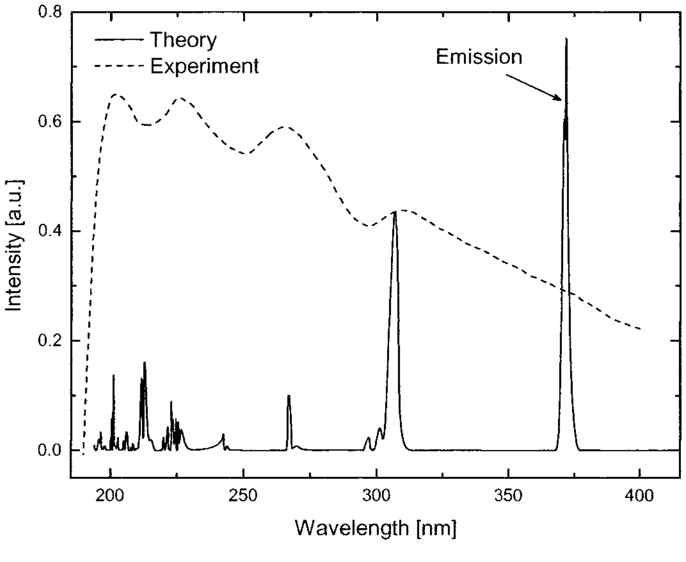

**Figure 8.5:** Calculated UV-visible spectrum for a single BBEP molecule in vacuum using the Zindo/S computational algorithm and an experimental absorption spectrum. The details are discussed in the text.

spectrum are blue shifted by 1-5 nm compared to the experimental absorption peaks. The strong peak at about 375 nm is associated with the emission peak, but blue shifted by 80-100 nm. This is thought to be due to intermolecular interactions which the molecules experience in thin film form that the software does not account for.

Since the theoretical calculations show the results for a single molecule in the gas phase in vacuum, we do not expect to reproduce the optical spectra for a thin film sample exactly at the semi-empirical level. We do expect that strong transitions will be common to the theoretical and experimental spectra with the experimental peaks positions red shifted and broadened compared to the theoretical peaks. If we consider the configuration coordinate diagram of a single molecule in the gas phase in the absence of any external perturbations, it resembles the one shown schematically in Figure 8.6a. In the gas phase, the molecule will have many degrees

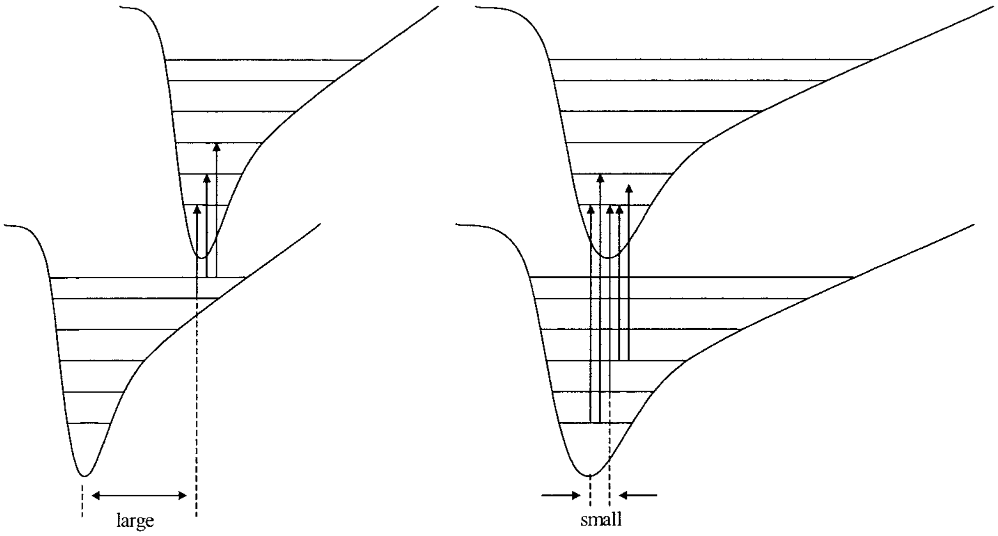

(a) (b)

**Figure 8.6:** Example schematic configuration coordinate diagram of a molecule in the (a) gas and (b) solid phase. In the gas phase, the molecule experiences no external perturbations, but possesses a large number of degrees of freedom. In (b) the molecule experiences external perturbations but has fewer degrees of freedom.

of freedom (torsion about bonds, for example) and can experience a large change in configuration when excited. This leads to a large shift in the potential energy wells. However, in vacuum it does not experience any external perturbations which results in a narrow potential well. This implies that the $n^{th}$ transition will be well defined and there will be minimal overlap between the $n$-1 and $n$+1 transitions. When the molecule is in the solid state, it does not possess the same number of degrees of freedom as it did in the gas phase due to the proximity of other molecules. This means that when the molecules are excited they do not undergo as large of a configuration change and the potential well does not shift as much. In addition, the proximity of other molecules will generate external perturbations which effect the shape of the well. The well will broaden and many more transitions will be possible. This situation is illustrated in Figure 8.6b. The closeness of the vibronic levels will cause some overlap in the peaks, causing them to become broad.

### 8.3.2 8H- BBEP

Figure 8.7a illustrates the UV-visible absorption spectrum for 8H-BBEP at different substrate temperatures. The main absorption peak is at 310 ± 2 nm with minor peaks at 242 and 265 nm, similar to BBEP, and the spectra are not temperature dependent. The emission spectra are shown in Figure 8.7b and show three distinct peaks at 450, 482, and 514 nm. Both the absorption and emission spectra are similar to BBEP, shown in Figure 8.3, which is expected because the $C_8H_{17}$ chains do contribute to the $\pi$-$\pi^*$ absorption process. However, they do increase the rigidity of the molecule and decrease torsion about bonds when in the solid state.

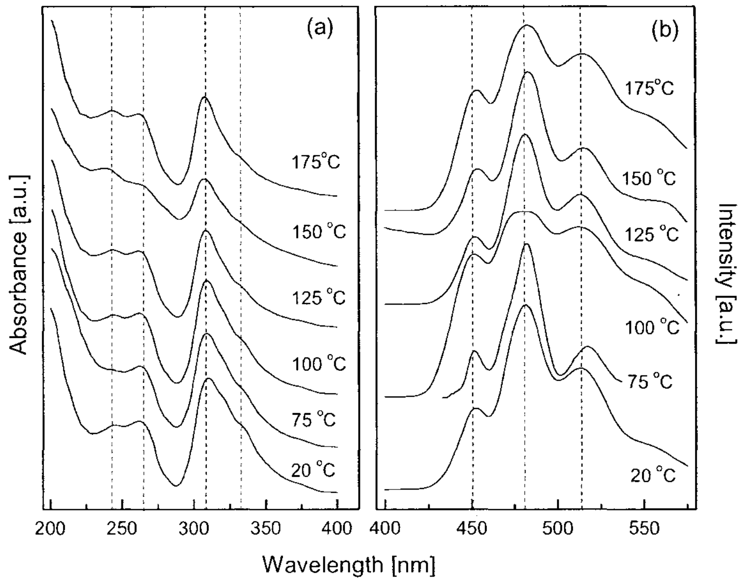

**Figure 8.7:** (a) Absorption and (b) emission spectra of 8H-BBEP for various substrate temperatures. The peak positions are invariant with temperature. Each spectrum was normalized with respect to itself and tiled.

The calculated UV-visible spectrum for 8H-BBEP is shown in Figure 8.8. The series of peaks in the simulated spectrum between approximately 295 nm and 315 nm are associated with the main absorption peak at 310 nm. The peaks below 295 nm agree with the experimentally observed peaks to within a few nanometers. As with the simulated BBEP spectrum, there is a triplet of peaks around 375 nm which are attributed to the emission peaks. The experimental emission peaks are red shifted by approximately 100-150 nm and are significantly broader. The calculated spectrum in Figure 8.8 represents the absorption spectra for the cis-cis, cis-trans and trans-trans conformations that are possible with 8H-BBEP. Because of the synthesis route outlined in Appendix A, there was no preferential selection between conformers, resulting in

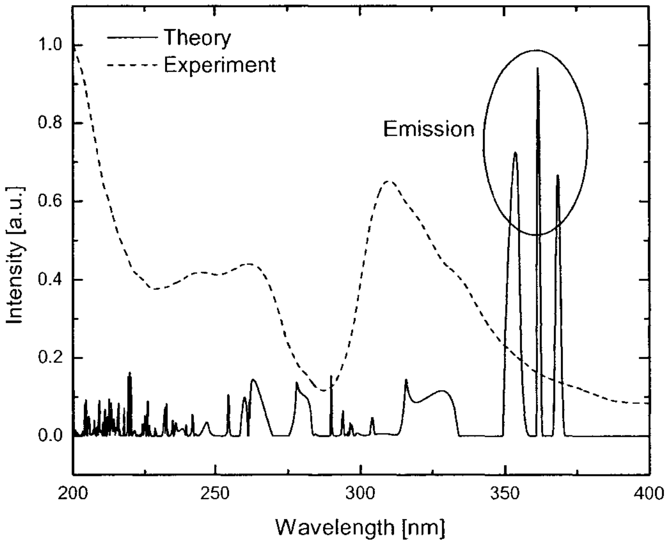

**Figure 8.8:** Calculated Zindo/S UV-visible spectrum (solid line) and the experimental absorption spectrum (dashed line). Each spectrum was normalized with respect to itself and overlaid. The details are discussed in the text.

an unknown mixture of conformers in the final product. The simulated UV-visible spectrum gave equal weight to each of the three conformations. In practice, the composition of the films likely does not contain unequal amounts of each conformer. A more rigorous *ab initio* calculation should be performed for each conformation and then fit to the experimentally obtained curve with weighting factors to account for the different conformations present in the films.

## 8.4 Structure of BBEP and 8H-BBEP Thin Films

### 8.4.1 Powder X-ray Diffraction

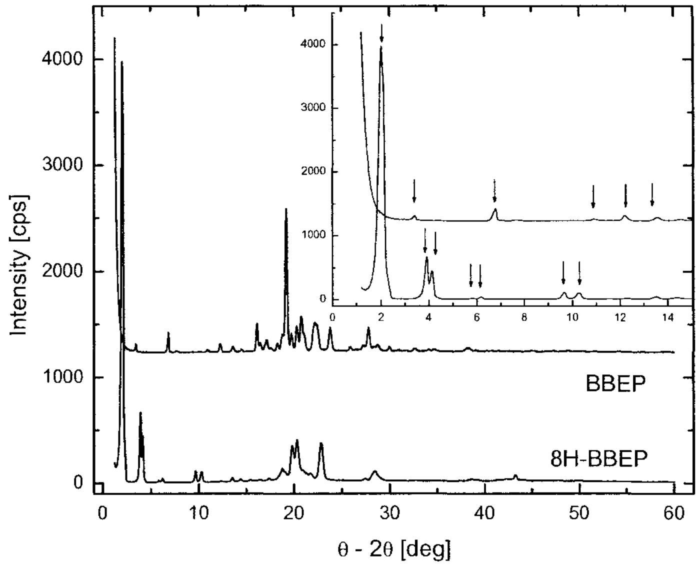

**Figure 8.9:** XRD spectra of powder BBEP and 8H-BBEP. The spectrum of BBEP shows more crystalline structure than that of 8H-BBEP. The inset shows the low angle region for both materials. The BBEP spectra are offset to allow comparison.

Low angle XRD measurements were performed on powder samples of BBEP and 8H-BBEP. The diffraction spectra are shown in Figure 8.9. The spectrum of BBEP clearly shows more structure than the spectrum of 8H-BBEP. This is expected because the $C_8H_{17}$ end groups in 8H-BBEP will hinder the movement of the molecules and will not easily allow them to orient themselves within the unit cell. In contrast, BBEP is a relatively compact molecule which should result in a densely packed unit cell.

### 8.4.2 XRD of BBEP Thin Films

Thin films of BBEP were evaporated onto plain and modified $SiO_2$ surfaces. θ-2θ XRD

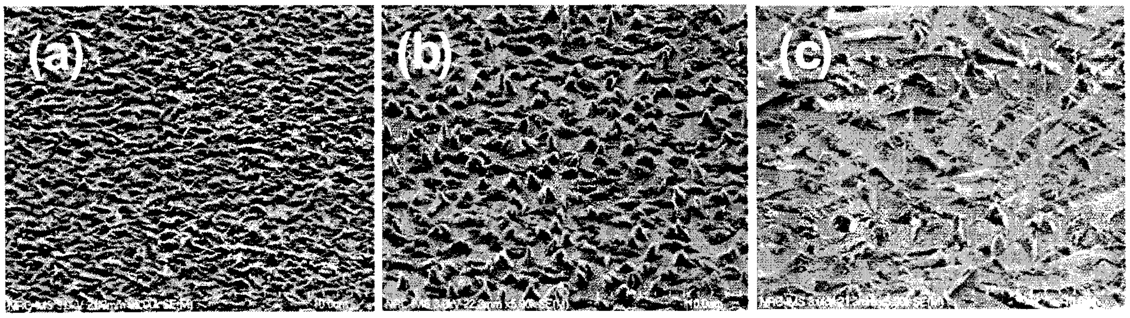

**Figure 8.10:** SEM images of BBEP films on (a) HMDS and (b) OTS-18coated $SiO_2$ substrates. (c) Illustrates a BBEP film deposited onto a $Si_3N_4$ substrate. None of the films were continuous.

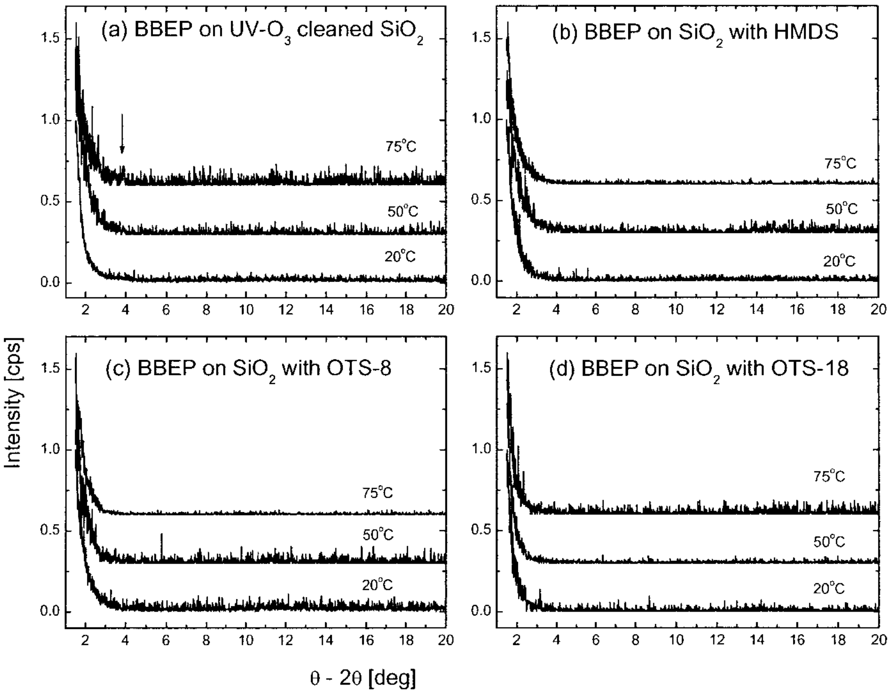

**Figure 8.11:** The XRD spectra of BBEP at three different substrate temperatures for (a) UV-$O_3$ cleaned $SiO_2$, (b) HMDS, (c) OTS-8, and (d) OTS-18. The only (minor) peak that corresponds to that of the XRD of the powder samples is at $T_{sub}$ = 75°C in (a) at 3.42°. Each spectrum was normalized with respect to itself and tiled.

was performed on the films but no peaks were observed. The results are shown in Figure 8.9. BBEP was also deposited on $Si_3N_4$ substrates and similar behaviour was found. Regardless of the quantity of material deposited, BBEP would not form smooth continuous films. Figure 8.10 illustrates SEM images of 800 Å thick BBEP films deposited on HMDS, OTS-18 (both SAMs formed on a $SiO_2$ substrate) and $Si_3N_4$ substrates held at 75°C during growth. BBEP tended to form islands on the surface which were not continuous across the surface. Similar morphology was observed with BBEP films deposited at 20°C and 50°C. At temperatures of 125°C or higher, no material adhered to the surface.

### 8.4.3 XRD of 8H-BBEP Thin Films

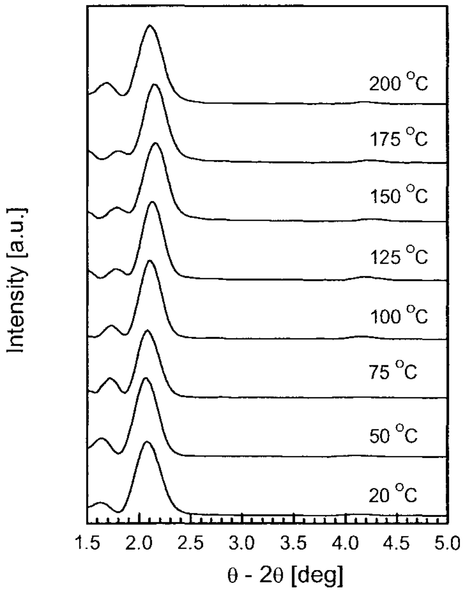

**Figure 8.12:** XRD spectra of 8H-BBEP on UV-$O_3$ cleaned $SiO_2$ at different substrate temperatures. Each spectrum was normalized with respect to itself and tiled.

Figure 8.12 illustrates the XRD spectra obtained for 8H-BBEP on $SiO_2$ which has been exposed to UV-$O_3$ for one hour as a function of growth temperature. The minor peak between 1.5° and 2° is attributed to thin film reflection effects. Assuming that the peak at about 2° is a first order peak, we use Bragg's equation, $2d_{XRD} \sin\theta = n\lambda$, with n=1 to calculate $d_{XRD}$ (see Table 8.3). We find that the diffraction peak position at about 2.08±0.05° agrees with the main peak in the XRD spectrum of the powder 8H-BBEP

**Table 8.3:** Summary of peak positions and calculated $d_{XRD}$ values from the raw XRD spectra of 8H-BBEP for different growth temperatures and substrate treatments. The uncertainty of 2θ is ±0.05° and ±2 Å for $d_{XRD}$.

| Temp | $SiO_2$ | | HMDS | | OTS-8 | | OTS-18 | |
|---|---|---|---|---|---|---|---|---|
| | 2θ | $d_{XRD}$ [Å] | 2θ | $d_{XRD}$ [Å] | 2θ | $d_{XRD}$ [Å] | 2θ | $d_{XRD}$ [Å] |
| 20 °C | 2.08 | 42 | 2.08 | 42 | 2.07 | 43 | 2.04 | 43 |
| 50 °C | 2.06 | 43 | 2.02 | 44 | 2.11 | 42 | 2.11 | 42 |
| 75 °C | 2.08 | 42 | 2.15 | 41 | 2.06 | 43 | 2.05 | 43 |
| 100 °C | 2.10 | 42 | 2.16 | 41 | 2.09 | 42 | 2.03 | 44 |
| 125 °C | 2.13 | 41 | 2.14 | 41 | 2.09 | 42 | 2.03 | 44 |
| 150 °C | 2.15 | 41 | 2.12 | 42 | 2.11 | 42 | 2.07 | 43 |
| 175 °C | 2.14 | 41 | 2.13 | 41 | 2.10 | 42 | 2.07 | 43 |
| 200 °C | 2.11 | 42 | 2.01 | 44 | 2.16 | 41 | 2.04 | 43 |

sample. The $d_{XRD}$ values obtained from the 2θ peaks were in the range between 41±2 Å and 43±2 Å, which is comparable to the theoretical length of the trans-trans isomer of 8H-BBEP, calculated to be 42 Å in Chapter 7, neglecting the hydrogen atoms at each end of the molecule. This implies that the molecules are oriented with the backbones perpendicular to the surface and arrange themselves in a lamellar type structure with each lamella being one molecule thick.

The same analysis was performed on 8H-BBEP deposited on HMDS, OTS-8 and OTS-18. The peak positions and d values are summarized in Table 8.3 and the spectra for 8H-BBEP on HMDS are shown in Figure 8.13. We still observe the main first order peak between 2.00° and 2.10° and $d_{XRD}$ values between 41Å and 44 Å. The spectra for the 50°C and 200°C samples are shifted by 0.1° to the left due to a mis-calibration of the spectrometer. The first order peak displays evidence of a shoulder, indicating the possible existence of two different orientations of the molecules at 75°C, 100°C, and 200°C. The difference in the linewidth of the diffraction

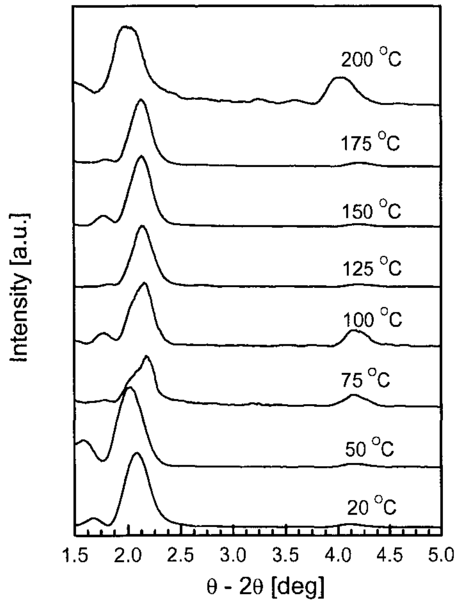

**Figure 8.13:** XRD spectra of 8H-BBEP deposited on HMDS coated $SiO_2$ at different substrate temperatures. The 50°C and 200°C spectra are shifted 0.10° to the left due to a mis-calibration of the diffractometer. Each spectrum was normalized with respect to itself and tiled.

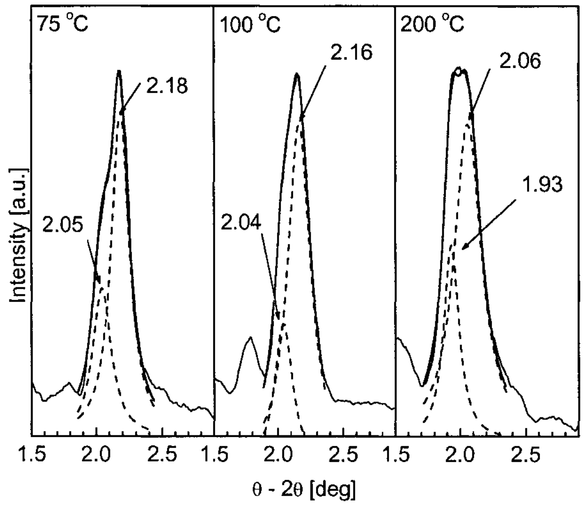

**Figure 8.14:** Multiple Lorentzian curve fitting of the 8H-BBEP XRD spectra at 75°C, 100°C, and 200°C. The spectrum at 200°C is shifted 0.10° to the left due to a mis-calibration of the diffractometer.

peaks is most likely due to a distribution in the grain sizes. The deconvolution of the main first order peak is shown in Figure 8.14. Two sets of peaks were extracted: a minor peak between 2.03-2.05° and a major peak between 2.16-2.18°. If we replace the peak positions in Table 8.3 with the new main peaks from Figure 8.14 and correct for the 0.1° shift in the 50°C and 200°C spectra, we see that the calculated $d_{XRD}$ values are between 41 ± 2 Å and 44 ± 2 Å. The different linewidths are due the variation of grain sizes in the film.

The XRD spectra for the 8H-BBEP samples grown on the OTS-8 coated $SiO_2$ substrates are shown in Figure 8.15. All of the peaks were deconvoluted using a multiple Lorentzian peak fitting algorithm. A major peak emerge at 2.09-2.15° and a minor peak at 2.01-2.05°, shown

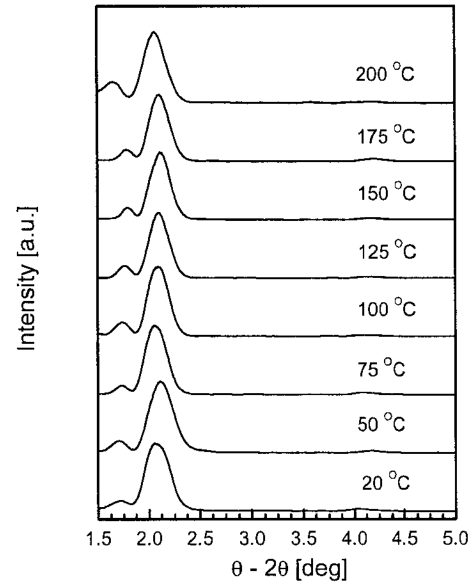

**Figure 8.15:** XRD spectra of 8H-BBEP films deposited on OTS-8 coated $SiO_2$ surfaces at various substrate temperatures. Each spectrum was normalized with respect to itself and tiled.

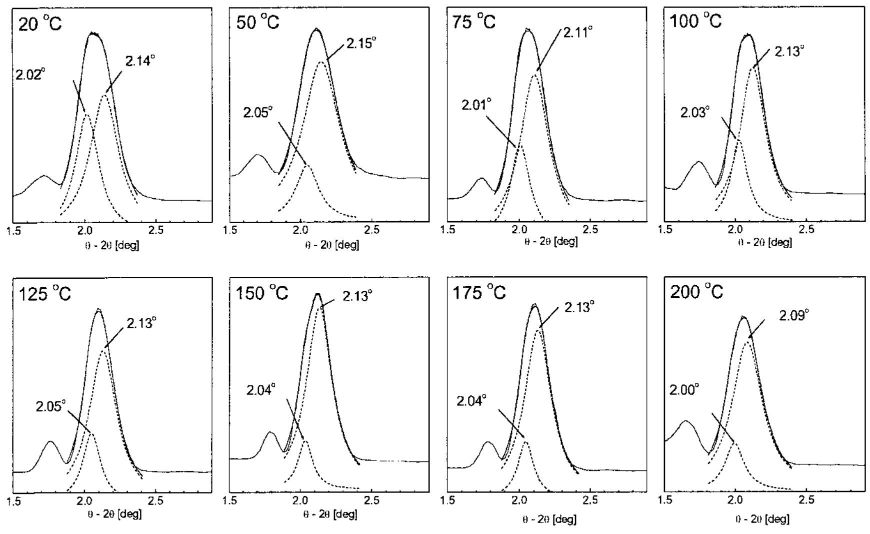

**Figure 8.16:** Multiple Lorentzian peak fitting to the main 8H-BBEP peak in the XRD spectra as a function of substrate temperature. The main peak position remains relatively constant between 2.09° and 2.15° with a minor peak appearing between 2.01° and 2.05°.

in Figure 8.16. The $d_{XRD}$ values are between 41-43 Å and are summarized in Table 8.3. The XRD spectra for the 8H-BBEP samples that were deposited onto the OTS-18 coated $SiO_2$ at various substrate temperatures are shown in Figure 8.17. The samples deposited at a substrate temperature of 20°C and 100°C were repeated multiple times but consistently showed poor signal to noise ratios. The $d_{XRD}$ values are between 42 Å and 44 Å.

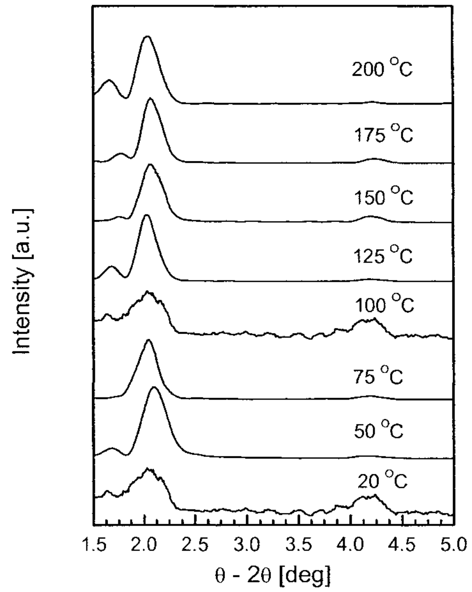

**Figure 8.17:** XRD spectra of 8H-BBEP deposited on OTS-18 coated $SiO_2$ surfaces at various substrate temperatures. Each spectrum was normalized with respect to itself and tiled.

### 8.4.4 8H-BBEP Thin Film Morphology

8H-BBEP films deposited on $SiO_2$, HMDS, OTS-8, and OTS-18 treated $SiO_2$ grown at different substrate temperatures were characterized using scanning electron microscopy (SEM) and atomic force microscopy (AFM). The SEM images are shown in Figure 8.18 to Figure 8.21. The AFM images are shown in Figure 8.22 to Figure 8.25.

There was no visible difference between the films grown on $SiO_2$ at 20°C and 50°C as viewed by the SEM. On a modified $SiO_2$ surface, the films did appear to be smoother at 50°C compared to 20°C. Between 75°C and 125°C, the morphology changes from a relatively rough surface to a smooth surface with grains composed of lamellar structures. As the substrate temperature was increased the size of the grains increased. The number of lamellae generally decreases with increasing temperature and the film becomes smoother. In the 175-225°C range, the grains tend to become larger, but are not continuous and contain holes and cracks. This is especially evident in the HMDS samples where there is only 1 grain comprised of a single lamella present. The cracks can be seen in the SEM shown in Figure 8.19i and in the AFM in Figure 8.23h. The same amount of material was deposited for all samples (300 ± 1 Å).

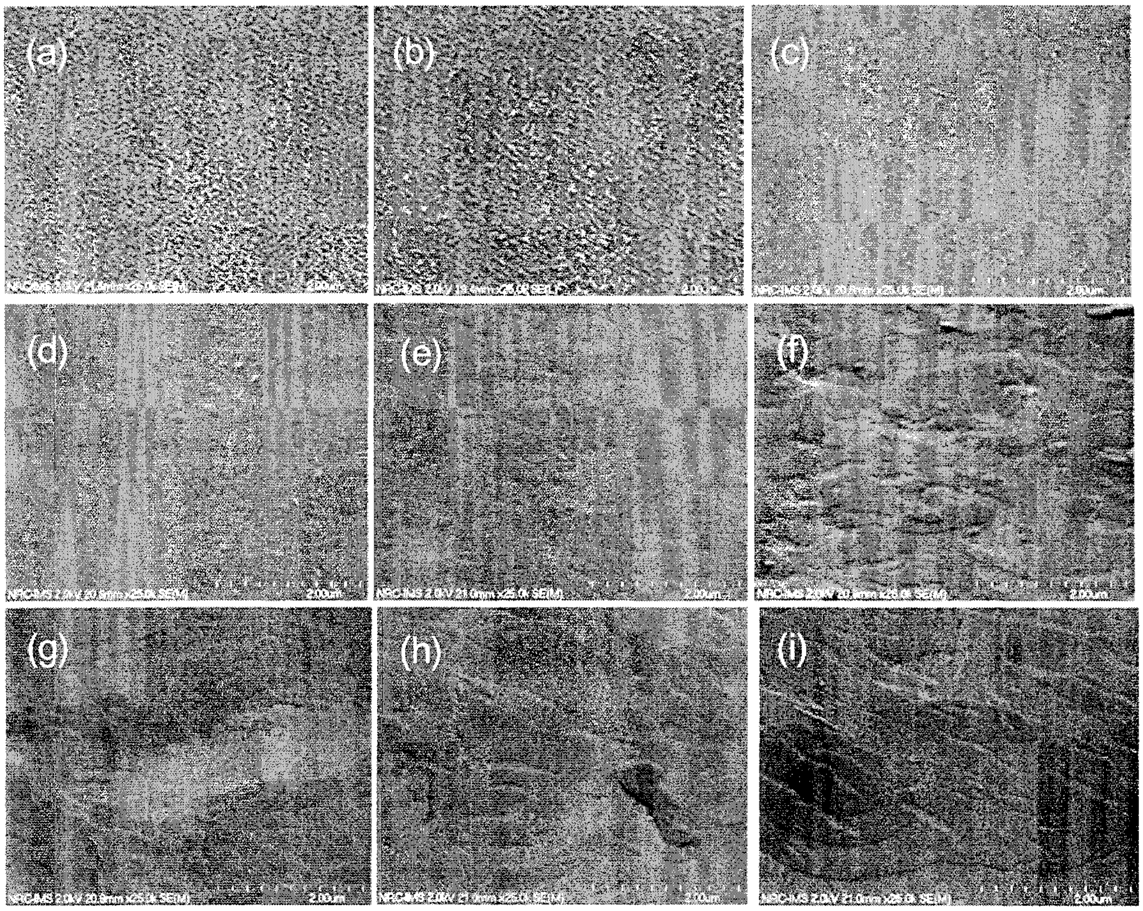

**Figure 8.18:** SEM images of 8H-BBEP deposited onto UV-$O_3$ cleaned $SiO_2$ surfaces: (a) 20°C, (b) 50°C, (c) 75°C, (d) 100°C, (e) 125°C, (f) 150°C, (g) 175°C, (h) 200°C, and (i) 225°C.

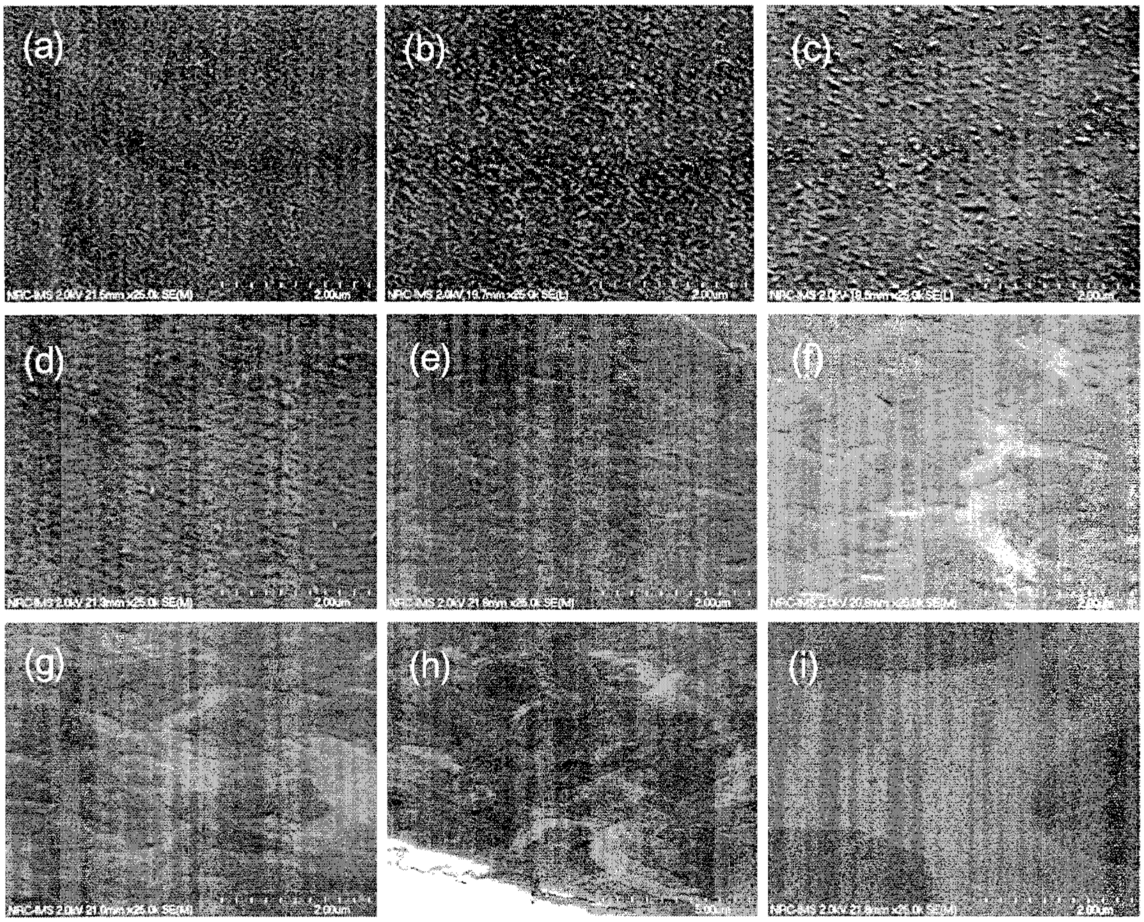

**Figure 8.19:** SEM images of 8H-BBEP deposited onto HMDS coated $SiO_2$ surfaces: (a) 20°C, (b) 50°C, (c) 75°C, (d) 100°C, (e) 125°C, (f) 150°C, (g) 175°C, (h) 200°C, and (i) 225°C.

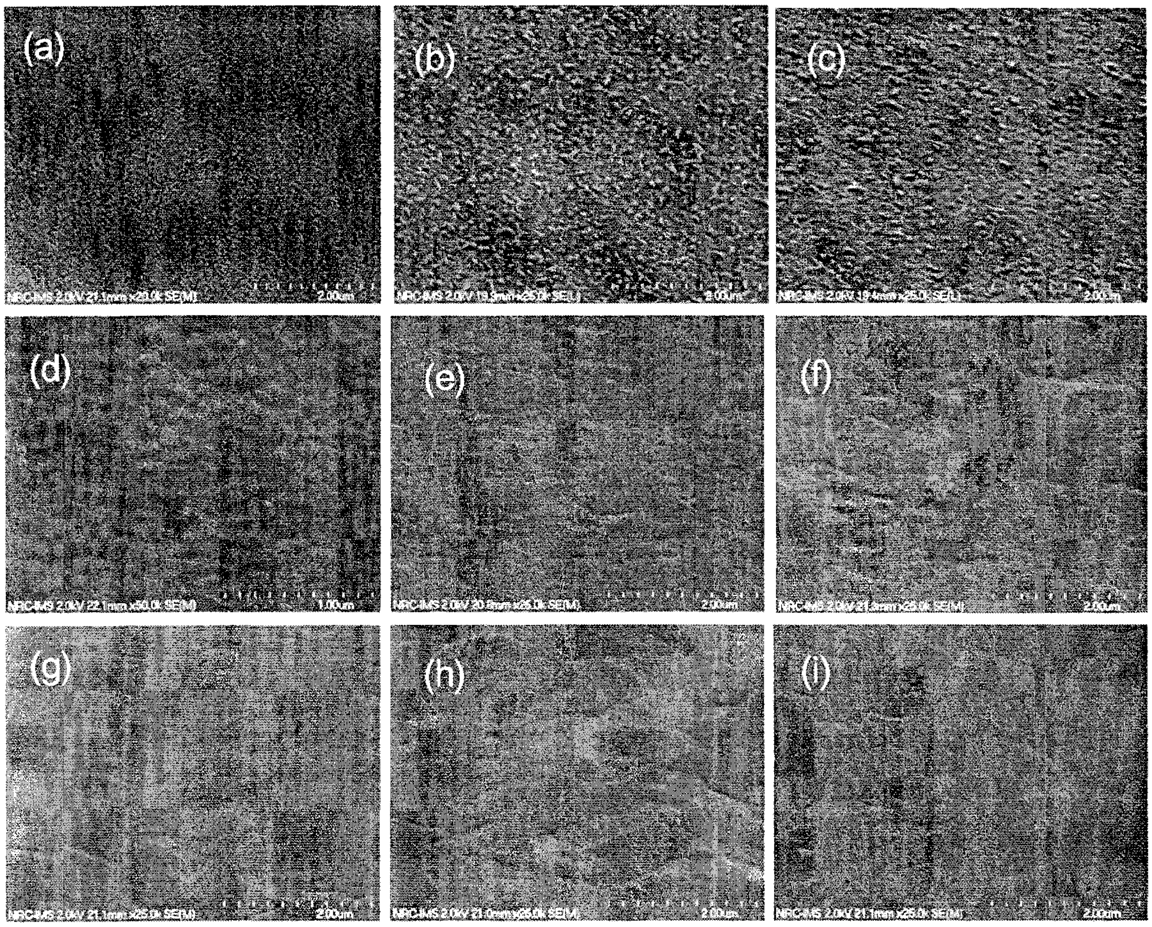

**Figure 8.20:** SEM images of 8H-BBEP deposited onto OTS-8 coated $SiO_2$ surfaces: (a) 20°C, (b) 50°C, (c) 75°C, (d) 100°C, (e) 125°C, (f) 150°C, (g) 175°C, (h) 200°C, and (i) 225°C.

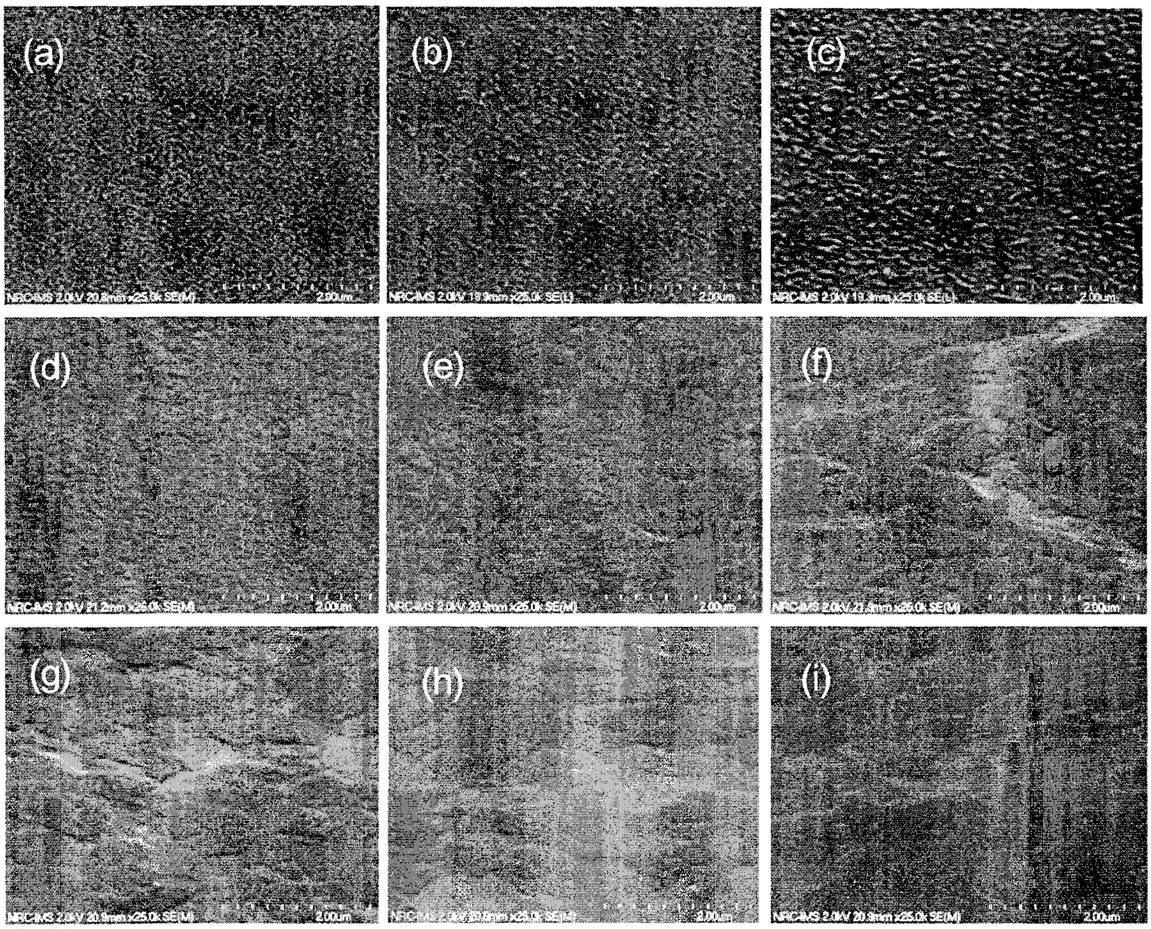

**Figure 8.21:** SEM images of 8H-BBEP deposited onto OTS-18 coated $SiO_2$ surfaces: (a) 20°C, (b) 50°C, (c) 75°C, (d) 100°C, (e) 125°C, (f) 150°C, (g) 175°C, (h) 200°C, and (i) 225°C.

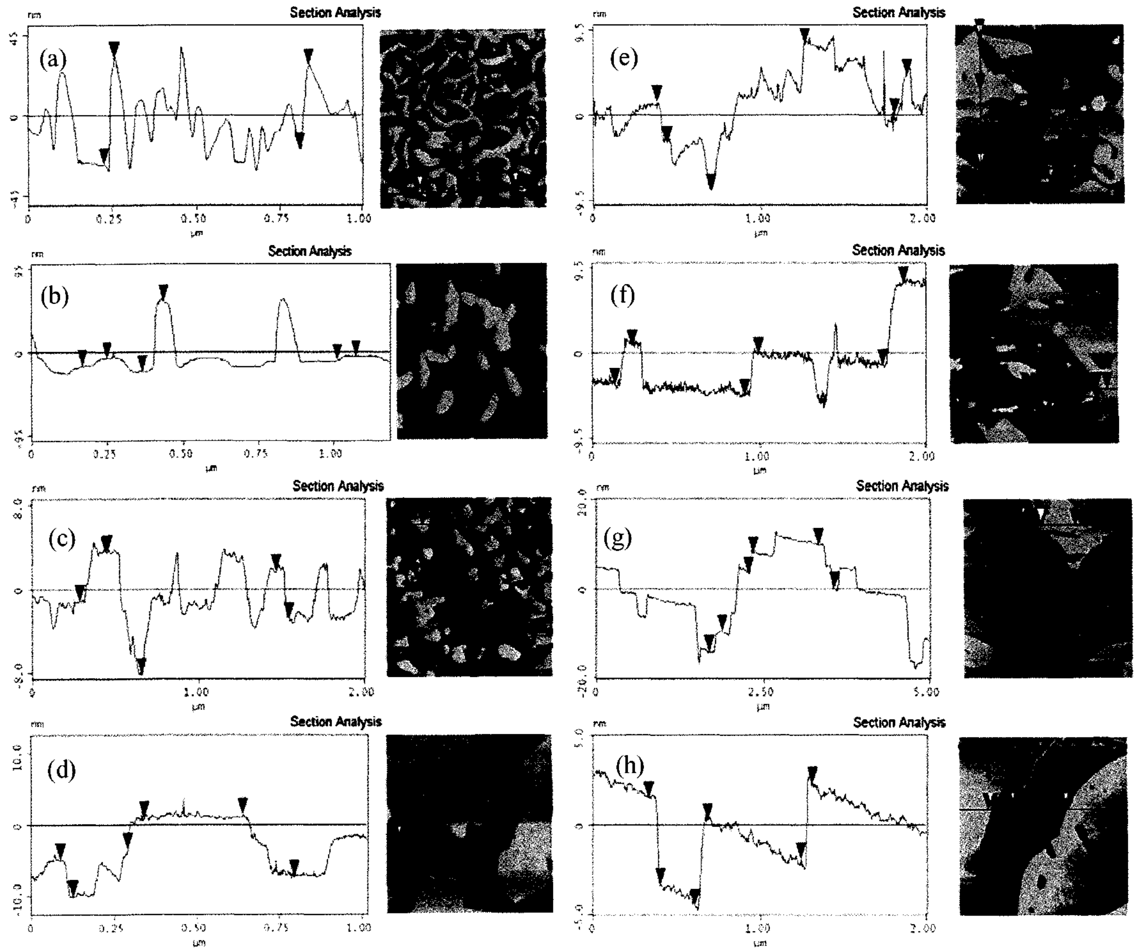

**Figure 8.22:** AFM images of 8H-BBEP deposited onto UV-$O_3$ cleaned $SiO_2$ surfaces: (a) 20°C, (b) 75°C, (c) 100°C, (d) 125°C, (e) 150°C, (f) 175°C, (g) 200°C, and (h) 225°C.

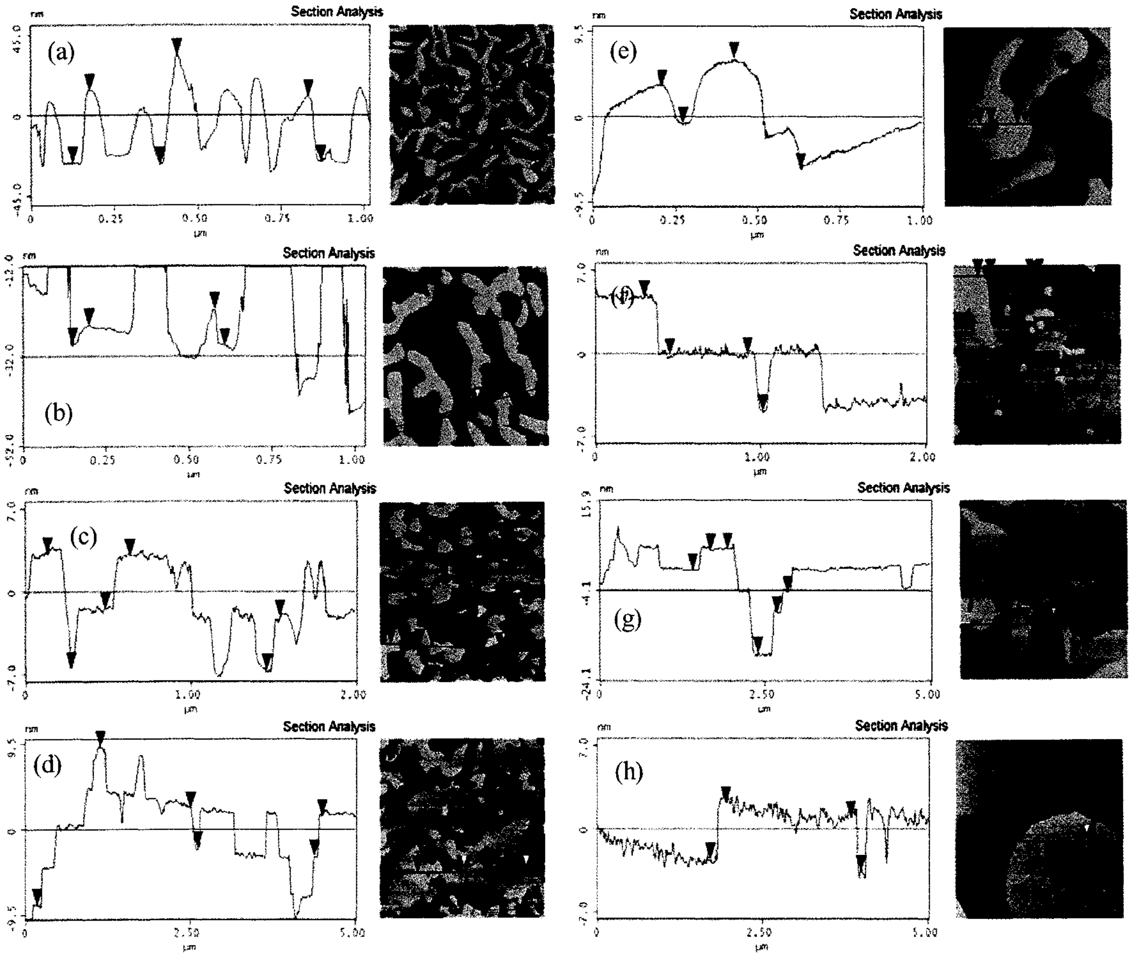

**Figure 8.23:** AFM images of 8H-BBEP deposited onto HMDS coated $SiO_2$ surfaces: (a) 20°C, (b) 75°C, (c) 100°C, (d) 125°C, (e) 150°C, (f) 175°C, (g) 200°C, and (h) 225°C.

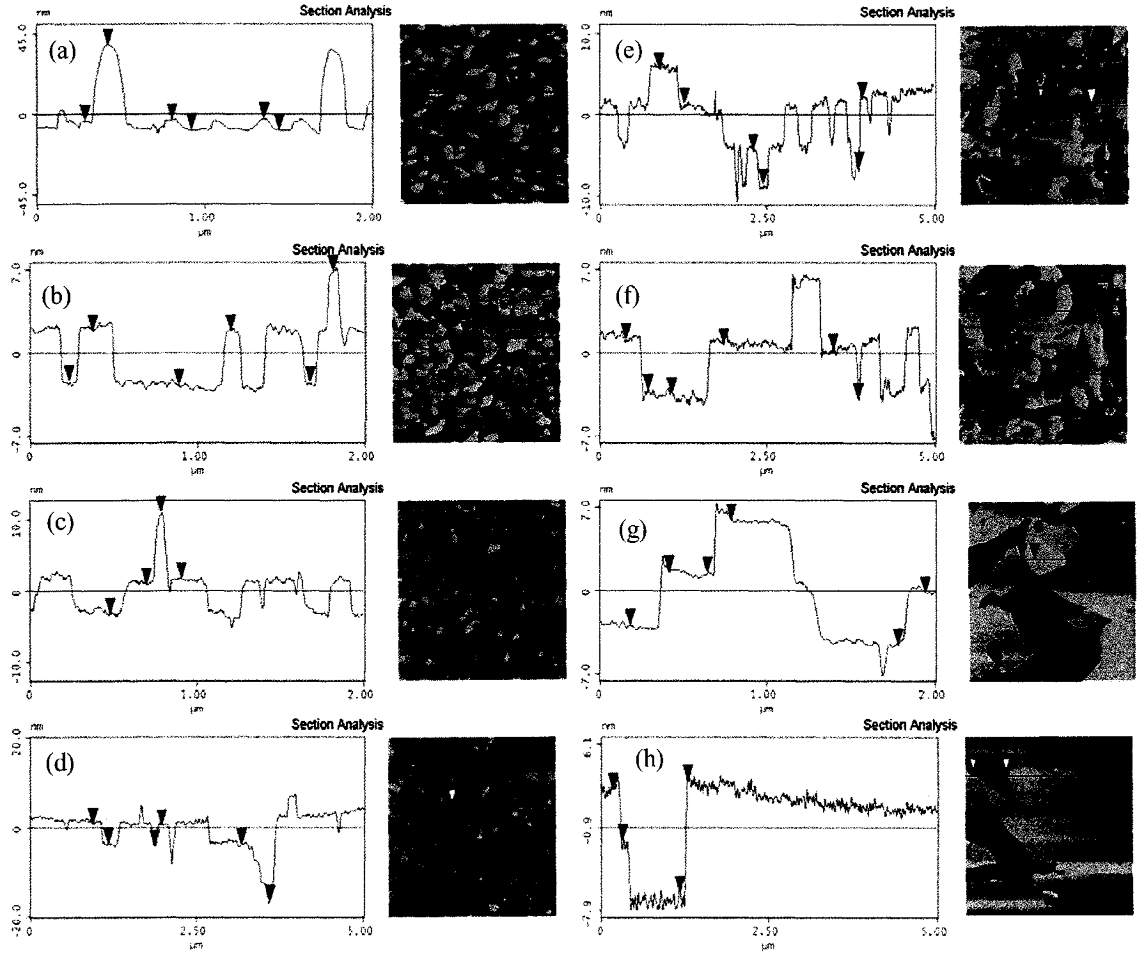

Figure 8.24: AFM images of 8H-BBEP deposited onto OTS-8 coated $SiO_2$ surfaces: (a) 20°C, (b) 75°C, (c) 100°C, (d) 125°C, (e) 150°C, (f) 175°C, (g) 200°C, and (h) 225°C.

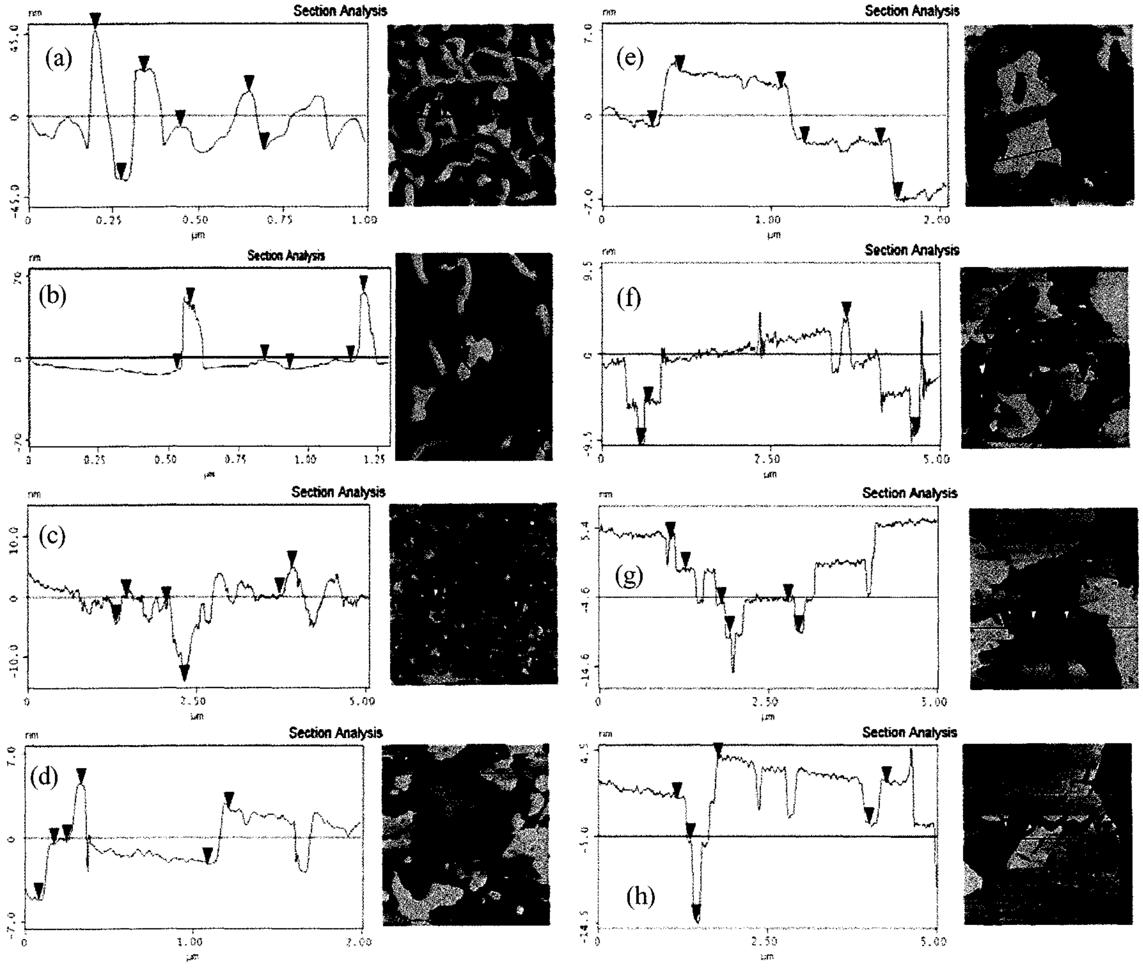

**Figure 8.25:** AFM images of 8H-BBEP deposited onto OTS-18 coated $SiO_2$ surfaces: (a) 20°C, (b) 75°C, (c) 100°C, (d) 125°C, (e) 150°C, (f) 175°C, (g) 200°C, and (h) 225°C.

**Table 8.4:** Summary of the step heights obtained from AFM sectional analysis for different temperatures and surface treatments. The XRD-determined thicknesses are also included for reference.

| | SiO$_2$ | | | | HMDS | | | | OTS-8 | | | | OTS-18 | | | |
|---|---|---|---|---|---|---|---|---|---|---|---|---|---|---|---|---|
| Temp | $d_1$ | $d_2$ | $d_3$ | $d_{XRD}$ | $d_1$ | $d_2$ | $d_3$ | $d_{XRD}$ | $d_1$ | $d_2$ | $d_3$ | $d_{XRD}$ | $d_1$ | $d_2$ | $d_3$ | $d_{XRD}$ |
| 20°C [a] | - | - | - | 42 | - | - | - | 42 | - | - | - | 43 | - | - | - | 43 |
| 75°C | 43 | - | 44 | 43 | 44 | $41^{2}$ | - | 44 | 42 | 45 | $46^{2}$ | 42 | - | 40 | - | 42 |
| 100°C | 46 | $41^{3}$ | 46 | 42 | $48^{2}$ | 45 | 45 | 41 | 41 | $46^{2}$ | - | 43 | 43 | $44^{3}$ | 44 | 43 |
| 125°C | 50 | $43^{2}$ | 43 | 42 | $44^{4}$ | 45 | 45 | 41 | 45 | 46 | $42^{3}$ | 42 | 46 | 47 | 46 | 44 |
| 150°C | 45 | $41^{3}$ | 44 | 41 | 42 | $41^{3}$ | - | 41 | 43 | 42 | $43^{2}$ | 42 | 46 | 45 | 46 | 44 |
| 175°C | 43 | 47 | $46^{2}$ | 41 | 47 | 47 | - | 42 | 41 | 42 | 43 | 42 | 49 | $43^{3}$ | - | 43 |
| 200°C | 45 | 45 | $47^{2}$ | 41 | 43 | $46^{5}$ | 45 | 41 | 45 | 44 | 44 | 42 | 43 | 43 | 41 | 43 |
| 225°C | 47 | 42 | 47 | 42 | 46 | 45 | - | 44 | 43 | $46^{2}$ | - | 41 | 45 | $45^{4}$ | 45 | 43 |

All AFM thickness values have an uncertainty of ± 2 Å.

Table 8.4 summarizes the step heights recorded in the AFM sectional analysis and the layer spacing extracted from the XRD peaks, rounded to the nearest 1Å. At 75°C there is good agreement between the AFM and XRD with the exception of the HMDS sample. As the temperature increases, however, the thickness value determined by XRD remains mostly constant while the thickness determined by AFM increases. A likely reason for $d_{XRD}$ to be lower than the thicknesses determined by AFM is that the hydrogens surrounding the $CH_3$ endgroups of the molecule do not have a significant electron density and therefore the X-rays do not interact with them, shortening the effective length of the molecule by about 2 Å, as shown in Figure 8.26.

Considering the thickness of the lamellar structures observed in the AFM images and the XRD d values, there is strong empirical evidence to suggest that the 8H-BBEP molecules

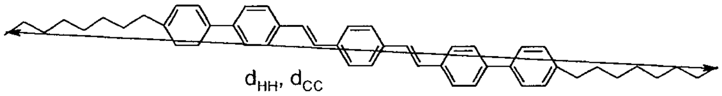

**Figure 8.26:** Length of the 8H-BBEP molecule calculated from the PM3 geometry minimization. The length from hydrogen to hydrogen is $d_{HH}$ = 44 Å and the carbon to carbon length is $d_{CC}$ = 42 Å.

are oriented perpendicular to the surface at a possible inclination, shown in Figure 8.27. The amount of alkyl chain overlap between adjacent layers of 8H-BBEP affects the step height measured by AFM, but will not affect the XRD results as the electron density is essentially zero between the layers. If the alkyl chain overlap is large, then the step height will appear smaller when the inclination angle is kept constant. Similarly, if the overlap is minimal, the step height will appear larger in the AFM surface profile.

The XRD data also suggests that the long axis of the molecules are perpendicular to the surface as the calculated carbon to carbon length of the molecule was found to be about 42 Å for the trans-trans configuration, shown in Figure 8.26.

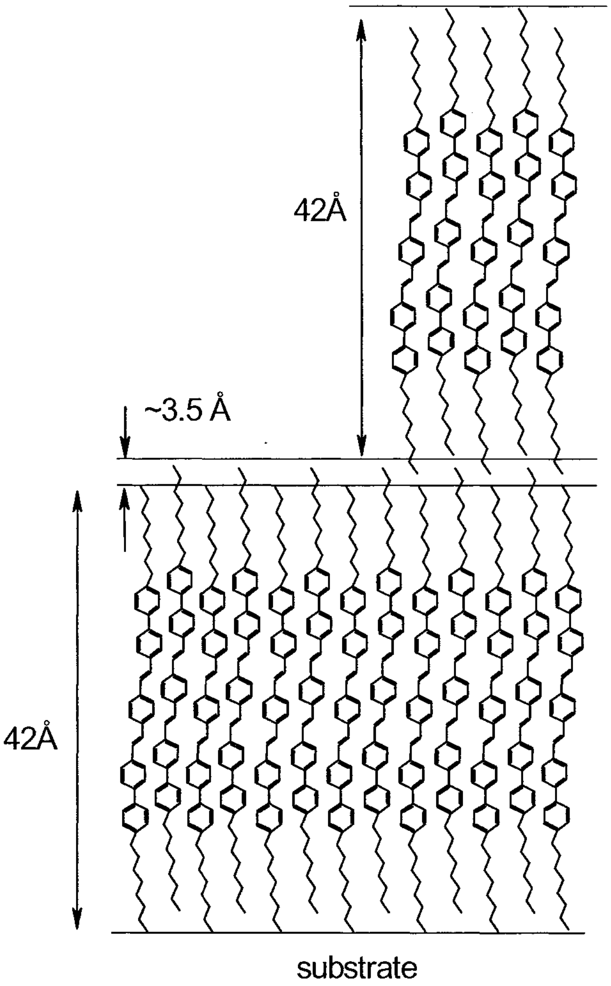

**Figure 8.27:** Proposed molecular arrangement of 8H-BBEP in thin film form. The calculated length of the backbone is 42 Å. The addition of the hydrogens at each end (2 Å) and the offsets at the interface (3-4 Å) can explain the discrepancy between the AFM step heights and the XRD layer thickness. The AFM steps which are lower can be attributed to a larger tilt angle with respect to the surface normal or less offset (i.e. lower packing density).

The generally accepted theory regarding the effect of a SAM on the ordering of organic semiconductors is that the alkyl chains on the OTS-18 molecule interact with alkyl chains on the organic semiconductor, either by preferentially attracting the alkyl chains towards the SAM and/or interdigitation of the alkyl chains of the semiconductor, resulting in better packing and electrical performance in a transistor. Pentacene, however, is an organic semiconductor which does not fit this model: it has no alkyl chains, yet displays a substantial increase in mobility when used in an OFET with an OTS-18 SAM. It is also unclear how, using the above theory, one could account for the HMDS results as the single methyl group cannot form any kind of interdigitation or overlap with the alkyl chain of the organic semiconductor.

Based on the AFM and XRD results, it is proposed that, while the SAM does influence the organization of the organic semiconductor, it does not do so through a physical or chemical interaction between the alkyl chains of the SAM and organic semiconductor, but by a decrease of the surface energy of the substrate allowing a natural self-assembly mechanism to dominate the formation of the organic semiconductor film. When the surface is transformed from a polar hydrophillic surface to a non-polar hydrophobic surface, the surface energy is decreased. As the surface energy decreases, the test liquid (water) in the contact angle goniometer will evolve from wetting the entire solid surface (low contact angle, high surface energy) to not wetting the surface at all (high contact angle, low surface energy).

In the model proposed, the organic molecules will arrange themselves in a thermodynamically favourable orientation if the substrate temperature provides adequate thermal energy for the molecules to be mobile on the surface. As verified by AFM and XRD, the 8H-BBEP molecules will orient themselves perpendicular to the $SiO_2$ surface even in the absence of a SAM, as indicated in the AFM images in Figure 8.22. When the $SiO_2$ is coated with HMDS, the contact angle increases to 75-80° while the surface energy is decreased and the lamellar structure is visible at a lower temperature compared to the bare $SiO_2$ samples. As the temperature increases, the grain size of the HMDS samples also increases when compared to the bare $SiO_2$ samples. Similarly, when OTS-8 or OTS-18 are used, the contact angles are very similar implying that the surface energies are similar as well. As the temperature is increased, the size of the grains increases, the films are smoother and have more continuity, and the number of lamellae decreases.

As stated in Section 8.1, 8H-BBEP displays a liquid crystal phase change between 115°C and 135°C (Figure 8.1b). Although the thermodynamics of the liquid crystal transition are beyond the scope of this work, an important characteristic to consider is that the LC phase transition is a dynamic process. During the deposition, no allowances were made to ensure that the LC phase transition was complete before allowing the substrates to cool. When the material is in the LC phase there is the opportunity to induce "natural" order within the film due to natural thermodynamic processes. Low magnification SEM imaging of samples deposited at a substrate temperature of 125°C does indicate the presence of a large number of cracks or voids in the film, shown in Figure 8.28.

The SAM also affects the electrical properties of the OFET and will be discussed in Section 8.5.

### 8.4.5 Pentacene Thin Film Morphology

OFETs using pentacene as the active organic semiconductor were fabricated as control samples. All of the surface modification techniques were used with pentacene OFETs as the performance and morphology of pentacene on $SiO_2$ and OTS-18 has been widely reported in the literature. Literature searches have not revealed any reports on pentacene OFETs using HMDS and minimal reports on any type of OFETs using OTS-8.[7,8]

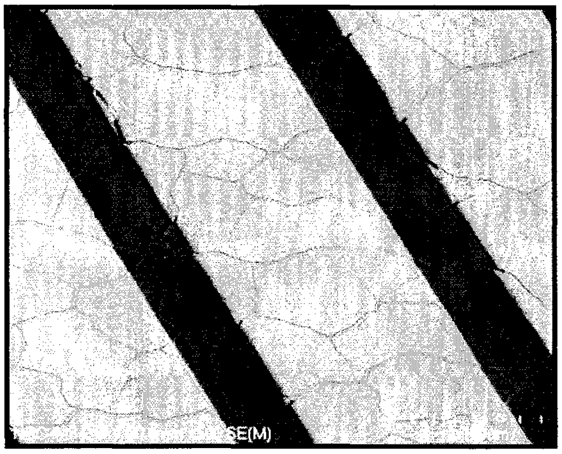

**Figure 8.28:** Low magnification (500x) SEM image of an 8H-BBEP film deposited on HMDS at 125°C. The large cracks are present in all four types of devices and are believed to be a result of the LC phase transition.

Figure 8.29 illustrates the morphology of a 300 Å thick pentacene film deposited at ambient temperature at 2 Å/sec. The portion labeled as the drain is covered with a layer of gold. The dendritic growth mechanism of pentacene is obvious from the morphology. The lighter coloured objects are new layers of pentacene which are beginning to form.

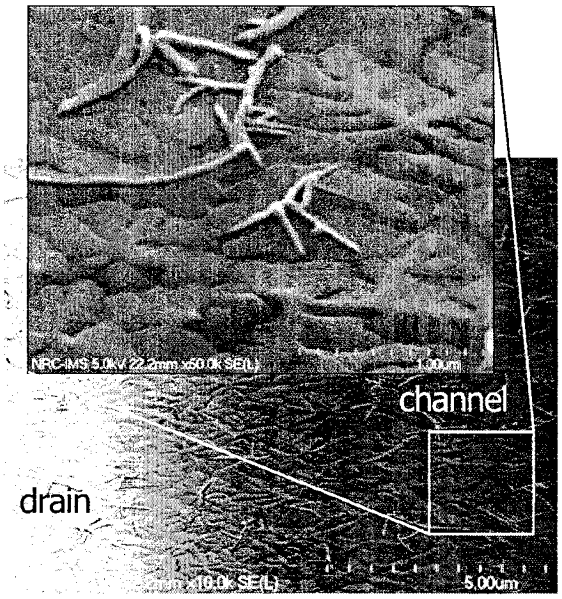

**Figure 8.29:** SEM of a pentacene film deposited at room temperature onto bare $SiO_2$. The film is approximately 300 Å thick and was deposited at a rate of 2 Å/sec.

Figure 8.30 illustrates the film morphology of pentacene deposited onto (a)

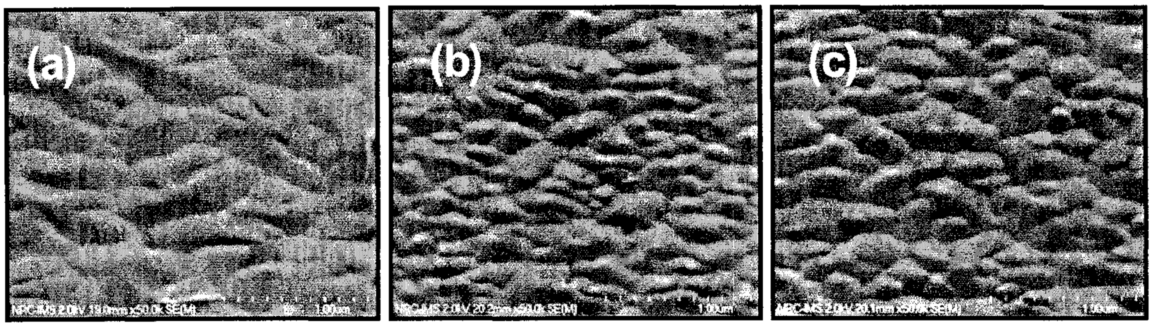

**Figure 8.30:** SEMs of pentacene deposited on (a) HMDS, (b) OTS-8, and (c) OTS-18 coated $SiO_2$ at ambient temperature.

HMDS, (b) OTS-18 and (c) OTS-8 modified $SiO_2$ surfaces at ambient temperature. The films on HMDS exhibit grains of consistent size across the film while the OTS samples exhibit large grains of similar size with small grains dispersed between them.

The effect of raising the substrate temperature to 60°C is shown in Figure 8.31 for (a) HMDS, (b) OTS-18 and (c) OTS-8. Figure 8.32 depicts the AFM sectional analysis of the pentacene films deposited at 60 °C on $SiO_2$, HMDS, OTS-8, and OTS-18. All of the pentacene films showed lamellar structure with a step height between 14 and 18 Å, which is consistent with literature reports of 15.5 Å for the desired "thin film" phase of pentacene.[9,10]

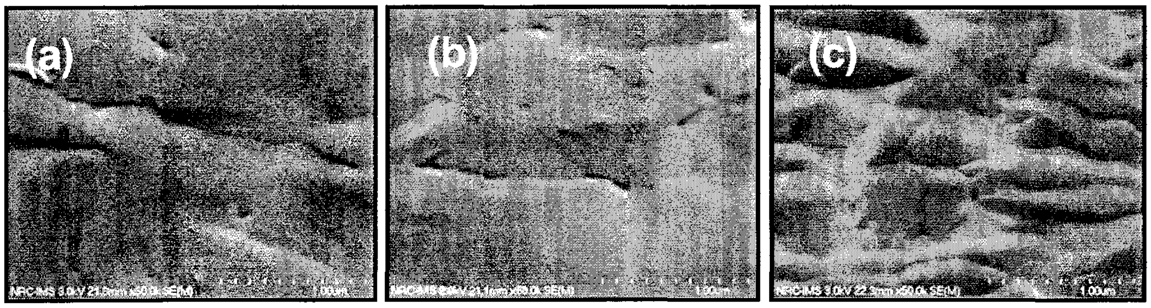

**Figure 8.31:** SEMs of pentacene deposited on (a) HMDS, (b) OTS-8 and (c) OTS-18 coated $SiO_2$ at a substrate temperature of 60°C.

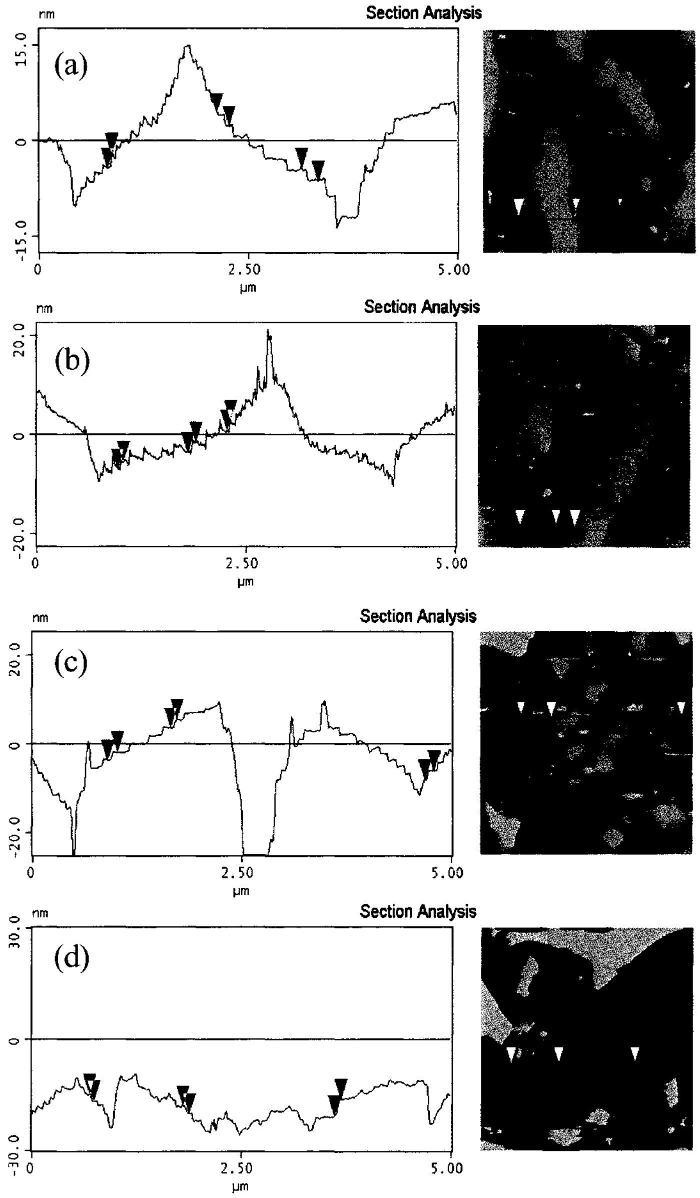

**Figure 8.32:** Sectional analysis of pentacene films deposited at a substrate temperature of 60°C for (a) UV-$O_3$ treated $SiO_2$, (b) HMDS, (c) OTS-8, and (d) OTS-18. The step height is between 14-18 Å.

## 8.5 Organic Field Effect Transistors

### 8.5.1 Pentacene

The pentacene-based OFETs that were fabricated are summarized in Table 8.5: the gate dielectric ($SiO_2$) thickness (±5% from the manufacturer), the source (S) and drain (D) thickness, the thickness of the organic semiconductor, and the substrate temperature during deposition. The uncertainty in the thicknesses was ± 1 Å. All of the samples fabricated after pent-15 consisted of UV-$O_3$, HMDS, OTS-8 and OTS-18 treated $SiO_2$ samples (two of each). The samples prior to and including pent-15 were control samples to ensure that the fabrication process yielded pentacene OFETs which were comparable to the literature and to verify the quality of the SAM layers. For each sample, 7-10 devices were tested.

**Table 8.5**: Summary of the TC-OFET devices fabricated with pentacene. The error in the organic and source and drain layers is ± 1 Å. The error in the temperature is ± 5 °C

| Sample ID | $d_{gate}$ [ kÅ ] | $d_{org}$ [ Å ] | $d_{S \& D}$ [ Å ] | Temp [ °C ] |
|---|---|---|---|---|
| pent-01 | 6 | 200 | 1000 | 20 |
| pent-02 | 3 | 200 | 1000 | 20 |
| pent-03 | 3 | 200 | 1000 | 90 |
| pent-04 | 3 | 180 | 1000 | 100 |
| pent-05 | 3 | 350 | - | 90 |
| pent-06 | 3 | - | - | 100 |
| pent-07 | 6 | 300 | 650 | 20 |
| pent-08 | 6 | 300 | 900 | 20 |
| pent-09 | 6 | 300 | 600 | 20 |
| pent-10 | 3, 6 | 300 | 600 | 90 |
| pent-11 | 6 | 300 | 600 | 90 |
| pent-12 | 6 | 300 | - | 90 |
| pent-13 | 6 | 300 | 750 | 20 |
| pent-14 | 6 | 300 | - | 90 |
| pent-15 | 6 | 300 | 750 | 20 |
| pent-16 | 3, 6 | 300 | 750 | 20 |
| pent-17 | 3, 6 | 300 | 700 | 60 |
| pent-18 | 3, 6 | 300 | 700 | 90 |
| pent-19 | 3, 6 | 350 | 700 | 60 |
| pent-20 | 3, 6 | 350 | 525 | 90 |
| pent-21 | 6 | 350 | 700 | 60 |
| pent-22 | 6 | 350 | 700 | 90 |

Bottom contact (BC) OFETs were fabricated with pentacene and the typical current-voltage graph is shown in Figure 8.33a. The transfer characteristics for the saturation regime are shown in Figure 8.33b. In this device, the channel length is 1000 µm, the channel width is 75 µm, and the pentacene film is 300 Å thick. The positive drain current denoted by the arrow in Figure 8.33a at zero applied $V_d$ is due to leakage current passing through the organic film from the gate electrode to the source. While in this particular sample the leakage current is small, in some samples the leakage current is of the same order of magnitude as the current passing through the device when operating normally. Mechanically removing the organic material around the perimeter of the source and drain electrodes helps to minimize the leakage

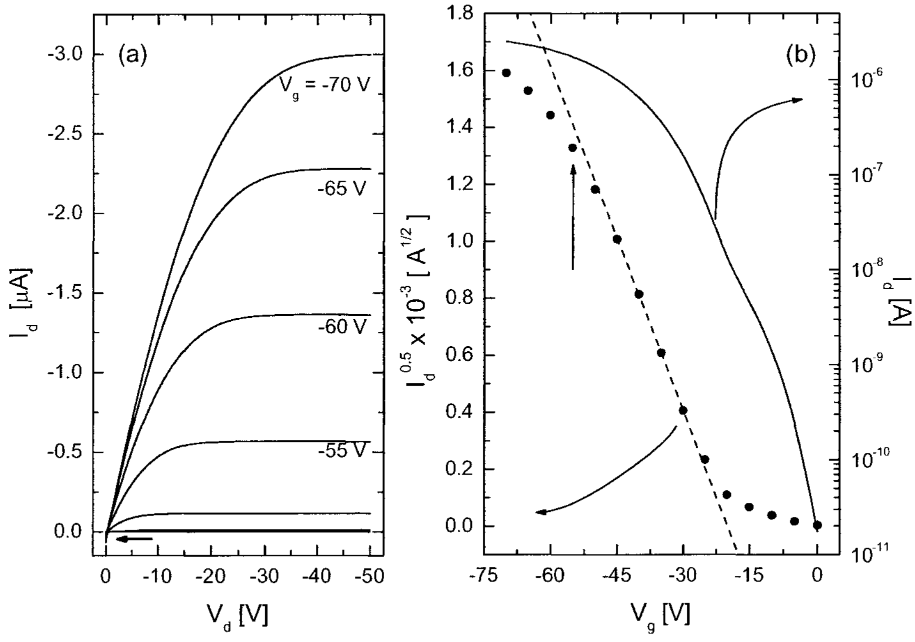

**Figure 8.33:** The (a) output and (b) transfer characteristics of a bottom contact pentacene OFET with an aspect ratio of 1000:75.

current. Table 8.6 summarizes the electrical parameters of this BC-OFET.

**Table 8.6:** Summary of the pentacene BC-OFET device parameters from Figure 8.30.

| $\mu$ [ cm$^2$/Vs] | $V_t$ [V] | $I_{on/off}$ | S [V/dB] |
|---|---|---|---|
| $1.4 \pm 0.1 \times 10^{-2}$ | $-20 \pm 2$ | $1.4 \times 10^5$ | 5.2 |

In Figure 8.33b the data points deviate from the straight line at $V_g = -60$ V. This phenomenon is attributed to so-called gate bias stress, and is observed in OFETs using many different types of organic semiconductors. Several groups have studied this non-linearity and have suggested that it originates from the trapping of charges at the gate dielectric-organic interface and from repeated poling of the electric field which can cause structural changes in the molecule.[11-14] Contact resistance between the source and drain electrodes and the organic semiconductors is another possible source for the non-linearity.

There were three significant technical issues with this bottom contact design. First, the contact area between the source and drain and the organic semiconductor is extremely small. The source and drain electrodes have dimensions of 1000 μm wide by 20 μm long by 0.3 μm high. Assuming the best case scenario where the organic layer is in contact with the entire 0.3 μm high sidewall, there is a maximum 300 μm$^2$ surface area which is available for charge injection. Moreover, if a 300 Å thick organic film is used and assuming perfect contact at the sidewall, the surface area available for injection is an order of magnitude less at 30 μm$^2$. The second problem is related to the physical size of the electrode and its ability to withstand the high operating voltages applied to the transistor. Usually voltages up to -100 V are applied between the source and drain electrodes. Since the electrodes are so small, arcing and short circuits occur easily with the potential to destroy the device. For this reason, it is proposed that if a new photomask is to be fabricated that the electrode size should be increased to accommodate the large electric fields. The third major problem occurs during surface modification. The RCA cleaning process requires the use of ammonium and hydrochloric acid. Ammonia or hydrochloric acid are generated as byproducts of the HMDS or trichlorosilane priming process, respectively. In all cases, these chemicals may affect the source and drain electrodes in a negative way. For example, pinholes were observed in the electrodes after soaking in an OTS solution for 24 hours. The bottom contact geometry was not used for any other devices.

Pentacene top contact (TC) OFETs displayed substantially improved electrical characteristics over their bottom contact counterparts. The transfer characteristics for pentacene OFETs deposited at room temperature for different substrate treatments are shown in Figure 8.34. The results are summarized in Table 8.7. All of the surface treatments increased the mobility, on/off ratio and the subthreshold slope. The threshold voltage was substantially decreased with the OTS treatments but was slightly increased on the HMDS treated sample. However, the HMDS sample displayed an outstanding on/off ratio greater than $10^8$ and the best subthreshold slope of the series of samples.

**Table 8.7:** Summary of pentacene TC-OFETs deposited at a substrate temperature of 20°C.

| | $\mu$ [cm$^2$/Vs] | $V_t$ [V] | $I_{on/off}$ | S [V/dB] | $N_t$ [ x $10^{11}$ cm$^{-2}$] | $E_b$$^a$ [meV] | $\mu_o$$^a$ [cm$^2$/Vs] |
|---|---|---|---|---|---|---|---|
| $SiO_2$ | 0.30 ± 0.05 | -25 ± 3 | ~ $10^4$ | 13.7 | 7.2 ± 0.3 | 25.0 ± 0.6 | 0.79 ± 0.01 |
| HMDS | 0.54 ± 0.05 | -26 ± 2 | > $10^8$ | 3.4 | 6.3 ± 0.3 | 19.3 ± 0.4 | 1.14 ± 0.01 |
| OTS-8 | 1.2 ± 0.1 | -5 ± 1 | > $10^7$ | 4.7 | 4.0 ± 0.2 | 7.6 ± 1.0 | 1.56 ± 0.05 |
| OTS-18 | 0.6 ± 0.1 | -8 ± 1 | > $10^6$ | 4.2 | 5.3 ± 0.2 | 13.9 ± 0.5 | 0.96 ± 0.03 |

[a] calculated at $V_g$ = -100 V

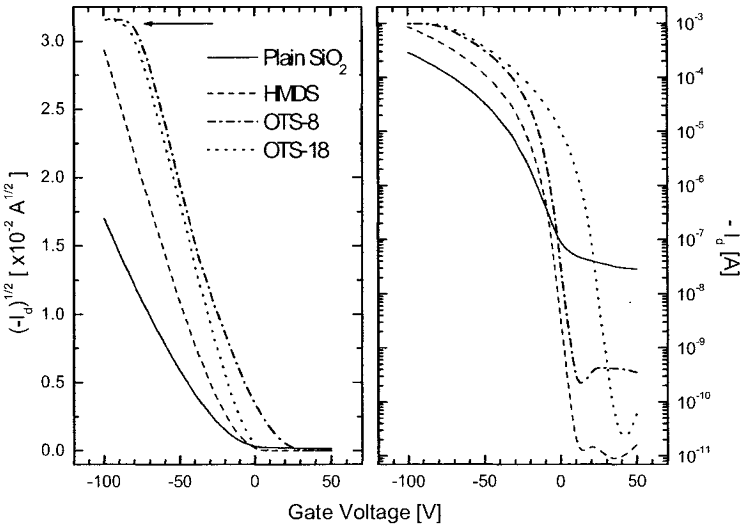

**Figure 8.34:** Transfer characteristics for TC-OFETs using pentacene deposited at room temperature. Four substrate treatments are shown: plain $SiO_2$ (cleaned with UV-$O_3$), HMDS, OTS-8, and OTS-18. The arrow denotes where the HP4155c reached its compliance limit of 1mA.

Figure 8.35 shows Levinson plots for all four types of devices and the parameters that were extracted from the plots are summarized in Table 8.7. Using the grain boundary model, we can see that the interface trap density $N_t$ is of the order of $10^{11}$ cm$^{-2}$ and decreases from $SiO_2$, HMDS, OTS-18, and OTS-8, which is consistent with reports in the literature.[15] Similar trends are shown for the grain boundary barrier height, $E_b$, decreasing from 25.0 meV for $SiO_2$ to 7.6 meV for OTS-8 at $V_g$ = -100 V. The trap-free mobility at $V_g$= -100 V also varies from 0.79 cm$^2$/Vs for $SiO_2$ to 1.56 cm$^2$/Vs for OTS-8. This is the mobility which is expected in a trap-free film.

Table 8.8 summarizes the electrical properties of the pentacene TC-OFETs when the substrate temperature was increased to 60°C. The $SiO_2$ sample was so poor that it was not

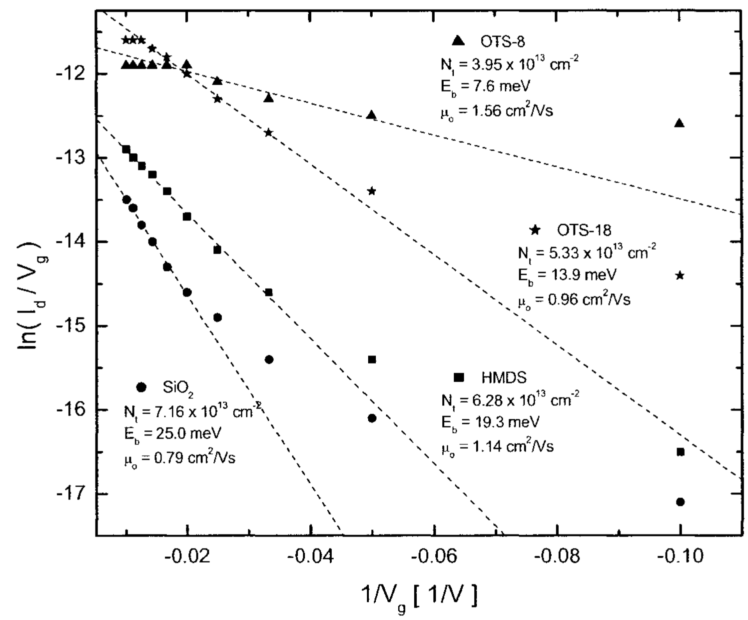

**Figure 8.35:** Levinson plot for the room temperature pentacene TC-OFETs listed in Table 8.7. The details are discussed in the text.

possible to extract any meaningful results from the electrical data. The extremely poor performance of the $SiO_2$ device is attributed to the UV-$O_3$ cleaning process which generates a sheet of conductive hydroxyl groups on the surface. This sheet charge provided a channel for

**Table 8.8:** Summary of pentacene TC-OFETs deposited at a substrate temperature of 60 °C.

| | $\mu$ [$cm^2$/Vs] | $V_t$ [V] | $I_{on/off}$ | S [V/dB] | $N_t$ [x $10^{11}$ $cm^{-2}$] | $E_b$$^c$ [meV] | $\mu_o$$^c$ [$cm^2$/Vs] |
|---|---|---|---|---|---|---|---|
| $SiO_2$$^a$ | - | - | - | - | - | - | - |
| HMDS | 0.81 ± 0.07 | -28.0 ± 3.0 | 6.5 x $10^7$ | 4.9 | 7.0 ± 0.3 | 24.2 ± 1.0 | 2.1 ± 0.4 |
| OTS-8 | 1.00 ± 0.08 | -5.0 ± 1.0 | 1.7 x $10^6$ | 5.8 | 4.5 ± 0.3 | 10.1 ± 0.8 | 1.5 ± 0.2 |
| OTS-18 | 2.40 ± 0.20 | -4.6 ± 0.6 | > $10^8$ $^b$ | 7.5 | 4.2 ± 0.3 | 8.4 ± 0.7 | 3.3 ± 0.3 |

[a] unable to measure
[b] extrapolated
[c] calculated at $V_g$ = -100 V

the leakage current between the drain and gate electrodes. It has also been suggested that moisture in the air can greatly affect the leakage current and other electrical characteristics of pentacene transistors.[15]

The OTS-8 sample showed a slight decrease in the mobility, threshold voltage and on/off ratio with an increase in the subthreshold slope. The HMDS and OTS-18 devices showed an increase in mobility. The threshold voltage increased slightly for the HMDS sample but decreased for the OTS-18 sample. The subthreshold slope of both samples increased. The mobility of the OTS-18/pentacene TC-OFET was 2.40 cm$^2$/Vs and is one of the highest reported values for polycrystalline pentacene.

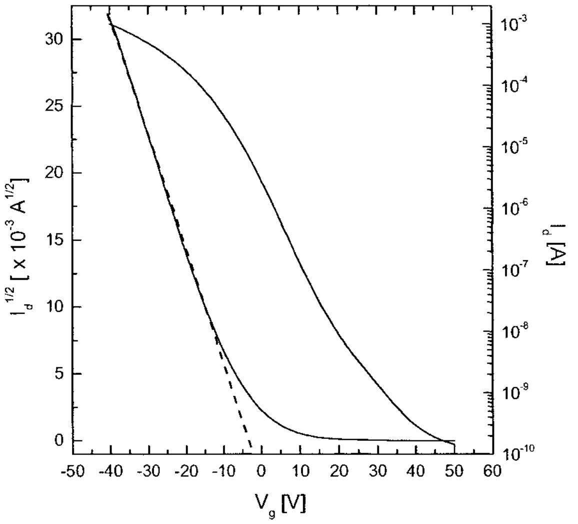

**Figure 8.36:** The transfer characteristics for a pentacene TC-OFET deposited at a substrate temperature of 60 °C. The results are summarized in the text.

The transfer characteristics for the OTS-18/pentacene sample are shown in Figure 8.36. If we extrapolate the linear fit in the saturation region to $V_g$ = -100 V, the on/off ratio is estimated to be greater than $10^8$. Despite the excellent mobility and on/off ratio, there is a non-negligible leakage current when $V_g \geq 0$ V, which increases the subthreshold slope to 7.4 V/dB, which is too large for practical applications. Current state of the art polycrystalline pentacene OFETs typically exhibit mobilities between 1-2 cm$^2$/Vs, $V_t$ around 1-3 V, $I_{on/off} > 10^7$ and S < 2 V/dB.[16]

The Levinson plots of the HMDS, OTS-8 and OTS-18 pentacene devices are shown in Figure 8.37. The deviation from the straight line for small inverse gate voltage ( large $V_g$) is attributed to the clipping of the IV curves as the compliance limit of the HP 4155c is reached. The results of the Levinson plot are summarized in Table 8.8. The OTS-18 sample had the lowest trap density at the grain boundaries with a value of 4.15 x $10^{11}$ $cm^{-2}$ while HMDS had the highest at 7.04 x $10^{11}$ $cm^{-2}$. Correspondingly, the OTS-18 sample had the highest field effect mobility of 2.40 $cm^2/Vs$ and highest trap-free mobility of 3.3 $cm^2/Vs$ while HMDS had the lowest: 0.81 $cm^2/Vs$ and 2.1 $cm^2/Vs$, respectively.

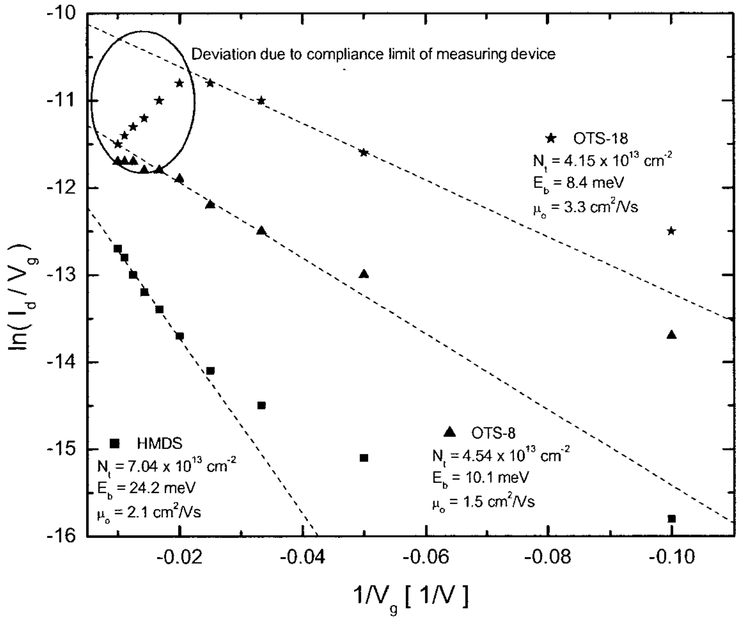

**Figure 8.37:** Levinson plots of pentacene TC-OFETs on HMDS, OTS-8 and OTS-18 coated $SiO_2$ at a substrate temperature of 60°C. The results are summarized in Table 8.8.

### 8.5.2 BBEP OFETs

Table 8.9 summarizes the transistors that were fabricated using BBEP: the gate dielectric ($SiO_2$) thickness ($d_{gate}$), source and drain thickness ($d_{S\ \&\ D}$), organic semiconductor thickness ($d_{org}$), and the substrate temperature during deposition (Temp).

The electrical results for BBEP are extremely poor. Only one device, the $SiO_2$ sample from the o2-08 series, displayed any field effect. The output and transfer characteristics are shown in Figure 8.38. The calculated results were $\mu = 10^{-7}$ cm²/Vs, $V_t = -41$ V, and $I_{on/off} < 3$. It was not possible to measure the subthreshold slope.

A probable explanation for the extremely poor electrical characteristics of the BBEP samples are from the poor film forming characteristics and the synthesis route (see Appendix

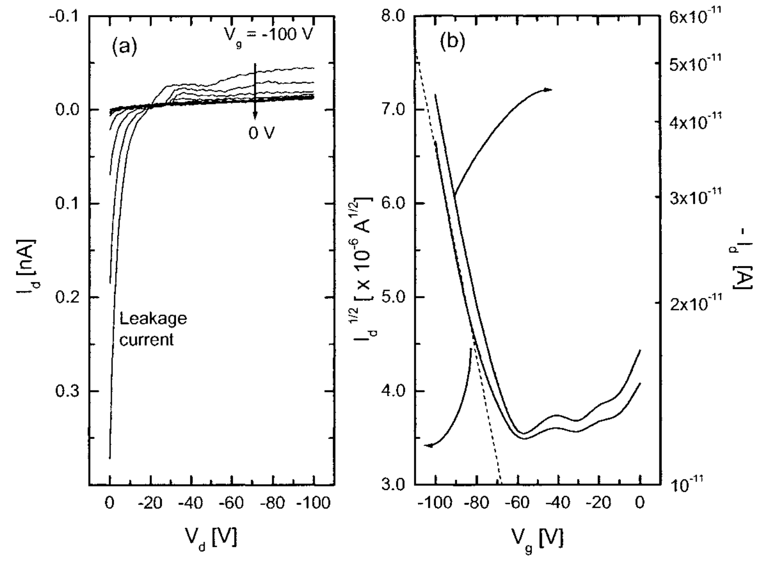

**Figure 8.38:** (a) Output and (b) transfer characteristics for a BBEP TC-OFET at $V_d$ = -100 V.

A for a detailed description of the synthesis process). In the Wittig reaction, there is no selectivity between the cis-cis, cis-trans, and trans-trans configurations. As a result, it is expected that 25% will have the cis-cis configuration, 25% with the trans-trans configuration, and 50% with the cis-trans or trans-cis configurations. There has been evidence in PPV that vinylene moieties in the cis configuration can enhance the solid state luminescence by disrupting chain packing.[17-19] This finding implies that although BBEP may possess a large hole mobility, the cis conformations in the molecule prevent efficient packing of the molecules, reducing the $\pi$-$\pi^*$ overlapping between nearest neighbour molecules and greatly reducing the mobility of holes in the material. This behaviour is also expected considering the semi-empirical quantum mechanical modeling results presented in Chapter 7. All of the BBEP configurations with cis linkages showed kinks in the backbone which disrupts the $\pi$ conjugation along the backbone.

**Table 8.9**: Summary of the TC-OFET devices fabricated using BBEP. The error in the organic and source and drain layers is ± 1 Å. The error in the temperature is ± 5 °C

| Sample ID | $d_{gate}$ [ kÅ ] | $d_{org}$ [ Å ] | $d_{S\ \&\ D}$ [ Å ] | Temp [ °C ] |
|---|---|---|---|---|
| o2-01 | 6 | 300 | 900 | 20 |
| o2-02 | 6 | 300 | 900 | 75 |
| o2-03 | 3 | 350 | - | 20 |
| o2-04 | 3 | 350 | - | 50 |
| o2-05 | 3 | 350 | - | 75 |
| o2-06 | 3 | 400 | - | 100 |
| o2-07 | 3 | 400 | - | 125 |
| o2-08 | 6 | 300 | 1000 | 90 |

### 8.5.3 8H-BBEP OFETs

All of the top contact OFETs fabricated with 8H-BBEP are summarized in Table 8.10. All of the samples fabricated after o4a-29 consisted of UV-$O_3$, HMDS, OTS-8 and OTS-18 treated $SiO_2$ samples (two of each).

The typical transfer characteristics of each of the four different types of samples are shown in Figure 8.39, the Levinson plots are shown in Figure 8.40, and the parameters for the best devices at each of the deposition temperatures between 20°C and 225°C are summarized in Table 8.11 through Table 8.18.

While the data presented in the tables was reproducible, there was considerable variation in mobility and threshold voltage from device to device, even those separated by only a few hundred micrometers on the same substrate. Considering the high threshold voltages for a series of devices on the same chip could span a range as high as 20-30 V, we conclude that there were severe electrical contact issues present between 8H-BBEP and the gold source and drain

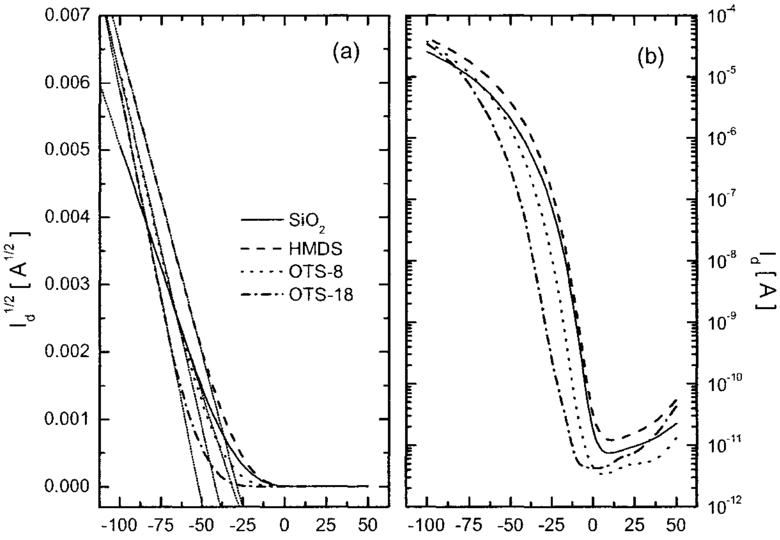

**Figure 8.39:** Transfer characteristics for a TC-OFET using 8H-BBEP as the organic semiconductor. (a) denotes the saturation regime $I_d^{0.5}$ vs. $V_g$ curves and (b) denotes $I_d$ vs $V_g$ plotted on a semi-log scale.

**Table 8.10**: Summary of the OFETs that were fabricated using 8H-BBEP.The error in the organic and source and drain layers is ± 1 Å. The error in the temperature is ± 5 °C

| ID | $d_{gate}$ [ kÅ ] | $d_{org}$ [ Å ] | $d_{S \& D}$ [ Å ] | Temp [ °C ] | ID | $d_{gate}$ [ kÅ ] | $d_{org}$ [ Å ] | $d_{S \& D}$ [ Å ] | Temp [ °C ] |
|---|---|---|---|---|---|---|---|---|---|
| o4a-01 | 6 | 300 | 1000 | 20 | o4a-26 | 6 | 300 | 1000 | 75 |
| o4a-02 | 6 | 300 | 1000 | 125 | o4a-27 | 6 | 300 | 1100 | 125 |
| o4a-03 | 6 | 300 | 1000 | 90 | o4a-28 | 6 | 300 | 800 | 150 |
| o4a-04 | 6 | 300 | 1000 | 50 | o4a-29 | 6 | 300 | 775 | 75 |
| o4a-05 | 3 | 150 | 1000 | 75 | o4a-30 | 6 | 300 | 1000 | 75 |
| o4a-06 | 3, 6 | 200 | 1000 | 20 | o4a-31 | 6 | 300 | 930 | 150 |
| o4a-07 | 6 | 220 | 1000 | 50 | o4a-32 | 6 | 300 | 830 | 20 |
| o4a-08 | 6 | 300 | 1000 | 20 | o4a-33 | 6 | 300 | 900 | 100 |
| o4a-09 | 6 | 200 | 1000 | 20 | o4a-34 | 6 | 300 | 500 | 125 |
| o4a-10 | 6 | 200 | 1000 | 20 | o4a-35 | 6 | 300 | 1000 | 175 |
| o4a-11 | 6 | 400 | 700 | 20 | o4a-36 | 6 | 300 | 1000 | 125 |
| o4a-12 | 6 | 300 | 666 | 20 | o4a-37 | 6 | 150 | 750 | 150 |
| o4a-13 | 3, 6 | 300 | 1000 | 90 | o4a-38 | 6 | 400 | 850 | 150 |
| o4a-14 | 6 | 300 | 1000 | 75 | o4a-39 | 6 | 300 | 950 | 20 |
| o4a-15 | 6 | 300 | 1000 | 50 | o4a-40 | 3, 6 | 300 | - | 20 |
| o4a-16 | 6 | 300 | 1000 | 50 | o4a-41 | 6 | 300 | 1000 | 20 |
| o4a-17 | 6 | 300 | 500 | 75 | o4a-42 | 6 | 300 | 1000 | 20 |
| o4a-18 | 6 | 300 | 1000 | 100 | o4a-43 | 6 | - | - | - |
| o4a-19 | 6 | 300 | 1500 | 125 | o4a-44 | 6 | 300 | 1000 | 20 |
| o4a-20 | 6 | 300 | 1000 | 100 | o4a-45 | 6 | 300 | - | 20 |
| o4a-21 | 6 | 300 | 1300 | 150 | o4a-46 | 6 | 300 | 600 | 20 |
| o4a-22 | 6 | 300 | 930 | 175 | o4a-47 | 6 | 300 | 650 | 20 |
| o4a-23 | 6 | 300 | 1300 | 20 | o4a-48 | 3, 6 | 300 | 650 | 75 |
| o4a-24 | 6 | 300 | 1000 | 175 | o4a-49 | 3, 6 | 300 | 750 | 75 |
| o4a-25 | 6 | 300 | 930 | 100 | o4a-50 | 6 | 300 | 750 | 200 |

**Table 8.10**: Continued.

| ID | $d_{gate}$ [ kÅ ] | $d_{org}$ [ Å ] | $d_{S\&D}$ [ Å ] | Temp [ °C ] | ID | $d_{gate}$ [ kÅ ] | $d_{org}$ [ Å ] | $d_{S\&D}$ [ Å ] | Temp [ °C ] |
|---|---|---|---|---|---|---|---|---|---|
| o4a-51 | 6 | 300 | 750 | 225 | o4a-64 | 6 | 300 | 700 | 225 |
| o4a-52 | 6 | 300 | 750 | 20 | o4a-65 | 6 | 300 | - | 200 |
| o4a-53 | 3, 6 | 300 | 700 | 20 | o4a-66 | 6 | 300 | - | 50 |
| o4a-54 | 3, 6 | 300 | 750 | 75 | o4a-67 | 3 | 300 | - | 20 |
| o4a-55 | 3, 6 | 300 | 750 | 100 | o4a-68 | 3 | 300 | - | 75 |
| o4a-56 | 6 | 300 | - | 75 | o4a-69 | 3 | 300 | - | 100 |
| o4a-57 | 6 | 300 | - | 20 | o4a-70 | 3 | 300 | - | 125 |
| o4a-58 | 6 | 300 | - | 100 | o4a-71 | 3 | 300 | - | 150 |
| o4a-59 | 6 | 300 | - | 125 | o4a-72 | 3 | 300 | - | 175 |
| o4a-60 | 6 | 300 | 700 | 125 | o4a-73 | 6 | 300 | 700 | 20 |
| o4a-61 | 6 | 300 | 600 | 150 | o4a-74 | 6 | 300 | 700 | 150 |
| o4a-62 | 6 | 300 | 700 | 175 | o4a-75 | 6 | 150 | 900 | 125 |
| o4a-63 | 6 | 300 | 700 | 200 | o4a-76 | 6 | 400 | 700 | 100 |

**Table 8.11**: Summary of 8H-BBEP TC OFETs deposited at a substrate temperature of 20 °C.

| | $\mu$ [cm$^2$/Vs] | $V_t$ [V] | $I_{on/off}$ | S [V/dB] | $N_t$ [x 10$^{11}$ cm$^{-2}$] | $E_b{}^a$ [meV] | $\mu_o{}^a$ [cm$^2$/Vs] |
|---|---|---|---|---|---|---|---|
| $SiO_2$ | 0.04 ± 0.01 | -29 ± 2 | 3.6 x $10^6$ | 4.7 | 8.9 ± 0.4 | -38.6 ± 0.9 | 0.20 ± 0.01 |
| HMDS | 0.07 ± 0.01 | -27 ± 2 | 3.8 x $10^6$ | 4.9 | 8.5 ± 0.4 | -35.7 ± 0.8 | 0.28 ± 0.02 |
| OTS-8 | 0.07 ± 0.01 | -43 ± 5 | 1.2 x $10^7$ | 6.7 | 10.8 ± 0.5 | -56.6 ± 1.4 | 0.62 ± 0.06 |
| OTS-18 | 0.13 ± 0.01 | -51 ± 3 | 8.3 x $10^6$ | 7.8 | 14.1 ± 0.5 | -97.6 ± 1.3 | 5.63 ± 0.31 |

[a] Calculated at $V_g$ = -100 V

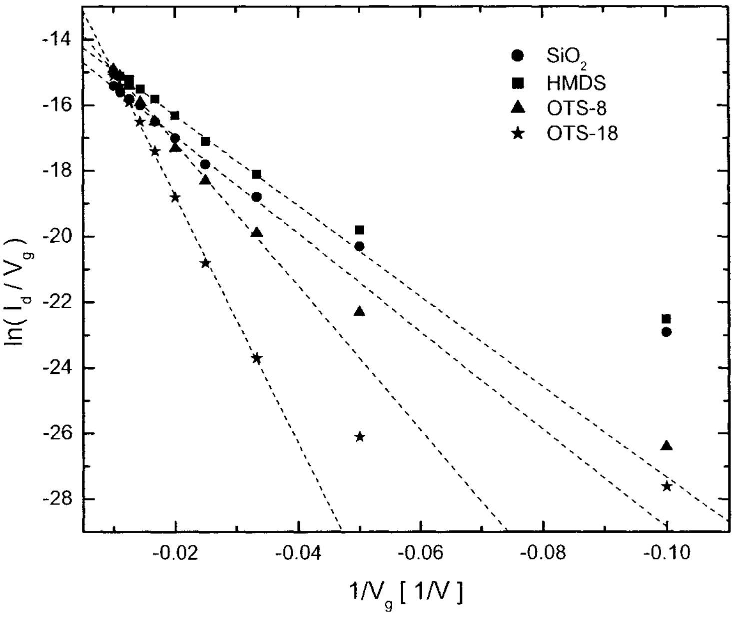

**Figure 8.40:** Levinson plot for room temperature deposited 8H-BBEP on SiO$_2$, HMDS, OTS-8, and OTS-18. The parameters are summarized in Table 8.11.

**Table 8.12:** Summary of 8H-BBEP TC OFETs deposited at a substrate temperature of 75 °C. Note the positive threshold voltage for the HMDS sample.

| | $\mu$ [cm$^2$/Vs] | $V_t$ [V] | $I_{on/off}$ | S [V/dB] | $N_t$ [x 10$^{11}$ cm$^{-2}$] | $E_b$$^a$ [meV] | $\mu_0$$^a$ [cm$^2$/Vs] |
|---|---|---|---|---|---|---|---|
| SiO$_2$ | 0.10 ± 0.01 | -34 ± 2 | 3.8 x 10$^6$ | 5.0 | 8.8 ± 0.3 | -37.8 ± 0.8 | 0.43 ± 0.02 |
| HMDS | 0.08 ± 0.01 | 9 ± 2 | 1.2 x 10$^6$ | 2.7 | 4.2 ± 0.2 | -4.3 ± 0.2 | 0.10 ± 0.01 |
| OTS-8 | 0.22 ± 0.01 | -36 ± 3 | 1.7 x 10$^6$ | 9.2 | 15.1 ± 0.3 | -55.0 ± 1.2 | 1.84 ± 0.04 |
| OTS-18 | 0.30 ± 0.01 | -29 ± 2 | 1.2 x 10$^7$ | 4.9 | 9.5 ± 0.3 | -43.8 ± 0.9 | 1.63 ± 0.04 |

[a] calculated at $V_g$ = -100 V

**Table 8.13:** Summary of 8H-BBEP TC OFETs deposited at a substrate temperature of 100 °C.

| | $\mu$ [cm$^2$/Vs] | $V_t$ [V] | $I_{on/off}$ | S [V/dB] | $N_t$ [ x $10^{11}$ cm$^{-2}$] | $E_b$$^a$ [meV] | $\mu_o$$^a$ [cm$^2$/Vs] |
|---|---|---|---|---|---|---|---|
| SiO$_2$ | 0.08 ± 0.01 | -30 ± 3 | 4.7 x $10^6$ | 8.9 | 10.1 ± 0.5 | -50.0 ± 1.5 | 0.55 ± 0.03 |
| HMDS | 0.10 ± 0.01 | -14 ± 2 | 4.2 x $10^6$ | 8.2 | 6.1 ± 0.3 | -18.2 ± 0.5 | 0.20 ± 0.01 |
| OTS-8 | 0.31 ± 0.01 | -17 ± 2 | 2.0 x $10^7$ | 5.3 | 10.0 ± 0.5 | -23.9 ± 0.7 | 0.78 ± 0.04 |
| OTS-18 | 0.19 ± 0.01 | -47 ± 5 | 8.6 x $10^6$ | 6.5 | 11.4 ± 0.5 | -63.1 ± 1.5 | 2.18 ± 0.20 |

[a] calculated at $V_g$ = -100 V

**Table 8.14:** Summary of 8H-BBEP TC OFETs deposited at a substrate temperature of 125 °C.

| | $\mu$ [cm$^2$/Vs] | $V_t$ [V] | $I_{on/off}$ | S [V/dB] | $N_t$ [ x $10^{11}$ cm$^{-2}$] | $E_b$$^a$ [meV] | $\mu_o$$^a$ [cm$^2$/Vs] |
|---|---|---|---|---|---|---|---|
| SiO$_2$ | 0.04 ± 0.01 | -16 ± 2 | 1.4 x $10^6$ | 6.1 | 7.0 ± 0.4 | -24.3 ± 0.6 | 0.10 ± 0.01 |
| HMDS | 0.18 ± 0.01 | -16 ± 2 | 2.1 x $10^6$ | 8.7 | 6.6 ± 0.3 | -21.3 ± 0.5 | 0.41 ± 0.02 |
| OTS-8 | 0.15 ± 0.01 | -49 ± 4 | 6.4 x $10^6$ | 6.2 | 12.8 ± 0.5 | -80.4 ± 1.7 | 3.35 ± 0.30 |
| OTS-18 | 0.17 ± 0.01 | -53 ± 5 | 3.5 x $10^6$ | 8.3 | 8.6 ± 0.4 | -36.0 ± 0.8 | 0.68 ± 0.02 |

[a] calculated at $V_g$ = -100 V

**Table 8.15:** Summary of 8H-BBEP TC OFETs deposited at a substrate temperature of 150 °C.

| | $\mu$ [cm$^2$/Vs] | $V_t$ [V] | $I_{on/off}$ | S [V/dB] | $N_t$ [x $10^{11}$ cm$^{-2}$] | $E_b$$^a$ [meV] | $\mu_o$$^a$ [cm$^2$/Vs] |
|---|---|---|---|---|---|---|---|
| SiO$_2$ | 0.09 ± 0.01 | -4.3 ± 0.9 | 0.5 x $10^6$ | 7.6 | 4.1 ± 0.2 | -8.10 ± 0.01 | 0.12 ± 0.01 |
| HMDS | 0.12 ± 0.01 | -9 ± 1 | 2.0 x $10^6$ | 6.9 | 5.4 ± 0.2 | -14.3 ± 0.1 | 0.21 ± 0.01 |
| OTS-8 | 0.07 ± 0.01 | -34 ± 2 | 1.5 x $10^6$ | 5.9 | 9.1 ± 0.3 | -40.4 ± 0.7 | 0.33 ± 0.02 |
| OTS-18 | 0.18 ± 0.01 | -45 ± 2 | 11.0 x $10^6$ | 5.9 | 12.3 ± 0.5 | -73.7 ± 1.6 | 3.10 ± 0.30 |

[a] calculated at $V_g$ = -100 V

**Table 8.16:** Summary of 8H-BBEP TC OFETs deposited at a substrate temperature of 175 °C.

| | $\mu$ [cm$^2$/Vs] | $V_t$ [V] | $I_{on/off}$ | S [V/dB] | $N_t$ [ x $10^{11}$ cm$^{-2}$] | $E_b$$^a$ [meV] | $\mu_o$$^a$ [cm$^2$/Vs] |
|---|---|---|---|---|---|---|---|
| SiO$_2$ | 0.10 ± 0.01 | -24 ± 2 | 1.2 x $10^6$ | 8.7 | 7.6 ± 0.4 | -28.4 ± 0.5 | 0.30 ± 0.02 |
| HMDS | 0.10 ± 0.01 | -7.1 ± 0.8 | 1.8 x $10^6$ | 6.0 | 4.1 ± 0.1 | -8.1 ± 0.1 | 0.14 ± 0.01 |
| OTS-8 | 0.24 ± 0.01 | -56 ± 5 | 5.1 x $10^6$ | 4.9 | 13.4 ± 0.4 | -87.7 ± 1.0 | 7.10 ± 0.60 |
| OTS-18 | 0.20 ± 0.01 | -42 ± 4 | 5.2 x $10^6$ | 7.7 | 11.3 ± 0.4 | -61.9 ± 0.8 | 2.19 ± 0.30 |

[a] calculated at $V_g$ = -100 V

**Table 8.17:** Summary of 8H-BBEP TC OFETs deposited at a substrate temperature of 200 °C.

| | $\mu$ [cm$^2$/Vs] | $V_t$ [V] | $I_{on/off}$ | S [V/dB] | $N_t$ [x $10^{11}$ cm$^{-2}$] | $E_b$$^a$ [meV] | $\mu_o$$^a$ [cm$^2$/Vs] |
|---|---|---|---|---|---|---|---|
| SiO$_2$ | 0.01 ± 0.01 | -14 ± 2 | 0.6 x $10^6$ | 5.8 | 6.7 ± 0.4 | -21.8 ± 0.8 | 0.02 ± 0.01 |
| HMDS | 0.10 ± 0.01 | -47 ± 5 | 1.5 x $10^6$ | 7.0 | 14.8 ± 0.4 | -107.7 ± 1.8 | 6.39 ± 0.40 |
| OTS-8 | 0.14 ± 0.01 | -57 ± 6 | 4.2 x $10^6$ | 6.5 | 13.3 ± 0.4 | -86.3 ± 1.4 | 3.92 ± 0.10 |
| OTS-18 | 0.13 ± 0.01 | -61 ± 6 | 3.3 x $10^6$ | 7.9 | 14.2 ± 0.4 | -97.9 ± 1.2 | 5.70 ± 0.30 |

$^a$ calculated at $V_g$ = -100 V

**Table 8.18:** Summary of 8H-BBEP TC OFETs deposited at a substrate temperature of 225 °C.

| | $\mu$ [cm$^2$/Vs] | $V_t$ [V] | $I_{on/off}$ | S [V/dB] | $N_t$ [x $10^{11}$ cm$^{-2}$] | $E_b$$^a$ [meV] | $\mu_o$$^a$ [cm$^2$/Vs] |
|---|---|---|---|---|---|---|---|
| SiO$_2$$^b$ | - | - | - | - | - | - | - |
| HMDS $^b$ | - | - | - | - | - | - | - |
| OTS-8 $^b$ | - | - | - | - | - | - | - |
| OTS-18 | 0.06 ± 0.02 | -69 ± 7 | 1.4 x $10^6$ | 8.5 | 16.1 ± 0.6 | -127.3 ± 2.1 | 8.17 ± 0.9 |

$^a$ calculated at $V_g$ = -100 V
$^b$ devices did not show any field effect

electrodes. If the work function of gold is taken to be 5.1 eV,[20] there is a 0.9 eV Schottky barrier present at the interface, using the 8H-BBEP HOMO energy of 6.0 eV from the electrochemical data. Platinum, with a work function of 5.7 eV,[21] could have been used with 8H-BBEP, but platinum could not be evaporated within our deposition system. Theoretically, if the problem is only related to the barrier height, switching to platinum should decrease the threshold voltage. The barrier height between gold and pentacene is only 0.2 eV,[22] yet high threshold voltages were also observed with some pentacene devices. For example, the SiO$_2$ and HMDS samples in Table 8.7 and Table 8.8 have threshold voltages in excess of -20 V while the OTS-8 and OTS-18 samples were less than -10V. From this empirical data, there must be some other factor which generates this high threshold voltage.

Another possible explanation for some of the large variances observed from device to device is the quality of the metal film. It is well known that thermally evaporated metals are inferior to sputtered and e-beam deposited films of the same metal in terms of density. Technical issues do not allow this approach to be tested.

Finally, the physical characteristics of the metal-organic interface may be another possible source of the high threshold voltages. Figure 8.41 illustrates what was observed in some samples after the electrical measurements were performed. The gold electrode has been physically torn away from the underlying 8H-BBEP film. There is some gold present on the organic material indicating that the tearing occurred after the gold had been deposited. It is believed that the tear is a result of removing the shadow mask after metallization. The shadow mask, a TEM grid, was in direct contact with the surface. In some cases, the grids "stuck" to the surface and the only way to remove them was by tapping the back side of the chip to dislodge the grid. During this process the contacts could have been damaged. The other possible source for this damage is during the electrical measurements at the probing station when the needles were lowered onto the metal contacts. The issue of metal-organic contacts must be studied further and an accurate description of the injection barrier heights should also be investigated

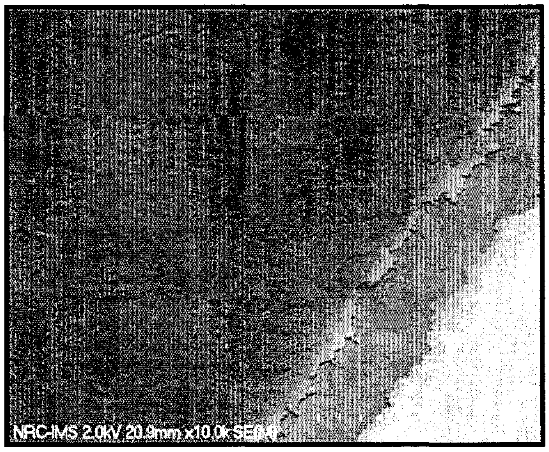

**Figure 8.41:** SEM of an 8H-BBEP film physically separated from a gold contact (OTS-8 sample at 150°C).

in greater detail.

The data extracted from the Levinson plots indicates that the grain boundary trap densities fall between 5.5x10$^{11}$ cm$^{-2}$ for HMDS at 150°C and 16.1x10$^{11}$ cm$^{-1}$ for OTS-18 at 225°C. In all cases, the grain boundary barrier heights were fairly high compared to pentacene, ranging from approximately -20 meV to 130 meV, with two exceptions being -8.1 meV for $SiO_2$ at 150°C and HMDS at 175°C. These high trap densities and barrier heights are obviously factors which lower the mobility and increase the magnitude of the threshold voltage, degrading the overall device performance. If the samples are held at the substrate temperature for a period of time after the deposition is stopped and permitted to cool slowly, the quality of the film might be increased, especially at temperatures in the range of the LC transition peak. The trap-free mobilities predicted by the Levinson plots are in the 1-10 cm$^2$/Vs range, which is comparable to pentacene. If the quality of the 8H-BBEP films can be improved, mobilities much higher than 0.3 cm$^2$/Vs should be attainable.

The highest field effect mobilities and corresponding threshold voltages for all four types of samples as a function of the substrate temperature during deposition are summarized in Figure 8.42. The shaded region between 115°C and 135°C corresponds to the LC region in Figure 8.1.

As can be seen in Figure 8.42a, the $SiO_2$ and OTS-18 samples show the same trends with the mobility increasing to a local maximum of 0.10 and 0.30 cm$^2$/Vs at 75°C followed by a local minimum of 0.04 and 0.17 cm$^2$/Vs at 125°C and then rising to another local maximum of 0.10 and 0.20 cm$^2$/Vs at 175°C, respectively. The mobility declines rapidly due to degradation of the oligomer and desorption of the oligomer from the substrate surface. OTS-8 showed similar trends reaching local maxima of 0.31 cm$^2$/Vs and 0.24 cm$^2$/Vs at 100°C and 175°C with a minimum of 0.07 cm$^2$/Vs at 150°C. The HMDS samples, however, did not seem to follow this trend, with the mobility increasing and reaching a maximum mobility of 0.18 cm$^2$/Vs at 125°C and then decreasing.

The decrease observed around 125°C is thought to be related to the LC phase change observed in the DSC curve. During the phase change, the film structure is being modified which can lead to a large number of grain boundaries and traps states. As mentioned, keeping the substrate temperature constant for a specific period of time after the deposition has been completed and then quenching with liquid nitrogen might aid in keeping the molecular

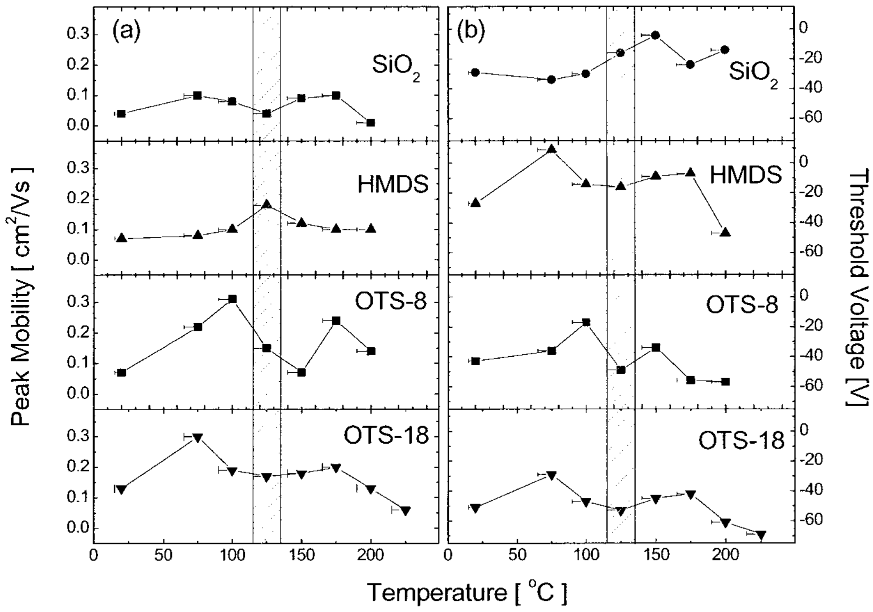

**Figure 8.42:** (a) Highest mobility and (b) threshold voltage for each of the four different types of devices as a function of substrate temperature. The shaded region represents the temperature range in which the LC phase change occurs.

orientation obtained from the LC phase and could possibly increase the mobility.

Figure 8.43 illustrates the average mobilities of the four different types of devices at various substrate temperatures. For each type of device, the measurements were made on at least 4 different samples, each containing between 6-10 devices. The *y*-axis error bars represent the standard deviation of all of the measurements made on identical devices. Overall, the same trends were observed as in Figure 8.42. The highest average mobilities were 0.056 ± 0.005 cm$^2$/Vs at 100°C for SiO$_2$, 0.183 ± 0.002 cm$^2$/Vs at 125°C for HMDS, 0.231 ± 0.103 cm$^2$/Vs at 100°C for OTS-8 and two maxima for OTS-18 of 0.144 ± 0.009 cm$^2$/Vs at 100°C and 0.144 ± 0.020 cm$^2$/Vs at 175°C. The bare SiO$_2$ samples showed consistent results on all measurements

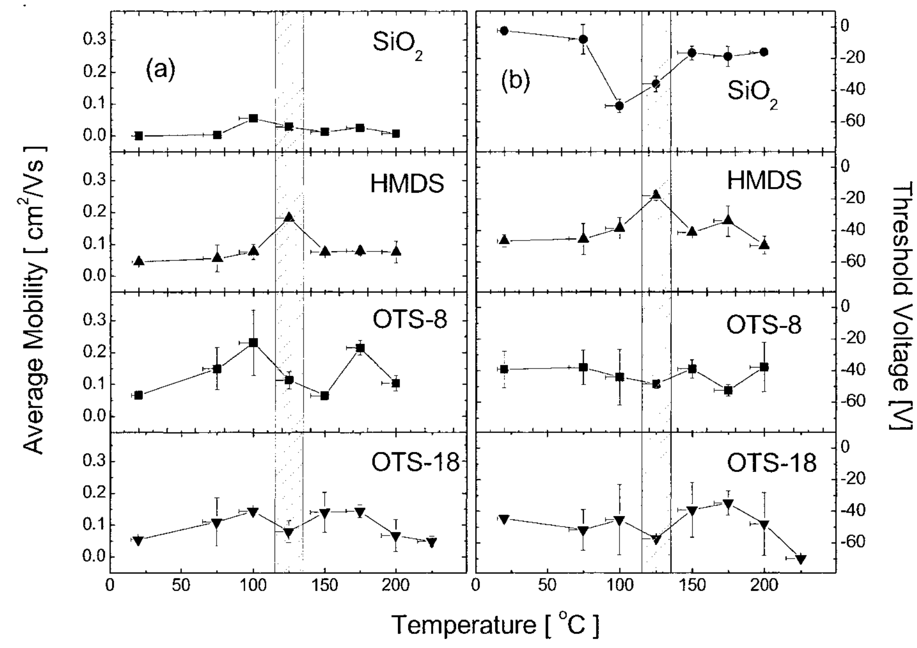

**Figure 8.43:** Average mobility and threshold voltage for each of the four types of samples as a function of substrate temperature. The error bars represent the standard deviation in the results between all identically prepared devices.

as did the series using HMDS. The samples fabricated with OTS-8 and OTS-18 had more variation from sample to sample thus resulting in a larger standard deviation. This is attributed to poor gold-organic contacts and, to a lesser extent, inhomogeneous SAMs.

The shape of the HMDS mobility versus temperature curve did not follow the same trend as the other three curves and reached its highest mobility at 125°C. A possible explanation is that while the HMDS SAM reduced the surface energy of the $SiO_2$, it did not interact with the 8H-BBEP molecules as much as the OTS samples because of the smaller methyl end groups as opposed to the longer alkyl chains present in the OTS SAMs. The weaker Van der Waals interactions between the HMDS SAM and 8H-BBEP molecules in the LC phase would allow the 8H-BBEP molecules to re-arrange themselves (a) on a shorter time scale due to the weaker Van der Waals interactions and (b) the HMDS SAM would not influence the orientation of the SAM as much as the OTS-8 or OTS-18. If we consider the difference between OTS-8 and OTS-18, the former shows a slightly higher mobility at 125°C than the latter. This supports the hypothesis that the Van der Waals interactions between the SAM and 8H-BBEP molecules do affect the orientation of the molecules in the LC phase. In order to verify this, further experiments would be required to maintain the substrate temperature at 125°C to allow the complete transformation of 8H-BBEP into the LC phase.

## 8.6 Organic Light Emitting Diodes

### 8.6.1 OLEDs Using BBEP

The structures of the four different types of OLEDs that were fabricated using BBEP are summarized in Table 8.19. Device 1 was a single layer device using BBEP only while Devices 2 and 3 used TPD and NPB as hole transport materials, respectively, with BBEP as the electron transporting and emitting material. A fourth device geometry consisting of BBEP as the hole

**Table 8.19:** Summary of the OLED structures used with BBEP. TPD and NPB are hole transport materials while PBD is an electron transport material. None of them contribute to the EL spectrum.

| Device Type | Anode | Organic 1 | Organic 2 | Cathode |
|---|---|---|---|---|
| 1 | ITO | BBEP | - | Al |
| 2[a] | ITO | TPD | BBEP | Al/Ag |
| 3 | ITO | NPB | BBEP | Al |

[a] Devices fabricated and characterized by Dr. I. Lévesque

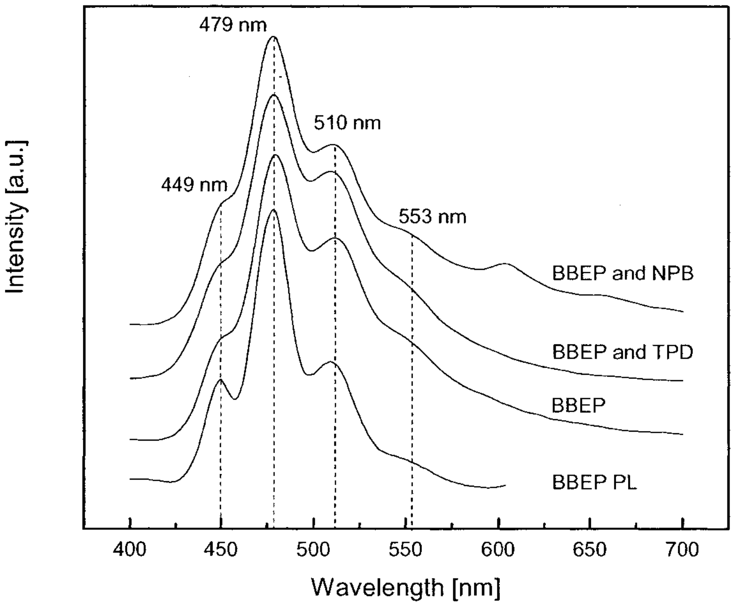

**Figure 8.44:** Emission spectra for BBEP. The lower curve is the photoluminescence spectrum of a thin film of BBEP on quartz. The remaining three curves are the electroluminescence spectra for OLEDs using only BBEP, BBEP with TPD, and BBEP with NPB. The main emission peaks are at 449 nm, 479 nm, and 510 nm with a minor shoulder at 553 nm. This indicates that all of the recombination processes occur within the BBEP layer. Each spectrum was normalized with respect to itself and tiled.

transporting and emitting material and PBD as the electron transporting material was attempted but technical issues prevented this device from being fabricated.

The EL spectra for the BBEP OLEDs are shown in Figure 8.44 with the solid state PL spectrum included for a comparison. The main EL peaks are at 449 nm, 479 nm, and 510 nm. Comparing these peaks to the peaks in the PL spectrum, it is evident that the light generated in the EL process originates within the BBEP layer with only a 1-2 nm red shift in the spectra compared to the solid state PL.

The current density-voltage curves for the BBEP-based diodes are shown in Figure 8.45. The OLEDs based on TPD and BBEP were fabricated and characterized by Dr. I. Lévesque.[1] The TPD/BBEP combination yielded the best results while the NPB/BBEP structure gave the

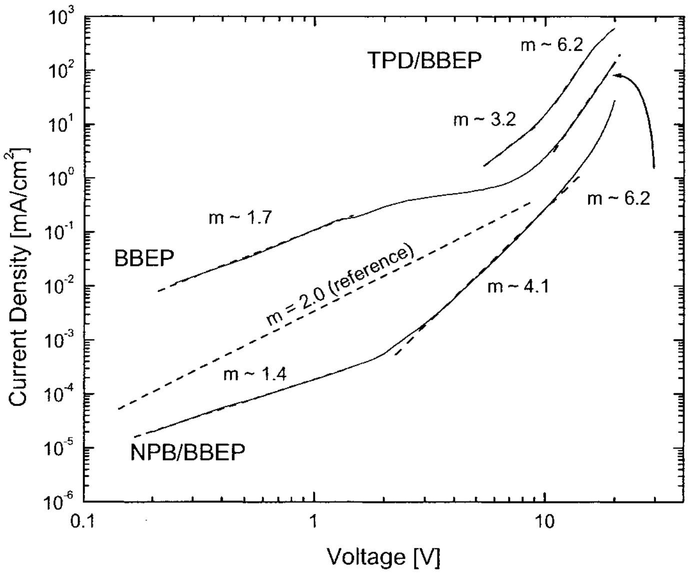

**Figure 8.45:** Current density as a function of applied bias for three different OLED geometries using BBEP as the emitting layer. m = 2.0 is shown as a reference.

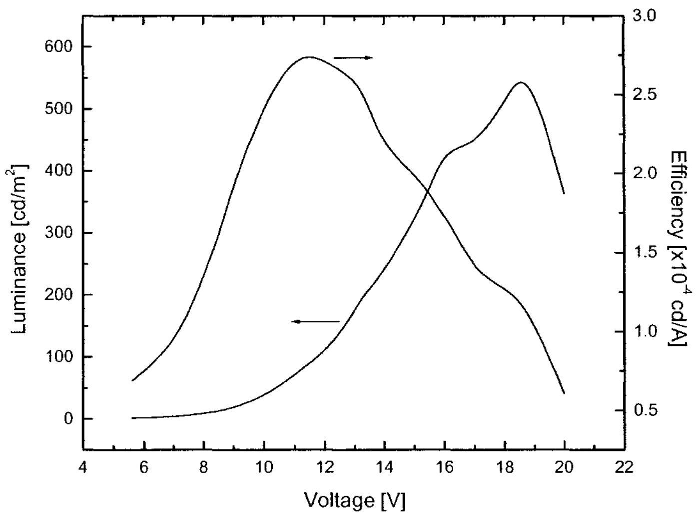

**Figure 8.46:** Luminance-voltage and efficiency-voltage for a TPD/BBEP OLED. The peak efficiency occurred at 11.3 V and the maximum luminance was 580 cd/m$^2$ at 18.75 V.

worst results. At lower voltages, the slope of the graph is between 1 and 2, which indicates that there is some other phenomenon that is limiting transport such as carrier injection, although it is not completely certain and should be examined further. At higher voltages the slope m (= L-1 in Equation 26 of Chapter 4) increases to values greater than 4, consistent with trap charge limited current. The luminance vs. voltage and current efficiency vs. voltage curves are shown in Figure 8.46 for the TPD/BBEP device. The maximum luminescence observed was 580 cd/m$^2$ at 18.75 V and the highest current efficiency was 2.76 x 10$^{-4}$ cd/A at 11.3V. This efficiency is very low and could probably be increased if the OLED structure was optimized (layer thicknesses, electrode material, for example).

### 8.6.2 OLEDs Using 8H-BBEP

8H-BBEP was used in four different types of OLEDs, summarized in Table 8.20. Device 1 used 8H-BBEP in a single layer geometry with ITO and Al electrodes. Devices 2 and 3 used TPD and NPB as hole transport materials, respectively, with 8H-BBEP as the electron transporting and emitting material. Device 3 used 8H-BBEP as the hole transporting and emitting material but also used PBD as the electron transporting material with a LiF/Al cathode.

**Table 8.20:** Summary of the OLED structures used with 8H-BBEP. TPD and NPB are hole transport materials while PBD is an electron transport material. None of them contribute to the EL spectrum.

| Device Type | Anode | Organic 1 | Organic 2 | Cathode |
|---|---|---|---|---|
| 1 | ITO | 8H-BBEP | - | Al |
| 2[a] | ITO | TPD | 8H-BBEP | Al/Ag |
| 3 | ITO | 8H-BBEP | PBD | LiF/Al |

[a] Devices fabricated and characterized by Dr. I. Lévesque

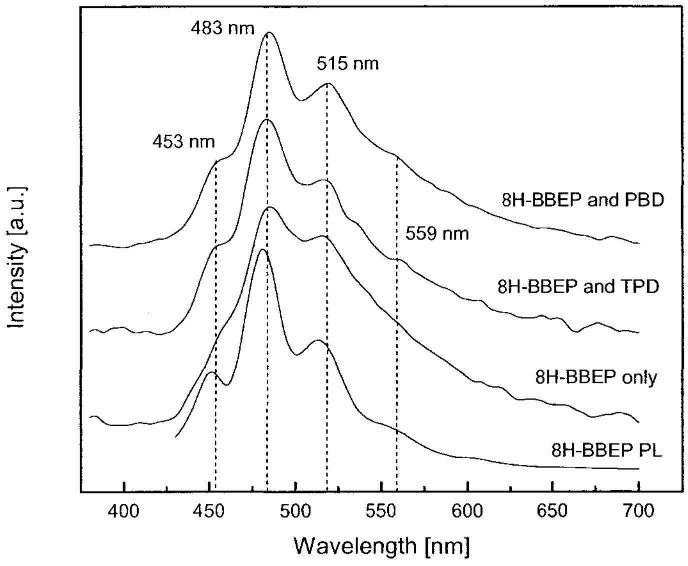

**Figure 8.47:** EL spectra for three different OLEDs based on 8H-BBEP. The solid state PL spectrum is also shown as a reference. Each spectrum was normalized with respect to itself and tiled.

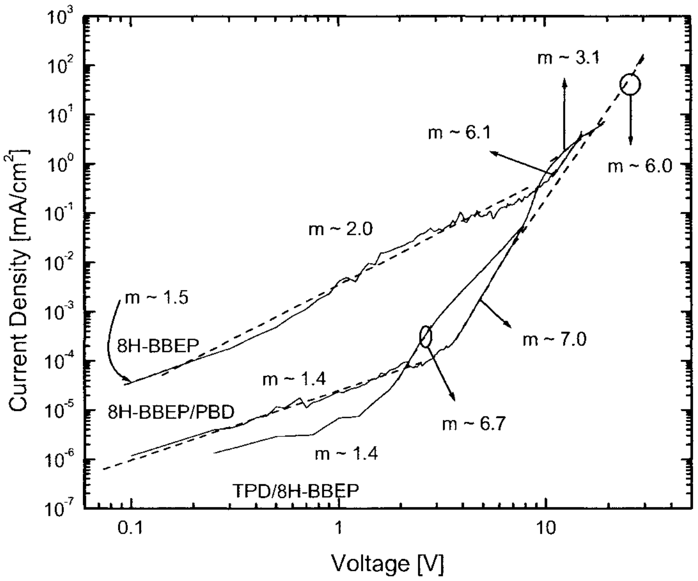

**Figure 8.48:** Current density as a function of applied bias plotted on a logarithmic scale for each of the three types of devices fabricated with 8H-BBEP.

The EL spectra for these three devices are shown in Figure 8.47 with the solid state PL spectra included for reference. The main emission peaks occurred at 453 nm, 483 nm, and 515 nm. Comparing the EL spectra to the PL spectrum, the EL peaks have been red shifted by approximately 5 nm. The similarity between the EL and PL spectra indicates that the generation of light occurred within the 8H-BBEP layer.

The current density-voltage curves are shown in Figure 8.48. The single layer 8H-BBEP device displayed the highest current density while the TPD/8H-BBEP and 8H-BBEP/PBD devices had lower current densities for voltages below 9 V.

For the single layer 8H-BBEP device, Child's law is observed at voltages less than about

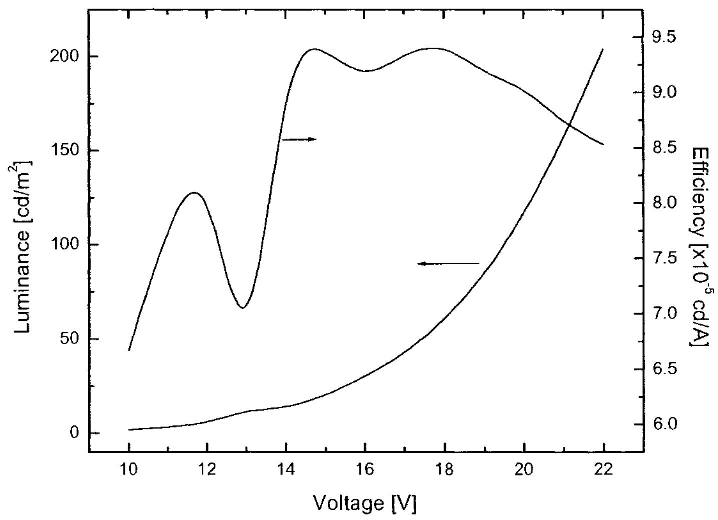

**Figure 8.49:** Luminance and efficiency as a function of applied voltage for a TPD/8B-BBEP OLED. The maximum luminance was 174 cd/m$^2$ at 22 V and the peak efficiency was reached at 14 V.

10 V. The current then enters the trap charge limited (TCL) regime. As with the BBEP devices, the current density is approximately proportional to $V^{1.4}$ below 2 V, indicating possible carrier injection phenomena which decrease the voltage dependence. The 8H-BBEP/PBD device entered the TCL regime while the TPD/8H-BBEP device seemed to pass through an intermediary region before entering the second TCL region. If this intermediary region is assumed to be a TCL region, then this would indicate the presence of two discrete traps levels at 0.15 meV and 0.13 meV, characterized by slopes of 6.7 and 6.0, respectively.

Figure 8.49 depicts the luminance-voltage and the efficiency-voltage curves for a TPD/8H-BBEP OLED. Compared to the same type of device using BBEP, the maximum luminance value is approximately 3 times lower and the efficiency is lower as well. The single layer and 8H-BBEP/PBD devices did display some EL, but it was not very intense and could not be measured due to the degradation of the devices. Based on previous experience with OLEDs, the brightness of these devices was estimated to be less than 50 cd/m$^2$.

These results are encouraging as there are few materials which possess high mobilities as well as the ability to generate light. By optimizing the diode structures it can be expected to increase the luminance and efficiency of the diodes.

## 8.7 Summary

In the preceding sections, the findings of this thesis have been presented. It was found that the melting point of BBEP is approximately 372°C and 367°C for 8H-BBEP. It was also discovered that 8H-BBEP possesses a liquid crystalline phase with a transition temperature of approximately 123°C. Cyclic voltammetry was performed on the materials and the HOMO level was found to be -5.9 eV for BBEP and -6.0 eV for 8H-BBEP. The energy of the onset of absorption was used to determine the LUMO level, -3.4 eV for BBEP and -3.3 eV for 8H-BBEP.

The optical absorption and emission spectra were recorded for both materials at various substrate temperatures. The peak positions were invariant with temperature but became less defined, broader, and showed a larger background signal. Semi-empirical quantum chemical calculations were performed using PM3 and Zindo/S algorithms and obtained the experimental absorption spectra.

The thin film morphology of BBEP and 8H-BBEP was examined. XRD on powder samples indicated that the materials did possess structure with BBEP showing more peaks than 8H-BBEP. The XRD of thin film samples was also examined. It was found that BBEP had extremely poor film forming characteristics and no peaks were observed in the BBEP thin film samples. The 8H-BBEP samples consistently showed a peak in the XRD spectra in the 2.00-2.15° range, corresponding to a d value of approximately 41-44 Å. AFM analysis indicated that at temperatures above 75°C the films form smooth grains and lamellar structures can be seen. The thickness of the lamella are measured to be approximately 45 Å. Comparing to the calculated molecular lengths, it is proposed that the 8H-BBEP molecules arrange themselves perpendicular to the substrate surface.

OFETs were fabricated using chemically modified $SiO_2$ gate dielectrics at substrate temperatures between ambient and 225°C. The highest measured mobility was 0.31 $cm^2/Vs$ with an OTS-8 SAM at a substrate temperature of 100°C. Pentacene was also used in OFETs and the highest measured mobility was 2.4 $cm^2/Vs$ with OTS-18 at a substrate temperature of 60°C.

A series of OLEDs were fabricated using BBEP and 8H-BBEP in single and multi layer configurations. The best results were found when TPD was used as the hole transport layer and BBEP or 8H-BBEP was used as the emitter. The OLED with 8H-BBEP had a maximum luminance of 172 $cd/m^2$ at 22 V while the BBEP device showed a maximum luminance of 580 $cd/m^2$ at 18.75 V. Both materials emitted light in the blue-green portion of the spectrum.

## 8.8 References

[1] I. Lévesque, (Unpublished Results, 2000).

[2] I. Lévesque, (Personal Communication, 2004).

[3] J.-F. Wang, Y. Kawabe, S. E. Shaheen, M. M. Morrell, G. E. Jabbour, P. A. Lee, J. Anderson, N. R. Armstrong, B. Kippelen, E. A. Mash, and N. Peyghambarian, Adv. Mater. **10,** 230 (1998).

[4] H. Reiss and A. Heller, J. Phys. Chem. **89,** 4207 (1985).

[5] A. J. Nozik and R. Memming, J. Phys. Chem. **100,** 13061 (1996).

[6] N. F. Colaneri, D. D. C. Bradley, R. H. Friend, P. L. Burn, A. B. Holmes, and C. W. Spangler, Phys. Rev. B. **42,** 11670 (1990).

[7] Y. Wu, P. Liu, S. Gardner, and B. Ong, Chem. Mater. **17,** 221 (2005).

[8] Y. Wu, Y. Li, S. Gardner, and B. Ong, J. Amer. Chem. Soc. **127,** 614 (2005).

[9] I. P. M. Bouchoms, W. A. Schoonveld, J. Vrijmoeth, and T. M. Klapwijk, Synth. Met. **104,** 175 (1999).

[10] J. G. Laquindanum, H. E. Katz, A. J. Lovinger, and A. Dodabalapur, Chem. Mater. **8,** 2542 (1996).

[11] H. L. Gomes, P. Stallinga, F. Dinelli, M. Murgia, F. Biscarini, D. M. de Leeuw, T. Muck, J. Geurts, L. W. Molenkamp, and V. Wagner, Appl. Phys. Lett. **84,** 3184 (2004).

[12] S. J. Zilker, C. Detcheverry, E. Cantatore, and D. M. de Leeuw, Appl. Phys. Lett. **79,** 1124 (2001).

[13] A. Salleo and R. A. Street, J. Appl. Phys. **94,** 4231 (2003).

[14] A. Salleo, M. L. Chabinyc, M. S. Yang, and R. A. Street, Appl. Phys. Lett. **81,** 4383 (2002).

[15] Y.-W. Wang, H.-L. Cheng, Y.-K. Wang, T.-H. Hu, J.-C. Ho, C.-C. Lee, T.-F. Lei, and C.-F. Yeh, Thin Solid Films **467,** 215 (2004).

[16] Y.-Y. Lin, D. J. Gundlach, S. F. Nelson, and T. N. Jackson, IEEE Electron Dev. Lett. **18,** 606 (1997).

[17] J. Cornil, D. Beljonne, J.-P. Calbert, and J.-L. Brédas, Adv. Mater. **13,** 1053 (2001).

[18] S. Son, A. Dodabalapur, A. J. Lovinger, and M. E. Galvin, Science **269,** 376 (1995).

[19] W. Tachelet, S. Jacobs, H. Ndayikengurukiye, H. J. Geise, and J. Grüner, Appl. Phys. Lett. **64,** 2364 (1994).

[20] http://environmentalchemistry.com/yogi/periodic/Au.htm.

21 http://environmentalchemistry.com/yogi/periodic/Pt.html.

22 I. H. Campbell and D. L. Smith, in *Solid State Physics: Advances in Research and Applications*; *Vol. 55*, edited by H. Ehrenreich and F. Spaepen (Academic Press, New York, 2000).

# Chapter 9
# Conclusions and Outlook

## 9.1 Conclusions

In addition to OFETs based on pentacene, this thesis reports on OLEDs and OFETs based on two novel oligomers: BBEP and 8H-BBEP.

DSC was performed on the oligomers to determine their melting points. It was discovered that 8H-BBEP possessed a liquid crystalline phase while BBEP did not. Cyclic voltammetry measurements indicated that the HOMO level of BBEP was -5.9 eV and -6.0 eV in 8H-BBEP. Semi-empirical modeling using PM3 and Zindo/S algorithms estimated the HOMO level to be -6.94 eV, -7.21 eV, and -7.43 eV for BBEP and -6.86 eV, -7.19 eV, and -7.54 eV for 8H-BBEP in the trans-trans, cis-trans, and cis-cis conformations, respectively. Due to the differences between the molecule in a vacuum and in a thin film, the approximate 1 eV difference was expected.

A detailed study of the chemical modification of $SiO_2$ surfaces was performed. The effect of different cleaning processes on the contact angle of water on the $SiO_2$ surface was quantified. It was discovered that the $SiO_2$ samples that were cleaned using a combination of organic solvents, RCA 1 & 2, and a 1 hour exposure to UV-$O_3$ radiation produced the most hydrophillic surfaces. With this process, recipes were developed to grow high quality SAMs of HMDS, OTS-8 and OTS-18 on the $SiO_2$ surfaces. They were characterized using contact angles, AFM, and SEM. The resulting films displayed exceptionally smooth surfaces and contact angles greater than those usually reported in the literature.

Pentacene OFETs were used as controls to characterize the effect of the different SAMs on the performance of the devices. Polycrystalline pentacene films deposited at a substrate temperature of 60°C displayed mobilities of 2.4 $cm^2/Vs$. To our knowledge, this is one of the highest reported mobilities for polycrystalline pentacene OFETs.

BBEP and 8H-BBEP were evaporated onto substrates held at temperatures between ambient and 225°C. Optical absorption and emission spectroscopy was performed and the peak positions appeared to be invariant with substrate temperature. The background in the absorption spectra changed significantly in BBEP, indicating that some decomposition of the material might have occurred. The thin film morphology of BBEP and 8H-BBEP was studied using XRD, SEM, and AFM techniques. The oligomers were deposited at different substrate temperatures on samples with different surface treatments. Regardless of the surface treatment, BBEP showed poor film forming characteristics and did not form continuous films. The thin film morphology of 8H-BBEP evolved from a porous film to a smooth lamellar film. The XRD and AFM results indicated that the thicknesses of the lamella were between 42-47Å. Semi-empirical modeling determined that the carbon to carbon length of the 8H-BBEP molecule in the trans-trans conformation is approximately 42 Å and the hydrogen to hydrogen length is approximately 44 Å. This indicates that the films are composed of the trans-trans conformation and the molecules are oriented perpendicular to the surface. A model was proposed to explain the effect of the SAM on the film forming characteristics of 8H-BBEP.

OFETs were fabricated with 8H-BBEP using bare and chemically modified $SiO_2$ gate dielectrics at different substrate temperatures. The highest measured mobility was 0.31 $cm^2/Vs$ with OTS-8 at $T_{sub}$ = 100°C. The OFETs were analyzed using the Levinson model for polycrystalline thin film transistors and grain boundary trap densities, trap binding energies and trap free mobilities were obtained as well as threshold voltages, on/off ratios and subthreshold slopes.

BBEP and 8H-BBEP were used in single and multi layer OLEDs. Both of the oligomers generated blue-green EL. The multi layer devices using an ITO/TPD/oligomer/Al-Ag structure gave the highest luminance values of 580 cd/m$^2$ at 18.75 V for BBEP and 174 cd/m$^2$ at 22 V for 8H-BBEP. By optimizing the OLED geometry, it is anticipated that the operating voltages can be decreased and the brightness can be increased significantly.

## 9.2 Outlook

Based on the results obtained in this thesis, there are many more experiments which should be performed to gain further insight into the structure-property relationship of the oligomers and device performance, as well as the modifications to the experimental apparatus to create higher quality devices.

The most fundamental issue is the synthesis route used to make the oligomers. If the synthesis scheme was modified to yield only the trans-trans conformations, it is expected that the OFET and OLED performance will be increased. The structure and crystallographic properties should be studied and the feasibility of growing single crystals should be examined. An interesting series of experiments would be to synthesize BBEP molecules while progressively increasing the length of the alkyl chains at the $\alpha$ and $\alpha'$ positions and to study these effects. A corollary to this is to use several other SAMs with different alkyl chain lengths to study the relationship between the chain lengths on the SAM and oligomers.

While the contact angle measurements of the SAMs were made with water, using various solvents will give a quantitative value for the surface energies contrary to the qualitative value obtained with only water. X-ray reflectivity measurements using a synchrotron light source should also be performed to obtain an accurate estimate of the thickness of the SAM.

The lithography masks for the bottom contact devices should be redesigned to increase the size of the source and drain electrodes. The sidewalls of the source and drain electrodes should be tapered to ensure that the organic film is continuous across the electrode. Once completed, the surface area available for the injection of charges can be increased and made comparable to that for the top contact devices. Surface treatment processes similar to those used for $SiO_2$ are available for metals to help with carrier injection and to improve the film quality over the electrode area.

For the top contact OFETs, a "real" shadow mask should be designed to eliminate the need for exposing the samples to atmosphere between organic and metal depositions. Which could be a major factor in the large variation in device operation. The issue of contact resistance needs to be addressed. While the top contact design is superior in terms of simplicity, the bottom contact design is more flexible in terms of the types of devices that can be made. By designing a new set of lithography masks, the devices can be designed to be compatible with existing cryostats and related hardware to perform low temperature electrical measurements on the OFETs (and OLEDs). This would provide considerable insight into the transport process involved in the films. Other techniques such as capacitance-voltage measurements using a MOS structure would give an estimate of the carrier density in the film.

Optimizing the thickness of the layers in the OLEDs and using injection enhancement layers such as CuPc and LiF will improve performance. In addition, the use of hole transport and/or electron transport layers should also be examined.

The fact that 8H-BBEP has a liquid crystalline phase is of great importance to OFETs and OLEDs. In OFETs, the liquid crystal phase can be oriented in a specific direction by specialized techniques such a rubbing or pre-patterning the substrate. This induced orientation would allow the conductivity to be measured in different directions on the surface to determine if any anisotropy exists. Inducing order in this manner can lead to the generation of polarized light, which would be of great technological interest.

# Appendix A
# Synthesis Schemes

In 1997, Dimitrakopoulos and co-workers synthesized a new thiophene-based oligomer: *trans-trans*-2,5-Bis-[2-{5-(2,2'-tithienyl)ethenyl]}thiophene, or BTET, shown in Figure A.1.[1] This material was synthesized by a Wittig reaction between a bisphonium salt and a2,2'-bithienyl-5-carboxaldehyde to yield the final oligomer. They reported a field effect mobility of 0.01 cm$^2$/Vs using a TC-OFET geometry which was grown at room temperature.

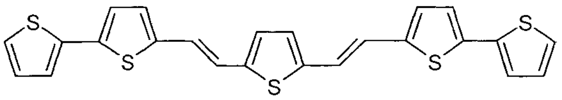

**Figure A.1**: Structure of BTET sythesized by Dimitrakopoulos *et al.*

A compound similar to this was synthesized by Lévesque in 2000 using phenyl moieties as opposed to thiophene moieties, shown in Figure A.2. This compound was called bis-(4,4'-(biphenyl)ethenyl)phenyl, or BBEP, and was made primarily to evaluated charge carrier mobilities and as an emitting material in an OLED.

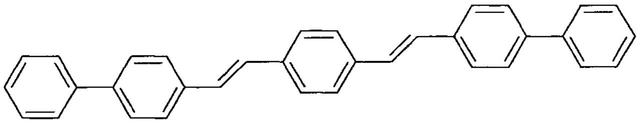

**Figure A.2**: Modified phenyl-based oligomer, BBEP.

The synthesis route for this molecule was relatively simple and is outlined in Figure A.3. The bisphosphonium salt (1) was obtained by adding 10.0 g (38 mmol) of α,α-dibromo-p-

---

[1] C. D. Dimitrakopoulos, A. Afzali-Ardakani, B. Furman, J. Kymissis, and S. Purushothaman, Synth. Met. **89**, 193 (1997).

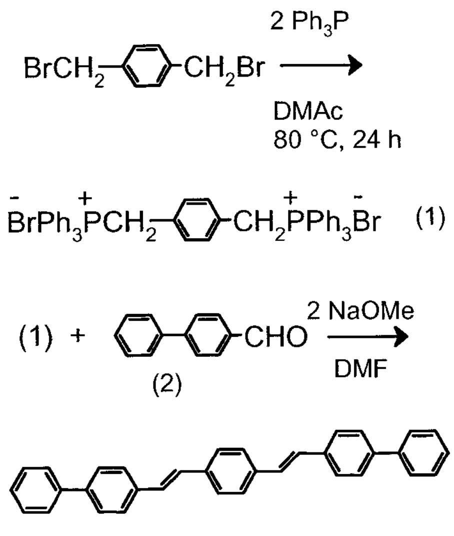

BBEP

**Figure A.3**: BBEP synthesis scheme.

xylene and 19.9 g (7.6 mmol) of triphenylphosphine into 200 mL of anhydrous N,N-dimethylacetamide (DMAc). The solution was heated at 80 °C and a precipitate was formed. The mixture was stirred for 24 h, and then cooled down to room temperature. The resulting mixture was poured into 400 mL of anhydrous ethanol. The precipitate was filtered, and washed with diethyl ether. The product was dried under vacuum at 55 °C, and 21.06 g of white powder were obtained.

To synthesize BBEP, 0.46 g (2.5 mmol) of biphenylcarboxaldehyde (2) was added to a suspension of 8.65g (11 mmol) bisphosphonium salt (1) in 200 mL of dimethylformamide. A 46 mL solution of sodium methoxide (0.5M) in methanol was added dropwise under a agron flow. A yellow product started to precipitate after a few minutes and the process was continued overnight. The mixture was poured into 1L of water, filtered, and then washed with water, cold and hot ethanol, then dried under vacuum at 40°C. The recovered BBEP was collected and stored in a dry nitrogen cabinet and later purified using the vapour train sublimation system outlined earlier in this work.

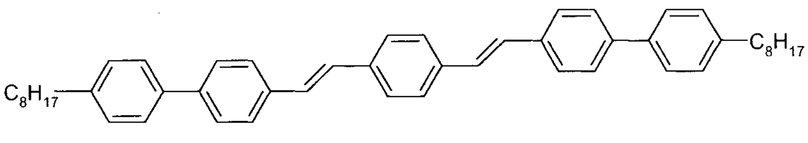

**Figure A.4**: Structure of 8H-BBEP.

A second compound similar to BBEP was also synthesized, but with $C_8H_{17}$ alkyl chains at the $\alpha,\alpha'$ positions, as shown in Figure A.4, called bis-(4,4'-(octylbiphenyl)ethenyl)phenyl, or 8H-BBEP. In principle, the side chains should make the oligomer more soluble and increase the order in thin films, however in practice it was found that the oligomer was still sparingly soluble in most solvents.

The synthesis reaction is very similar to that shown in Figure A.3, with the exception of product (2) which has the $C_8H_{17}$ alkyl chain. The reaction was carried out in DMF at room temperature for 12 hours and the precipitate was recovered and purified using the same process as for BBEP.

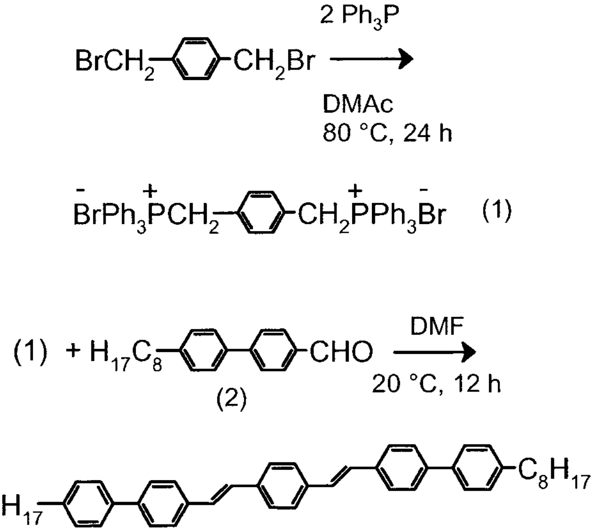

8H-BBEP

**Figure A.5:** Synthesis scheme for 8H-BBEP.

# Appendix B
# Processing Recipes

## B.1 Sample Preparation

In this section, we summarize all of the sample pre-processing recipes used in this work.

1. Photoresist s1813 spun at 5000 RPM for 30 seconds,
2. Bake 5 minutes at 115 °C,
3. Etch 5 or 10 minutes in 7:1 buffered oxide etch (depending on thermal oxide thickness),
4. Rinse in DI water,
5. Strip photoresist in hot PRS-1000 (approximately 15 minutes)
6. Rinse 15 minutes in room temperature acetone,
7. Rinse 15 minutes in hot isopropyl alcohol,
8. Rinse in DI water,
9. Plasma descum for 45 seconds to remove residual photoresist.

**Recipe B.1**: Backside oxide removal for top contact OFETs only.

1. Soak samples in the organic clean solution (RCA1) for 15 minutes,
2. Remove samples and rinse in DI water for 30 seconds,
3. Soak samples in the ionic clean solution (RCA2) for 15 minutes,
4. Remove samples and rinse in DI water until resistivity is "normal".

**Recipe B.2**: Wafer cleaning process.

## B.2 Bottom Contact OFET Fabrication

Recipes used in the fabrication of bottom contact OFETs.

1. Photoresist LOR-5a spun at 3000 RPM for 30 seconds,
2. Bake 5 minutes at 170°C,
3. Photoresist s1813 spun at 5000 RPM for 30 seconds,
4. Bake 1 minute at 115°C,
5. Expose 4 seconds at 12.5 $mW/cm^2$ in mask aligner to transfer pattern,
6. Develop in LDD 26 for exactly 150 seconds,
7. Rinse in DI water and blow dry.

**Recipe B.3**: Patterning process for metallic electrodes in bottom contact OFETs.

1. Prime samples with HMDS (1 minute exposure),
2. Photoresist s1813 spun at 5000 RPM for 30 seconds,
3. Bake 5 minutes at 115°C,
4. Expose 5 seconds at 12.5 mW/cm$^2$ in mask aligner to transfer pattern,
5. Develop 60 seconds in MF321 developer,
6. Bake 4 minutes at 135°C to stabilize photoresist,
7. Plasma descum for 45 seconds to remove HMDS from exposed areas,
8. Etch 6 minutes in 7:1 Buffered oxide etch,
9. Rinse in DI water,
10. Strip photoresist in acetone (or J-100 if needed),
11. Rinse 2 minutes in hot isopropyl alcohol,
12. Rinse 10 minutes in DI water,
13. Plasma descum for 45 seconds to remove residual photoresist.

**Recipe B.4**: Process for defining and etching the gate dielectric layer.

When a simple single layer lift-off process was used, the resulting metallic electrodes would resemble those shown in Figure B.1. A metal trace on the $SiO_2$ surface is shown in (a) from the top and (b) in cross-section. Part (c) illustrates a magnified view of the indicated section of (a). The discontinuity in the pentacene film caused by the delamination of the metal is obvious. This creates extremely poor metal-semiconductor contacts.

When the bilayer photoresist process is used we obtain sidewall profiles as shown in Figure B.2. The metal traces do not exhibit the delamination or cusping as shown in Figure B.1.

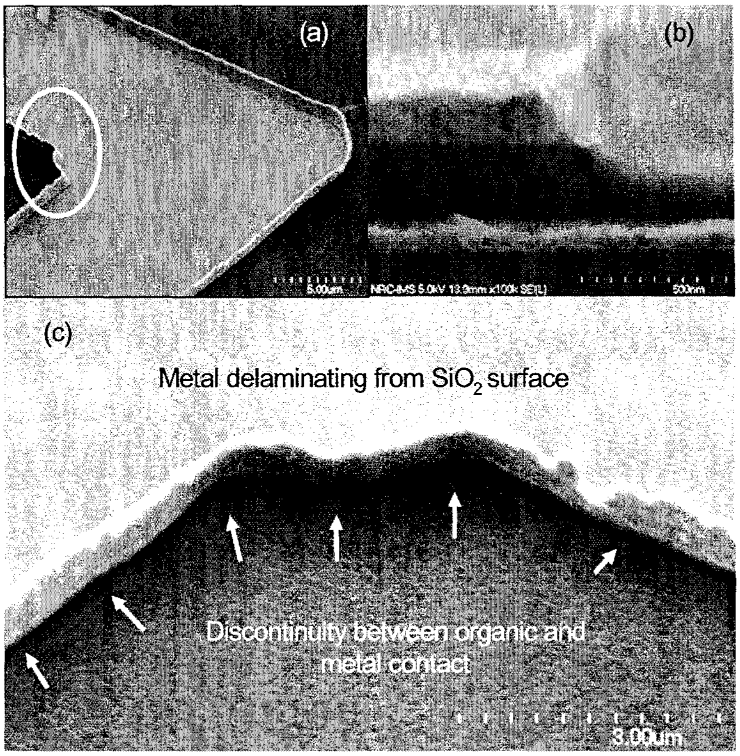

**Figure B.1:** (a) Metal trace on a BC-OFET without bi-layer photoresist recipe. (b) is a cross-sectional view of the device. (c) is an enlargement of the indicated portion of (a). The discontinuity caused by the delamination of the metal is clearly visible.

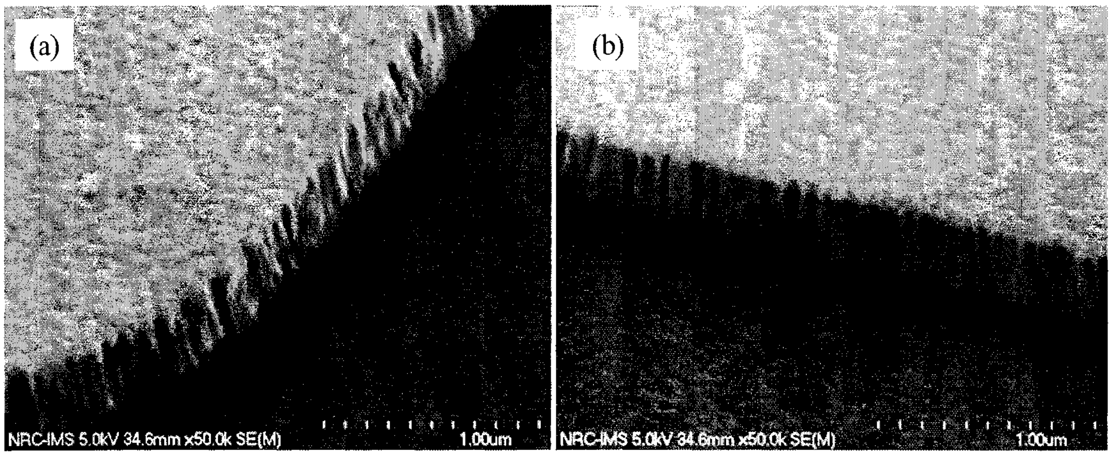

**Figure B.2:** Sidewall profile of a BC-OFET using the bi-layer photoresist lift off process.

## B.3 OLED Fabrication Process

Recipes for the fabrication of OLEDs on ITO coated glass substrates.

1. Photoresist s1813 spun at 5000 RPM for 30 seconds,
2. Let dry 5 minutes in air,
3. Bake 5 minutes at 110°C,
4. Expose 7.5 seconds at 12.5 mW/cm$^2$ in mask aligner to transfer anode pattern,
5. Expose 60 seconds at 12.5 mW/cm$^2$ in mask aligner to remove edge bead,
6. Develop approximately 60 seconds in MF321 developer,
7. Rinse 5 minutes in DI Water ,
8. Bake 5 minutes at 135°C,
9. Etch 15 minutes in a 25:25:2 $H_2O$:HCl:$HNO_3$ acid solution with agitation,
10. Rinse in DI water,
11. Strip photoresist in acetone (or J-100 if needed) in ultrasonic cleaner,
12. Rinse 5 minutes in isopropyl alcohol at 65°C in ultrasonic cleaner.

**Recipe B.5**: ITO patterning process.

1. Photoresist s1813 spun at 5000 RPM for 30 seconds,
2. Let dry 5 minutes in air,
3. Bake 5 minutes at 110°C,
4. Expose 7.5 seconds at 12.5 mW/cm$^2$ in mask aligner to transfer spacer pattern,
5. Develop approximately 60 seconds in MF321 developer,
6. Rinse 5 minutes in DI Water ,
7. Bake 5 minutes at 135°C,

**Recipe B.6**: Integrated photoresist spacer process.